LASER-ENABLED TREATMENTS FOR SURFACE FUNCTIONALISATION: FROM DESIGN TO INDUSTRIAL APPLICATIONS

by

THEMISTOKLIS KARKANTONIS

A thesis submitted to the University of Birmingham for the degree of

DOCTOR OF PHILOSOPHY

Department of Mechanical Engineering

School of Engineering

College of Engineering and Physical Sciences

The University of Birmingham

January 2023

ABSTRACT

Plastic materials have become a ubiquitous part of our economy, and as a result their improper disposal can pose high risks to the ecosystem. Although recycling can help to mitigate plastic waste, the sustainable management of unclean/contaminated ones due to fouling is still a challenge. Lubricant-Impregnated Surfaces (LIS) have gained much attention recently because of their excellent anti-adhesive performance against various liquids. Compared to other surface modification techniques that are capable of producing such bio-inspired surfaces, Laser-based Micro-Machining (LMM) offers attractive benefits especially when considering its flexibility, reliability and selectivity. However, intrinsic shortcomings of this technology with respect to high-throughput, cost-effectiveness and 3D processing hamper its broader application at an industrial scale. Therefore, the research reported in this thesis aims to address these key limitations and thus to enable the industrial uptake of LMM for functionalising surfaces. In particular, a cost-effective process chain, which combines LMM and polymer micro/nano replication technologies, is proposed to fabricate polymer-based surfaces with long-lasting multifunctional responses. Such functional surfaces were achieved by lubricant impregnation of Laser-Induced Periodic Surface Structures (LIPSS), and their suitability for food packaging and optical lens was investigated. Thereafter, an alternative laser surface treatment was demonstrated to generate highly regular and uniform LIPSS by utilising cost-effective nanosecond pulsed lasers, and thus to reduce even further the manufacturing costs in producing polymer replicas with such textured topographies. Lastly, a generic method for assessing the capabilities and limitations of simultaneous multi-axis laser strategies for processing complex 3D parts/replication masters is presented and validated for a given multi-axis LMM system.

ACKNOWLEDGEMENTS

I would like to dedicate this thesis to everyone who played a decisive role during this incredible journey. First and foremost, I would like to express my deepest gratitude to my academic supervisor, Prof. Stefan Dimov, for his invaluable support, guidance and patience over these past four years. I am also extremely thankful to my industrial supervisor, Dr. Tian Long See, for sharing his knowledge/expertise with me and giving constructive feedback. Additionally, words cannot describe my appreciation to The University of Birmingham and Manufacturing Technology Centre as this endeavour would not have been possible without their financial support.

I would like to extend my sincere thanks to my colleagues from the "Laser Lab", Anvesh Gaddam, Pavel Penchev and Vahid Nasrollahi, whose practical suggestions and experience were of vital importance in the completion of this research. Thanks should also go to my office mates, Hoang Le and Adam Szekely, for their moral support and all the good moments (inside and outside the Staff House) that we enjoyed during this period.

Lastly, I could not have done this journey without my family (Spyridon Karkantonis, Maria Poultidou and Nikolaos Karkantonis) and my partner (Ioanna Kila), whose unconditional love and support were a source of inspiration for me to carry on the hard work.

TABLE OF CONTENTS

ABSTRACT i

ACKNOWLEDGEMENTS ii

TABLE OF CONTENTS iii

LIST OF FIGURES ix

LIST OF TABLES xxi

LIST OF ABBREVIATIONS xxiii

LIST OF SYMBOLS xxv

LIST OF PUBLICATIONS AND PRESENTATIONS xxviii

CHAPTER 1: INTRODUCTION 1

1.1. Motivation 1

1.2. Research aims and objectives 4

1.3. Thesis organisation 7

References 9

CHAPTER 2: LITERATURE REVIEW 13

2.1. Biological structures with special wettability 13

2.2. Wettability and superhydrophobicity 17

2.3. Lubricant-impregnated surfaces 21

2.3.1. Design principles and applications 21

2.3.2. Fabrication methods 26

2.3.3. Infusing lubricants 29

2.3.4. Durability 30

2.3.5. Applications in food packaging and optical medical devices: state-of-the-art, properties and durability 34

2.4. Laser-based micro machining technology 38

2.4.1. Fundamental principles of lasers 38

2.4.2. Laser-material interactions 41

2.4.3. Laser processing setups 44

2.4.4. Laser-enabled surface treatments 47

2.4.5. Multi-axis laser processing 53

2.5. Synopsis of open research questions 57

References 59

CHAPTER 3: FEMTOSECOND LASER-INDUCED SUB-MICRON AND MULTI-SCALE TOPOGRAPHIES FOR DURABLE LUBRICANT IMPREGNATED SURFACES FOR FOOD PACKAGING APPLICATIONS 87

Abstract 88

3.1. Introduction 89

3.2. Materials and methods 92

3.2.1. Fabrication of sub-micron textured metallic moulds 92

3.2.2. Polymer micro/nano replication and LIS preparation 95

3.2.3. Surface characterisation 96

3.2.4. LIS durability analysis 97

3.3. Results and discussion 98

3.3.1. Analysis of surface topographies 98

3.3.2. Wettability characterisation 102

3.3.3. Durability characterisation of LIS 105

3.3.3.1. Vibration assessments 105

3.3.3.2. Shear assessments 108

3.3.3.3. Immersion assessments 109

3.4. Conclusions 110

Acknowledgements 111

References 113

CHAPTER 4: LASER-ENABLED SURFACE TREATMENT OF DISPOSABLE ENDOSCOPE LENS WITH SUPERIOR ANTIFOULING AND OPTICAL PROPERTIES 119

Abstract 120

4.1. Introduction 121

4.2. Materials and methods 125

4.2.1. Fabrication of metallic masters 125

4.2.2. Fabrication of lubricant impregnated polymer lenses 127

4.2.3. Morphology and optical characterisation 128

4.2.4. Wettability characterisation 129

4.2.5. Durability characterisation 130

4.2.6. Anti-fouling characterisation 130

4.2.7. Proof-of-concept demonstration 132

4.3. Results and discussion 132

4.3.1. Surface morphology analysis 132

4.3.2. Wettability analysis 136

4.3.3. Durability of LIS under shear flow conditions 138

4.3.4. Optical analysis 142

4.3.5. Anti-fouling properties 144

4.3.5.1. Anti-fogging and blood fouling resistance 144

4.3.5.2. Protein and microalgae fouling resistance 145

4.3.6. Pilot application 149

4.4. Conclusions 152

Supporting Information 153

Acknowledgements 153

References 154

CHAPTER 5: THE INFLUENCE OF PROCESSING ENVIRONMENT ON LASER-INDUCED PERIODIC SURFACE STRUCTURES GENERATED WITH GREEN NANOSECOND LASER 162

Abstract 163

5.1. Introduction 164

5.2. Materials and methods 167

5.2.1. Experimental setup and process parameters 167

5.2.2. Surface characterisation techniques 170

5.3. Results and discussion 171

5.3.1. LIPSS evolution and quality in ambient environment 171

5.3.2. LIPSS quality in argon gas environment 177

5.3.3. Surface chemistry analysis 180

5.3.4. Contact angle analysis 185

5.4. Conclusions 187

Acknowledgments 188

References 189

CHAPTER 6: LASER MICRO-MACHINING OF FREEFORM SURFACES: ACCURACY, REPEATABILITY AND REPRODUCIBILITY ACHIEVABLE WITH MULTI-AXIS PROCESSING STRATEGIES 195

Abstract 196

6.1. Introduction 197

6.2. Multi-axis simultaneous laser processing 200

6.3. Methodology 202

6.3.1. Effective processing window 203

6.3.2. Dynamic effects of optical beam deflectors 204

6.3.3. Method for assessing simultaneous multi-axis laser processing strategies 205

6.4. Pilot implementation 210

6.4.1. Experimental set-up and analysis tools 211

6.4.2. Process design requirements 215

6.4.2.1. Effective processing window 215

6.4.2.2. Dynamic effects of optical beam deflectors 216

6.4.3. Design of laser processing tests 217

6.4.4. Uncertainty assessment 220

6.4.5. Results and discussion 222

6.4.5.1. Laser processing test 1 223

6.4.5.2. Laser processing test 2 226

6.4.5.3. Laser processing test 3 and 4 229

6.5. Conclusions 234

Acknowledgments 237

References 238

CHAPTER 7: CONTRIBUTIONS TO KNOWLEDGE AND FUTURE RESEARCH 244

7.1. Contributions to knowledge 244

7.2. Future research 251

APPENDIX 253

LIST OF FIGURES

Chapter 2

Fig. 2.1. Examples of biological structures exhibiting superhydrophobicity and low liquid-solid adhesion: (a) photo of a water droplet covered with lipoidic particles on a lotus leaf and SEM micrographs of the plant's surface topography at different magnifications [14]; (b) image of a blue butterfly at different magnifications [15]; a water spider walking on water and SEM images of its feet surface at different magnifications [16]; photo of a rain droplet formed on rice leaf and SEM micrographs of the leaf's surface topography at different magnifications [17]. 14

Fig. 2.2. Natural organisms showing superhydrophobicity with high adhesion: optical and SEM images of a (a-d) rose petal [21] and (e) gecko's foot [22] surfaces. *Note:* the characters ST, SP and BR in (e) refer to the seta, spatula and branch, respectively. 15

Fig. 2.3. The surface morphology of Nepenthes pitcher plant: optical and SEM images showing the unique structural topography of the peristome's upper rim [18]. 16

Fig. 2.4. Classification of surfaces based on apparent CAs [28]. 17

Fig. 2.5. Methods for characterising the adhesive properties of surfaces: schematic diagram of (a) a droplet that is just starting to flow down an inclined surface at a particular CSA [33] and (b) the needle method used for measuring the advancing and receding CAs [34]. 18

Fig. 2.6. The promising application fields where SHS with low adhesion can be successfully utilised. 19

Fig. 2.7. Fundamental wetting theories: (a) Young's model, (b) Wenzel's model and (c) Cassie–Baxter model [51]. 21

Fig. 2.8. Schematic illustration of a substrate infiltrated with lubricant. 22

Fig. 2.9. Schematic representation of a static drop on LIS when the spreading coefficient is positive (left) and negative (right) [58]. 23

Fig. 2.10. Schematic diagram showing the possible wetting configurations underneath a water droplet placed on LIS when the spreading coefficient is positive (top) and negative (bottom) [58]. 24

Fig. 2.11. The various promising applications of LIS in healthcare sector [87]. 26

Fig. 2.12. LIS produced from inherently porous materials: (a) an illustration of the steps involved to prepare LIS with a colloidal approach based on inverse opal scaffolds (left) and SEM micrograph of the as-prepared surface topography (right) [94]; (b) schematic diagram (right) and SEM image (left) of the Teflon-based porous nanofiber surface topography that was impregnated with a lubricant to obtain LIS [57]. 27

Fig. 2.13. SEM micrographs of surfaces covered with highly regular and homogeneous micropillar structures, which were fabricated through lithographic processes [102]. 28

Fig. 2.14. Schematic illustration of the laser-enabled surface treatment used to fabricate LIS on carbon steel [103]. 28

Fig. 2.15. Shear-induced lubricant depletion: (a) SEM micrograph of the sanded PTFE surface topography; (b) schematic diagram of shear-induced loss of lubricant infused into the PTFE-sample; (c) plot showing the pressure drop over time as a result of lubricant depletion [128]. 31

Fig. 2.16. Schematic illustrations showing lubricant depletion from the surface structures due to: (a) gravitational forces; (b) evaporation; (c) droplet impact; (d) ice formation; (e) cloaked liquid droplets; (f) shear forces [102]. 32

Fig. 2.17. Durability of LIS under shear flow conditions: (a) a cross-section of the microfluidic flow cell prior to conducting the experiment. The green colour represents the infused lubricant;

(b) lubricant depletion over time and the determination of a steady-state length $L\infty$. *Note:* the shear-induced lubricant depletion was investigated at a constant flow rate of 2 mL/min and shear stress of 5.2 Pa [121]. 33

Fig. 2.18. Schematic diagram depicting the main components of a laser source. 39

Fig. 2.19. A graph showing the applicability of different ultrashort pulse laser oscillator technologies [155]. 40

Fig. 2.20. Absorptivity of common metals at different laser wavelengths in the (a) wide spectrum [161] and (b) short-wavelength spectrum [162]. 41

Fig. 2.21. Laser-material interactions: (a) SEM micrographs of a round hole drilled in a 100 μm thick metallic substrate by a femtosecond (left) and a nanosecond (right) pulsed laser [173]; (b) graphical illustrations of the laser-material interactions involved in the ultrashort (left) and short (right) ablation regimes [174]. *Note:* Based on the processing parameters provided in [173], the laser percussion-drilled holes presented in (a) were made with a beam spot size of ~ 175 μm. 43

Fig. 2.22. A typical laser setup for multi-axis processing [175]. 44

Fig. 2.23. Optical elements in laser processing: (a) schematic illustration of a quarter waveplate for converting the linearly polarised beam into circularly polarised one [181]; (b) intensity profiles of a typical Gaussian beam (left) and flat-top beam (right). (Image courtesy of IL Photonics); (c) diagram of a diffractive optical element used to split the input laser beam. (Image courtesy of Holo/Or); (d) the two common types of F-theta lenses used in laser material processing and their principal function. 46

Fig. 2.24. Cost-effective process chain for producing hydrophobic polymer surfaces by combining LMM and polymer replication technologies: (a) schematic diagram of the manufacturing procedures involved; (b) the employed laser processing setup. The characters

d and h indicate the pulse-to-pulse and hatch distance, respectively; (c) and (d) schematic illustrations of the injection moulding procedure followed to fabricate the textured polymer replicas [191]. 48

Fig. 2.25. Plot presenting the actual number of published papers on LIPSS between the years 1980 and 2020 [202]. 49

Fig. 2.26. Influence of laser polarisation on LIPSS formation: (a-c) SEM micrograph of highly regular LIPSS produced on Titanium, Molybdenum and Steel with an ultrashort laser, respectively [206]. The yellow arrows represent the direction of laser polarisation when processing the different metallic materials; (d) SEM image, with a 2D Fast Fourier Transform (2D-FFT) inset, of triangular LIPSS formed upon irradiation with a circularly polarised laser beam [207]. 51

Fig. 2.27. SEM micrographs of different MS surface topographies textured on SS: (a-b) microscale posts and grooves fully covered by nano-ripples, respectively [219]; (b-c) microscale grooves and square-shaped pillars decorated with nanoparticles, respectively [221]. *Note:* The surface topographies presented in (a-b) were fabricated by a femtosecond pulsed laser, whilst the ones shown in (c-d) were produced with a nanosecond pulsed laser. 52

Fig. 2.28. Schematic illustration of processing errors generated at the overlapping regions of laser beam [226]. 53

Fig. 2.29. 3D laser processing strategies: (a) interface of the software developed in [227] (left) and image of a pattern engraved on a freeform surface using this method (right); (b) triangulation of a curved surface in CALM software (left) and the actual feature machined on the surface (right) [228]; (c) illustration of the method used in [229] to project the patterns onto a freeform part (left) and image showing the patterns textured on its surface. 55

Chapter 3

Fig. 3.1. The experimental set-ups: (a) a schematic of the used beam delivery system; (b) two scanning strategies for fabricating LIPSS (left) and MS (right) topographies; (c) an illustration of the process chain used to produce LIS. 94

Fig. 3.2. The surface topography analysis of LIPSS substrates: (a-c) SEM micrographs SS, PS and PP substrate, respectively with a 2D-FFT image inset in (a); (d-f) AFM micrographs of SS, PS and PP substrates, respectively; (g-i) plots showing height profiles of SS, PS and PP substrates, respectively. Scale bar: 5 μm. 99

Fig. 3.3. The surface topography analysis of MS substrates: (a-c) the 3D micrographs of SS, PS and PP substrates, respectively; (d-f) plots showing height profiles on SS, PS and PP substrates; (g) the SEM micrograph of SS topographies (scale bar: 20 μm) with a magnified view of sub-micron features on pillars in the inset (scale bar: 5 μm); (h-i) the AFM micrographs showing sub-micron features on top of the pillar of PS and PP replicas, respectively.....101

Fig. 3.4. The water CA measurements obtained after two weeks: (a) static water CA on as-received, textured and LIS topographies of SS, PS and PP substrates; (b) Images of the water droplet on textured and LIS of the SS and PP substrates.....103

Fig. 3.5. CSA on as-received, textured and LIS topographies of the SS, PS and PP substrates for: (a) water, (b) milk and (c) honey droplets. (d) An image of water, milk and honey droplets on the MS-LIS surfaces of PS and SS samples together with different droplet shedding behaviours is shown.....104

Fig. 3.6. An investigation into the lubricant retention capacity of LIS: (a) the experimental setup used for subjecting LIS substrates to vibration; (b) the lubricant retention capacity of MS topographies on the PS and PP substrates with time; (c) an illustration of vibration-induced loss of lubricant infused into LIPSS and MS topographies. 106

Fig. 3.7. CSA measurements of water (a), milk (b) and honey (c) droplets on LIS topographies before and after subjecting them to vibrations; (d) Images showing small 'satellite' droplets left behind by the milk droplet on MS-LIS topographies of PP and PS after the vibration test. 107

Fig. 3.8. Analysis of lubricant depletion due to shear forces: (a) an illustration of the shear test performed on LIS topographies; the variations of sliding velocity with the increasing number of milk (b) and honey (c) droplets on the PP surfaces with LIS topographies. *Note:* the red lines show the position where droplet velocity reached zero abruptly. 109

Fig. 3.9. Analysis of the shedding behaviour of lubricant infused textured substrates: (a) the sliding behaviour of 250 µL honey and ketchup droplets on as-received and LIPSS - LIS treated PP; (b) the dripping behaviour of as-received and LIPSS-LIS and MS-LIS treated PP and PS substrates after honey dipping cycles. 110

Chapter 4

Fig. 4.1. An overview of the process chain employed to fabricate disposable endoscope lenses. 125

Fig. 4.2. Surface morphologies of LIPSS: (a-c) SEM and (d-f) 3D AFM micrographs of LIPSS on the SS, PC and COC surfaces, respectively; (g) a plot showing the surface profiles of LIPSS on the SS master and PC and COC replicas. Scale bar: 6 µm. 134

Fig. 4.3. Surface morphologies of MS: (a-c) the 3D height map and (d-f) the SEM images of MS on the SS master and PC and COC substrates, respectively; (g-h) the plots showing the height profiles of micro-peaks on the SS master and PC and COC substrates along X and Y, respectively. Scale bar: 20 µm. 135

Fig. 4.4. Wettability analysis: (a) the static CAs measured on as-received, textured and lubricated surfaces of PC and COC substrates; (b) representative images of the water droplet

on textured and lubricated surfaces of the COC substrate; the CSAs obtained on as-received, textured and lubricated surfaces of the PC and COC substrates for (c) water and (d) Xanthan Gum solution; the CSAs obtained on the lubricated surfaces of (e) PC and (f) COC. 138

Fig. 4.5. The shear-induced lubricant depletion: (a) an image showing a tilted substrate before the shear test and a water droplet sliding on the LIPSS-LIS sample impregnated with 5 cSt lubricant; (b-c) the shedding velocities as a function of the increasing number of water droplets deposited on the MS-LIS and LIPSS-LIS substrates for the investigated lubricant viscosities, respectively. Inset shows an image of water droplet pinned to the surface of the LIPSS-LIS sample after the lubricant depletion; (d) an illustration showing the lubricant depletion on LIPSS and MS topographies; (e) an illustration showing lubricant redistribution after a droplet leaving the LIPSS-LIS treated surface; (f) images depicting the loss of the infused lubricant from the MS-LIS samples. 141

Fig. 4.6. Analysis of optical properties: (a) the transmittance of the as-received, textured and lubricated surfaces of PC and COC, respectively; (b) schematic illustrations of the improved light transmittance after the lubricant infusion; (c) the captured images of a logo through the as-received, textured and lubricated PC surfaces. 143

Fig. 4.7. Evaluation of anti-fouling/anti-fogging performance: (a) the shedding behaviour of 10 μL blood droplet on the PC plain and LIPSS-LIS samples; (b) the fouling resistance of PC and COC plain and LIPSS-LIS samples after the blood dipping test. It should be noted that the plain back sides of LIPSS-LIS samples were covered with a yellow coloured tape to prevent their fouling by blood; (c) the sequential images taken from the PC plain and LIPSS-LIS samples after their exposure to hot vapour; (d) fluorescence micrographs depicting the protein adsorption onto the PC and COC plain and LIPSS-LIS samples; (e) a plot showing the fluorescence intensity of adsorbed protein as measured on the PC and COC plain and LIPSS-

LIS samples; (f) the experimental setup used for assessing and quantifying the adhesion of algae onto the surfaces; (g) autofluorescence and optical images of algae adhesion onto the PC and COC plain surfaces together with their respective LIPSS-LIS samples before and after subjecting them to shear forces; (h) the area coverage with algae calculated on the samples. 148

Fig. 4.8. A pilot application of the LIPSS-LIS treated endoscope lenses: (a) the test procedure used to verify the vision performance after integrating the plain (left) and LIPSS-LIS (right) treated COC lenses into an endoscope device; (b) the blood dipping experimental setup and the visual fields retained by the plain and LIPSS-LIS treated COC lenses after a single dip; (c) the visible area in percentages of an endoscope with LIPSS-LIS lenses as a function of the dipping cycles number. *Note:* Insets in (c) depict the surface of LIPSS-LIS lens after a certain number of dips; (d) sequential images showing the field of view after 35, 40, 45 and 50 dips, again for the LIPSS-LIS lens. 151

Chapter 5

Fig. 5.1. Schematic illustration of: (a) laser processing set-up; (b) the process used to texture the samples in argon environment; (c) the scanning strategy used to generate LIPSS. The optical image shows diffraction colors resulted from generated LIPSS (scale bar: 10 mm). 168

Fig. 5.2. Evolution of LIPSS with the increase of accumulated fluence at a scanning speed of 2 m/s (scale bar: 10 μm). *Note:* The black dashed rectangle on the upper right corner is a magnified view showing the first LIPSS formation. 172

Fig. 5.3. (a) An illustration of the experimental set-up to obtain first-order diffraction blue light images from LIPSS. (b) The periodicity of LIPSS produced with 209 pulses and pulse fluences varying from 150.5 up to 220.5 mJ/cm^2. (c) 2D FFT image showing the regularity of

the LIPSS generated with 209 pulses and pulse fluence of 171.2 mJ/cm^2. The LIPSS formation with (d) the increase of pulse fluence in the range of 153.6 to 220.5 mJ/cm^2 and a constant effective number of pulses set at 126 (scale bar: 5 μm) and (e) the increase of effective number of pulses from 126 to 209 at a constant pulse fluence of 171.2 mJ/cm^2 (scale bar: 5 μm). The corresponding blue light diffraction images are also shown. *Note*: The yellow double-sided arrows represent laser beam polarisation vector. 174

Fig. 5.4. Oxidation colors on SS substrates: (a) the matrix shows the colors appearing at high pulse fluences and a higher number of pulses (scale bar: 5 mm); (b) the corresponding magnified optical images showing yellow, orange, and purple colors as a result of the increasing accumulated fluence (scale bar: 1 mm). The corresponding inset image shows the blue color at the edge of the squares due to beam deceleration/acceleration and the resulting high accumulated fluence there. 176

Fig. 5.5. LIPSS morphologies as a function of the pulse fluence and the effective number of pulses..... 177

Fig. 5.6. (a) The SEM images of LIPSS generated under ambient and argon atmospheres with 209 pulses and pulse fluences of 150.5 and 171.2 mJ/cm^2 (scale bar: 5 μm). Their corresponding blue light diffraction images are shown as insets. (b) Comparison of blue light intensities of LIPSS generated with pulse fluences of 150.5, 171.2 and 206.2 mJ/cm^2 and 209 pulses in ambient and argon atmospheres. *Note*: The yellow double-sided arrows show the laser beam polarization vector. 178

Fig. 5.7. (a) AFM images of LIPSS and (b) the height profiles of the samples processed in ambient and argon environments at a pulse fluence of 171.2 mJ/cm^2 and an effective number of 209 pulses. (c) The comparison of the LIPSS amplitude at different pulse fluences and a fixed effective number of 209 pulses. 179

Fig. 5.8. The XPS survey spectra for: (a-d) LIPSS fabricated on SS substrates with 209 pulses and pulse fluences of 150.5 and 171.2 mJ/cm^2 after irradiation in argon and air environments, respectively; (e) untreated SS surface. 181

Fig. 5.9. High-resolution O1s spectra of LIPSS treated under (a) argon and (b) ambient environments. 182

Fig. 5.10. High-resolution XPS spectra of (a) Cr2p and (b) Fe2p of untreated surface and LIPSS generated in argon and ambient environments. 184

Fig. 5.11. An illustration showing the influence of processing environment on oxide layer formation at low and high accumulated fluences with a green nanosecond laser. 185

Fig. 5.12. Contact angle evolution as a function of time in number of days on untreated and LIPSS treated substrates in the air and argon environments. 186

Chapter 6

Fig. 6.1. A schematic representation of: (a) a single beam path on a curved surface; (b) a geometry projected on a spherical surface that should be scribed using a simultaneous multi-axis LMM strategy. *Note:* The red and blue dashed lines in (b) represent the motions of optical axes when the laser source is inactive. 202

Fig. 6.2. The sequence of steps to execute the proposed assessment method. 203

Fig. 6.3. Negative dynamic effects of beam deflectors at a scanning speed of 500 mm/s without applying any compensation method: (a) dimensional discrepancies between the programmed (red lines on the left side) and the actual beam scribing (line-like structures on the right side); (b) a height map of the processed area (left) and surface profile (right) of a pocket with non-uniform ablation at the walls (beam trajectories change points). *Note:* The blue profile in (b) shows the effect of the beam acceleration and deceleration in executing the processing strategies. 205

Fig. 6.4. The LPTs in the proposed method for assessing the performance of different simultaneous multi-axis LMM strategies: (a) a schematic illustration of the patterns that should be scribed on the spherical surface in the four LPTs; (b) the scribing strategies employed to produce the four patterns in the tests. 208

Fig. 6.5. Flowchart summarising the procedure to evaluate the performance of a LMM system. 210

Fig. 6.6. Schematic illustration of the employed multi-axis LMM set up. 214

Fig. 6.7. The effective ablation range analysis: (a) the scribing lines produced with a single pass that were used to identify the acceptable FOD limit; (b) the measured depth of the scribing lines at different FODs. 216

Fig. 6.8. Analysis of negative dynamic effects along the optical axes: (a) the test procedure used to identify the acceleration/deceleration regions along the beam vectors; (b) the varying craters' distance along one of the beam vectors used to determine the respective acceleration/deceleration regions at a scanning speed of 100 mm/s. 217

Fig. 6.9. The implemented LPTs to assess the performance of the employed multi-axis LMM system. 219

Fig. 6.10. The measurements conducted by using the two methods: (a) a representative 3D image of the scribing lines with 10 measurements between two consecutive ones; (b) a plot of the standard uncertainties and average values obtained when measuring the distances between two scribing lines with the three objectives and the two methods. 222

Fig. 6.11. The patterns in PS 1 that were produced with the four LPTs: (a-d) top view of the four patterns in PS 1 produced with a scanning speed of 10 mm/s; (e) a close view of three scribing lines in (b), which depicts the procedure followed to measure the d_1 (the arrow red dashed line), d_2 (the arrow blue line) and g (the orange 90^0 angle sign). *Note:* The black arrow

dashed lines and numbers in (a-d) signify the scribing lines measured on the patterns produced in the four LPTs. Scale bar: 500 μm. 223

Fig. 6.12. The effects of multi-axis laser processing errors on d_1, d_2 and g of the scribing lines produced in LPT 1 under quasi-static (a-c) and dynamic (e-f) conditions, respectively. 226

Fig. 6.13. The effects of multi-axis processing errors on d_1, d_2 and g of the scribing lines produced in LPT 2 under quasi-static (a-c) and dynamic (e-f) conditions, respectively. 229

Fig. 6.14. The effects of multi-axis processing errors on d_1, d_2 and g of the scribing lines produced in LPTs 3 (a-c) and 4 (e-f) under quasi-static conditions, respectively. 231

Fig. 6.15. The effects of multi-axis processing errors on d_1, d_2 and g of the scribing lines produced in LPTs 3 (a-c) and 4 (e-f) under dynamic conditions, respectively.....234

LIST OF TABLES

Chapter 3

Table 3.1. Optimum laser processing parameters for LIPSS and MS topographies. 94

Table 3.2. Material and processing conditions for hot embossing of PS and PP replicas. 96

Chapter 4

Table 4.1. The key laser parameters used to produce the MS and LIPSS onto the SS moulds together with their corresponding processing time. 127

Table 4.2. The optimised settings used to produce the PC and COC replicas together with their respective glass transition temperatures. 128

Chapter 5

Table 5.1. Elemental composition extracted from the XPS survey spectra of untreated and laser processed SS surfaces. 180

Chapter 6

Table 6.1. The processing strategies with their respective simultaneous axes motions employed in executing the four tests on a LMM system with either B or A rotary-axis. 207

Table 6.2. Technical specifications of component technologies (as provided by the manufacturer) integrated into the LS4 workstation. 212

Table 6.3. The measurement uncertainty associated with the three objectives when using the 2DImageMeasurement module. 221

Appendix

Table A.1. The water CA and CSA values measured on all the tested plain surfaces. 253

Table A.2. The water CA and CSA values measured on all the textured topographies. 253

Table A.3. The water CA measurements obtained from all the different LIS substrates. ...254

Table A.4. The water CSA and CAH values measured on the various LIS substrates. 254

Table A.5. The CSA values of milk and honey droplets measured on the plain, textured and LIS topographies of SS, PS and PP substrates. 255

Table A.6. The CSA values of water, milk and honey droplets measured on the various LIS substrates after subjecting them to vibrations. 256

Table A.7. The CSA values obtained from the plain, textured and LIS topographies of PC and COC substrates for droplets of Xanthan Gum solution. 256

Table A.8. The CSA values of pH-adjusted droplets measured on the LIS of PC and COC. 257

Table A.9. The evolution of water CA on the LIPSS produced in air and argon environments. 257

LIST OF ABBREVIATIONS

AFM	Atomic Force Microscopy
ARR	Accuracy, Repeatability and Reproducibility
CA	Contact Angle
CAD/CAM	Computer-Aided Design/Computer-Aided Manufacturing
CAH	Contact Angle Hysteresis
CBC	Cassie-Baxter State
CFSE	Carboxyfluorescein Succinimidyl Ester
COC	Cyclic Olefin Copolymer
CSA	Critical Sliding Angle
CV	Chlorella Vulgaris
FFT	Fast Fourier Transformation
FOD	Focal Offset Distance
FOV	Field Of View
FV	Focus Variation
HSFL	High Spatial Frequency LIPSS
LASER	Light Amplification by Stimulated Emission of Radiation
LIPSS	Laser-Induced Periodic Surface Structures
LIS	Lubricant-Impregnated Surfaces
LMM	Laser-based Micro-Machining
LPT	Laser Processing Test
LSFL	Low Spatial Frequency LIPSS
MS	Multi-scale Structures

PC	Polycarbonate
PP	Polypropylene
PS	Polystyrene (in Chapter 3), Pattern Set (in Chapter 6)
XPS	X-ray Photon Spectroscopy
SEM	Scanning Electron Microscope
SHS	Superhydrophobic Surfaces
SS	Stainless Steel

LIST OF SYMBOLS

Chapter 2

θ_A	Advancing contact angle
θ_R	Receding contact angle
θ_Y	Contact angle of a water droplet on an ideal smooth surface
γ	Interfacial surface energy
SV	Solid/Vapor interface
LV	Liquid/Vapor interface
SL	Solid/Liquid interface
θ_W	Contact angle of a water droplet in Wenzel state
θ_{CB}	Contact angle of a water droplet in Cassie–Baxter state
r	Roughness factor
f	Fraction of the liquid-air area
o	Infused lubricant
w	Water droplet
a	Ambient environment
S	Spreading coefficient
L_∞	Steady-state length

Chapter 3 and 4

S_a	Average surface roughness
f	Pulse repetition rate
P	Average power

v	Scanning speed
Ω	Beam spot radius
h	Hatch distance
O	Pulse overlap
φ_0	Pulse fluence
$\lambda_{excitation}$	Wavelength of excitation
$\lambda_{emmision}$	Wavelength of emission
E	Beam polarisation vector
l_c	Capillary length
γ	Surface tension
$\Delta\rho$	Density difference
g	Gravitational constant

Chapter 5

S_a	Average surface roughness
λ	Nominal wavelength
w_0	Beam spot radius
h	Hatch distance
v	Scanning speed
P	Average power
f	Pulse repetition rate
d	Pulse-to-pulse distance
N_{eff}	Number of pulses per unit area
F_0	Pulse fluence

F_{acc}	Accumulated fluence per unit area
m	Order of diffraction
θ	Incident angle
I	Intensity of diffracted light
t	Thickness of the oxide layer

Chapter 6

θ	Incident angle
h	Offset distance
d_1	Deviation in the length of machined lines
d_2	Deviation in the pitch of machined lines
g	Perpendicularity
M^2	Beam quality factor
u	Standard type A uncertainty
U	Overall uncertainty

LIST OF PUBLICATIONS AND PRESENTATIONS

A number of publications and presentations arose from the research conducted within the scope of this PhD thesis, which are listed below.

Journal publications as the lead author:

1. **T. Karkantonis**, A. Gaddam, T. L. See, S. S. Joshi, and S. Dimov, "Femtosecond laser-induced sub-micron and multi-scale topographies for durable lubricant impregnated surfaces for food packaging applications," *Surface and Coatings Technology*, vol. 399, p. 126166, 2020, doi: https://doi.org/10.1016/j.surfcoat.2020.126166.
2. **T. Karkantonis**, A. Gaddam, H. Sharma, G. Cummins, T. L. See, and S. Dimov, "Laser-Enabled Surface Treatment of Disposable Endoscope Lens with Superior Antifouling and Optical Properties," *Langmuir*, vol. 38, no. 37, pp. 11392-11405, 2022, doi: https://doi.org/10.1021/acs.langmuir.2c01671.
3. **T. Karkantonis**, A. Gaddam, X. Tao, T. L. See, and S. Dimov, "The influence of processing environment on laser-induced periodic surface structures generated with green nanosecond laser," *Surfaces and Interfaces*, vol. 31, p. 102096, 2022, doi: https://doi.org/10.1016/j.surfin.2022.102096.
4. **T. Karkantonis**, P. Penchev, V. Nasrollahi, H. Le, T. L. See, D. Bruneel, J. A. Ramos-de-Campos, and S. Dimov, "Laser micro-machining of freeform surfaces: Accuracy, repeatability and reproducibility achievable with multi-axis processing strategies," *Precision Engineering*, vol. 78, pp. 233-247, 2022, doi: https://doi.org/10.1016/j.precisioneng.2022.08.009.

Journal publications as a co-author:

1. A. Gaddam, H. Sharma, **T. Karkantonis**, and S. Dimov, "Anti-icing properties of femtosecond laser-induced nano and multiscale topographies," *Applied Surface Science*, vol. 552, p. 149443, 2021, doi: https://doi.org/10.1016/j.apsusc.2021.149443.
2. H. Le, C. Pradhani, P. Penchev, V. Nasrollahi, **T. Karkantonis**, Y. Wang, S. Dimov, and J. A. Ramos-de-Campos, "Laser precession machining of cross-shaped terahertz bandpass filters," *Optics and Lasers in Engineering*, vol. 149, p. 106790, 2022, doi: https://doi.org/10.1016/j.optlaseng.2021.106790.
3. H. Le, **T. Karkantonis**, V. Nasrollahi, P. Penchev, and S. Dimov, "MHz burst mode processing as a tool for achieving removal rates scalability in ultrashort laser micro-machining," *Applied Physics A*, vol. 128, no. 8, p. 711, 2022, doi: 10.1007/s00339-022-05864-8.
4. L. González-Fernández, A. Anagnostopoulos, **T. Karkantonis**, O. Bondarchuk, S. Dimov, M. Chorążewski, Y. Ding, Y. Grosu, "Laser-induced carbonization of stainless steel as a corrosion mitigation strategy for high-temperature molten salts applications," *Journal of Energy Storage*, vol. 56, p. 105972, 2022, doi: https://doi.org/10.1016/j.est.2022.105972.

Conference presentations:

1. 7th Industrial Laser Applications Symposium (ILAS), 24 – 25 March 2021, Virtual Attendance. (Oral Presentation)
2. 4th World Congress on Micro and Nano Manufacturing (WCMNM), Mumbai, India, 20 – 23 September 2021. (Oral Presentation)
3. 5th World Congress on Micro and Nano Manufacturing (WCMNM), Leuven, Belgium, 19 – 22 September 2022. (Oral Presentation)

Proceeding papers:

1. **T. Karkantonis**, P. Penchev, T. L. See, and S. Dimov, "Method for Assessing the Performance of Multi-Axis Laser Processing Strategies," *Proceedings of the World Congress on Micro and Nano Manufacturing (WCMNM)*, Leuven, Belgium, 2022.
2. H. Le, **T. Karkantonis**, V. Nasrollahi, P. Penchev, and S. Dimov, "Removal Rates Scalability with MHz Burst Mode Ultrashort Laser Processing," *Proceedings of the World Congress on Micro and Nano Manufacturing (WCMNM)*, Leuven, Belgium, 2022.

CHAPTER 1: INTRODUCTION

1.1. Motivation

Over the last decade, municipal solid waste has emerged as a major challenge for societies in developing countries [1]. Around 11.2 billion tons of such a waste is accumulated annually, with a significant amount of it not treated in a sustainable way and thus ending up in landfills [2]. Among the different types of solid waste, plastics represent a great part of this and their uncontrolled disposal is increasingly posing high risks to the ecosystem [3]. However, due to the wide applicability of plastic materials in industry, the rate of products with plastic components and/or packaging is constantly growing and they are expected to reach 500 million tons in three years' time [4]. To mitigate the environmental impact from such plastic wastes, a series of waste management strategies have been initiated by governments. For instance, there is a new European Union requirement, any plastic packaging must be eco-friendly, i.e. reusable or recyclable in a cost-efficient manner, to enter the market after 2030 [5]. Currently, although plastic products can be recycled, the sustainable management of unclean/contaminated ones is still a major barrier due to their relatively high recycling cost [6]. A typical example of that is the so-called difficult-to-empty packaging, where viscous food substances stick to their walls and hence requiring lengthy cleaning procedures prior to their recycling. In addition, biofouling of plastic components used in healthcare and medical sectors can lead to not only increasing recycling costs but also to severe microbial growth and surgical site infections [7, 8]. Therefore, a promising solution to overcome the aforementioned challenges is the fabrication of polymer-based surfaces that exhibit superior anti-adhesive and anti-biofouling characteristics with a minimal environmental footprint.

Generally, several biological structures in living organisms demonstrate such unique functionalities, which can serve as a source of inspiration for developing innovative products. In fact, considerable research efforts have been dedicated to designing and creating biomimetic structures by tailoring the wetting behaviour of materials [9]. More specifically, artificial Superhydrophobic Surfaces (SHS), inspired by lotus leaves, have gained much attention in the last decade due to their exceptional anti-wetting, anti-fouling/anti-bacterial and self-cleaning properties. These surfaces exhibit very low solid-liquid adhesion forces, and thus droplets can roll-off easily even at a small tilting angle [10]. Usually, the fabrication of a hierarchical surface topography to entrap air together with the use of low surface energy chemicals are required to achieve superhydrophobicity. However, the practical application of artificial SHS is strongly hampered by the poor long-term stability of their liquid-air interfaces, especially when they are exposed to liquids with low surface tension or subjected to external pressure and mechanical stresses [11]. Therefore, another surface functionalisation technique has gained a lot of attention recently, which is inspired by the Nepenthes pitcher plant and is referred to as Lubricant-Impregnated Surfaces (LIS). Unlike SHS, LIS rely on the formation of a smooth slippery interface by infusing a lubricating liquid into a textured scaffold [12]. Owing to their extreme liquid-repelling capabilities, long-lasting durability and optical transparency, this type of functional surfaces has emerged as a promising candidate to mitigate fouling and cross-contamination phenomena faced by various industrial sectors, e.g. food-processing, healthcare and medical technologies [13-15].

Based on the existing practices, the main step in producing LIS involves the fabrication of scaffolds first that are capable of stabilising/retaining lubricants. In this regard, a variety of traditional surface treatment methods, such as electrodeposition [16], chemical etching [17], sol-gel [18], self-assembly [19], have been deployed by researchers to modify the surface

topography and/or chemistry of materials. Nevertheless, inherent shortcomings of these technologies limit their broader use, especially when considering their scalability and environmental impact. On the contrary, Laser-based Micro-Machining (LMM) is an attractive alternative that offers relatively high processing accuracy, efficiency, and reliability. At the same time, it can be employed as a simple one-step surface treatment to selectively fabricate both micron and submicron, i.e. Laser-Induced Periodic Surface Structures (LIPSS), structures on almost any engineering material, including ceramics [20], glass [21] and polymers [22]. Compared to some other surface treatment methods, LMM does not require the use of hazardous chemicals and hence it is a much more eco-friendly process. However, it should be stated that direct LMM approaches for structuring large surface areas cannot be considered cost-effective because of their high operational costs, which in turn constrains their wider use by industry.

To address the aforementioned shortcoming, several approaches have been proposed to increase the efficiency of direct laser processing operations. In particular, these methods involve the usage of beam splitters [23], laser sources with burst mode capabilities [24] and high speed beam deflection systems [25, 26], e.g. polygon scanners. Even though such devices can reduce the overall processing cycle, they will substantially increase the required capital investment and ultimately the manufacturing costs. Therefore, indirect surface treatment methods are the prime option in achieving both cost-effective and high-throughput production of laser-enabled surface structures. Especially, the polymer replication, e.g. roll-to-roll, injection moulding and hot embossing processes, is a well-established method that can satisfy the requirements for mass production of plastic components. Therefore, a process chain for functionalising polymer surfaces by combining the capabilities of LMM with replication technologies can offer a much quick industrial uptake than any existing stand-alone direct laser

processing operation. At the same time, the use of much more cost-effective nanosecond laser sources than the ultrashort ones to produce well-ordered and uniform micro/nanoscale structures onto the surface of metallic masters can reduce their fabrication costs, significantly.

Lastly, another important advantage of employing the LMM technology as a tool for texturing replication masters is its processing flexibility, especially to texture curved or even freeform surfaces. State-of-the-art multi-axis LMM platforms are already available that offer a simultaneous motion control of multiple optical and mechanical axes when executing laser processing operations. As a result, such systems can be programmed to perform laser processing operations requiring simultaneous multi-axis movements that were considered not achievable until now. However, the capabilities of such complex LMM systems are difficult to assess, especially their Accuracy, Repeatability and Reproducibility (ARR) and thus to judge about their suitability to process 3D surfaces. Hence further efforts are needed to develop a systematic method for assessing their processing capabilities.

1.2. Research aims and objectives

The overall aim of this PhD research is to broaden the use of the LMM technology for functionalising surfaces at an industrial scale. Especially, to enable the fabrication of polymer-based components with multifunctional surface responses by addressing key limitations regarding the cost-effectiveness and durability of laser-enabled functional topographies and the necessary capabilities for producing such topographies onto complex 3D surfaces. Firstly, a cost-effective method for producing recyclable thermoplastic surfaces with an antifouling functionality is proposed in this research. A passive approach, namely LIS, is investigated to achieve such functional response on treated surfaces. Especially, a process chain is proposed that combines synergistically the capabilities of the LMM technology for texturing metallic

masters with their polymer micro/nano replication that is then followed by lubricant infiltration. Furthermore, to gain a better understanding of the LIS rationale design, the influence of surface topography on their functionality and durability is evaluated. The functional characteristics of LIS with different length scale topographies are investigated together with their applicability in food and medical sectors.

While ultrashort pulsed lasers are commonly deployed to fabricate LIPSS and consequently to imprint attractive functionalities onto surfaces, such topographies could be achieved by employing more cost-effective nanosecond laser sources. Therefore, it is important to study the formation and properties of LIPSS generated with such laser sources. However, due to the longer laser-material interaction time and the negative thermal side effects associated with this, a strategy to mitigate them is very important and thus to obtain high-quality and homogeneous LIPSS.

Finally, the proposed process chain should be applied for producing complex 3D components and so the capabilities of the LMM process to structure curved or even freeform surfaces have to be investigated, too. Thus, the execution of complex laser processing strategies, requiring the simultaneous control of both optical and mechanical axes, should be studied. Therefore, a systematic methodology is proposed to assess the processing capabilities and limitations of multi-axis LMM platforms, especially in the context of texturing/structuring requirements of replication masters with intricate geometries.

The aim of the PhD research is achieved through the following objectives:

1. *Develop an efficient and cost-effective process chain for producing recyclable polymer LIS.* The multi-step processing will include: (i) laser texturing of metallic masters; (ii) the replication of the laser-enabled surface topographies onto polymer sheets and (iii) the stable

impregnation of textured replicas with lubricating liquid. More specifically, two types of topographies, i.e. single-tier LIPSS and two-tier Multi-scale Structures (MS), are formed onto Stainless Steel (SS) masters by an ultrashort pulsed laser and then these topographies are replicated onto both transparent and opaque thermoplastic substrates using hot embossing. To judge about the replication capabilities, the quality and homogeneity of the structures on the replicas are studied.

2. *Investigate the functional properties and durability of as-prepared polymer LIS.* The thermoplastic replicas are impregnated with silicone oil and then their shedding capabilities are characterised against various liquids. Thereafter, additional tests are carried out on such samples to determine their functional characteristics. The tests are designed, both, to demonstrate the potential of as-prepared polymer LIS and prove their effectiveness in food packaging and in producing endoscope lens. Finally, a series of experiments are conducted on the LIS samples with the investigated two types of topographies to study and compare their lubricant retention capabilities when subjected to shear forces. The effect of lubricant viscosity on the LIS durability is investigated, too.
3. *Investigate the influence of processing environment on LIPSS generated with a green nanosecond laser.* The formation of LIPSS on SS surfaces upon irradiation in air and argon gas environments is investigated. Especially, the effects of processing environment on LIPSS geometrical characteristics, quality and surface chemistry are quantified, and subsequently their combined influence on the wetting properties are examined.
4. *Develop a method for evaluating the capabilities of multi-axis LMM systems for processing complex 3D components.* A generic method is proposed for assessing the impact of different error sources on ARR of such LMM systems when executing multi-axis processing strategies. A series of laser processing tests are conducted to quantify and compare ARR

when both optical and mechanical axes are simultaneously utilised. The tests are designed to investigate the capabilities of multi-axis processing strategies for precision laser texturing/structuring under quasi-static and dynamic conditions. Lastly, the applicability and validity of the proposed method is demonstrated in its pilot implementation on a representative multi-axis LMM system.

1.3. Thesis organisation

This thesis is divided into seven chapters as follows:

Chapter 1 introduces the overall motivation for this PhD research, its main aims and objectives, and also outlines the thesis organisation.

Chapter 2 reviews the basic theories, latest advances and current challenges related to the research fields covered in this thesis, i.e. bio-inspired surfaces and their principle designs, wetting theories, surface modifications techniques, fundamentals of the laser technology, laser-enabled surface topographies with their potential applications and 3D laser processing strategies.

Chapter 3 reports an investigation into the LIS properties achieved on LIPSS and MS topographies produced on thermoplastic substrates for food packaging applications. The anti-adhesive response of these samples against three liquids, i.e. water, whole milk and honey, is studied whilst their lubricant retention capacities under vibration and shear loading are quantified.

Chapter 4 presents an efficient and cost-effective process chain for producing recyclable disposable endoscopic lenses with superior durability while exhibiting excellent antifouling properties and transparency. The effectiveness of such lens treatment for preventing vision loss

during endoscopy are demonstrated by subjecting the as-prepared lenses to protein adsorption, microalgae adhesion, blood fouling, and fogging tests.

Chapter 5 reports an investigation into the formation, evolution, and properties of LIPSS generated with a green nanosecond pulsed laser on SS substrates under ambient and argon enriched conditions. The influence of processing environment on LIPSS geometrical characteristics, surface chemistry and wetting properties is analysed. A qualitative approach is followed to assess the regularity and homogeneity of LIPSS based on their first-order diffracted light.

Chapter 6 describes the generic empirical method for assessing ARR of LMM systems when conducting multi-axis texturing/structuring operations on curved/freeform surfaces under quasi-static and dynamic conditions. A pilot implementation of this method is presented to demonstrate its applicability.

Chapter 7 summarises the contributions of this PhD research to the existing knowledge and also discloses future research directions.

References

[1] L. A. Guerrero, G. Maas, and W. Hogland, "Solid waste management challenges for cities in developing countries," *Waste Management*, vol. 33, no. 1, pp. 220-232, 2013.

[2] United Nations Environment Programme, "Solid waste management," 2022. [Online]. Available at: https://www.unep.org/explore-topics/resource-efficiency/what-we-do/cities/solid-waste-management. Accessed date: 25 September 2022.

[3] N. Wichai-utcha and O. Chavalparit, "3Rs Policy and plastic waste management in Thailand," *Journal of Material Cycles and Waste Management*, vol. 21, no. 1, pp. 10-22, 2019.

[4] F. Zhang *et al.*, "Current technologies for plastic waste treatment: A review," *Journal of Cleaner Production*, vol. 282, p. 124523, 2021.

[5] R. Franz and F. Welle, "Recycling of Post-Consumer Packaging Materials into New Food Packaging Applications—Critical Review of the European Approach and Future Perspectives," *Sustainability*, vol. 14, no. 2, p. 824, 2022.

[6] L. Rigamonti, M. Grosso, J. Møller, V. Martinez Sanchez, S. Magnani, and T. H. Christensen, "Environmental evaluation of plastic waste management scenarios," *Resources, Conservation and Recycling*, vol. 85, pp. 42-53, 2014.

[7] D. Kreeft, E. A. Arkenbout, P. W. J. Henselmans, W. R. van Furth, and P. Breedveld, "Review of Techniques to Achieve Optical Surface Cleanliness and Their Potential Application to Surgical Endoscopes," *Surg Innov*, vol. 24, no. 5, pp. 509-527, 2017.

[8] F. Sahin, N. Celik, A. Ceylan, S. Pekdemir, M. Ruzi, and M. S. Onses, "Antifouling superhydrophobic surfaces with bactericidal and SERS activity," *Chemical Engineering Journal*, vol. 431, p. 133445, 2022.

[9] E. Stratakis *et al.*, "Laser engineering of biomimetic surfaces," *Materials Science and Engineering: R: Reports,* vol. 141, p. 100562, 2020.

[10] F. Geyer *et al.*, "When and how self-cleaning of superhydrophobic surfaces works," *Science Advances,* vol. 6, no. 3, p. eaaw9727, 2020.

[11] C. Wang and Z. Guo, "A comparison between superhydrophobic surfaces (SHS) and slippery liquid-infused porous surfaces (SLIPS) in application," *Nanoscale,* vol. 12, no. 44, pp. 22398-22424, 2020.

[12] T.-S. Wong *et al.*, "Bioinspired self-repairing slippery surfaces with pressure-stable omniphobicity," *Nature,* vol. 477, no. 7365, pp. 443-447, 2011.

[13] L. Sun *et al.*, "Tailoring Materials with Specific Wettability in Biomedical Engineering," *Advanced Science,* vol. 8, no. 19, p. 2100126, 2021.

[14] C. Howell, A. Grinthal, S. Sunny, M. Aizenberg, and J. Aizenberg, "Designing Liquid-Infused Surfaces for Medical Applications: A Review," *Advanced Materials,* vol. 30, no. 50, p. 1802724, 2018.

[15] D. Wang and Z. Guo, "A bioinspired lubricant infused surface with transparency, hot liquid boiling resistance and long-term stability for food applications," *New Journal of Chemistry,* vol. 44, no. 11, pp. 4529-4537, 2020.

[16] J. Liang, D. Li, D. Wang, K. Liu, and L. Chen, "Preparation of stable superhydrophobic film on stainless steel substrate by a combined approach using electrodeposition and fluorinated modification," *Applied Surface Science,* vol. 293, pp. 265-270, 2014.

[17] H. Luo, S. Yin, S. Huang, F. Chen, Q. Tang, and X. Li, "Fabrication of slippery Zn surface with improved water-impellent, condensation and anti-icing properties," *Applied Surface Science,* vol. 470, pp. 1139-1147, 2019.

[18] Q. Li and Z. Guo, "Lubricant-infused slippery surfaces: Facile fabrication, unique liquid repellence and antireflective properties," *Journal of Colloid and Interface Science,* vol. 536, pp. 507-515, 2019.

[19] X. Zhou, Y.-Y. Lee, K. S. L. Chong, and C. He, "Superhydrophobic and slippery liquid-infused porous surfaces formed by the self-assembly of a hybrid ABC triblock copolymer and their antifouling performance," *Journal of Materials Chemistry B,* vol. 6, no. 3, pp. 440-448, 2018.

[20] M. Friedrich, M. Seiler, S. Waechter, J. Bliedtner, and J. P. Bergmann, "Precision structuring and functionalization of ceramics with ultra-short laser pulses," *Journal of Laser Applications,* vol. 30, no. 3, p. 032501, 2018.

[21] Y. Lin *et al.*, "Durable and robust transparent superhydrophobic glass surfaces fabricated by a femtosecond laser with exceptional water repellency and thermostability," *Journal of Materials Chemistry A,* vol. 6, no. 19, pp. 9049-9056, 2018.

[22] A. Riveiro, A. L. B. Maçon, J. del Val, R. Comesaña, and J. Pou, "Laser surface texturing of polymers for biomedical applications," *Frontiers in Physics,* vol. 6, p. 16, 2018.

[23] O. Hofmann, J. Stollenwerk, and P. Loosen, "Design of multi-beam optics for high throughput parallel processing," *Journal of Laser Applications,* vol. 32, no. 1, p. 012005, 2020.

[24] G. Bonamis *et al.*, "High efficiency femtosecond laser ablation with gigahertz level bursts," *Journal of Laser Applications,* vol. 31, no. 2, p. 022205, 2019.

[25] F. Roessler and A. Streek, "Accelerating laser processes with a smart two-dimensional polygon mirror scanner for ultra-fast beam deflection," *Advanced Optical Technologies,* vol. 10, no. 4-5, pp. 297-304, 2021.

[26] F. Ränke, R. Baumann, B. Voisiat, and A. Fabián Lasagni, "High throughput laser surface micro-structuring of polystyrene by combining direct laser interference patterning with polygon scanner technology," *Materials Letters: X,* vol. 14, p. 100144, 2022.

CHAPTER 2: LITERATURE REVIEW

2.1. Biological structures with special wettability

Nature has always been an infinite source of inspiration for scientists to design and develop novel materials/products. In fact, considerable research efforts have been made over the last years to understand the underlying principles of biological structures, and thus to fabricate bio-inspired surfaces that exhibit unique properties [1-3]. Among the different functional structures of natural living organisms, those that demonstrate impressive anti-wetting characteristics have gained much interest due to their high potential in applications related to energy storage [4, 5], human health [6] and environmental protection [7].

The most famous example in nature exhibiting such functional responses is the Nelumbo nucifera plant, which is also well-known as “sacred” lotus. In reality, the leaves of this aquatic plant have received lots of attention by researchers not only for their excellent anti-wetting properties, but also for their self-cleaning capabilities. As can be seen from the Scanning Electron Microscope (SEM) micrographs given in Fig. 2.1, the lotus leaf is made up of a hierarchical topography that is covered by a low surface energy wax layer [8-10]. Owing to this surface composition, water droplets appear to have a spherical shape on the lotus leaf and their adhesion to its surface is significantly low. Meanwhile, it should be stated that other biological surfaces with similar properties to those of lotus plant have also been studied, such as butterfly wings [11], water spider’s legs [12] and rice leaf [13] to name a few. The surface morphology of these natural organisms is shown in Fig. 2.1b-d, respectively.

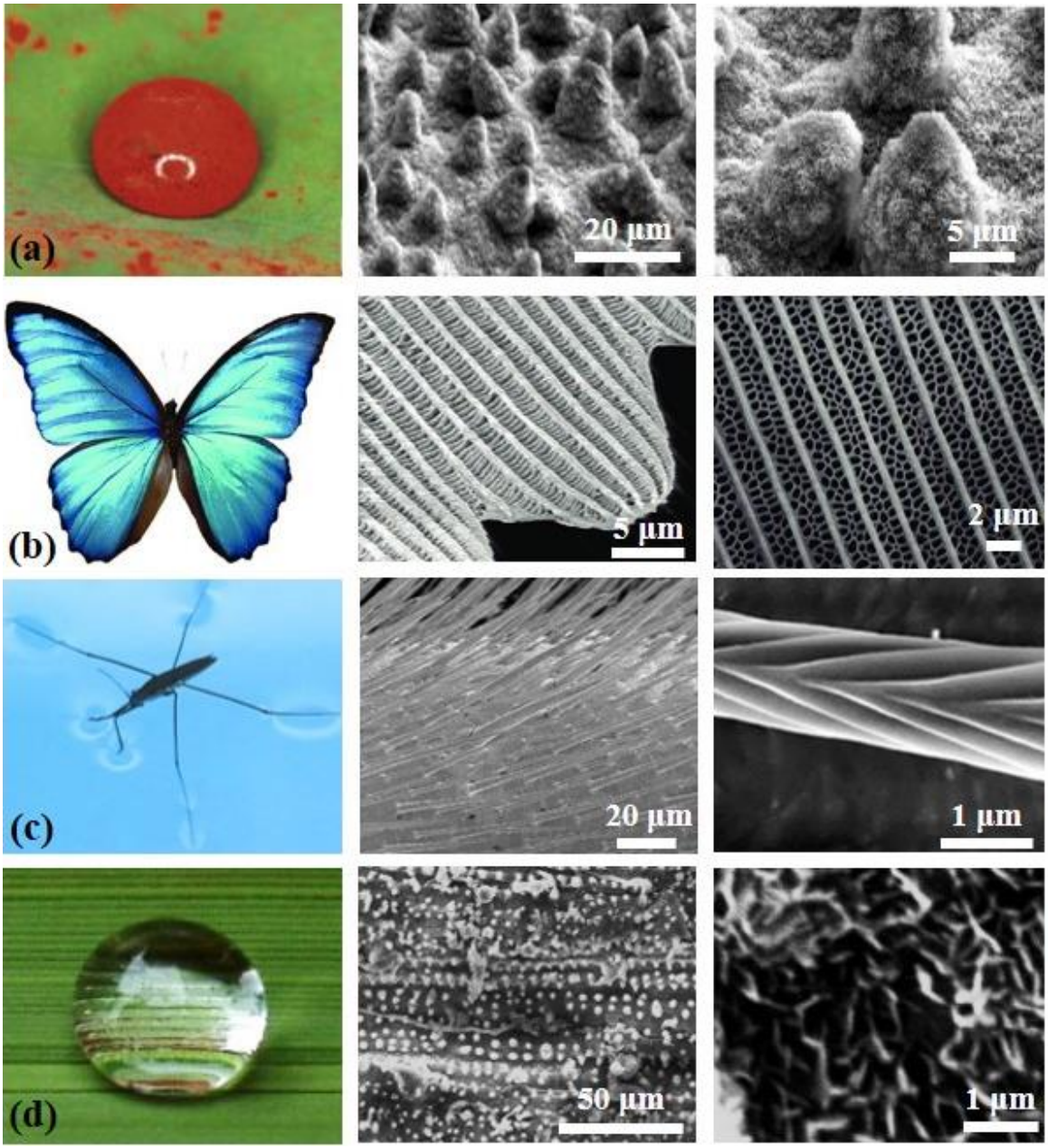

Fig. 2.1. Examples of biological structures exhibiting superhydrophobicity and low liquid-solid adhesion: (a) photo of a water droplet covered with lipoidic particles on a lotus leaf and SEM micrographs of the plant's surface topography at different magnifications [14]; (b) image of a blue butterfly at different magnifications [15]; a water spider walking on water and SEM images of its feet surface at different magnifications [16]; photo of a rain droplet formed on rice leaf and SEM micrographs of the leaf's surface topography at different magnifications [17].

On the other hand, there are plenty of animals or plants on the planet whose surfaces exhibit anti-wetting behaviour and high adhesion simultaneously. This special wetting state is well-demonstrated by the rose petals and the feet of Tokay gecko. For instance, rain droplets formed on the rose flowers completely pin to their dual-scale rough surface (see Fig. 2.2a), enabling them to flourish in humid conditions [18]. At the same time, the ability of geckos to climb almost any surface is attributed to the high adhesion forces induced by the complex morphological structures (see Fig. 2.2b), i.e. a hierarchical topography consisting of lamellae, setae, branches, and spatula, located on their toes [19, 20].

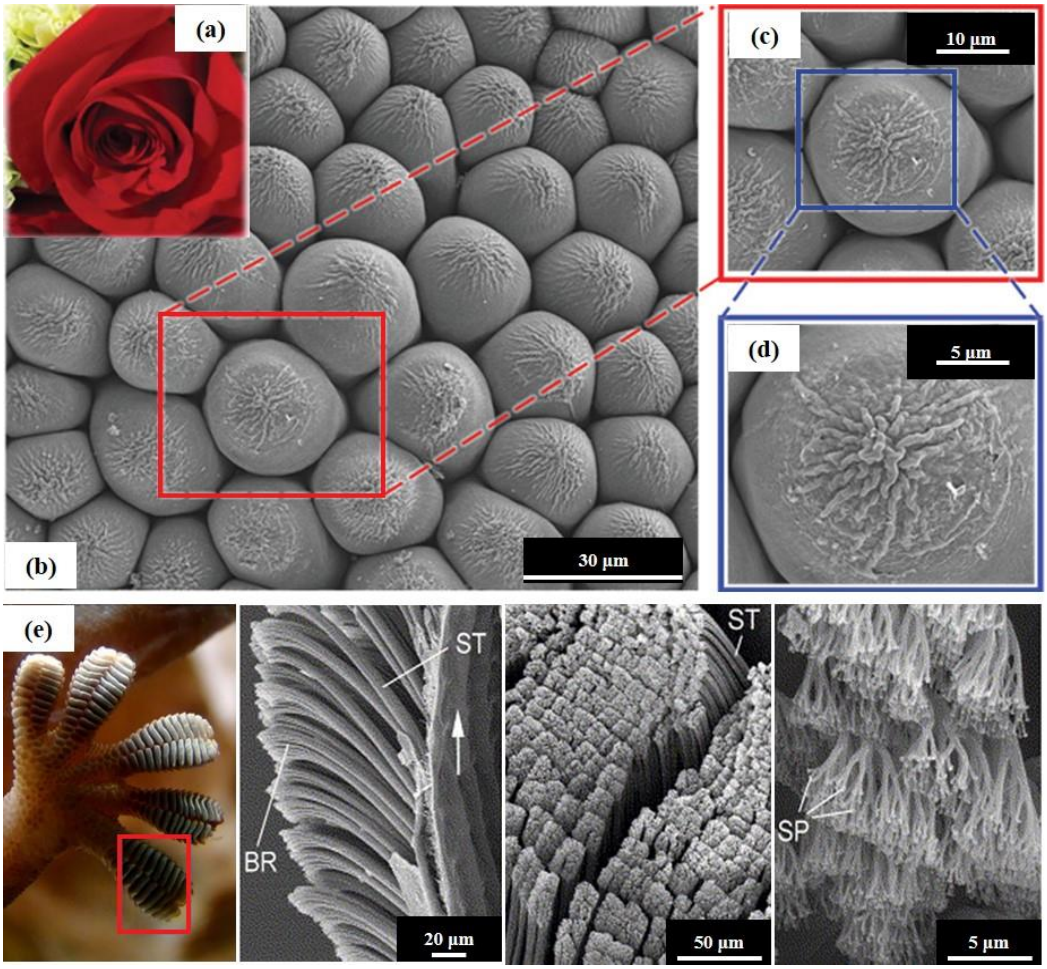

Fig. 2.2. Natural organisms showing superhydrophobicity with high adhesion: optical and SEM images of a (a-d) rose petal [21] and (e) gecko's foot [22] surfaces. *Note:* the characters ST, SP and BR in (e) refer to the seta, spatula and branch, respectively.

Lastly, the structural morphology of some carnivorous plants has also gained much attention recently due to their interesting anti-adhesive characteristics. In particular, these plants have developed functional organs for capturing their prey and thus surviving even in harsh environments, e.g. tropical climates. A great example of such plants is the pitchers from the genus of Nepenthes, which have a special pitfall mechanism to entrap small insects. Especially, the Nepenthes pitchers are characterised by various morphological districts (see Fig. 2.3), such as leaf-shaped lid, peristome, slippery zone and digestive district, and each one has a different functionality [23]. The upper rim of this peristome is hydrophilic/oleophilic and consists of a microstructure topography with radial ridges [24]. At the same time, its surface, especially the inner edge, is filled with nectaries secreted by glands for attracting insects [25]. Once the peristome gets wet by a mixture of liquids (e.g. water and nectar), it forms a stable slippery film that forces the prey to fall into the digestive fluid [26].

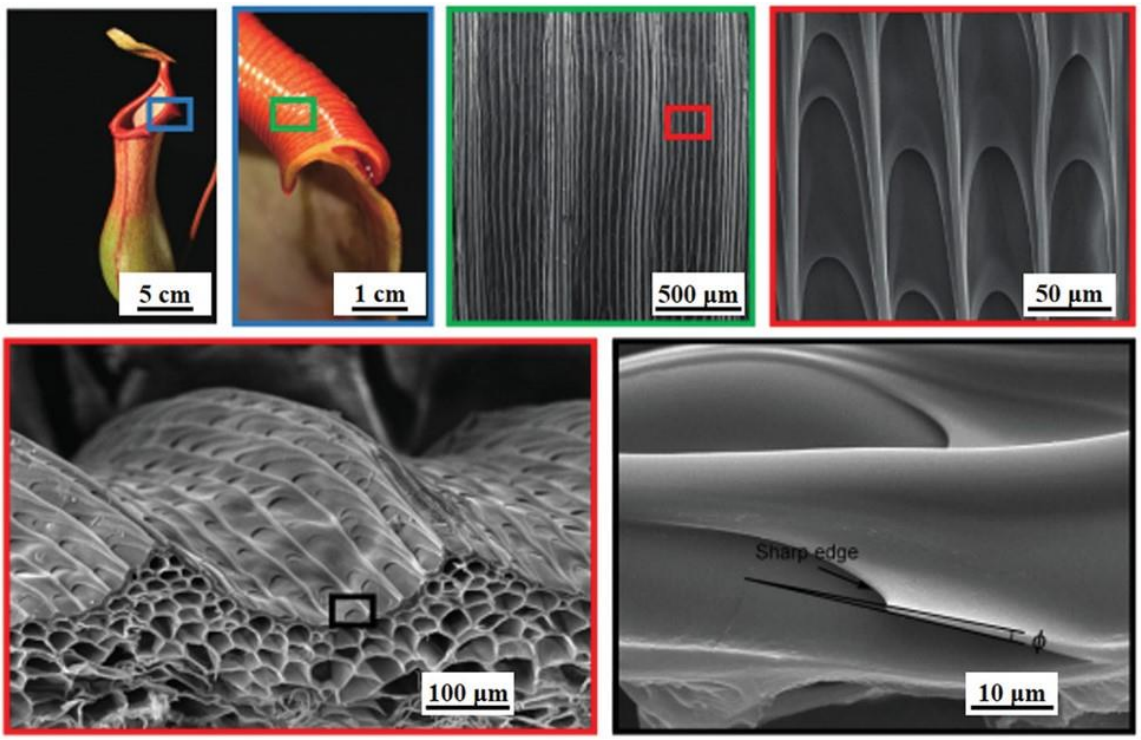

Fig. 2.3. The surface morphology of Nepenthes pitcher plant: optical and SEM images showing the unique structural topography of the peristome's upper rim [18].

2.2. Wettability and superhydrophobicity

Generally, the term wettability describes the ability of liquids to spread over a particular surface and it has been recognised over the last years as one of the most critical characteristics of solid materials [27]. Traditionally, the sessile drop method is used to quantify the surface wettability, which involves measuring the static Contact Angle (CA) of a droplet at the liquid-solid interface. Especially, it can be stated that surfaces exhibiting a CA value lower than 90° are considered as hydrophilic, whereas surfaces with a CA value above 90° demonstrate a hydrophobic behaviour. Meanwhile, superhydrophobicity is credited to a surface when water droplets form a nearly spherical shape, i.e. CA larger than 150°, and the unique adhesion characteristics of such surfaces are discussed in the next paragraph. For the shake of clarity, a schematic illustration of surfaces showing different wetting levels is given in Fig. 2.4.

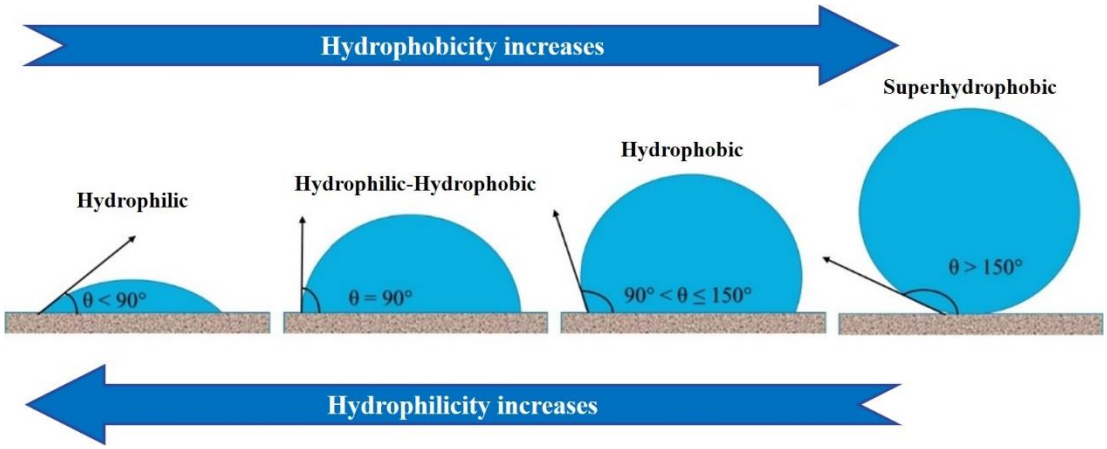

Fig. 2.4. Classification of surfaces based on apparent CAs [28].

Furthermore, it is well-known that not all SHS exhibit the same adhesion behaviour and thus they can be classified into two categories [29]. More specifically, there are artificial SHS with low ("lotus leaf effect") and high ("rose petal effect") adhesion [30, 31]. In the former case, water droplets are highly mobile and can easily roll off the surfaces. On the contrary, droplets have a tendency to strongly attach on the latter surfaces and remain in place till they evaporate.

Typically, the adhesion forces at the interface between a liquid and a solid surface can be characterised using the Critical Sliding Angle (CSA) and Contact Angle Hysteresis (CAH). In brief, the first parameter is defined as the minimum tilting angle required to initiate droplet mobility as illustrated in Fig. 2.5a, whilst CAH reflects the least energy required to move a droplet from one metastable state to another on a surface and it can be obtained by getting the difference between advancing (θ_A) and receding (θ_R) CAs [32]. The most common technique to determine these two angles for SHS is the so-called needle method (see Fig. 2.5b), in which the volume of a sessile drop is slowly increased and decreased via a syringe.

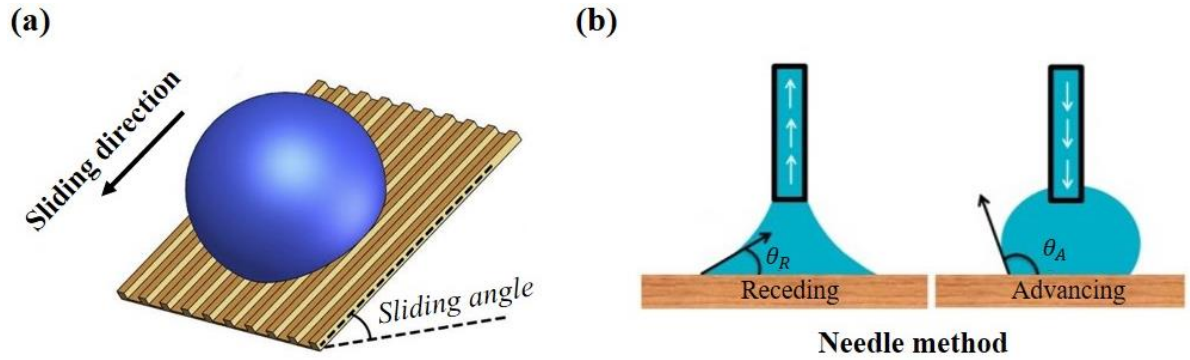

Fig. 2.5. Methods for characterising the adhesive properties of surfaces: schematic diagram of (a) a droplet that is just starting to flow down an inclined surface at a particular CSA [33] and (b) the needle method used for measuring the advancing and receding CAs [34].

Typically, SHS that demonstrate extreme water repellency are defined by having a very low CAH and/or CSA, i.e. less than 10° [35, 36]. These surfaces owe their unique shedding capabilities to their hierarchical micro/nanostructured topography, which can effectively entrap air to form a gas barrier and prevent diffusion of liquids [37]. However, it should be noted that SHS with low adhesion cannot be achieved solely by texturing a surface and thus in most cases a chemical treatment is required, too. In particular, several studies have reported that a combination of surface roughness and low surface energy is essential to produce artificial

SHS on different type of materials, including metals, glass and polymers [38]. For example, various perfluorinated compounds, such as perfluorinated phosphates, perfluorinated silanes, fluorinated monomers, polymers and copolymers, have been utilised over the years to lower the surface energy of materials and enhance their anti-wetting/anti-adhesive properties [39]. Considering the attractive functionalities of such SHS, there are plenty of potential applications, as shown in Fig. 2.6, in which these surfaces could be extremely beneficial.

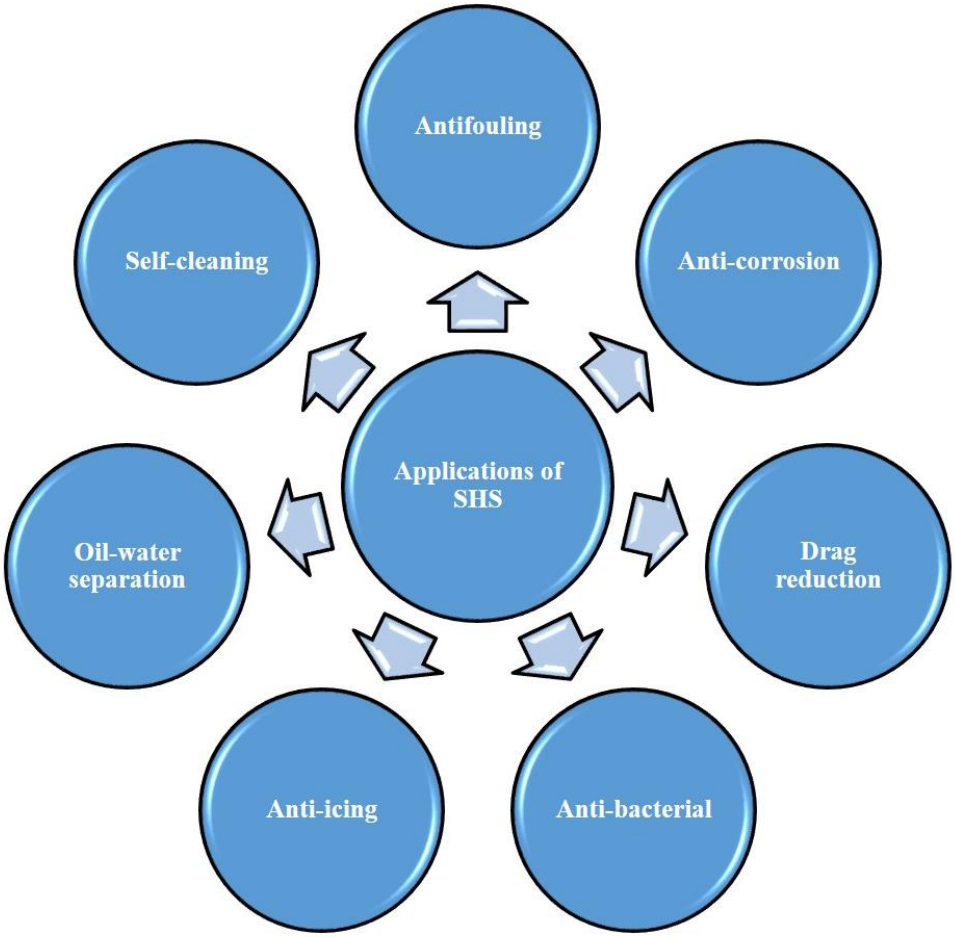

Fig. 2.6. The promising application fields where SHS with low adhesion can be successfully utilised.

One of the main shortcomings that hampers the broader use of SHS in practical applications is their poor long-term durability [40]. To address this crucial problem, considerable research efforts have recently been invested into the development of novel strategies for fabricating

robust SHS and consequently improving their overall performance under harsh operating conditions [41-43]. However, to better understand the mechanisms responsible for the degradation of SHSs' unique functionalities, it is necessary to firstly introduce the fundamental theories that elucidate the wetting phenomena on these surfaces. In this regard, the original theory that can predict the CA of a liquid droplet on an ideal smooth surface (θ_Y) was proposed by Young. This wetting scenario (see Fig. 2.7a) takes into consideration the different interfacial surface energies at the solid/vapor (γ_{SV}), liquid/vapor (γ_{LV}) and solid/liquid (γ_{SL}) interfaces and is given by Equation (2.1) [44]. Despite that, it should be noted that most solid materials in practice have a rough surface topography, which is chemically heterogeneous, and thus Young's model cannot be used to estimate the wetting state of such surfaces [45].

$$\cos\theta_Y = \frac{\gamma_{SV} - \gamma_{SL}}{\gamma_{LV}} \tag{2.1}$$

Therefore, other theoretical models have been proposed to describe the surface wetting behaviour of homogeneous surfaces covered with hierarchical micro/nano-scale structures, i.e. the Wenzel, Cassie-Baxter and intermediate metastable regimes [46]. More specifically, the Wenzel's model can be used to explain the apparent CA on a rough solid material when its surface topography is fully wetted by liquid droplets as shown in Fig. 2.7b [47]. On the contrary, Cassie-Baxter reported a case where air can be entrapped within the cavities of a hierarchical surface topography as illustrated in Fig. 2.7c, resulting in a solid-liquid-air interface [31]. The apparent CAs, i.e. θ_W and θ_{CB}, according to the two aforementioned wetting regimes can be calculated using the Equations (2.2) and (2.3), respectively [48].

$$\cos\theta_W = r\cos\theta_Y \tag{2.2}$$

$$\cos\theta_{CB} = f(1 + \cos\theta_Y) - 1 \tag{2.3}$$

Where r is a roughness factor that represents the ratio of solid surface area to the projected one and f refers to the relative fraction of the liquid-air area at the interface. Even though SHS in a stable Cassie-Baxter regime are typically preferred, especially in applications where liquid repellency is required, this state is metastable and a transition to the Wenzel one can result in complete loss of their anti-wetting/anti-adhesive functionalities [49, 50].

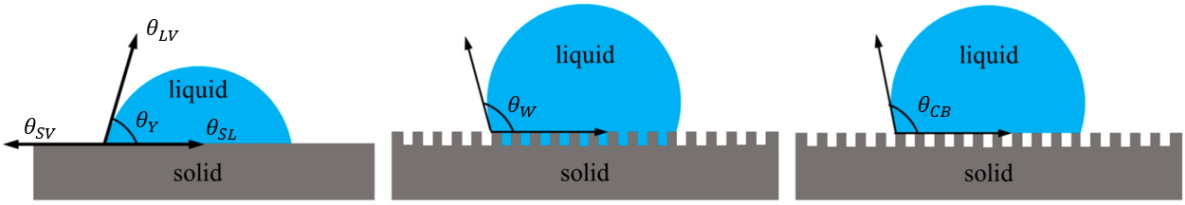

Fig. 2.7. Fundamental wetting theories: (a) Young's model, (b) Wenzel's model and (c) Cassie–Baxter model [51].

In general, there are various factors that can affect the stability of Cassie–Baxter regime. These factors can be divided into two main groups: (i) mechanical damage to the hierarchical topography of the SHS and (ii) damage to their surface chemistry [35, 44]. To date, numerous attempts have been carried out by researchers to characterise the performance of SHS under such conditions and also to identify ways for mitigating their negative effects. However, the fabrication of robust and stable SHS is still a challenging task, and thus their broader application in industrial processes has yet to come.

2.3. Lubricant-impregnated surfaces

2.3.1. Design principles and applications

A relatively new surface functionalisation technique, which is based on lubricant impregnation of rough surface topographies, has received significant attention among the research community recently. In particular, the design principles of LIS, also known as slippery liquid-

infused porous surfaces, have been inspired by living organisms and the popularity of these surfaces arises from their impressive shedding capabilities against both Newtonian and non-Newtonian liquids (i.e. liquids with shear-dependent viscosity) [52-54]. As already mentioned, an illustrative example of such functional surfaces existing in nature is the Nepenthes pitcher plant. Different from SHS, the preparation of LIS requires a rough scaffold to be fabricated that is then impregnated with a lubricant as shown in Fig. 2.8. Especially, the underlying textured surface should be capable of stabilizing the lubricant into its cavities, resulting in the formation of a smooth slippery layer at the interface [55, 56].

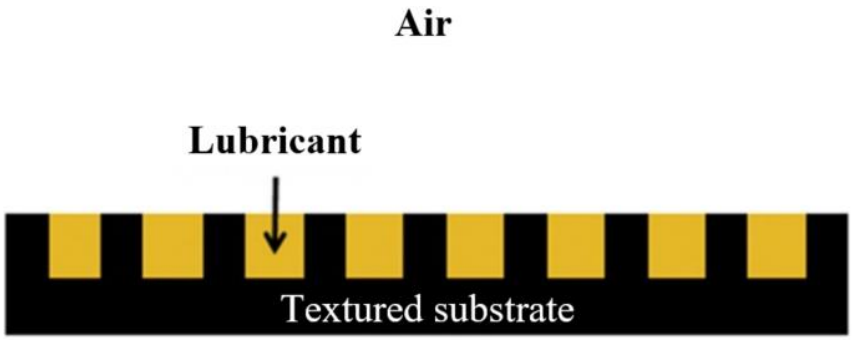

Fig. 2.8. Schematic illustration of a substrate infiltrated with lubricant.

In general, Aizenberg's group [57] was among the first ones to report the fabrication of LIS and the main criteria behind their design can be summarised as follows: (i) the employed lubricant should wet and stably impregnated into the textured scaffold; (ii) the textured substrate should only be wetted by the lubricant and not by the liquid to be repelled; and (iii) to achieve a stable impregnation, suitable lubricants, i.e. immiscible and incompatible with the working fluids, should be considered. Thereafter, Smith et al. [58] analysed the complex interaction between liquid droplets and LIS. In particular, this research revealed that a drop on LIS can appear in 12 different wetting configurations, which are explained below. These thermodynamic states can be divided into two categories depending on the spreading behaviour of the infused lubricant (o) on the water droplet (w) in the presence of ambient

environment (a) [59]. The individual interfacial tensions, i.e. liquid/solid, lubricant/solid and lubricant/liquid, that define the spreading coefficient can be calculated by the methods already available in literature [60, 61]. In case the spreading coefficient ($S_{ow(a)}$) is positive, the liquid drop will be covered by the lubricant and thus forming a "cloaking" film. Based on a previous study reported in [62], the thickness of this film can be up to a few nanometers. In contrast, the lubricant does not cover the droplet when the spreading coefficient is negative, i.e. $S_{ow(a)} < 0$. However, it should be stated that a wetting ridge (see Fig. 2.9), also known as meniscus, can be observed at the periphery of the liquid droplet in both wetting scenarios, which is responsible for its hemispherical shape on the surface. The formation of such wetting ridge is typically attributed to the vertical component of the water's surface tension, and its height mainly depends on the thickness of the "cloaking" film [63, 64].

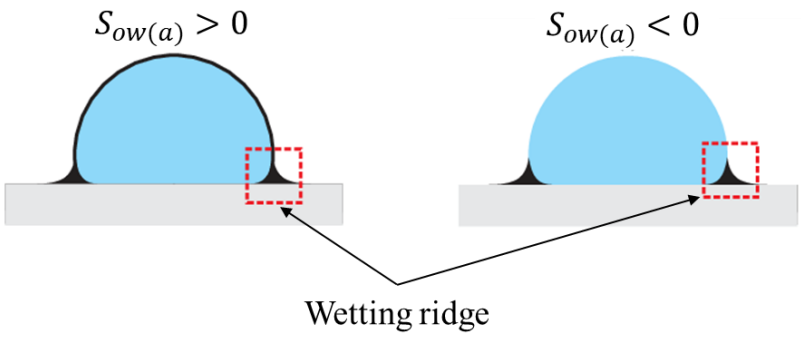

Fig. 2.9. Schematic representation of a static drop on LIS when the spreading coefficient is positive (left) and negative (right) [58].

Furthermore, in each aforementioned category, there are six discrete wetting configurations at which a static droplet can exist on LIS. They can be distinguished by how the infused lubricant interacts with the rough surface topography in the presence of air and water [58]. Fig. 2.10 depicts the three possible configurations underneath a droplet deposited on LIS when the spreading coefficient is either positive or negative. In the first configuration (see state *W1*), the

droplet displaces the lubricant from the textured surface and penetrates into the structures. As a result, the droplet completely adheres to the surface. It should be stated that LIS in this state are not stable and consequently they do not exhibit any shedding characteristics. On the contrary, stable LIS can only be achieved in the other two wetting regimes, i.e. *W2* and *W3*, where the textured topography underneath the drop is partially or fully covered by the lubricant, respectively [65]. Meanwhile, the last two configurations can also be observed in the textured topography outside the deposited droplet, thus adding another three possible wetting combinations in each category. However, it is worth noting that LIS in a fully encapsulated state can exhibit higher droplet mobility due to low pining forces [66].

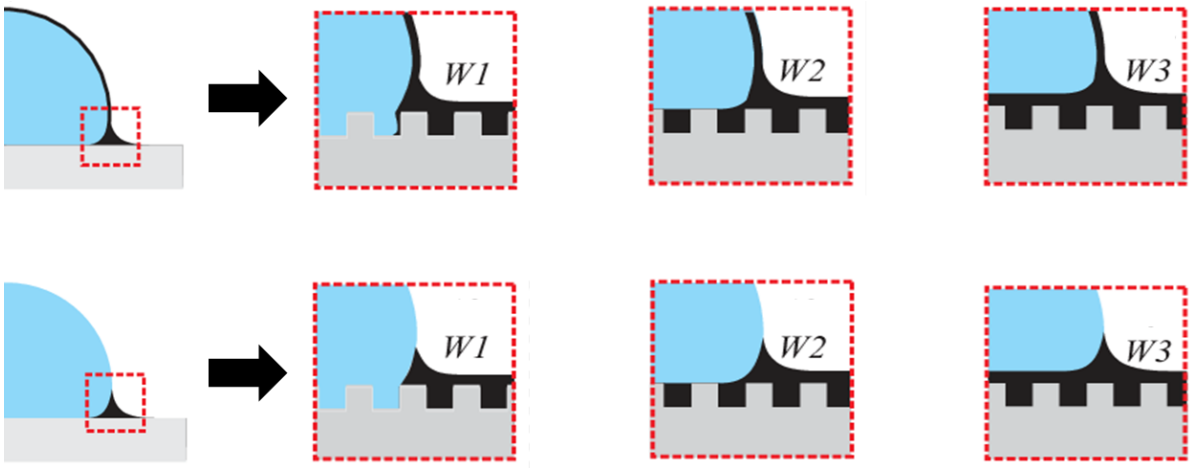

Fig. 2.10. Schematic diagram showing the possible wetting configurations underneath a water droplet placed on LIS when the spreading coefficient is positive (top) and negative (bottom) [58].

In most theoretical studies on LIS, it is presumed that the underlying surface structures are fully submerged by the infused lubricant. Though, achieving such a wetting state is a challenging task that requires to properly modify both the surface topography and its chemistry. Specifically, the textured scaffold of LIS should exhibit an oleophilic behaviour in order to be wetted by the utilised lubricant instead of repelling it. Thus, coating-based

techniques, as discussed in the previous section, are commonly utilised to treat the surface of solids and acquire the desired wettability for preparing LIS. At the same time, it should be noted that the lubricant is entrapped into the surface structures by capillary and also van der Waals forces [67]. As a result, surface topographies consisting of relatively small periodic structures are preferred to benefit from their strong induced capillary pressure. Overall, LIS produced with such underlying surface topographies have superior stability and consequently demonstrate more durable anti-adhesive characteristics. Additionally, lubricant viscosity is another critical parameter that influences the mobility of liquid droplets, and thus it should be taken into consideration when designing LIS. In particular, a reduced shedding droplet velocity was observed with the increase of lubricant viscosity owing to the enhanced viscous dissipation at the liquid−lubricant interface [68, 69]. However, it should be emphasised that even nanostructured LIS impregnated with high-viscosity lubricants are susceptible to failure, and the main mechanisms responsible for that are discussed in Sub-section 2.3.4.

Once a fully encapsulated state is attained, LIS can offer attractive multi-functional properties. In reality, these surfaces display extreme liquid repellency with both CAH and CSA values less than 5° [70]. Compared to SHS, LIS are characterised by superior stability under harsh environmental conditions, i.e. high-pressure and –temperature [57]. Owing to these advantages, LIS have emerged as promising candidates for various applications related to self-cleaning [71], food processing [72, 73], anti-icing [74, 75], drag reduction [76], anti-corrosion [77], droplet manipulation [78], water harvesting/transportation [79] and enhanced condensation [80]. On top of that, it should be stated that LIS possess impressive antifouling functionalities even against biological fluids, proteins and bacteria [81-83]. Thus, they have extensively been introduced as an effective solution to inhibit biofouling and cross-contamination phenomena faced in several medical applications (see Fig. 2.11) [84-86].

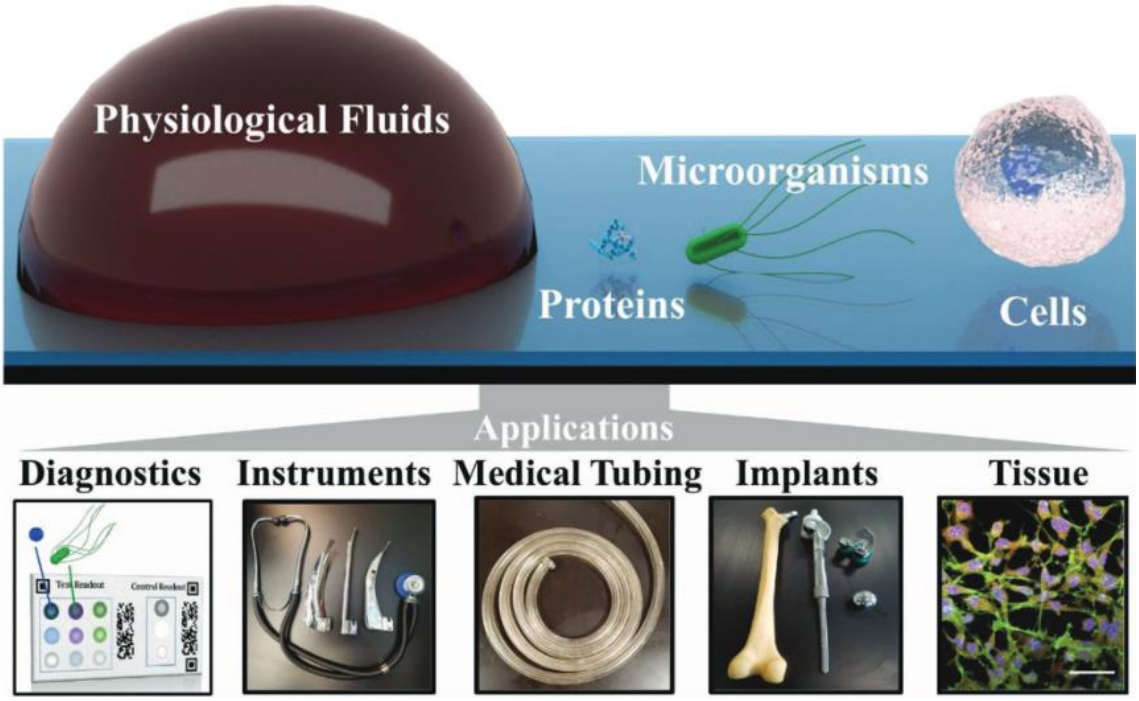

Fig. 2.11. The various promising applications of LIS in healthcare sector [87].

2.3.2. Fabrication methods

As stated, LIS consist of two main components, i.e. the scaffold and the infused lubricant, that must be chemically compatible in order to form a stable slippery interface. Therefore, their preparation commences with the fabrication of a suitable scaffold that can stabilize the utilised lubricant [88]. In this regard, a broad range of substrate materials with different physical, chemical and surface morphological characteristics have been investigated to produce LIS. More specifically, solid materials, e.g. metals [89, 90], ceramics [91] and polymers [92, 93], have widely been reported as scaffolds for LIS. In addition, the fabrication of such functional surfaces on glass [94] and wood [95] has been demonstrated, too. Overall, there are three key strategies to produce LIS, which involve: (i) the use of a chemical treatment to alter the surface chemistry of inherently porous/rough substrates (see Fig. 2.12); (ii) the use of a surface modification technique to roughen the topography of low-surface-energy materials and (iii) a combination of the two aforesaid approaches [96].

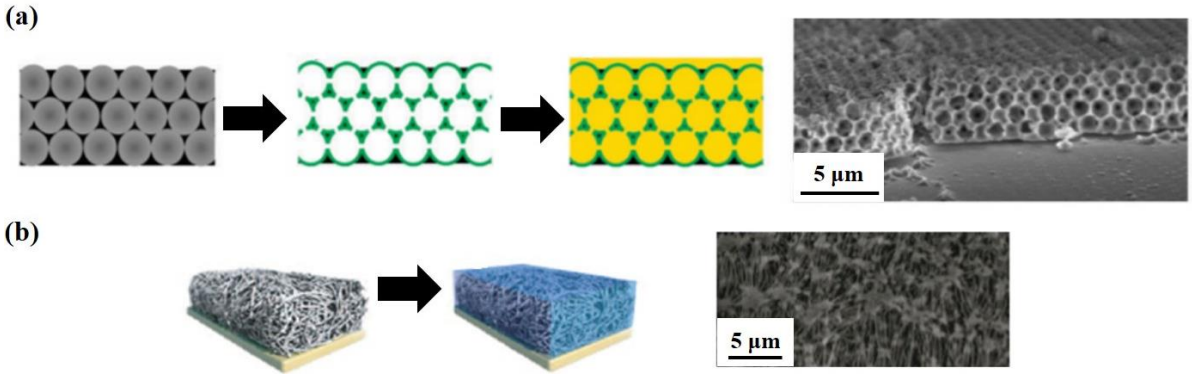

Fig. 2.12. LIS produced from inherently porous materials: (a) an illustration of the steps involved to prepare LIS with a colloidal approach based on inverse opal scaffolds (left) and SEM micrograph of the as-prepared surface topography (right) [94]; (b) schematic diagram (right) and SEM image (left) of the Teflon-based porous nanofiber surface topography that was impregnated with a lubricant to obtain LIS [57].

To roughen the surface topography of flat substrates and hence achieve lubricant retention, a wide variety of surface modification techniques can be applied. Especially, these methods can be employed to produce LIS with different underlying surface topographies, i.e. regular or irregular. For instance, highly regular and homogeneous microscale pillars can be generated on the surface of solid substrates using a photolithographic process as shown in Fig. 2.13. Compared to surface topographies with single-tier microstructures, those consisting of two-tier MS structures, i.e. micro/nano structures, have proved to display significantly lower contact line pining forces and thus they have gained more attention from researches [68]. As a result, several manufacturing processes have been proposed and successfully implemented to fabricate LIS with such topographies, which include plasma treatment [97], spin-coating [98], electroplating [99], chemically etching [100] and self-assembly [101] among others.

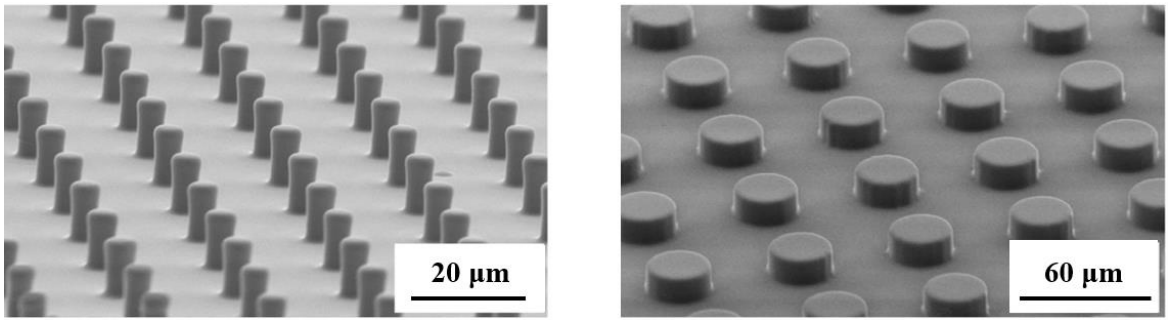

Fig. 2.13. SEM micrographs of surfaces covered with highly regular and homogeneous micropillar structures, which were fabricated through lithographic processes [102].

However, it should be stated that the majority of these surface treatments cannot meet the requirements for scale-up production and also their usage involves hazardous chemicals that can be extremely harmful to both the human health and environment. To address some of these challenging issues, Ma et al. [103] proposed an alternative surface treatment to fabricate LIS on metallic substrates by direct laser texturing (see Fig. 2.14). Shortly after, a similar laser-enabled surface treatment for producing LIS on glass was reported by Lee et al. [104], too. In fact, these two studies demonstrate the huge potential of LMM technology as a tool for functionalising materials. The advantages, capabilities and limitations of this technology will be introduced and analytically discussed in Sub-section 2.4.

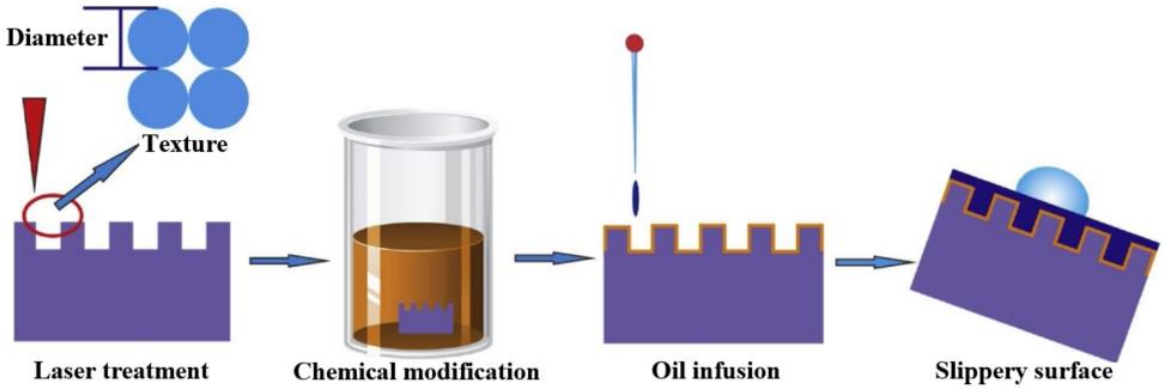

Fig. 2.14. Schematic illustration of the laser-enabled surface treatment used to fabricate LIS on carbon steel [103].

2.3.3. Infusing lubricants

After texturing the scaffold, its surface topography must be impregnated with a suitable lubricant. In fact, the selection of lubricant is one of the most crucial steps when preparing LIS, and thus it should be made according to the application-specific requirements. Based on literature, it is apparent that a wide variety of lubricants with different properties can be used for producing LIS. For instance, water-based lubricants were deployed in fields associated with biological systems [105]. However, it is worth noting that such lubricants exhibit extremely low stability, because they can easily evaporate when exposed to elevated temperatures. As a result, oil-based lubricants were mostly investigated by researchers. In particular, perfluorinated oils, e.g. perfluorodecalin [106], Fluorinert FC-40 [107] or Krytox oils [108], have commonly been employed as lubricants to assess the capabilities of LIS for various applications. Despite the great stability and immiscibility of these oils against many working liquids, their usage releases toxic gases, i.e. fluorine, that can pose a high risk to the ecosystem [109].

Therefore, various studies have promoted the use of essential [110] and vegetable [111, 112] oils as an alternative to perfluorinated ones for preparing LIS. However, such oils cannot be considered as an option for food applications due to their strong aroma and incompatibility with some food substances [113]. At the same time, although these natural oils are likely to be harmless for the human body, further efforts are still required to validate their biocompatibility before using them in healthcare sector. On the other hand, silicone-based oils are widely available at different viscosities whilst preserving their chemical characteristics. As such, LIS with highly viscous silicon oils can be prepared to achieve a better stability and hence to prolong their functional response. Finally, another major benefit of choosing this type of oils is that they are nontoxic and also their use has already been approved by both FDA [2] and

EFSA [114] for medical applications as well as food additives. Thanks to these advantages, silicon-based oils have attracted considerable attention as lubricants to create LIS [115-117].

Lastly, after selecting the proper lubricant, it is necessary for the textured substrate to be impregnated in a repeatable manner. Overall, there are three popular techniques that can be used for infusing the lubricant into the surface structures. In the first case, the textured substrate should be fully submerged into a container filled with lubricant and then slowly pulled out [118]. This method is well-known as dip-coating. The second technique requires the use of a spin coater or spinner [119, 120]. Especially, the lubricant is spread over the textured surface owing to the centrifugal forces induced by this device. In the last case, the substrate should be tilted slightly and then one of its edges should be placed into contact with a lubricant reservoir [102]. As a result, the lubricant will immediately fill the structures due to capillary action.

2.3.4. Durability

To benefit from long-lasting anti-adhesive properties, it is essential the as-prepared LIS to display great stability and hence durability. Therefore, their performance has been tested against various conditions over the last years. In most cases, the depletion of impregnated lubricant has been determined as the main reason responsible for the degradation of LISs' functionality. More specifically, several methods have been proposed to evaluate the amount of lubricant depleted from the surface structures and thus to judge about the durability of LIS. For instance, optical systems, such as fluorescence macrophotography [121], confocal microscopy [122], interference microscopy [123] and white light interferometry [124], were mostly deployed to analyze the displacement of lubricant. However, it should be noted that these techniques can only be used for transparent scaffold materials. On the contrary, other

experimental approaches to characterise lubricant depletion involved measuring potential alterations in the wetting properties [125], weight [126] and pressure (see Fig. 2.15) [127].

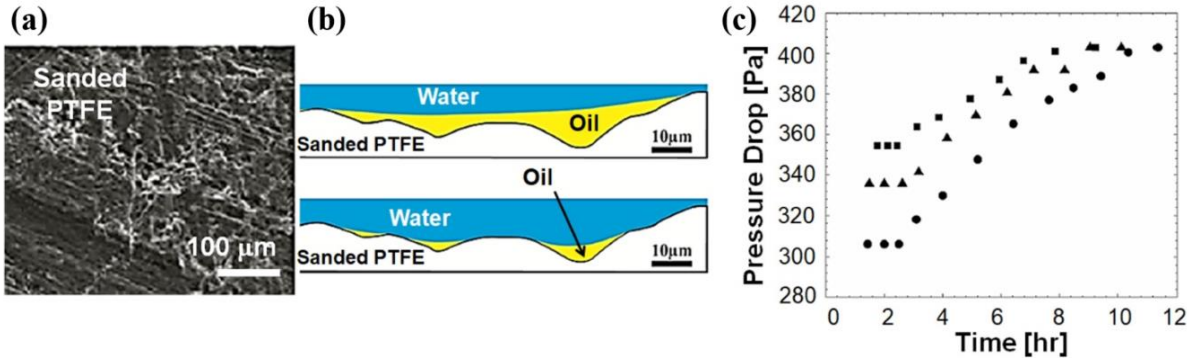

Fig. 2.15. Shear-induced lubricant depletion: (a) SEM micrograph of the sanded PTFE surface topography; (b) schematic diagram of shear-induced loss of lubricant infused into the PTFE-sample; (c) plot showing the pressure drop over time as a result of lubricant depletion [128].

Overall, there are numerous mechanisms causing the loss of lubricant from the infused surface structures. Specifically, lubricant depletion can occur due to gravitational forces (see Fig. 2.16a) [129] and evaporation (see Fig. 2.16b) [130]. At the same time, liquid droplets deposited on LIS at a high velocity can displace the impregnated lubricant as illustrated in Fig. 2.16c [62], exposing the underlying surface topography. However, this phenomenon is typically more pronounced on LIS prepared with lubricants of low viscosity. Previous studies have also reported that ice formation and condensation can lead to depletion of impregnated lubricant from the structures, resulting in LIS failure (see Fig. 2.16d) [131, 132]. In addition, it has been observed that the infused lubricant can gradually be removed by cloaked liquid droplets when flowing down the surface (see Fig. 2.16e) [68]. Finally, the functionality of LIS can be damaged when the lubricant layer is severely drained by external forces, e.g. under persistent shear flow conditions (see Fig. 2.16f) [133].

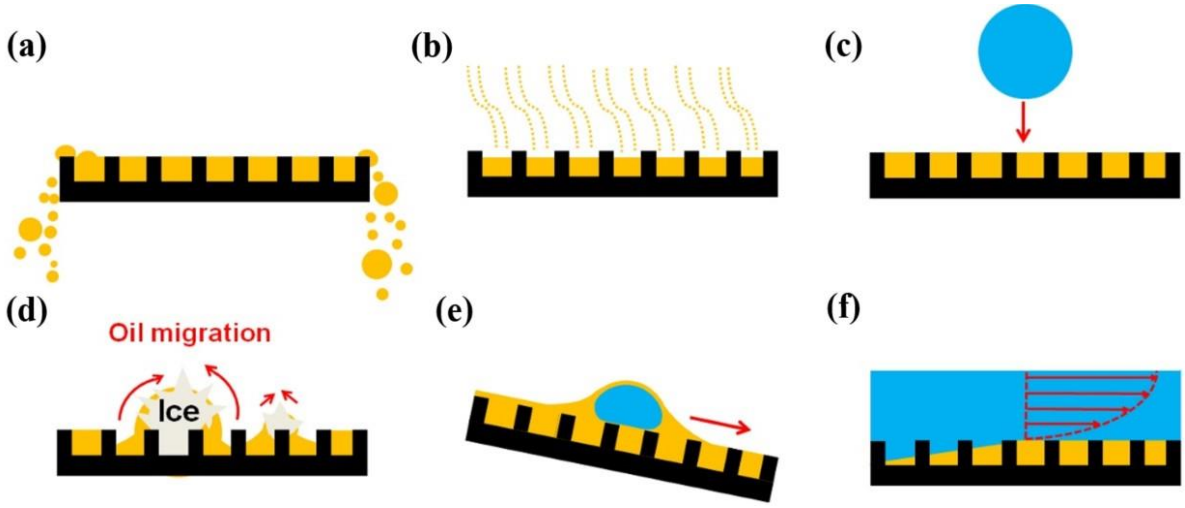

Fig. 2.16. Schematic illustrations showing lubricant depletion from the surface structures due to: (a) gravitational forces; (b) evaporation; (c) droplet impact; (d) ice formation; (e) cloaked liquid droplets; (f) shear forces [102].

However, some of the aforementioned mechanisms responsible for the failure of LIS can be counteracted or at least mitigated. For instance, lubricant displacement and evaporation can be minimised by utilising high viscosity lubricants when producing LIS, which is attributed to the enhanced viscous dissipation and their low evaporation rate, respectively [68, 102]. As stated earlier, lubricant is entrapped into the surface structures by capillary forces and thus various attempts have been carried out to improve the durability of LIS by modifying the underlying surface topography of LIS. In particular, scaffolds with a micro/nanostructured surface topography have widely been investigated as a means of enhancing lubricant retention and consequently the functional response of LIS. Yet, the capillary forces induced by the microscale cavities of such structures are weak and as a result the stored lubricant can easily escape under persistent shear flow conditions [102]. In contrast, a systematic investigation of LIS produced with different length scale topographies revealed that the ones with homogeneous nanostructures exhibited superior stability and accomplished to preserve their functionalities even when subjected to extreme centrifugal forces [126]. In reality, the durable

performance of such LIS was attributed to the relatively strong capillary pressure manifested by the underlying nanostructures, enabling a better lubricant retention. Thereafter, further efforts were made to identify the critical parameters that can help to reduce shear-induced lubricant depletion. Especially, it was reported that underlying surface structures with interstitials equal to or less than a particular length (L_∞), also known as steady-state length, can mitigate lubricant loss by shear forces (see Fig. 2.17) [121]. In addition, this length depends on the dimensional and geometrical characteristics of the surface structures and thus it is possible to be manipulated, which can then help to improve lubricant retention [102]. For instance, surfaces with both deeper and narrower interstitials exhibit a larger steady-state length [102].

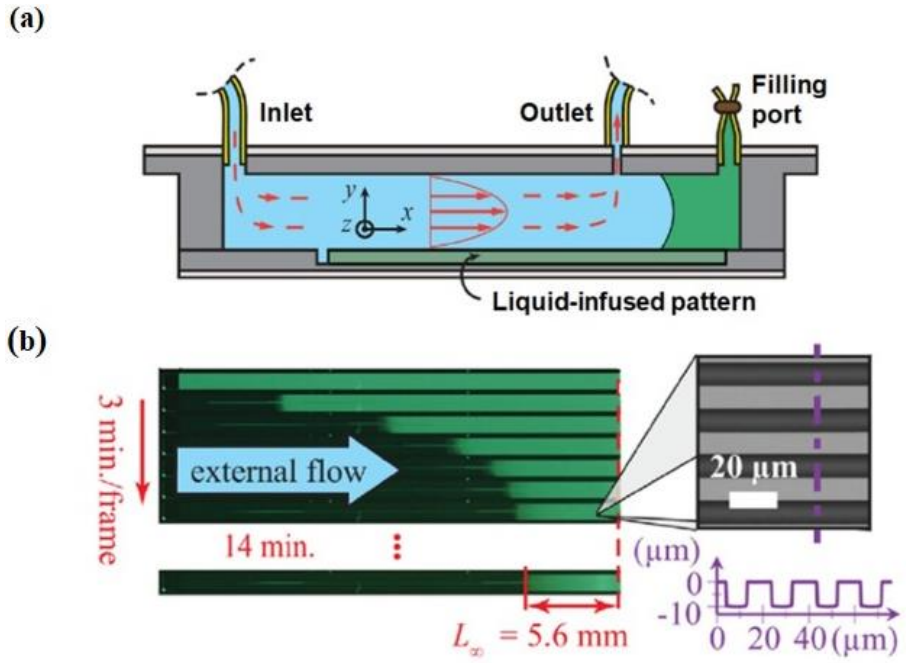

Fig. 2.17. Durability of LIS under shear flow conditions: (a) a cross-section of the microfluidic flow cell prior to conducting the experiment. The green colour represents the infused lubricant; (b) lubricant depletion over time and the determination of a steady-state length L_∞. *Note:* the shear-induced lubricant depletion was investigated at a constant flow rate of 2 mL/min and shear stress of 5.2 Pa [121].

2.3.5. Applications in food packaging and optical medical devices: state-of-the-art, properties and durability

As discussed analytically in Sub-section 2.3.2, various "bottom-up" and "top-down" manufacturing techniques have been developed over the years to fabricate stable LIS. In the majority of the studies, the functionality of LIS was evaluated against simple Newtonian liquids, especially water. For instance, Adera et al. [69] reported the fabrication of nanostructured LIS on copper tubes with superior water repellency (CAH of ~ 1°). By monitoring weight changes in their mass over time, they demonstrated that half of the impregnated oil was retained by the nanostructures after 7 hours in condensation conditions. However, LIS would most likely be exposed to complex liquids, e.g. viscous food liquids or biological fluids, in applications related to food, medical and healthcare industries. Therefore, their functional response and durability should be investigated against such liquids, too.

In this regard, significant efforts were made recently to assess the interaction of complex liquids with LIS, targeting easy-to-empty packaging/containers that are in the focus of this research. To begin with, Zhang et al. [134] produced nanoporous aluminium LIS by combining sol-gel and hydrothermal treatments, and their antifouling functionalities were demonstrated against various food liquids (i.e. milk, juice, coffee and ketchup). The as-prepared LIS displayed excellent anti-adhesive characteristics with CSA values below 5°, but an analysis of their durability and long-term performance was not reported in this study. On the contrary, Lee et al. [135] employed an anodizing process to generate different nanostructured topographies on aluminium surfaces, which were covered by a thin layer of Teflon prior to their lubrication. Thereafter, both the anti-adhesive and durability characteristics of these functional surfaces were characterised. This research showed that non-connecting topographies possessed a better resistance to lubricant depletion than the connecting ones, and thus they managed to retain

their slippery performance even after dripping a number of 176 water droplets on the surface or subjecting them to continuous jet flow for up to 48 hours. At the same time, these samples were able not only to repel ketchup and olive oil at a tilting angle of ~ 10° but also to reduce bacteria attachment by 99.2%. A coating-based process chain to fabricate LIS on glass substrates was also reported, in which three kinds of silanes and a curing adhesive were used [18]. CSA values of less than 7° were measured on these LIS samples for various low surface energy organic liquids, and thus they displayed outstanding omniphobicity. Apart from that, no fouling formation was observed on their surfaces even when immersed into different bulk food liquids (i.e. milk, honey, coffee and ketchup) for 60 consecutive times. In addition, another type of LIS, namely liquid-infused organogels, was successfully fabricated and used by researchers for antifouling applications [136, 137]. Benefitted from the entrapped lubricant inside the 3D porous structure, the proposed slippery organogels displayed long-lasting shedding functionalities against viscous emulsions. However, the use of these semi-solid materials in practical applications is hampered by their lack of mechanical robustness [138].

Interestingly, even though thermoplastic polymers are mainly used in the food packaging sector, only a few studies were focused on producing LIS on such materials and demonstrating their functional response against complex liquids. More specifically, Mukherjee et al. [139] deployed different oil absorbent hydrocarbon-based polymer films to prepare LIS and their anti-adhesive characteristics were evaluated towards viscous food liquids, such as ketchup and yogurt. All the polymer LIS were capable of repelling ketchup droplets at a CSA below 20°, whilst the one with the best performance preserved its slipperiness even when stored in a container filled with ketchup for 50 days. At the same time, another research reported the fabrication of porous thermoplastic polymer LIS via solvent casting, which exhibited impressive liquid-repellency against hexadecane droplets (CSA < 5°) [140]. Finally, a

femtosecond laser treatment was proposed to prepare LIS on polyamide sheets by generating a porous microstructure on the surface [141]. As experimentally demonstrated in this study, such polymer LIS had excellent anti-adhesive properties and hence they enabled a variety of food liquids (i.e. milk, coffee and egg fluids) to flow down their surfaces at a tilting angle of ~ 10°. Remarkably, the as-produced LIS had the ability to restore their unique functionalities upon mechanical damage, and thereby there was no significant degradation in their performance even after 100 abrasion cycles.

Furthermore, several other recent studies investigated the interaction of biological fluids with LIS, aiming to achieve transparent antifouling materials for medical optical devices. Manabe et al. [142] prepared biocompatible porous LIS on glass substrates using a layer-by-layer self-assembly method. Such LIS demonstrated excellent shedding (CSA of ~ 8° for blood droplets) and optical (transmittance of ~ 90%) properties. A reduction in the coagulation time of blood was observed on these surfaces, too. However, the LIS functionalities were completely lost when subjected to shear stress for 9 hours, i.e. blood droplets pinned to the surface. A year later another surface treatment was proposed to fabricate transparent LIS with anti-biofouling characteristics, which involved the deposition of silica particles onto bare glass surfaces [111]. To evaluate the potential of these LIS for medical applications, their sliding properties were investigated in this research against blood and droplets with different pH levels. Although the proposed LIS showed outstanding repellency towards all the tested liquids (CSA < 5°), their slippery performance was deteriorated under water jet impingement. Specifically, a total loss of functionality was observed in such conditions just after 3 hours. In addition, Sunny et al. [84] presented a very similar fabrication method to impart anti-biofouling functionalities onto glass lenses for endoscopes. In this case, the durability of LIS lens was assessed by continuously dipping them into containers filled with blood and mucus. It was demonstrated

that the as-prepared LIS could maintain a relatively clear endoscopic vision by repelling both body fluids for up to an average of 20 consecutive dipping cycles. Thereafter, their effectiveness to mitigate biofouling formation and consequently prevent vision loss was validated by in vivo clinical experiments. On the contrary, a recent study also reported the fabrication of such multifunctional lenses using a "top-down" process, i.e. direct laser texturing [104]. To enhance the longevity of their antifouling properties, the textured surfaces were covered with a fluorinated self-assembled monolayer. These LIS lenses displayed great anti-adhesive characteristics against different type of body fluids, with CSA values slightly below 15°. At the same time, the as-produced lens greatly inhibited not only biofouling and fogging but also protein attachment. Lastly, the directly engraved underlying topography of these LIS lenses led to a higher mechanical robustness compared to that of a reference particle-based coating.

In summary, considerable progress was made in designing LIS for shedding complex liquids away from surfaces and consequently preventing fouling phenomena. It is evident from the above review that LIS with such functional characteristics can also be produced on transparent materials without compromising their optical properties. However, only a small number prepared LIS on thermoplastic materials and investigated their functional performance, whilst they are of great interest to both food and medical industrial sectors. Furthermore, durability aspects of LIS were not sufficiently studied and also a better understanding of the effects of surface topography on their properties/durability is required. Lastly, the current state-of-the-art manufacturing techniques employed for producing LIS involve either complex multi-step procedures or high operating costs. On top of that, almost all of them include chemical treatments, e.g. fluorinated coatings, which can be extremely harmful to the ecological environment.

2.4. Laser-based micro machining technology

2.4.1. Fundamental principles of lasers

Laser is an exceptional source that emits light and its name stands for “Light Amplification by Stimulated Emission of Radiation”. Compared to other conventional light sources, laser radiation has four distinctive characteristics: high intensity, high monochromaticity, high directionality and high spatial-temporal coherence [143]. Due to these unique properties, a laser beam can propagate over relatively long distances with small divergence and also it can be focused upon small volumes with very high intensity [144]. Historically, Albert Einstein was the first to introduce the theory of stimulated emission in 1916, establishing the fundamental principles behind laser generation. However, it was many years later that the creation of the first commercial laser source, especially a ruby laser, was reported by the Theodore H. Maiman [145].

In general, a laser device can be divided into three major parts as illustrated in Fig. 2.18. Active mediums (or lasing mediums) are materials, i.e. gases, liquids or solids, that are used to produce an electromagnetic radiation, and their composition defines the nominal wavelength of laser light. However, it should be highlighted that in the case of solid-state and fiber lasers, glass or crystalline materials are mostly utilised as active mediums that are then fused with elements such as ytterbium or neodymium, among others. Upon excitation of the atoms and/or molecules contained in the various active mediums, their surrounding electrons can jump to a higher energy level. For laser action, it is necessary to achieve the so-called “population inversion”. More specifically, this phenomenon can only occur when there is a greater number of excited-state electrons than those in the ground-state [146]. Therefore, a pumping source is required to deliver an external source of energy and excite the lasing medium, which

determines the laser's output power [147]. In particular, such an energy source can be optical (lamps or other lasers), electrical and even chemical [146]. Lastly, an optical cavity (or resonator) is added to the system, which is an arrangement of two parallel mirrors placed at each end of the active medium. Specifically, one of these two mirrors is highly reflective while the other one is semi-transparent, resulting in the laser beam to travel back and forth [148]. Apart from amplifying the intensity of laser beam, the optical resonator also dictates its characteristics. However, this is not the case for all the different types of laser sources available on the market today. For instance, fibre lasers do not require such an optical arrangement and thus they exhibit a better beam quality and stability [149].

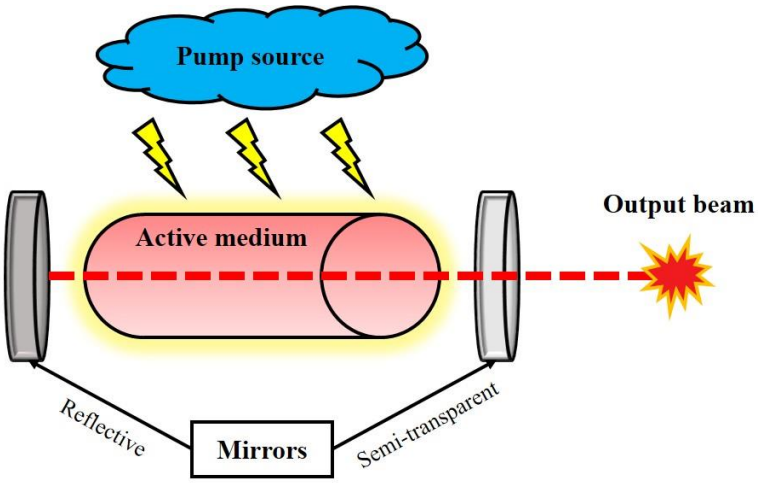

Fig. 2.18. Schematic diagram depicting the main components of a laser source.

Nowadays, lasers can deposit energy onto a substrate either in a continuous manner or by generating a sequence of pulses, with a particular duration, at a given repetition rate. Among the two aforementioned categories of lasers, those operating in the latter mode have attracted more attention in a number of fields, e.g. medical surgeries, material processing and communication [150]. Initially, long-pulsed millisecond lasers were adopted to execute different laser operations, e.g. cutting, engraving and drilling, in industrial processes.

However, over the years, technological advances in various sectors, i.e. biomedical, aerospace, electronics and telecommunications, have driven the demand for producing components with microscale features [151]. To address these challenging requirements, it was essential to minimise the thermal effects induced by long pulse lengths and hence to improve the overall precision of laser processing operations. Thus, remarkable efforts were invested to develop lasers emitting pulses with both high peak power and very short durations [152]. In particular, it was in 1991 when the first ultrashort laser source, i.e. a 60 fs self-mode-locked Ti:sapphire laser, was reported by Spence et al. [153]. Since ultrafast laser technologies were not mature at that time, the pulse energy of such lasers was not energetic enough to ablate material. As a result, they could not be used in manufacturing processes. A turning point in ultrafast lasers development came with the invention of chirped pulse amplification by Strickland and Mourou in 1985, which enabled the production of ultrashort laser sources with extremely high peak power [154]. Since this discovery, these lasers paved the way for many advances in both scientific and industrial fields (see Fig. 2.19) [155].

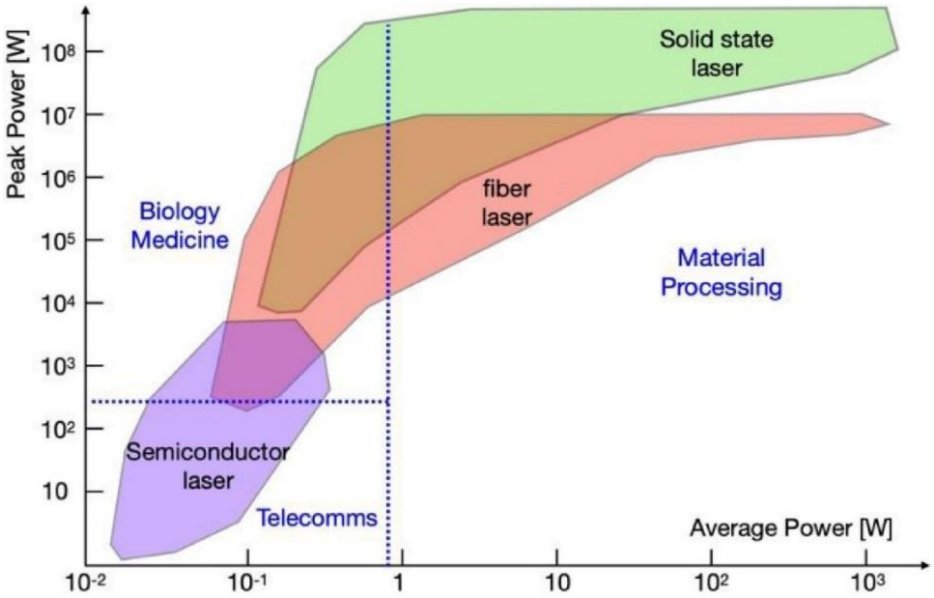

Fig. 2.19. A graph showing the applicability of different ultrashort pulse laser oscillator technologies [155].

2.4.2. Laser-material interactions

Over the last decade, several micro manufacturing operations have benefited from the advancements in laser technologies. So far, the number of research studies is increasing exponentially in this field and thus new opportunities of lasers in industrial applications are coming to light. Especially, significant progress has been made in the area of laser–material interaction with an emphasis on the effects of different pulse durations on the ablation of materials [156-158]. The findings of these investigations have revealed that the overall processing quality and precision can be improved substantially upon irradiation with shorter pulse durations. At the same time, the laser wavelength is another critical factor that influences the laser-material interaction and consequently the overall ablation efficiency [159, 160]. Since the absorptivity of most engineering materials depends on the incident radiation as shown in Fig. 2.20, there is a recent trend towards not only shorter and shorter laser pulse durations but also wavelengths. However, it should be stated that choosing the right source for laser material processing mainly depends on the type of application and its specific requirements.

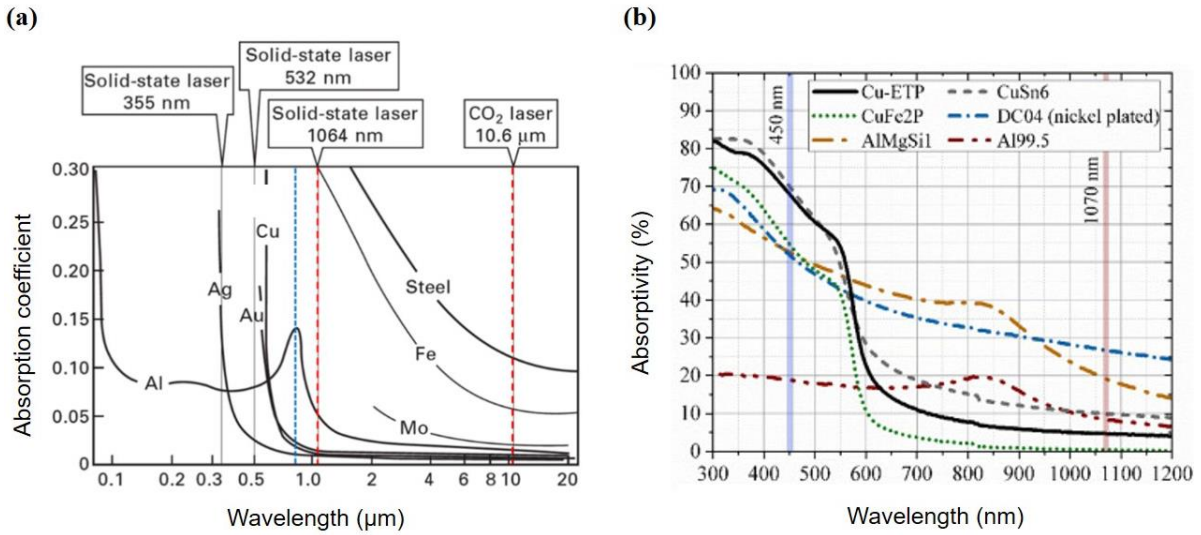

Fig. 2.20. Absorptivity of common metals at different laser wavelengths in the (a) wide spectrum [161] and (b) short-wavelength spectrum [162].

In recent years, the majority of LMM operations are carried out with either short (nanosecond) or ultrashort (picosecond and femtosecond) pulsed lasers, which can emit in a broad range of wavelengths, i.e. from ultraviolet (~ 100 nm) up to far infrared (~ 1 mm). However, it should be stated that the mechanisms of material ablation occurring between the two aforementioned pulse lengths are significantly different to each other [163]. For clarity purposes, SEM micrographs of a circular hole drilled with a nanosecond and a femtosecond laser are given in Fig. 2.21a, whilst graphical illustrations of their different laser ablation regimes are provided in Fig. 2.21b. As can be seen from these figures, ultrashort lasers offer superior machining quality and precision when compared to those with longer pulse durations. Actually, there is no sufficient time for the heat to diffuse into the bulk of material, and thus the surrounding irradiated areas display an almost negligible thermal damage [154]. In the ultrashort regime, the processed solid material undergoes the so-called 'cold ablation' and directly vapourises, resulting in machined structures with burr-free edges [164]. For example, it has been demonstrated that high-quality structures can be produced even onto polymer-based materials by using ultrashort pulsed lasers [165]. Lastly, another major advantage of such laser sources arises from their nonlinear pulse–material interaction, which enables to process inside highly transparent materials, e.g. polymers and glasses [166, 167].

On the other hand, ablation by nanosecond pulsed lasers is considered as a thermal process [168]. This is because the duration of each pulse is long enough so that the laser-induced heat can penetrate into the material. Since the thermal effects are more pronounced in this regime, the irradiated surface area starts to melt and then it is vaporised [169]. However, a substantial fraction of the melted material re-solidifies on the material surface, leading to the formation of a recast layer. In addition, the formation of surface oxidation, Heat Affected Zone (HAZ) and microcracks are some of the side effects of nanosecond laser treatments [154]. Despite

that, such treatments are associated with low operating costs and high efficiency [170], whilst their overall processing performance can be improved significantly upon irradiation in gaseous environments [171, 172]. Therefore, they have widely been utilised in numerous industrial machining operations, e.g. texturing, drilling, polishing and cutting.

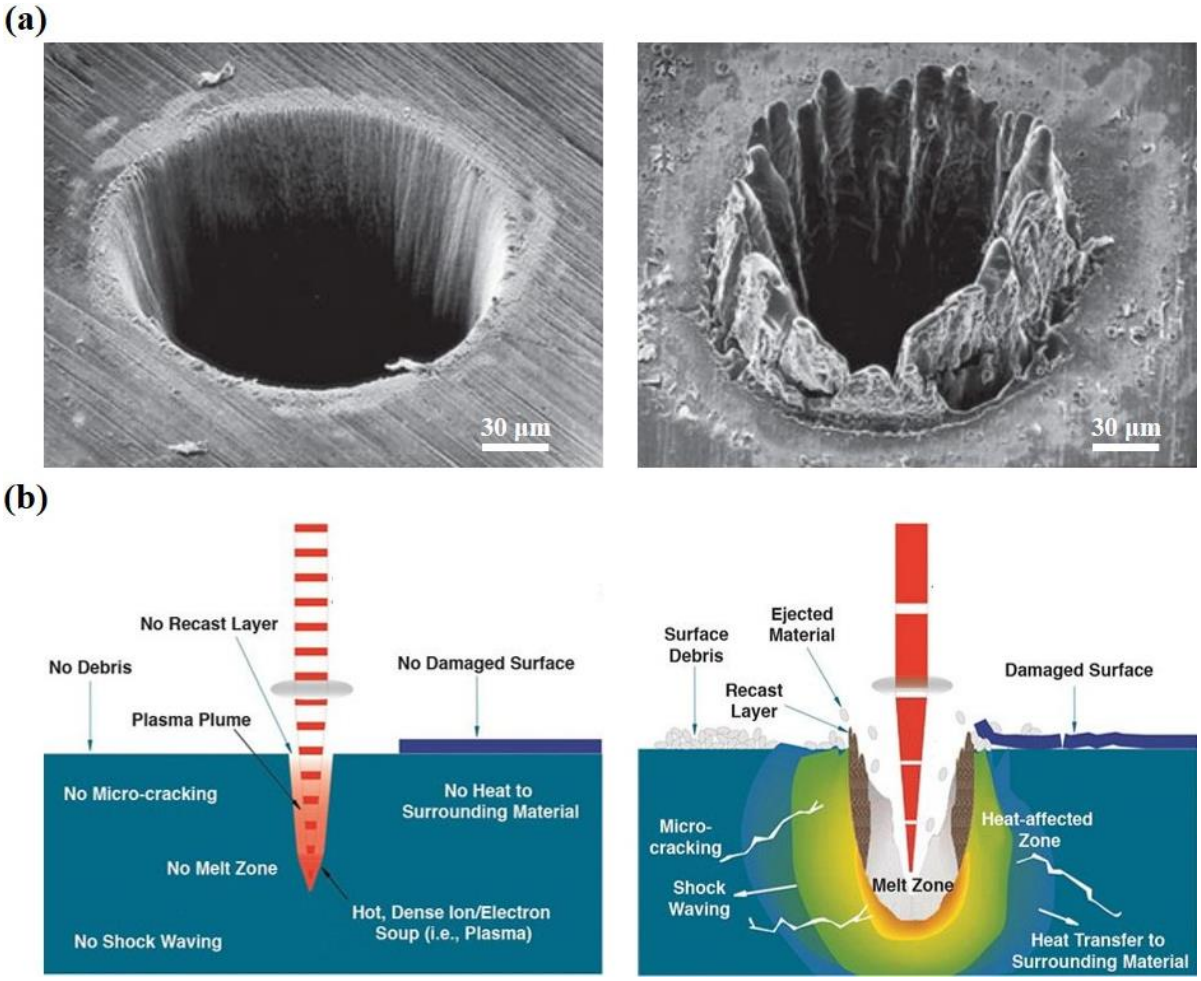

Fig. 2.21. Laser-material interactions: (a) SEM micrographs of a round hole drilled in a 100 µm thick metallic substrate by a femtosecond (left) and a nanosecond (right) pulsed laser [173]; (b) graphical illustrations of the laser-material interactions involved in the ultrashort (left) and short (right) ablation regimes [174]. *Note:* Based on the processing parameters provided in [173], the laser percussion-drilled holes presented in (a) were made with a beam spot size of ~ 175 µm.

2.4.3. Laser processing setups

Generally, there are various experimental setups that can be used in laser processing operations. These setups can have a very simple or complex design, depending on the application's specific requirements. At the same time, the capital cost of a LMM workstation can vary significantly and it can be estimated from the different component technologies included into the beam delivery sub-system. An illustrative example of an advanced LMM platform is given in Fig. 2.22, which specially designed for processing complex 3D parts.

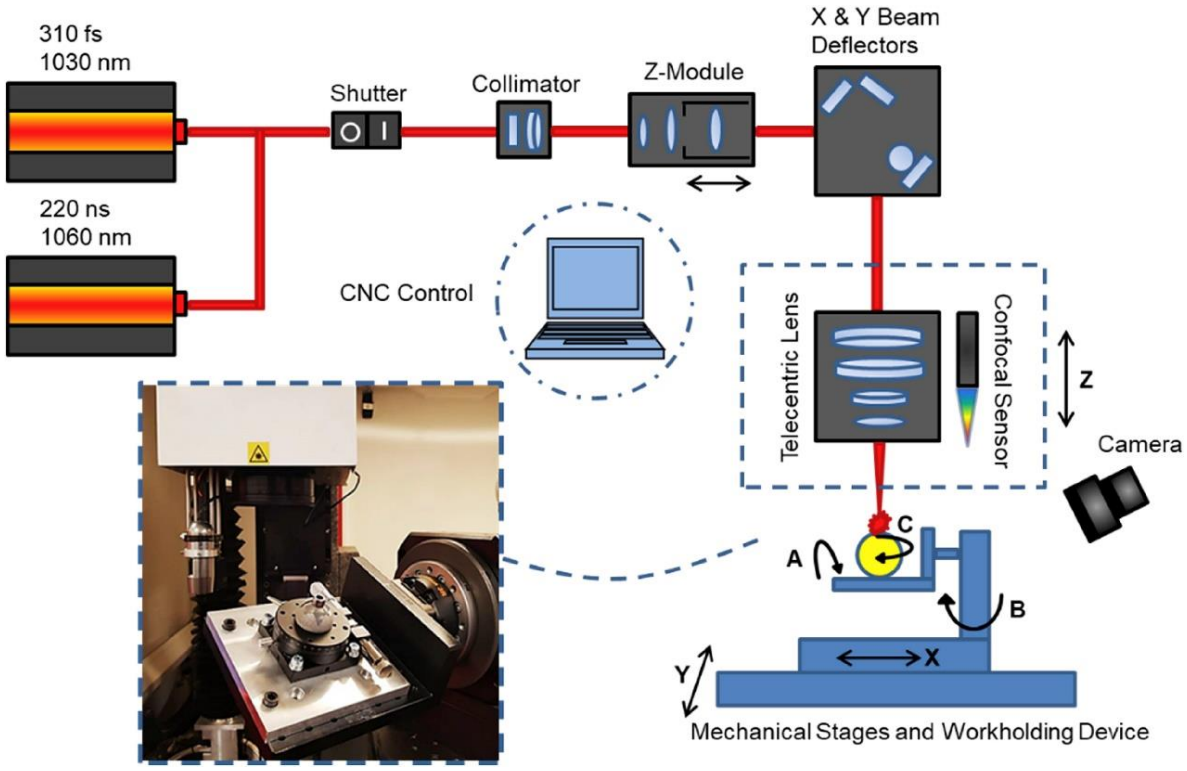

Fig. 2.22. A typical laser setup for multi-axis processing [175].

To begin with, a laser system consists of one or more laser sources, which may have different technical characteristics, e.g. femtosecond and nanosecond lasers. Commonly, a shutter device is added to the beam path that enables to precisely control the number of laser pulses deposited on the substrate, whilst beam expanders/reducers, i.e. either a Keplerian or Galilean telescope,

can also be integrated to adjust the size of a collimated input laser beam. Moreover, additional optical elements can be used to condition the beam and hence to improve the overall laser ablation efficiency. As can be seen in Fig. 2.23a, waveplates with a particular orientation can be employed to achieve the desired laser beam polarisation. The influence of laser polarisation on the ablation process was analytically discussed in [176]. At the same time, a LMM workstation can also be equipped with diffractive or refractive optical elements in order to benefit from extra functionalities. For instance, such optics can help to improve the quality of machined structures by converting a Gaussian beam into a flat-top one with uniform energy distribution (see Fig. 2.23b) or to increase productivity by splitting the incident beam into multiple ones (see Fig. 2.23c) [177, 178].

To move the laser beam in two lateral directions, LMM systems are usually equipped with galvo scanners, also known as scan-heads. Such devices consist of motorised mirrors that can deflect the beam across a substrate with high precision and speed. For high-throughput applications, polygon mirror-based scanners can be utilised as they offer much faster processing speeds, i.e. speeds up to 1000 m/s [179, 180]. Thereafter, it is necessary to focus the laser beam on the material and hence F-theta lenses are typically used to achieve this. In most cases, the focused beam is characterised by a beam profiler. Among the two types of focusing lenses shown in Fig. 2.23d, the telecentric ones are preferred when targeting high machining performance. More specifically, these lenses can maintain the Beam Incident Angle (BIA) normal to the irradiated surface within the field of view, resulting in superior processing uniformity than standard F-theta lenses. Meanwhile, a Z-module (see Fig. 2.22) can also be incorporated into the beam delivery sub-system, which enables to process parts with relatively small surface curvatures by dynamically adjusting the laser focus along the propagation direction. For laser processing large surface areas or components with intricate geometries, a

reconfigurable holding device together with a 5-axis CNC unit can be included in the LMM platform. Finally, the use of a high-resolution positioning camera and/or a confocal probe is essential in order to accurately place the samples at the focal plane and also calibrate both the focusing lenses and galvo scanners. It should be stated that all the aforementioned independent devices can be controlled through a dedicated Computer Aided Design/Computer Aided Manufacture (CAD/CAM) software, in which the desired laser scanning strategy and processing parameters can be defined for execution on a given LMM setup.

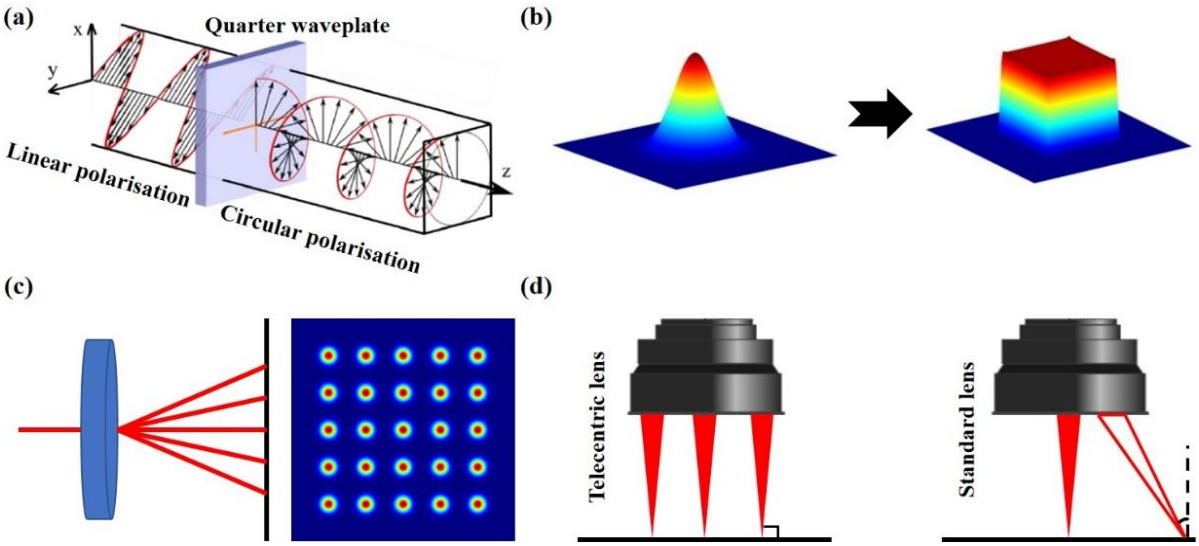

Fig. 2.23. Optical elements in laser processing: (a) schematic illustration of a quarter waveplate for converting the linearly polarised beam into circularly polarised one [181]; (b) intensity profiles of a typical Gaussian beam (left) and flat-top beam (right). (Image courtesy of IL Photonics); (c) diagram of a diffractive optical element used to split the input laser beam. (Image courtesy of Holo/Or); (d) the two common types of F-theta lenses used in laser material processing and their principal function.

2.4.4. Laser-enabled surface treatments

In recent years, surface functionalisation techniques have gained considerable attention from research community as an important enabler for developing innovative products. As already mentioned in Sub-section 2.3.2, several micro-manufacturing technologies have been deployed to modify the surface topography and/or chemistry of materials and hence to alter their functional response [182]. However, the majority of employed surface treatments have intrinsic limitations, i.e. difficult to scale up procedures involving toxic substances and having a dependence on material types, that currently prevent their industrial uptake [183]. At the same time, functional surfaces prepared by coating-based methods display poor durability, especially when subjected to mechanical damage [184].

To address these challenges, LMM has recently emerged as a promising tool for functionalising solid materials. In particular, this technology enables to simultaneously change the surface chemistry and topography of almost any engineering material, eliminating the need for low surface energy coatings [185]. Apart from offering high accuracy and precision, laser processing can also be considered as a much more environmental friendly method when compared to other surface modification approaches. This is because laser operations do not require the use of a cleanroom. Despite the many advantages, it should be stated that stand-alone direct LMM strategies are still capital intensive and thus they are not suitable for large batch production [186]. However, the relatively high manufacturing costs associated with this technology can be reduced substantially when combined with well-established mass production methods, i.e. polymer replication [187-190]. Therefore, replication processes are gaining importance as a means to cost-effectively alter the surface topography of chemically stable polymers, which is accomplished by transferring the textures from a tooling insert onto their surfaces [191]. For clarity purpose, an example of such a process chain developed to

enhance the hydrophobic properties of thermoplastic polymers is provided in Fig. 2.24, which involves laser texturing of metallic masters and then polymer replication by injection moulding. Based on the study reported in [191], the surface chemistry of polymer substrates was not affected by the micro-injection moulding and thus the change in CA was solely attributed to the alteration of their surface topography.

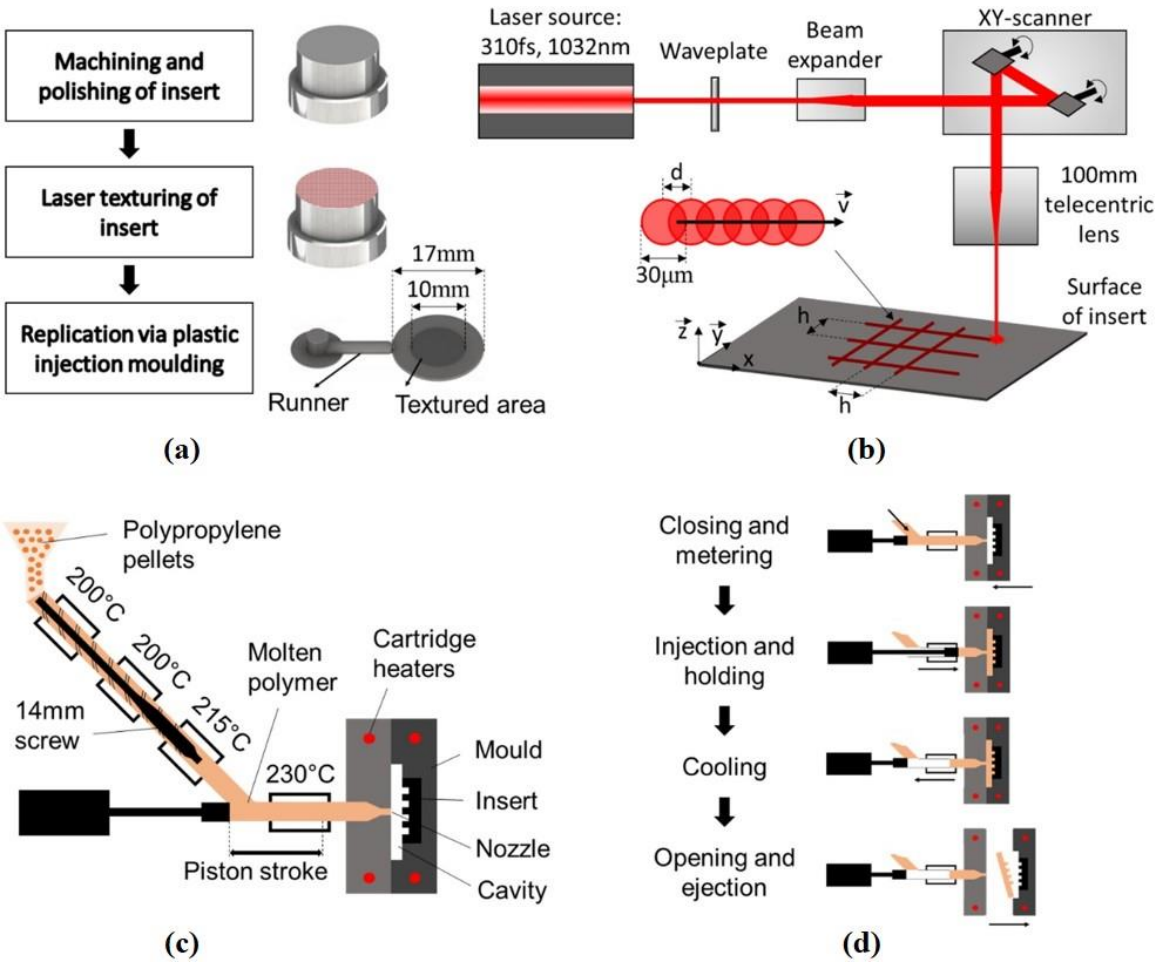

Fig. 2.24. Cost-effective process chain for producing hydrophobic polymer surfaces by combining LMM and polymer replication technologies: (a) schematic diagram of the manufacturing procedures involved; (b) the employed laser processing setup. The characters d and h indicate the pulse-to-pulse and hatch distance, respectively; (c) and (d) schematic illustrations of the injection moulding procedure followed to fabricate the textured polymer replicas [191].

Furthermore, another benefit of using LMM technology for functionalising materials is its capability to selectively fabricate micron-to-nanoscale features. Overall, several surface structures can be generated via laser texturing/structuring operations, which can be classified into two main groups: i) self-organized surface structures (random or periodic) and ii) laser-inscribed surface structures [192]. Among the different laser-enabled structures fall into the first category, LIPSS have drawn the most attention from researchers. As a proof, Fig. 2.25 depicts the number of research papers mentioning the word/phrase LIPSS through the years 1980 - 2022. In fact, LIPSS are periodical ripple-like nanostructures and their appearance was reported for the first time in 1965 [193]. Based on previous studies, it is apparent that these laser-induced structures can be imprinted onto a wide range of solid materials, e.g. metals [194], polymers [195], semiconductors [196], glass [197] and dielectrics [198]. Generally, LIPSS are divided into Low Spatial Frequency LIPSS (LSFL) and High Spatial Frequency LIPSS (HSFL) with periodicities close to and much smaller than the operating laser wavelength, respectively [199]. However, it should be stated that only the former type of LIPSS can be produced upon irradiation with both short [200] and ultrashort [201] pulsed lasers. Thus, LSFL LIPSS, referred to as LIPSS from now on in this PhD thesis (unless otherwise stated), have become a hot research topic.

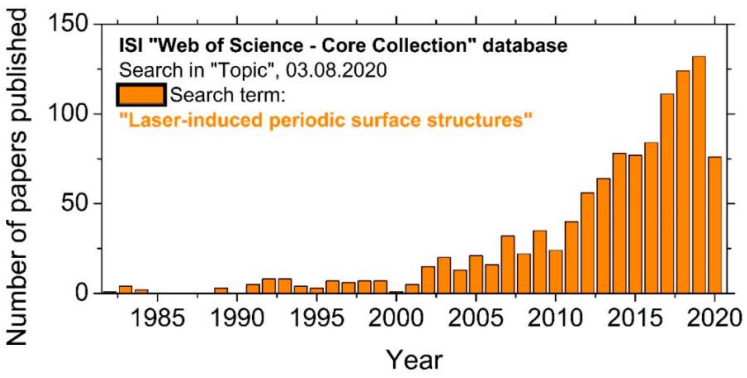

Fig. 2.25. Plot presenting the actual number of published papers on LIPSS between the years 1980 and 2020 [202].

Despite the numerous theoretical and experimental investigations, the physical mechanism behind the formation of LIPSS is still not fully understood. To date, the most well-accepted theory on LIPSS formation has been introduced by Sipe, which attributes their generation to the interference between the incident laser beam and the surface plasmon polaritons [203]. Typically, these structures start to appear on the surface when laser fluence is close to the ablation threshold of the target material [204], which can be determined using the so-called Liu's method [205]. The morphological characteristics of LIPSS can vary depending on the laser processing setup, and thus they can be tuned to achieve the desired surface functionality. For instance, highly regular LIPSS were observed on metallic materials with an orientation perpendicular to the laser beam polarisation as shown in Fig. 2.26a-c [206]. Whereas, homogenous triangular-like LIPSS (see Fig. 2.26d) in hexagonal arrangements were reported upon irradiation of SS with a circularly polarised laser beam [207, 208]. At the same time, many studies demonstrated that the spatial periodicity and amplitude of LIPSS can be controlled by varying the laser processing parameters, e.g. BIA and single pulse fluence [209-211]. Due to their distinctive physical characteristics, surfaces covered with such sub-wavelength surface undulations have widely been proposed as a means of colour-marking [212], improving cell adhesion [213], minimising reflections [214], reducing friction [215] and mitigating bacterial adhesion [216].

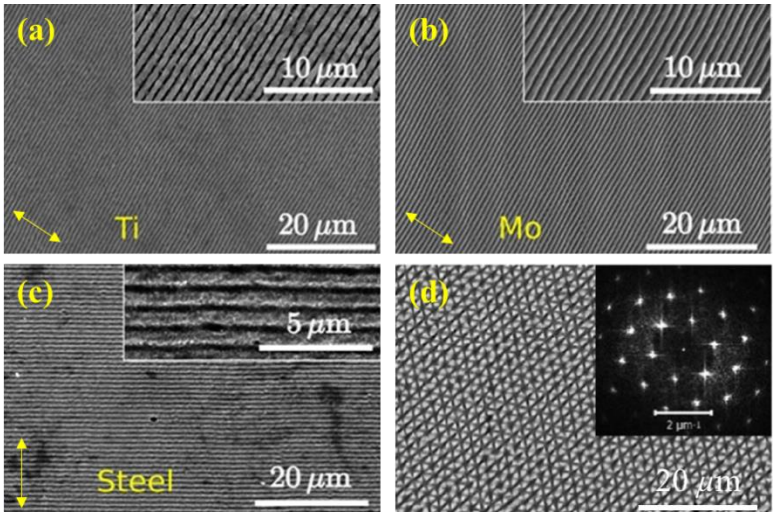

Fig. 2.26. Influence of laser polarisation on LIPSS formation: (a-c) SEM micrograph of highly regular LIPSS produced on Titanium, Molybdenum and Steel with an ultrashort laser, respectively [206]. The yellow arrows represent the direction of laser polarisation when processing the different metallic materials; (d) SEM image, with a 2D Fast Fourier Transform (2D-FFT) inset, of triangular LIPSS formed upon irradiation with a circularly polarised laser beam [207].

On the other hand, laser-inscribed MS surface structures have also received considerable attention by researchers because of their unique anti-wetting, anti-icing and anti-reflective functionalities [217, 218]. By properly adjusting the laser processing parameters, a wide variety of micro/nanoscale hierarchical structures can be formed on the surface with an ultrashort pulsed laser. For instance, one-dimensional microgrooves (see Fig. 2.27a) were produced on SS using a raster scanning strategy, whilst periodically arrayed microscale posts (see Fig. 2.27b) were formed on the same material by employing a grid-like scanning strategy [219]. A closer look on the SEM micrographs reveals that both microtopographies are fully covered with nanoscale ripple features, i.e. LIPSS. In reality, single pulse fluence levels above the material's ablation threshold are required to generate such laser-enabled MS structures. Based on Siddiquie et.al [220], the formation of micropillars with superimposed LIPSS was

attributed to the higher fluence accumulated at the intersecting points of beam vectors when scanning the surface multiple times.

However, it should be stated that the fabrication of MS topographies on metallic substrates has been reported with short pulsed lasers, too. More specifically, it was demonstrated that dual-scale parallel grooves (see Fig. 2.27c) and square-shaped pillars (see Fig. 2.27d) can be produced onto SS surfaces by taking advantage of the thermal-induced side effects associated with nanosecond laser processing [221]. From the SEM images, it is apparent that the microstructures were decorated with nanoscale features owing to the resolidification of melted material. Thereafter, a process chain to fabricate square-shaped pillars covered with LIPSS was proposed by combining two laser technologies, i.e. short and ultrashort pulsed lasers [222].

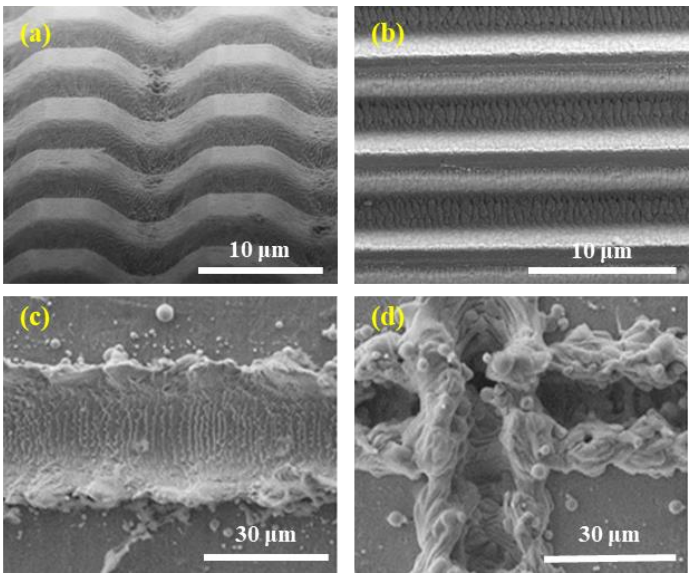

Fig. 2.27. SEM micrographs of different MS surface topographies textured on SS: (a-b) microscale posts and grooves fully covered by nano-ripples, respectively [219]; (b-c) microscale grooves and square-shaped pillars decorated with nanoparticles, respectively [221]. *Note:* The surface topographies presented in (a-b) were fabricated by a femtosecond pulsed laser, whilst the ones shown in (c-d) were produced with a nanosecond pulsed laser.

2.4.5. Multi-axis laser processing

Over the last years, technological advances in various industrial sectors have driven the demand for producing functional components/moulds with intricate geometries, e.g. freeform or curved surfaces [223]. However, unlike conventional machining, laser processing of curved surfaces is still a troublesome task. For instance, both the BIA from normal and Focal Offset Distance (FOD) vary with the surface curvature, resulting in distortion errors that can impact the morphological characteristics of laser-enabled structures and consequently their functional response [224, 225]. As a result, when employing complex 3D laser scanning strategies, these processing disturbances should be considered and then acceptable tolerance limits should be identified in order to achieve the desired process uniformity or functionality. On top of that, another difficulty arises in cases where surfaces should be laser processed at multiple scanning fields [226]. Fig. 2.28 shows the processing errors that can appear at the overlapping regions of different scanning fields.

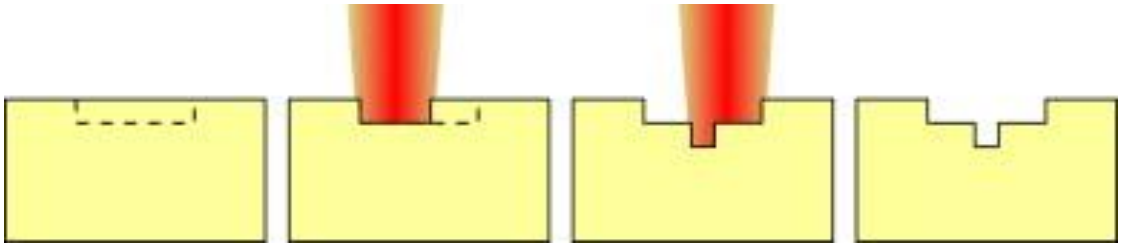

Fig. 2.28. Schematic illustration of processing errors generated at the overlapping regions of laser beam [226].

Despite the aforementioned challenges, several strategies have been proposed to enable laser processing of parts with complex geometries. Initially, such strategies relied on the use of a dynamic optical focusing system. More specifically, Diaci et al. [227] developed a method for engraving freeform substrates by first measuring their raw surface topography (see Fig. 2.29a) and then employing a Z-module to dynamically adjust the focus of laser beam. However, it

should be noted that the proposed methodology can only be used to process parts with a relatively small surface curvature due to the intrinsic constraints introduced by the dynamic focusing devices.

To overcome this issue, multi-axis LMM systems, i.e. equipped with both a 5 axes CNC unit and galvo scanner, have received considerable attention by researchers. Cuccolini et al. [228] were among the first to design a dedicated software, namely CALM, for partitioning a freeform surface into multiple planar scanning fields (see Fig. 2.29b). At the same time, a method to minimise stitching errors between the generated processing fields was proposed in this study, too. Thereafter, an alternative approach was reported by Wang et. al. [229], which enables to precisely produce patterns on curved surfaces (see Fig. 2.29c). In this case, the pattern projected on the surface needs to be divided into planar scanning fields and layers by taking into account both the lens's depth of focus and the negative effects of BIA. Lastly, Batal et al. [175] demonstrated a more comprehensive multi-axis laser processing strategy for processing freeform components. Specifically, this new method requires the laser processing constrains, i.e. acceptable BIA and FOD variations, to be predetermined for a given application and then used to drive the surface tessellation process.

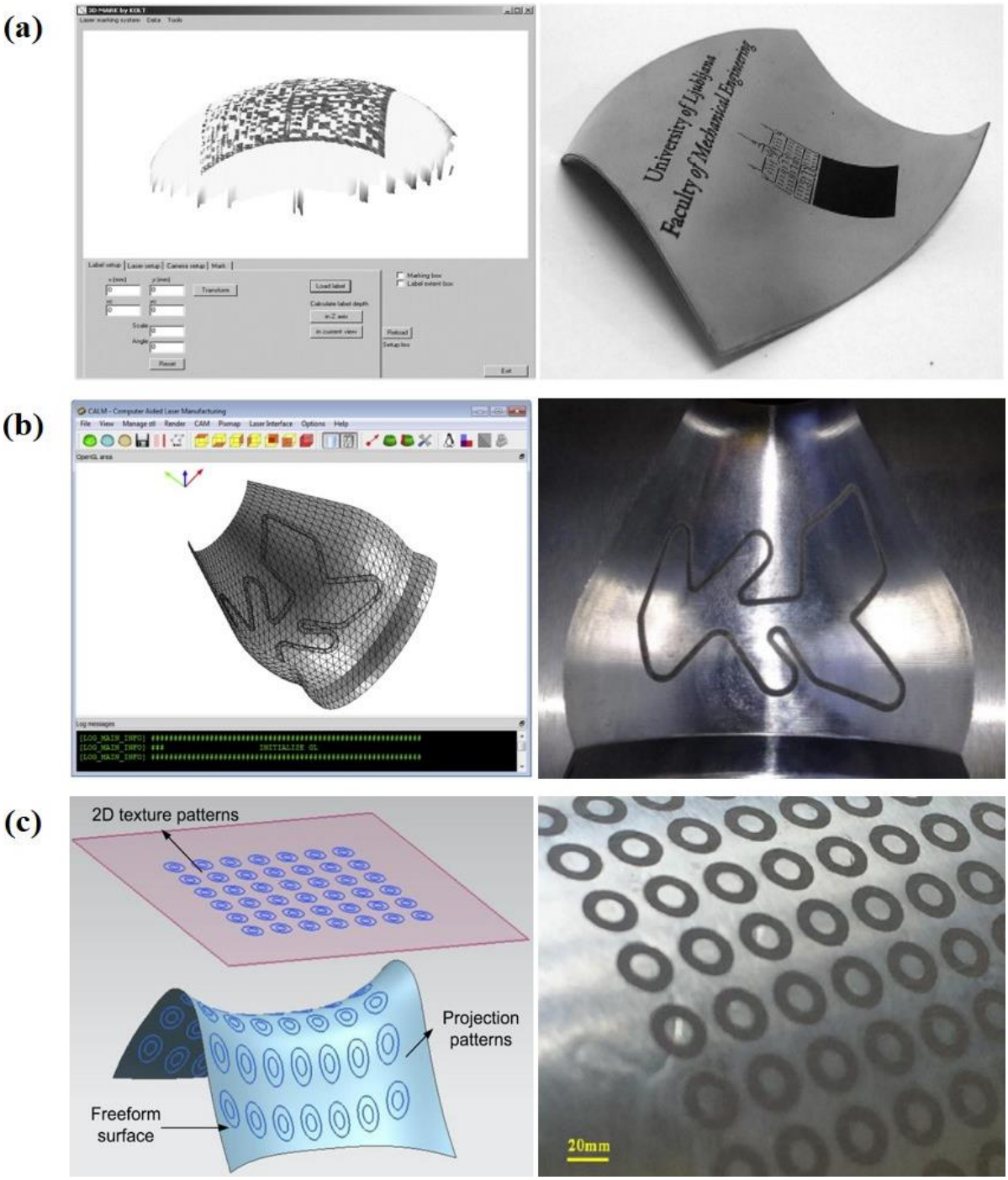

Fig. 2.29. 3D laser processing strategies: (a) interface of the software developed in [227] (left) and image of a pattern engraved on a freeform surface using this method (right); (b) triangulation of a curved surface in CALM software (left) and the actual feature machined on the surface (right) [228]; (c) illustration of the method used in [229] to project the patterns onto a freeform part (left) and image showing the patterns textured on its surface.

To meet the high demand for producing components with intricate geometries, multi-axis LMM systems have recently been developed that can operate in “simultaneous mode”. As a result, these systems can be employed to execute multi-axis simultaneous laser processing operations, which were considered not achievable till now. The basic principles of this technology will be introduced in Chapter 6. For laser processing of freeform surfaces, complex 3D laser scanning strategies can be programmed that involve the simultaneous control of both optical and mechanical axes. As demonstrated by Orazi et al. [230], significant improvements can be achieved with respect to the overall processing uniformity and efficiency when utilising such laser setups. However, it should be highlighted that multi-axis simultaneous laser texturing/structuring operations are not considered mature enough yet to be used on an industrial scale. This is partially due to their complexity and inferior machining accuracy. Although technical specifications of laser component technologies, e.g. optical beam deflectors and mechanical stages, are provided by their manufactures, it is not possible to predict the overall accuracy and precision achievable when implementing laser strategies that require multi-axis motions.

To obtain such information, various verification methods have been proposed for conventional 5-axis machine tools [231, 232]. Nevertheless, these techniques cannot be applied directly to evaluating the performance of laser systems, and a suitable test method has yet to be reported. Most likely this is because multi-axis simultaneous LMM capabilities have only been introduced to the market, recently. Therefore, further efforts should be devoted to assessing their effectiveness in processing curved/freeform surfaces and to identify a generic method for quantifying their performance. In fact, the development of an assessment method is of great importance as it can be used not only to evaluate the ARR of a multi-axis LMM system after

its installation on-site but also to determine potential systematic error sources and compensate them.

2.5. Synopsis of open research questions

Overall, the carried-out literature review revealed the huge potential of surface functionalisation techniques for developing innovative products with multifunctional responses. Among the different bio-inspired surfaces, LIS have recently emerged as a promising passive approach to impart durable anti-adhesive properties on materials and thus to mitigate fouling phenomena faced by several industrial sectors. In addition, a significant number of past studies have demonstrated the many advantages of LMM technology over other surface modification treatments, especially when used for producing such functional surfaces. However, there are still some open issues that should be addressed in order to enable the broader use of this technology in industry. The open research questions identified in this PhD thesis are as follows:

1. A significant progress has been made in developing surface treatment methods for fabricating LIS on different material types. However, there are still limited investigations of LIS on polymer-based materials, which are of great importance to food, cosmetic, agrochemical and healthcare sectors, among others. At the same time, the majority of these treatments are not scalable and/or their operation poses high ecological risks. Thus, it is essential to develop a cost-effective laser-enabled surface treatment for producing polymer LIS that display superior antifouling characteristics with a minimal environmental footprint.
2. Even though considerable research efforts have been dedicated to design stable LIS, durability aspects of these functional surfaces were not sufficiently characterised while they

are important for their broader use in practical applications. As a result, further investigations are required to better understand the effects and impact of LIS topographies on their durability and functionality. Since the LIS properties are shown to deteriorate upon lubricant depletion, their performance should be tested under both liquid shear and vibrational forces.

3. To date, although LIPSS have been extensively investigated as a means for imparting attractive functionalities onto surfaces, there has been limited research towards reducing their production costs. Especially, only a few studies were focused on the generation of LIPSS upon irradiation with short pulsed lasers, which are a cost-effective alternative to ultrashort ones. Nevertheless, the fabrication of high-quality LIPSS with such lasers still remains a challenging task due to their heat-induced side effects, and investigations into the improvement of their formation have not been reported yet. Therefore, it is essential to identify strategies for improving the overall LIPSS formation with short pulsed lasers and consequently enable their industrial applicability.
4. Extensive research has been dedicated to fabricate functional micro/nanostructures onto planar surfaces over the last decade, but there is now a pressing need to apply them onto components with intricate geometries. However, such laser operations require complex multi-axis simultaneous machining motions that were not technically achievable until recently. Since there is no sufficient knowledge about their processing performance, they are not considered mature enough to be used on an industrial scale. Therefore, it is of great significance to develop a systematic method for assessing the capabilities and limitations of simultaneous multi-axis laser strategies for processing freeform/curved parts.

References

[1] C. Hu, D. Ashok, D. R. Nisbet, and V. Gautam, "Bioinspired surface modification of orthopedic implants for bone tissue engineering," *Biomaterials,* vol. 219, p. 119366, 2019.

[2] E. Ozkan *et al.*, "Bioinspired ultra-low fouling coatings on medical devices to prevent device-associated infections and thrombosis," *Journal of Colloid and Interface Science,* vol. 608, pp. 1015-1024, 2022.

[3] Y. Su *et al.*, "Bioinspired surface functionalization of metallic biomaterials," *Journal of the Mechanical Behavior of Biomedical Materials,* vol. 77, pp. 90-105, 2018.

[4] J. Ma, T. Ma, W. Duan, W. Wang, J. Cheng, and J. Zhang, "Superhydrophobic, multi-responsive and flexible bottlebrush-network-based form-stable phase change materials for thermal energy storage and sprayable coatings," *Journal of Materials Chemistry A,* vol. 8, no. 42, pp. 22315-22326, 2020.

[5] L. Kong, X. Kong, Z. Ji, X. Wang, and X. Zhang, "Large-Scale Fabrication of a Robust Superhydrophobic Thermal Energy Storage Sprayable Coating Based on Polymer Nanotubes," *ACS Applied Materials & Interfaces,* vol. 12, no. 44, pp. 49694-49704, 2020.

[6] K. Bartlet, S. Movafaghi, L. P. Dasi, A. K. Kota, and K. C. Popat, "Antibacterial activity on superhydrophobic titania nanotube arrays," *Colloids and Surfaces B: Biointerfaces,* vol. 166, pp. 179-186, 2018.

[7] M. Song *et al.*, "Controlling liquid splash on superhydrophobic surfaces by a vesicle surfactant," *Science Advances,* vol. 3, no. 3, p. e1602188, 2017.

[8] J. Wang, H. Chen, T. Sui, A. Li, and D. Chen, "Investigation on hydrophobicity of lotus leaf: Experiment and theory," *Plant Science,* vol. 176, no. 5, pp. 687-695, 2009.

[9] W. Barthlott and C. Neinhuis, "Purity of the sacred lotus, or escape from contamination in biological surfaces," *Planta*, vol. 202, no. 1, pp. 1-8, 1997.

[10] P.-Y. Chen, J. McKittrick, and M. A. Meyers, "Biological materials: Functional adaptations and bioinspired designs," *Progress in Materials Science*, vol. 57, no. 8, pp. 1492-1704, 2012.

[11] Y. Zheng, X. Gao, and L. Jiang, "Directional adhesion of superhydrophobic butterfly wings," *Soft Matter*, vol. 3, no. 2, pp. 178-182, 2007.

[12] X. Gao and L. Jiang, "Water-repellent legs of water striders," *Nature*, vol. 432, no. 7013, pp. 36-36, 2004.

[13] T. Wang, L. Chang, L. Zhuang, S. Yang, Y. Jia, and C. Wong, "A hierarchical and superhydrophobic ZnO/C surface derived from a rice-leaf template," *Monatshefte für Chemie - Chemical Monthly*, vol. 145, no. 1, pp. 65-69, 2014.

[14] K. Koch, B. Bhushan, and W. Barthlott, "Multifunctional surface structures of plants: An inspiration for biomimetics," *Progress in Materials Science*, vol. 54, no. 2, pp. 137-178, 2009.

[15] D. Sekhar, S. Nachimutu, K. Ajay, and J. Seiko, "Review: Potential of biomimicry in the field of textile technology," *Bioinspired, Biomimetic and Nanobiomaterials*, vol. 6, no. 4, pp. 224-235, 2017.

[16] Z. Tang, P. Wang, B. Xu, L. Meng, L. Jiang, and H. Liu, "Bioinspired Robust Water Repellency in High Humidity by Micro-meter-Scaled Conical Fibers: Toward a Long-Time Underwater Aerobic Reaction," *Journal of the American Chemical Society*, vol. 144, no. 24, pp. 10950-10957, 2022.

[17] Z. Guo and W. Liu, "Biomimic from the superhydrophobic plant leaves in nature: Binary structure and unitary structure," *Plant Science,* vol. 172, no. 6, pp. 1103-1112, 2007.

[18] T. Kong, G. Luo, Y. Zhao, and Z. Liu, "Bioinspired Superwettability Micro/Nanoarchitectures: Fabrications and Applications," *Advanced Functional Materials*, vol. 29, no. 11, p. 1808012, 2019.

[19] K. Liu, J. Du, J. Wu, and L. Jiang, "Superhydrophobic gecko feet with high adhesive forces towards water and their bio-inspired materials," *Nanoscale,* vol. 4, no. 3, pp. 768-772, 2012.

[20] J.-S. Kwak and T.-W. Kim, "A review of adhesion and friction models for gecko feet," *International Journal of Precision Engineering and Manufacturing,* vol. 11, no. 1, pp. 171-186, 2010.

[21] M. Chakraborty, J. A. Weibel, J. A. Schaber, and S. V. Garimella, "The Wetting State of Water on a Rose Petal," *Advanced Materials Interfaces,* vol. 6, no. 17, p. 1900652, 2019.

[22] E. Stratakis *et al.*, "Laser engineering of biomimetic surfaces," *Materials Science and Engineering: R: Reports,* vol. 141, p. 100562, 2020.

[23] L. Wang and Q. Zhou, "Nepenthes pitchers: surface structure, physical property, anti-attachment function and potential application in mechanical controlling plague locust," *Chinese Science Bulletin,* vol. 59, no. 21, pp. 2513-2523, 2014.

[24] U. Bauer and W. Federle, "The insect-trapping rim of Nepenthes pitchers," *Plant Signaling & Behavior,* vol. 4, no. 11, pp. 1019-1023, 2009.

[25] M. A. Merbach, G. Zizka, B. Fiala, U. Maschwitz, and W. E. Booth, "Patterns of nectar secretion in five Nepenthes species from Brunei Darussalam, Northwest Borneo, and implications for ant-plant relationships," *Flora*, vol. 196, no. 2, pp. 153-160, 2001.

[26] L. Wang, Q. Zhou, Y. Zheng, and S. Xu, "Composite structure and properties of the pitcher surface of the carnivorous plant Nepenthes and its influence on the insect attachment system," *Progress in Natural Science*, vol. 19, no. 12, pp. 1657-1664, 2009.

[27] T. Huhtamäki, X. Tian, J. T. Korhonen, and R. H. A. Ras, "Surface-wetting characterization using contact-angle measurements," *Nature Protocols*, vol. 13, no. 7, pp. 1521-1538, 2018.

[28] B. Doshi, M. Sillanpää, and S. Kalliola, "A review of bio-based materials for oil spill treatment," *Water Research*, vol. 135, pp. 262-277, 2018.

[29] H. Zhu, Z. Guo, and W. Liu, "Adhesion behaviors on superhydrophobic surfaces," *Chemical Communications*, vol. 50, no. 30, pp. 3900-3913, 2014.

[30] S. Chen, M. Zhu, Y. Zhang, S. Dong, and X. Wang, "Magnetic-Responsive Superhydrophobic Surface of Magnetorheological Elastomers Mimicking from Lotus Leaves to Rose Petals," *Langmuir*, vol. 37, no. 7, pp. 2312-2321, 2021.

[31] B. Bhushan and E. K. Her, "Fabrication of Superhydrophobic Surfaces with High and Low Adhesion Inspired from Rose Petal," *Langmuir*, vol. 26, no. 11, pp. 8207-8217, 2010.

[32] L. Gao and T. J. McCarthy, "Contact Angle Hysteresis Explained," *Langmuir*, vol. 22, no. 14, pp. 6234-6237, 2006.

[33] Y. Ding, L. Jia, Q. Peng, and J. Guo, "Critical sliding angle of water droplet on parallel hydrophobic grooved surface," *Colloids and Surfaces A: Physicochemical and Engineering Aspects*, vol. 585, p. 124083, 2020.

[34] I. Ahmad and C.-w. Kan, "A Review on Development and Applications of Bio-Inspired Superhydrophobic Textiles," *Materials,* vol. 9, no. 11, p. 892, 2016.

[35] Q. Zeng, H. Zhou, J. Huang, and Z. Guo, "Review on the recent development of durable superhydrophobic materials for practical applications," *Nanoscale,* vol. 13, no. 27, pp. 11734-11764, 2021.

[36] Y.-M. Shin, S.-K. Lee, S. Jang, and J.-H. Park, "Superhydrophobic properties of a hierarchical structure using a silicon micro-tip array decorated with ZnO nanowires," *Current Applied Physics,* vol. 14, no. 5, pp. 665-671, 2014.

[37] A. Gharieh and M. Pourghasem, "Eco-friendly UV-curable polyurethane-silica superhydrophobic coating with superb mechanical durability," *Polymers for Advanced Technologies,* vol. 33, no. 10, pp. 3312-3322, 2022.

[38] K. Manoharan and S. Bhattacharya, "Superhydrophobic surfaces review: Functional application, fabrication techniques and limitations," *Journal of Micromanufacturing,* vol. 2, no. 1, pp. 59-78, 2019.

[39] A. K. Kota, G. Kwon, and A. Tuteja, "The design and applications of superomniphobic surfaces," *NPG Asia Materials,* vol. 6, no. 7, pp. e109-e109, 2014.

[40] W. Zhang, D. Wang, Z. Sun, J. Song, and X. Deng, "Robust superhydrophobicity: mechanisms and strategies," *Chemical Society Reviews,* vol. 50, no. 6, pp. 4031-4061, 2021.

[41] Y. Tang, X. Yang, Y. Li, Y. Lu, and D. Zhu, "Robust Micro-Nanostructured Superhydrophobic Surfaces for Long-Term Dropwise Condensation," *Nano Letters,* vol. 21, no. 22, pp. 9824-9833, 2021.

[42] W. Chen *et al.,* "Robust Superhydrophobic Surfaces via the Sand-In Method," *ACS Applied Materials & Interfaces,* vol. 14, no. 30, pp. 35053-35063, 2022.

[43] D. Wang *et al.*, "Design of robust superhydrophobic surfaces," *Nature,* vol. 582, no. 7810, pp. 55-59, 2020.

[44] E. Nyankson, H. Agbe, G. K. S. Takyi, Y. D. Bensah, and D. K. Sarkar, "Recent advances in nanostructured superhydrophobic surfaces: fabrication and long-term durability challenges," *Current Opinion in Chemical Engineering,* vol. 36, p. 100790, 2022.

[45] Y. Y. Yan, N. Gao, and W. Barthlott, "Mimicking natural superhydrophobic surfaces and grasping the wetting process: A review on recent progress in preparing superhydrophobic surfaces," *Advances in Colloid and Interface Science,* vol. 169, no. 2, pp. 80-105, 2011.

[46] A. Samanta, Q. Wang, S. K. Shaw, and H. Ding, "Roles of chemistry modification for laser textured metal alloys to achieve extreme surface wetting behaviors," *Materials & Design,* vol. 192, p. 108744, 2020.

[47] R. N. Wenzel, "RESISTANCE OF SOLID SURFACES TO WETTING BY WATER," *Industrial & Engineering Chemistry,* vol. 28, no. 8, pp. 988-994, 1936.

[48] A. O. Ijaola *et al.*, "Wettability Transition for Laser Textured Surfaces: A Comprehensive Review," *Surfaces and Interfaces,* vol. 21, p. 100802, 2020.

[49] C. Luo and M. Xiang, "Angle Inequality for Judging the Transition from Cassie–Baxter to Wenzel States When a Water Drop Contacts Bottoms of Grooves between Micropillars," *Langmuir,* vol. 28, no. 38, pp. 13636-13642, 2012.

[50] R. K. Annavarapu, S. Kim, M. Wang, A. J. Hart, and H. Sojoudi, "Explaining Evaporation-Triggered Wetting Transition Using Local Force Balance Model and Contact Line-Fraction," *Scientific Reports,* vol. 9, no. 1, p. 405, 2019.

[51] S. Han, R. Yang, C. Li, and L. Yang, "The Wettability and Numerical Model of Different Silicon Microstructural Surfaces," *Applied Sciences,* vol. 9, no. 3, p. 566, 2019.

[52] L. Rapoport, B. R. Solomon, and K. K. Varanasi, "Mobility of Yield Stress Fluids on Lubricant-Impregnated Surfaces," *ACS Applied Materials & Interfaces,* vol. 11, no. 17, pp. 16123-16129, 2019.

[53] M. Yu *et al.*, "Facile fabrication of biomimetic slippery lubricant-infused transparent and multifunctional omniphobic surfaces," *Journal of Materials Science,* vol. 55, no. 10, pp. 4225-4237, 2020.

[54] T. Karkantonis, A. Gaddam, T. L. See, S. S. Joshi, and S. Dimov, "Femtosecond laser-induced sub-micron and multi-scale topographies for durable lubricant impregnated surfaces for food packaging applications," *Surface and Coatings Technology,* vol. 399, p. 126166, 2020.

[55] J. Li, H. Zhao, and L. Wang, "Bioinspired Depletion-Resistant Lubricant-Infused Surfaces with Self-Replenishing Lubrication Through Capillary Filament," *Advanced Materials Interfaces,* vol. 8, no. 16, p. 2100561, 2021.

[56] H. Cha, S. Sett, P. Birbarah, T. Gebrael, J. Oh, and N. Miljkovic, "Recent advances in structured surface enhanced condensation heat transfer," *Nanoscale Energy Transport*: IOP Publishing, pp. 13-1-13-32, 2020.

[57] T.-S. Wong *et al.*, "Bioinspired self-repairing slippery surfaces with pressure-stable omniphobicity," *Nature,* vol. 477, no. 7365, pp. 443-447, 2011.

[58] J. D. Smith *et al.*, "Droplet mobility on lubricant-impregnated surfaces," *Soft Matter,* vol. 9, no. 6, pp. 1772-1780, 2013.

[59] B. R. Solomon, S. B. Subramanyam, T. A. Farnham, K. S. Khalil, S. Anand, and K. K. Varanasi, "CHAPTER 10 Lubricant-Impregnated Surfaces," in *Non-wettable Surfaces: Theory, Preparation and Applications*: The Royal Society of Chemistry, pp. 285-318, 2017.

[60] R. J. Good, "Contact angle, wetting, and adhesion: a critical review," *Journal of Adhesion Science and Technology,* vol. 6, no. 12, pp. 1269-1302, 1992.

[61] C. E. Stauffer, "The Measurement of Surface Tension by the Pendant Drop Technique," *The Journal of Physical Chemistry,* vol. 69, no. 6, pp. 1933-1938, 1965.

[62] S. Anand, K. Rykaczewski, S. B. Subramanyam, D. Beysens, and K. K. Varanasi, "How droplets nucleate and grow on liquids and liquid impregnated surfaces," *Soft Matter,* vol. 11, no. 1, pp. 69-80, 2015.

[63] M. Tress, S. Karpitschka, P. Papadopoulos, J. H. Snoeijer, D. Vollmer, and H.-J. Butt, "Shape of a sessile drop on a flat surface covered with a liquid film," *Soft Matter,* vol. 13, no. 20, pp. 3760-3767, 2017.

[64] T. Karkantonis, A. Gaddam, H. Sharma, G. Cummins, T. L. See, and S. Dimov, "Laser-Enabled Surface Treatment of Disposable Endoscope Lens with Superior Antifouling and Optical Properties," *Langmuir,* vol. 38, no. 37, pp. 11392-11405, 2022.

[65] Y. Liu, X. Yan, and Z. Wang, "Droplet dynamics on slippery surfaces: small droplet, big impact," *Biosurface and Biotribology,* vol. 5, no. 2, pp. 35-45, 2019.

[66] M. S. Sadullah, J. R. Panter, and H. Kusumaatmaja, "Factors controlling the pinning force of liquid droplets on liquid infused surfaces," *Soft Matter,* vol. 16, no. 35, pp. 8114-8121, 2020.

[67] X. He, P. Cao, F. Tian, X. Bai, and C. Yuan, "Infused configurations induced by structures influence stability and antifouling performance of biomimetic lubricant-infused surfaces," *Surface and Coatings Technology*, vol. 358, pp. 159-166, 2019.

[68] A. Keiser, L. Keiser, C. Clanet, and D. Quéré, "Drop friction on liquid-infused materials," *Soft Matter*, vol. 13, no. 39, pp. 6981-6987, 2017.

[69] S. Adera, J. Alvarenga, A. V. Shneidman, C. T. Zhang, A. Davitt, and J. Aizenberg, "Depletion of Lubricant from Nanostructured Oil-Infused Surfaces by Pendant Condensate Droplets," *ACS Nano*, vol. 14, no. 7, pp. 8024-8035, 2020.

[70] C. Wang and Z. Guo, "A comparison between superhydrophobic surfaces (SHS) and slippery liquid-infused porous surfaces (SLIPS) in application," *Nanoscale*, vol. 12, no. 44, pp. 22398-22424, 2020.

[71] J. Zhang, A. Wang, and S. Seeger, "Nepenthes Pitcher Inspired Anti-Wetting Silicone Nanofilaments Coatings: Preparation, Unique Anti-Wetting and Self-Cleaning Behaviors," *Advanced Functional Materials*, vol. 24, no. 8, pp. 1074-1080, 2014.

[72] D. Wang and Z. Guo, "A bioinspired lubricant infused surface with transparency, hot liquid boiling resistance and long-term stability for food applications," *New Journal of Chemistry*, vol. 44, no. 11, pp. 4529-4537, 2020.

[73] S. Zouaghi *et al.*, "Antifouling Biomimetic Liquid-Infused Stainless Steel: Application to Dairy Industrial Processing," *ACS Applied Materials & Interfaces*, vol. 9, no. 31, pp. 26565-26573, 2017.

[74] E. H. Yildirim, "Improvement of lubricant-infused surfaces for anti-icing applications," *Surface Innovations*, vol. 4, no. 4, pp. 214-217, 2016.

[75] D. Wu *et al.*, "Durable deicing lubricant-infused surface with photothermally switchable hydrophobic/slippery property," *Materials & Design*, vol. 185, p. 108236, 2020.

[76] S. J. Lee, H. N. Kim, W. Choi, G. Y. Yoon, and E. Seo, "A nature-inspired lubricant-infused surface for sustainable drag reduction," *Soft Matter*, vol. 15, no. 42, pp. 8459-8467, 2019.

[77] J. Lee, M.-H. Lee, and C.-H. Choi, "Design of Robust Lubricant-Infused Surfaces for Anti-Corrosion," *ACS Applied Materials & Interfaces*, vol. 14, no. 1, pp. 2411-2423, 2022.

[78] Q. Rao *et al.*, "NIR-driven fast construction of patterned-wettability on slippery lubricant infused surface for droplet manipulation," *Chemical Engineering Journal*, vol. 428, p. 131141, 2022.

[79] X. Gou and Z. Guo, "Reed leaf-inspired anisotropic slippery lubricant-infused surface for water collection and bubble transportation," *Chemical Engineering Journal*, vol. 411, p. 128495, 2021.

[80] D. J. Preston *et al.*, "Heat Transfer Enhancement During Water and Hydrocarbon Condensation on Lubricant Infused Surfaces," *Scientific Reports*, vol. 8, no. 1, p. 540, 2018.

[81] S. Yuan, S. Luan, S. Yan, H. Shi, and J. Yin, "Facile Fabrication of Lubricant-Infused Wrinkling Surface for Preventing Thrombus Formation and Infection," *ACS Applied Materials & Interfaces*, vol. 7, no. 34, pp. 19466-19473, 2015.

[82] K. Chae *et al.*, "Antibacterial infection and immune-evasive coating for orthopedic implants," *Science Advances*, vol. 6, no. 44, p. eabb0025, 2020.

[83] C. Wei, G. Zhang, Q. Zhang, X. Zhan, and F. Chen, "Silicone Oil-Infused Slippery Surfaces Based on Sol–Gel Process-Induced Nanocomposite Coatings: A Facile Approach to Highly Stable Bioinspired Surface for Biofouling Resistance," *ACS Applied Materials & Interfaces,* vol. 8, no. 50, pp. 34810-34819, 2016.

[84] S. Sunny *et al.*, "Transparent antifouling material for improved operative field visibility in endoscopy," *Proc Natl Acad Sci U S A,* vol. 113, no. 42, pp. 11676-11681, 2016.

[85] M. Badv, C. Alonso-Cantu, A. Shakeri, Z. Hosseinidoust, J. I. Weitz, and T. F. Didar, "Biofunctional Lubricant-Infused Vascular Grafts Functionalized with Silanized Bio-Inks Suppress Thrombin Generation and Promote Endothelialization," *ACS Biomaterials Science & Engineering,* vol. 5, no. 12, pp. 6485-6496, 2019.

[86] H. Agarwal, K. E. Nyffeler, H. E. Blackwell, and D. M. Lynn, "Fabrication of Slippery Liquid-Infused Coatings in Flexible Narrow-Bore Tubing," *ACS Applied Materials & Interfaces,* vol. 13, no. 46, pp. 55621-55632, 2021.

[87] C. Howell, A. Grinthal, S. Sunny, M. Aizenberg, and J. Aizenberg, "Designing Liquid-Infused Surfaces for Medical Applications: A Review," *Advanced Materials,* vol. 30, no. 50, p. 1802724, 2018.

[88] J. Li, E. Ueda, D. Paulssen, and P. A. Levkin, "Slippery Lubricant-Infused Surfaces: Properties and Emerging Applications," *Advanced Functional Materials,* vol. 29, no. 4, p. 1802317, 2019.

[89] Z. Qiu, R. Qiu, Y. Xiao, J. Zheng, and C. Lin, "Slippery liquid-infused porous surface fabricated on CuZn: A barrier to abiotic seawater corrosion and microbiologically induced corrosion," *Applied Surface Science,* vol. 457, pp. 468-476, 2018.

[90] Y. Tuo, H. Zhang, W. Chen, and X. Liu, "Corrosion protection application of slippery liquid-infused porous surface based on aluminum foil," *Applied Surface Science*, vol. 423, pp. 365-374, 2017.

[91] F. Maryami, A. Olad, and K. Nofouzi, "Fabrication of slippery lubricant-infused porous surface for inhibition of microorganism adhesion on the porcelain surface," *Journal of Industrial and Engineering Chemistry*, vol. 108, pp. 308-320, 2022.

[92] D. C. Leslie *et al.*, "A bioinspired omniphobic surface coating on medical devices prevents thrombosis and biofouling," *Nature Biotechnology*, vol. 32, no. 11, pp. 1134-1140, 2014.

[93] Y. H. Yeong, C. Wang, K. J. Wynne, and M. C. Gupta, "Oil-Infused Superhydrophobic Silicone Material for Low Ice Adhesion with Long-Term Infusion Stability," *ACS Applied Materials & Interfaces*, vol. 8, no. 46, pp. 32050-32059, 2016.

[94] F. Schellenberger *et al.*, "Direct observation of drops on slippery lubricant-infused surfaces," *Soft Matter*, vol. 11, no. 38, pp. 7617-7626, 2015.

[95] H. Guo *et al.*, "Bio-Inspired Superhydrophobic and Omniphobic Wood Surfaces," *Advanced Materials Interfaces*, vol. 4, no. 1, p. 1600289, 2017.

[96] M. Villegas, Y. Zhang, N. Abu Jarad, L. Soleymani, and T. F. Didar, "Liquid-Infused Surfaces: A Review of Theory, Design, and Applications," *ACS Nano*, vol. 13, no. 8, pp. 8517-8536, 2019.

[97] S. Zouaghi *et al.*, "Biomimetic surface modifications of stainless steel targeting dairy fouling mitigation and bacterial adhesion," *Food and Bioproducts Processing*, vol. 113, pp. 32-38, 2019.

[98] X. Zhu *et al.*, "Simple Way to a Slippery Lubricant Impregnated Coating with Ultrastability and Self-Replenishment Property," *Industrial & Engineering Chemistry Research,* vol. 58, no. 19, pp. 8148-8153, 2019.

[99] T. Xiang *et al.*, "Slippery liquid-infused porous surface for corrosion protection with self-healing property," *Chemical Engineering Journal,* vol. 345, pp. 147-155, 2018.

[100] H. Luo, S. Yin, S. Huang, F. Chen, Q. Tang, and X. Li, "Fabrication of slippery Zn surface with improved water-impellent, condensation and anti-icing properties," *Applied Surface Science,* vol. 470, pp. 1139-1147, 2019.

[101] X. Zhou, Y.-Y. Lee, K. S. L. Chong, and C. He, "Superhydrophobic and slippery liquid-infused porous surfaces formed by the self-assembly of a hybrid ABC triblock copolymer and their antifouling performance," *Journal of Materials Chemistry B,* vol. 6, no. 3, pp. 440-448, 2018.

[102] P. Baumli *et al.*, "The challenge of lubricant-replenishment on lubricant-impregnated surfaces," *Advances in Colloid and Interface Science,* vol. 287, p. 102329, 2021.

[103] Q. Ma, W. Wang, and G. Dong, "Facile fabrication of biomimetic liquid-infused slippery surface on carbon steel and its self-cleaning, anti-corrosion, anti-frosting and tribological properties," *Colloids and Surfaces A: Physicochemical and Engineering Aspects,* vol. 577, pp. 17-26, 2019.

[104] Y. Lee *et al.*, "Lubricant-infused directly engraved nano-microstructures for mechanically durable endoscope lens with anti-biofouling and anti-fogging properties," *Scientific Reports,* vol. 10, no. 1, p. 17454, 2020.

[105] G. Morgese, E. M. Benetti, and M. Zenobi-Wong, "Molecularly Engineered Biolubricants for Articular Cartilage," *Advanced Healthcare Materials,* vol. 7, no. 16, p. 1701463, 2018.

[106] A. Hosseini *et al.*, "Conductive Electrochemically Active Lubricant-Infused Nanostructured Surfaces Attenuate Coagulation and Enable Friction-Less Droplet Manipulation," *Advanced Materials Interfaces,* vol. 5, no. 18, p. 1800617, 2018.

[107] M. Ryu *et al.*, "Silica-nanoparticle reinforced lubricant-infused copper substrates with enhanced lubricant retention for maintenance-free heat exchangers," *Chemical Engineering Journal,* vol. 451, p. 138657, 2023.

[108] W. Lei, P. Krolla, T. Schwartz, and P. A. Levkin, "Controlling Geometry and Flow Through Bacterial Bridges on Patterned Lubricant-Infused Surfaces (pLIS)," *Small,* vol. 16, no. 52, p. 2004575, 2020.

[109] X. Trier, C. Taxvig, A. K. Rosenmai, and G. A. Pedersen, "PFAS in paper and board for food contact: Options for risk management of poly-and perfluorinated substances," *Nordic Council of Ministers,* 2018.

[110] H. J. Cox, C. P. Gibson, G. J. Sharples, and J. P. S. Badyal, "Nature-Inspired Substrate-Independent Omniphobic and Antimicrobial Slippery Surfaces," *Advanced Engineering Materials,* vol. 24, no. 6, p. 2101288, 2022.

[111] S. Nishioka *et al.*, "Facile design of plant-oil-infused fine surface asperity for transparent blood-repelling endoscope lens," *RSC Advances,* vol. 6, no. 53, pp. 47579-47587, 2016.

[112] D. Wang, Z. Guo, and W. Liu, "Bioinspired Edible Lubricant-Infused Surface with Liquid Residue Reduction Properties," *Research,* vol. 2019, p. 1649427, 2019.

[113] R. Ribeiro-Santos, M. Andrade, N. R. d. Melo, and A. Sanches-Silva, "Use of essential oils in active food packaging: Recent advances and future trends," *Trends in Food Science & Technology,* vol. 61, pp. 132-140, 2017.

[114] E. Panel o. F. Additives *et al.*, "Re-evaluation of dimethyl polysiloxane (E 900) as a food additive," *EFSA Journal*, vol. 18, no. 5, p. e06107, 2020.

[115] C. S. Ware *et al.*, "Marine Antifouling Behavior of Lubricant-Infused Nanowrinkled Polymeric Surfaces," *ACS Applied Materials & Interfaces*, vol. 10, no. 4, pp. 4173-4182, 2018.

[116] S. Peppou-Chapman and C. Neto, "Depletion of the Lubricant from Lubricant-Infused Surfaces due to an Air/Water Interface," *Langmuir*, vol. 37, no. 10, pp. 3025-3037, 2021.

[117] D. Paulssen, S. Hardt, and P. A. Levkin, "Droplet Sorting and Manipulation on Patterned Two-Phase Slippery Lubricant-Infused Surface," *ACS Applied Materials & Interfaces*, vol. 11, no. 17, pp. 16130-16138, 2019.

[118] J. Seiwert, C. Clanet, and D. QuÉRÉ, "Coating of a textured solid," *Journal of Fluid Mechanics*, vol. 669, pp. 55-63, 2011.

[119] H.-H. Tran, Y. Kim, C. Ternon, M. Langlet, D. Riassetto, and D. Lee, "Lubricant Depletion-Resistant Slippery Liquid-Infused Porous Surfaces via Capillary Rise Lubrication of Nanowire Array," *Advanced Materials Interfaces*, vol. 8, no. 7, p. 2002058, 2021.

[120] D. Kim, M. Lee, J.-H. Kim, and J. Lee, "Dynamic contact angle measurements on lubricant infused surfaces," *Journal of Colloid and Interface Science*, vol. 586, pp. 647-654, 2021.

[121] J. S. Wexler, I. Jacobi, and H. A. Stone, "Shear-Driven Failure of Liquid-Infused Surfaces," *Physical Review Letters*, vol. 114, no. 16, p. 168301, 2015.

[122] I. Jacobi, J. S. Wexler, and H. A. Stone, "Overflow cascades in liquid-infused substrates," *Physics of Fluids*, vol. 27, no. 8, p. 082101, 2015.

[123] M. Muschi, B. Brudieu, J. Teisseire, and A. Sauret, "Drop impact dynamics on slippery liquid-infused porous surfaces: influence of oil thickness," *Soft Matter,* vol. 14, no. 7, pp. 1100-1107, 2018.

[124] D. Daniel, J. V. I. Timonen, R. Li, S. J. Velling, and J. Aizenberg, "Oleoplaning droplets on lubricated surfaces," *Nature Physics,* vol. 13, no. 10, pp. 1020-1025, 2017.

[125] M. J. Kreder, J. Alvarenga, P. Kim, and J. Aizenberg, "Design of anti-icing surfaces: smooth, textured or slippery?," *Nature Reviews Materials,* vol. 1, no. 1, p. 15003, 2016.

[126] P. Kim, M. J. Kreder, J. Alvarenga, and J. Aizenberg, "Hierarchical or Not? Effect of the Length Scale and Hierarchy of the Surface Roughness on Omniphobicity of Lubricant-Infused Substrates," *Nano Letters,* vol. 13, no. 4, pp. 1793-1799, 2013.

[127] H. Bazyar, S. Javadpour, and R. G. H. Lammertink, "On the Gating Mechanism of Slippery Liquid Infused Porous Membranes," *Advanced Materials Interfaces,* vol. 3, no. 14, p. 1600025, 2016.

[128] J.-H. Kim and J. P. Rothstein, "Delayed lubricant depletion on liquid-infused randomly rough surfaces," *Experiments in Fluids,* vol. 57, no. 5, p. 81, 2016.

[129] J. S. Wexler, A. Grosskopf, M. Chow, Y. Fan, I. Jacobi, and H. A. Stone, "Robust liquid-infused surfaces through patterned wettability," *Soft Matter,* vol. 11, no. 25, pp. 5023-5029, 2015.

[130] J. Zhang, L. Wu, B. Li, L. Li, S. Seeger, and A. Wang, "Evaporation-Induced Transition from Nepenthes Pitcher-Inspired Slippery Surfaces to Lotus Leaf-Inspired Superoleophobic Surfaces," *Langmuir,* vol. 30, no. 47, pp. 14292-14299, 2014.

[131] K. Rykaczewski, S. Anand, S. B. Subramanyam, and K. K. Varanasi, "Mechanism of Frost Formation on Lubricant-Impregnated Surfaces," *Langmuir,* vol. 29, no. 17, pp. 5230-5238, 2013.

[132] Q. Liu, Y. Yang, M. Huang, Y. Zhou, Y. Liu, and X. Liang, "Durability of a lubricant-infused Electrospray Silicon Rubber surface as an anti-icing coating," *Applied Surface Science,* vol. 346, pp. 68-76, 2015.

[133] H. NyeokKim and S. JoonLee, "Shear-driven drainage of lubricant in a spherical cavity of lubricant-infused surface," *Physics of Fluids,* vol. 33, no. 12, p. 122011, 2021.

[134] M. Zhang et al., "Lubricant-infused coating by double-layer ZnO on aluminium and its anti-corrosion performance," *Journal of Alloys and Compounds,* vol. 764, pp. 730-737, 2018.

[135] J. Lee, Y. Jiang, F. Hizal, G.-H. Ban, S. Jun, and C.-H. Choi, "Durable omniphobicity of oil-impregnated anodic aluminum oxide nanostructured surfaces," *Journal of Colloid and Interface Science,* vol. 553, pp. 734-745, 2019.

[136] L. Zeng et al., "Tough antifouling organogels reinforced by the synergistic effect of oleophobic and dipole–dipole interactions," *Journal of Industrial and Engineering Chemistry,* vol. 114, pp. 205-212, 2022.

[137] C. Urata, G. J. Dunderdale, M. W. England, and A. Hozumi, "Self-lubricating organogels (SLUGs) with exceptional syneresis-induced anti-sticking properties against viscous emulsions and ices," *Journal of Materials Chemistry A,* vol. 3, no. 24, pp. 12626-12630, 2015.

[138] H. Pakzad, A. Nouri-Borujerdi, and A. Moosavi, "Drag reduction ability of slippery liquid-infused surfaces: A review," *Progress in Organic Coatings,* vol. 170, p. 106970, 2022.

[139] R. Mukherjee, M. Habibi, Z. T. Rashed, O. Berbert, X. Shi, and J. B. Boreyko, "Oil-Impregnated Hydrocarbon-Based Polymer Films," *Scientific Reports,* vol. 8, no. 1, p. 11698, 2018.

[140] P. S. Brown and B. Bhushan, "Liquid-impregnated porous polypropylene surfaces for liquid repellency," *Journal of Colloid and Interface Science,* vol. 487, pp. 437-443, 2017.

[141] J. Yong et al., "Nepenthes Inspired Design of Self-Repairing Omniphobic Slippery Liquid Infused Porous Surface (SLIPS) by Femtosecond Laser Direct Writing," *Advanced Materials Interfaces,* vol. 4, no. 20, p. 1700552, 2017.

[142] K. Manabe, K.-H. Kyung, and S. Shiratori, "Biocompatible Slippery Fluid-Infused Films Composed of Chitosan and Alginate via Layer-by-Layer Self-Assembly and Their Antithrombogenicity," *ACS Applied Materials & Interfaces,* vol. 7, no. 8, pp. 4763-4771, 2015.

[143] E. Carpene, D. Höche, and P. Schaaf, "Fundamentals of Laser-Material Interactions," in *Laser Processing of Materials: Fundamentals, Applications and Developments,* P. Schaaf Ed. Berlin, Heidelberg: Springer Berlin Heidelberg, pp. 21-47, 2010.

[144] S. Mishra and V. Yadava, "Laser Beam MicroMachining (LBMM) – A review," *Optics and Lasers in Engineering,* vol. 73, pp. 89-122, 2015.

[145] T. H. Maiman, "Stimulated Optical Radiation in Ruby," *Nature,* vol. 187, no. 4736, pp. 493-494, 1960.

[146] G. Thomas and R. Isaacs, "Basic principles of lasers," *Anaesthesia & Intensive Care Medicine,* vol. 12, no. 12, pp. 574-577, 2011.

[147] W. Koechner, "Introduction," in *Solid-State Laser Engineering,* W. Koechner Ed. New York, NY: Springer New York, pp. 1-10, 2006.

[148] W. T. Silfvast, "Lasers," in *Encyclopedia of Physical Science and Technology (Third Edition),* R. A. Meyers Ed. New York: Academic Press, pp. 267-281, 2003.

[149] C. Jauregui, J. Limpert, and A. Tünnermann, "High-power fibre lasers," *Nature Photonics,* vol. 7, no. 11, pp. 861-867, 2013.

[150] Y. Meng *et al.*, "Investigation of Nonlinear Optical Modulation Characteristics of MXene VCrC for Pulsed Lasers," *Molecules,* vol. 27, no. 3, 2022.

[151] T. Özel, "Editorial: Special Section on Micromanufacturing Processes and Applications," *Materials and Manufacturing Processes,* vol. 24, no. 12, pp. 1235-1235, 2009.

[152] T. Ditmire, "High-power Lasers: The invention of the laser 50 years ago has led to the latest generation of devices, with power bursts thousands of times that of the nation's entire electrical grid," *American Scientist,* vol. 98, no. 5, pp. 394-401, 2010.

[153] D. E. Spence, P. N. Kean, and W. Sibbett, "60-fsec pulse generation from a self-mode-locked Ti:sapphire laser," *Opt. Lett.,* vol. 16, no. 1, pp. 42-44, 1991.

[154] S. Lei *et al.*, "Ultrafast Laser Applications in Manufacturing Processes: A State of the Art Review," in *ASME 2019 14th International Manufacturing Science and Engineering Conference*, vol. 2, 2019.

[155] L. Orazi, L. Romoli, M. Schmidt, and L. Li, "Ultrafast laser manufacturing: from physics to industrial applications," *CIRP Annals,* vol. 70, no. 2, pp. 543-566, 2021.

[156] J. Možina and J. Diaci, "Optodynamics: dynamic aspects of laser beam–surface interaction," *Physica Scripta,* vol. 2012, no. T149, p. 014077, 2012.

[157] P. Shukla and J. Lawrence, "5 - Characterization and modification of technical ceramics through laser surface engineering," in *Laser Surface Engineering,* J. Lawrence and D. G. Waugh Eds.: Woodhead Publishing, pp. 107-134, 2015.

[158] H. Abubaker Hassan, "Effects of Different Laser Pulse Regimes (Nanosecond, Picosecond and Femtosecond) on the Ablation of Materials for Production of

Nanoparticles in Liquid Solution," in *High Energy and Short Pulse Lasers*, V. Richard Ed. Rijeka: IntechOpen, 2016.

[159] J. Han and Y. Li, "Interaction between pulsed laser and materials," *Lasers applications in Science and Industry*, 2011.

[160] C. Garban-Labaune *et al.*, "Effect of Laser Wavelength and Pulse Duration on Laser-Light Absorption and Back Reflection," *Physical Review Letters*, vol. 48, no. 15, pp. 1018-1021, 1982.

[161] I. Bunaziv, O. M. Akselsen, X. Ren, B. Nyhus, and M. Eriksson, "Laser Beam and Laser-Arc Hybrid Welding of Aluminium Alloys," *Metals*, vol. 11, no. 8, p. 1150, 2021.

[162] I. Bunaziv, O. M. Akselsen, X. Ren, B. Nyhus, M. Eriksson, and S. Gulbrandsen-Dahl, "A Review on Laser-Assisted Joining of Aluminium Alloys to Other Metals," *Metals*, vol. 11, no. 11, p. 1680, 2021.

[163] T. Kato *et al.*, "Comparison between femtosecond and nanosecond laser ablation of solution samples applied on a substrate," *Journal of Physics: Conference Series*, vol. 59, no. 1, p. 372, 2007.

[164] J. Diels and W. Rudolph, "Ultrashort laser pulse phenomena: fundamentals, techniques, and applications on a femtosecond time scale," *Academic Press*, 2006.

[165] R. Srinivasan, E. Sutcliffe, and B. Braren, "Ablation and etching of polymethylmethacrylate by very short (160 fs) ultraviolet (308 nm) laser pulses," *Applied Physics Letters*, vol. 51, no. 16, pp. 1285-1287, 1987.

[166] R. Kammel *et al.*, "Enhancing precision in fs-laser material processing by simultaneous spatial and temporal focusing," *Light: Science & Applications*, vol. 3, no. 5, pp. e169-e169, 2014.

[167] L. J. Jiang, S. Maruo, R. Osellame, W. Xiong, J. H. Campbell, and Y. F. Lu, "Femtosecond laser direct writing in transparent materials based on nonlinear absorption," *MRS Bulletin,* vol. 41, no. 12, pp. 975-983, 2016.

[168] D. Bäuerle, "Nanosecond-Laser Ablation," in *Laser Processing and Chemistry*, D. Bäuerle Ed. Berlin, Heidelberg: Springer Berlin Heidelberg, pp. 237-278, 2011.

[169] S. T. Hendow and S. A. Shakir, "Structuring materials with nanosecond laser pulses," *Opt. Express,* vol. 18, no. 10, pp. 10188-10199, 2010.

[170] Y. Wang *et al.*, "Ablation threshold modelling and validation of metal Nanosecond laser processing," *Optics Communications,* vol. 523, p. 128608, 2022.

[171] F. Luo *et al.*, "Study of micro/nanostructures formed by a nanosecond laser in gaseous environments for stainless steel surface coloring," *Applied Surface Science,* vol. 328, pp. 405-409, 2015.

[172] D. Bhaduri *et al.*, "Laser polishing of 3D printed mesoscale components," *Applied Surface Science,* vol. 405, pp. 29-46, 2017.

[173] K. Sugioka and Y. Cheng, "Ultrafast lasers—reliable tools for advanced materials processing," *Light: Science & Applications,* vol. 3, no. 4, pp. e149-e149, 2014.

[174] C. Donnet, J. Granier, G. Vergé, Y. Bleu, S. Reynaud, and F. Vocanson, "2D reproduction of the face on the Turin Shroud by infrared femtosecond pulse laser processing," *Appl. Opt.,* vol. 58, no. 9, pp. 2158-2165, 2019.

[175] A. Batal, A. Michalek, P. Penchev, A. Kupisiewicz, and S. Dimov, "Laser processing of freeform surfaces: A new approach based on an efficient workpiece partitioning strategy," *International Journal of Machine Tools and Manufacture,* vol. 156, p. 103593, 2020.

[176] Y. Guo, P. Qiu, and S. Xu, "Combined effects of polarization and secondary ablation on precision machining of microgrooves by laser-induced microjet-assisted ablation," *Opt. Express,* vol. 30, no. 25, pp. 44665-44680, 2022.

[177] H. Le *et al.,* "Effects of Top-hat Laser Beam Processing and Scanning Strategies in Laser Micro-Structuring," *Micromachines,* vol. 11, no. 2, p. 221, 2020.

[178] S. Nie, J. Yu, and Z. Fan, "Generation of shaped four-point pattern from splitting a flat-top laser beam," *Optik,* vol. 178, pp. 122-127, 2019.

[179] F. Ränke, R. Baumann, B. Voisiat, and A. Fabián Lasagni, "High throughput laser surface micro-structuring of polystyrene by combining direct laser interference patterning with polygon scanner technology," *Materials Letters: X,* vol. 14, p. 100144, 2022.

[180] S. Liu, F. Li, J. Wang, Z. Xing, and B. Cui, "Research on high-speed laser micro-machining and micro-hole arrays based on polygon mirror scanner," *SPIE,* 2022.

[181] T. W. Cronin, "A different view: sensory drive in the polarized-light realm," *Current Zoology,* vol. 64, no. 4, pp. 513-523, 2018.

[182] S. Zhang, Y. Zhou, H. Zhang, Z. Xiong, and S. To, "Advances in ultra-precision machining of micro-structured functional surfaces and their typical applications," *International Journal of Machine Tools and Manufacture,* vol. 142, pp. 16-41, 2019.

[183] P. Fan, R. Pan, and M. Zhong, "Ultrafast Laser Enabling Hierarchical Structures for Versatile Superhydrophobicity with Enhanced Cassie–Baxter Stability and Durability," *Langmuir,* vol. 35, no. 51, pp. 16693-16711, 2019.

[184] W. Si and Z. Guo, "Enhancing the lifespan and durability of superamphiphobic surfaces for potential industrial applications: A review," *Advances in Colloid and Interface Science,* vol. 310, p. 102797, 2022.

[185] A. Piqué, R. C. Y. Auyeung, H. Kim, N. A. Charipar, and S. A. Mathews, "Laser 3D micro-manufacturing," *Journal of Physics D: Applied Physics*, vol. 49, no. 22, p. 223001, 2016.

[186] H. Le *et al.*, "Laser precession machining of cross-shaped terahertz bandpass filters," *Optics and Lasers in Engineering*, vol. 149, p. 106790, 2022.

[187] F. Bouchard, M. Soldera, and A. F. Lasagni, "PMMA Optical Diffusers with Hierarchical Surface Structures Imprinted by Hot Embossing of Laser-Textured Stainless Steel," *Advanced Optical Materials*, p. 2202091, 2022.

[188] M. Gülçür *et al.*, "A cost-effective process chain for thermoplastic microneedle manufacture combining laser micro-machining and micro-injection moulding," *CIRP Journal of Manufacturing Science and Technology*, vol. 32, pp. 311-321, 2021.

[189] F. H. Rajab, Z. Liu, T. Wang, and L. Li, "Controlling bacteria retention on polymer via replication of laser micro/nano textured metal mould," *Optics & Laser Technology*, vol. 111, pp. 530-536, 2019.

[190] A. H. A. Lutey *et al.*, "Insight into replication effectiveness of laser-textured micro and nanoscale morphology by injection molding," *Journal of Manufacturing Processes*, vol. 65, pp. 445-454, 2021.

[191] J.-M. Romano, M. Gulcur, A. Garcia-Giron, E. Martinez-Solanas, B. R. Whiteside, and S. S. Dimov, "Mechanical durability of hydrophobic surfaces fabricated by injection moulding of laser-induced textures," *Applied Surface Science*, vol. 476, pp. 850-860, 2019.

[192] K. M. T. Ahmmed, C. Grambow, and A.-M. Kietzig, "Fabrication of Micro/Nano Structures on Metals by Femtosecond Laser Micromachining," *Micromachines*, vol. 5, no. 4, pp. 1219-1253, 2014.

[193] M. Birnbaum, "Semiconductor Surface Damage Produced by Ruby Lasers," *Journal of Applied Physics,* vol. 36, no. 11, pp. 3688-3689, 1965.

[194] L. P. Rivera, D. Munoz-Martin, A. Chávez-Chávez, M. Morales, G. Gómez-Rosas, and C. Molpeceres, "Subwavelength LIPSS formation on SS304 by picosecond laser irradiation under water confinement," *Materials Science and Engineering: B,* vol. 273, p. 115393, 2021.

[195] M. Mezera, M. van Drongelen, and G. R. B. E. Römer, "Laser-Induced Periodic Surface Structures (LIPSS) on Polymers Processed with Picosecond Laser Pulses," *Journal of Laser Micro Nanoengineering,* vol. 13, no. 2, pp. 105-116, 2018.

[196] M. Mastellone *et al.*, "LIPSS Applied to Wide Bandgap Semiconductors and Dielectrics: Assessment and Future Perspectives," *Materials,* vol. 15, no. 4, p. 1378, 2022.

[197] C.-Y. Yu *et al.*, "Picosecond laser induced periodic surface structures on K9 glass," *Surfaces and Interfaces,* vol. 23, p. 101026, 2021.

[198] S. Schwarz, S. Rung, C. Esen, and R. Hellmann, "Homogeneous low spatial frequency LIPSS on dielectric materials generated by beam-shaped femtosecond pulsed laser irradiation," *Journal of Laser Micro Nanoengineering,* vol. 13, no. 2, pp. 90-94, 2018.

[199] J. Bonse and S. Gräf, "Ten Open Questions about Laser-Induced Periodic Surface Structures," *Nanomaterials,* vol. 11, no. 12, p. 3326, 2021.

[200] J. G. A. B. Simões, R. Riva, and W. Miyakawa, "High-speed Laser-Induced Periodic Surface Structures (LIPSS) generation on stainless steel surface using a nanosecond pulsed laser," *Surface and Coatings Technology,* vol. 344, pp. 423-432, 2018.

[201] Y.-H. Liu, Y.-K. Tseng, and C.-W. Cheng, "Direct fabrication of rotational femtosecond laser-induced periodic surface structure on a tilted stainless steel surface," *Optics & Laser Technology,* vol. 134, p. 106648, 2021.

[202] J. Bonse, "Quo Vadis LIPSS?—Recent and Future Trends on Laser-Induced Periodic Surface Structures," *Nanomaterials,* vol. 10, no. 10, p. 1950, 2020.

[203] C. Florian, S. V. Kirner, J. Krüger, and J. Bonse, "Surface functionalization by laser-induced periodic surface structures," *Journal of Laser Applications,* vol. 32, no. 2, p. 022063, 2020.

[204] S. Gräf, "Formation of laser-induced periodic surface structures on different materials: fundamentals, properties and applications," *Advanced Optical Technologies,* vol. 9, no. 1-2, pp. 11-39, 2020.

[205] X. Liu, D. Du, and G. Mourou, "Laser ablation and micromachining with ultrashort laser pulses," *IEEE Journal of Quantum Electronics,* vol. 33, no. 10, pp. 1706-1716, 1997.

[206] I. Gnilitskyi, T. J. Y. Derrien, Y. Levy, N. M. Bulgakova, T. Mocek, and L. Orazi, "High-speed manufacturing of highly regular femtosecond laser-induced periodic surface structures: physical origin of regularity," *Scientific Reports,* vol. 7, no. 1, p. 8485, 2017.

[207] J.-M. Romano, A. Garcia-Giron, P. Penchev, and S. Dimov, "Triangular laser-induced submicron textures for functionalising stainless steel surfaces," *Applied Surface Science,* vol. 440, pp. 162-169, 2018.

[208] G. Giannuzzi *et al.*, "Short and long term surface chemistry and wetting behaviour of stainless steel with 1D and 2D periodic structures induced by bursts of femtosecond laser pulses," *Applied Surface Science,* vol. 494, pp. 1055-1065, 2019.

[209] F. Fraggelakis, E. Stratakis, and P. A. Loukakos, "Control of periodic surface structures on silicon by combined temporal and polarization shaping of femtosecond laser pulses," *Applied Surface Science,* vol. 444, pp. 154-160, 2018.

[210] K. Okamuro, M. Hashida, Y. Miyasaka, Y. Ikuta, S. Tokita, and S. Sakabe, "Laser fluence dependence of periodic grating structures formed on metal surfaces under femtosecond laser pulse irradiation," *Physical Review B,* vol. 82, no. 16, p. 165417, 2010.

[211] A. Batal *et al.*, "Effects of laser processing conditions on wettability and proliferation of Saos-2 cells on CoCrMo alloy surfaces," *Advanced Optical Technologies,* vol. 9, no. 1-2, pp. 67-78, 2020.

[212] B. Dusser *et al.*, "Controlled nanostructrures formation by ultra fast laser pulses for color marking," *Opt. Express,* vol. 18, no. 3, pp. 2913-2924, 2010.

[213] A. Batal, R. Sammons, and S. Dimov, "Response of Saos-2 osteoblast-like cells to laser surface texturing, sandblasting and hydroxyapatite coating on CoCrMo alloy surfaces," *Materials Science and Engineering: C,* vol. 98, pp. 1005-1013, 2019.

[214] S. Sarbada, Z. Huang, Y. C. Shin, and X. Ruan, "Low-reflectance laser-induced surface nanostructures created with a picosecond laser," *Applied Physics A,* vol. 122, no. 4, p. 453, 2016.

[215] A. Michalek *et al.*, "Sub-micron structuring/texturing of diamond-like carbon-coated replication masters with a femtosecond laser," *Applied Physics A,* vol. 126, no. 2, p. 144, 2020.

[216] B. Dashtbozorg *et al.*, "Development of surfaces with antibacterial durability through combined S phase plasma hardening and athermal femtosecond laser texturing," *Applied Surface Science,* vol. 565, p. 150594, 2021.

[217] M. Du *et al.*, "Fabrication of Antireflection Micro/Nanostructures on the Surface of Aluminum Alloy by Femtosecond Laser," *Micromachines (Basel)*, vol. 12, no. 11, 2021.

[218] A. Gaddam, H. Sharma, T. Karkantonis, and S. Dimov, "Anti-icing properties of femtosecond laser-induced nano and multiscale topographies," *Applied Surface Science*, vol. 552, p. 149443, 2021.

[219] A. Gaddam, H. Sharma, R. Ahuja, S. Dimov, S. Joshi, and A. Agrawal, "Hydrodynamic drag reduction of shear-thinning liquids in superhydrophobic textured microchannels," *Microfluidics and Nanofluidics*, vol. 25, no. 9, p. 73, 2021.

[220] R. Y. Siddiquie, A. Gaddam, A. Agrawal, S. S. Dimov, and S. S. Joshi, "Anti-Biofouling Properties of Femtosecond Laser-Induced Submicron Topographies on Elastomeric Surfaces," *Langmuir*, vol. 36, no. 19, pp. 5349-5358, 2020.

[221] J. T. Cardoso *et al.*, "Influence of ambient conditions on the evolution of wettability properties of an IR-, ns-laser textured aluminium alloy," *RSC Advances*, vol. 7, no. 63, pp. 39617-39627, 2017.

[222] D. Huerta-Murillo *et al.*, "Wettability modification of laser-fabricated hierarchical surface structures in Ti-6Al-4V titanium alloy," *Applied Surface Science*, vol. 463, pp. 838-846, 2019.

[223] P. Penchev *et al.*, "System-level integration tools for laser-based powder bed fusion enabled process chains," *Journal of Manufacturing Systems*, vol. 50, pp. 87-102, 2019.

[224] A. Garcia-Giron, J. M. Romano, A. Batal, A. Michałek, P. Penchev, and S. S. Dimov, "Experimental investigation of processing disturbances in laser surface patterning," *Optics and Lasers in Engineering*, vol. 126, p. 105900, 2020.

[225] A. Michalek *et al.*, "Modelling ultrafast laser structuring/texturing of freeform surfaces," *Applied Surface Science Advances,* vol. 2, p. 100036, 2020.

[226] L. Orazi, F. Montanari, G. Campana, L. Tomesani, and G. Cuccolini, "CNC Paths Optimization in Laser Texturing of Free Form Surfaces," *Procedia CIRP,* vol. 33, pp. 440-445, 2015.

[227] J. Diaci, D. Bračun, A. Gorkič, and J. Možina, "Rapid and flexible laser marking and engraving of tilted and curved surfaces," *Optics and Lasers in Engineering,* vol. 49, no. 2, pp. 195-199, 2011.

[228] G. Cuccolini, L. Orazi, and A. Fortunato, "5 Axes computer aided laser milling," *Optics and Lasers in Engineering,* vol. 51, no. 6, pp. 749-760, 2013.

[229] X. Wang, J. Duan, M. Jiang, S. Ke, B. Wu, and X. Zeng, "Study of laser precision ablating texture patterns on large-scale freeform surface," *The International Journal of Advanced Manufacturing Technology,* vol. 92, no. 9, pp. 4571-4581, 2017.

[230] L. Orazi, R. Pelaccia, O. Mishchenko, B. Reggiani, and M. Pogorielov, "Fast LIPSS based texturing process of dental implants with complex geometries," *CIRP Annals,* vol. 69, no. 1, pp. 233-236, 2020.

[231] N. Huang, Y. Jin, X. Li, L. Liang, and S. Wu, "Identification of integrated geometric errors of rotary axis and setup position errors for 5-axis machine tools based on machining test," *The International Journal of Advanced Manufacturing Technology,* vol. 102, no. 5, pp. 1487-1496, 2019.

[232] S. Ibaraki, S. Tsujimoto, Y. Nagai, Y. Sakai, S. Morimoto, and Y. Miyazaki, "A pyramid-shaped machining test to identify rotary axis error motions on five-axis machine tools: software development and a case study," *The International Journal of Advanced Manufacturing Technology,* vol. 94, no. 1, pp. 227-237, 2018.

CHAPTER 3: FEMTOSECOND LASER-INDUCED SUB-MICRON AND MULTI-SCALE TOPOGRAPHIES FOR DURABLE LUBRICANT IMPREGNATED SURFACES FOR FOOD PACKAGING APPLICATIONS

The research presented in this chapter was published online as a full-length article in the journal of "Surface and Coatings Technology" (2020):

T. Karkantonis[1], A. Gaddam[1], T. L. See[2], S. S. Joshi[3], and S. Dimov[1], "Femtosecond laser-induced sub-micron and multi-scale topographies for durable lubricant impregnated surfaces for food packaging applications," *Surface and Coatings Technology*, vol. 399, p. 126166, 2020.

[1]*Department of Mechanical Engineering, School of Engineering, The University of Birmingham, Edgbaston, Birmingham, B15 2TT, UK*

[2]*The Manufacturing Technology Centre Ltd, Coventry, CV7 9JU, UK*

[3]*Department of Mechanical Engineering, Indian Institute of Technology Bombay, Mumbai 400076, India*

Authors' contribution:

T. Karkantonis: Main author, conceived the methodology, conducted the experiments and characterisations, performed the analysis and written the original draft. **A. Gaddam**: Assisted with the design of experiments and interpretation of data. **T. L. See**: Supervision and proofreading. **S. S. Joshi:** Supervision and proofreading. **S. Dimov**: Supervision and proofreading.

Abstract

Adhesion of viscous liquids on packaging surfaces could lead to wastage, an increase of recycling costs, and even customers' dissatisfaction in applications related to food, cosmetics and agrochemical industries. Lubricant-impregnated surfaces (LIS) gained much attention recently over other surface functionalisation technologies due to their non-sticking response to highly viscous liquids. This work reports an investigation into anti-adhesive properties of LIS, with an emphasis on their durability. It provides an insight into the rationale design of LIS topographies in order to maximise their lubricant retention in potential food packaging applications. Femtosecond laser processing and hot embossing were employed to produce two types of topographies for LIS on stainless steel, polypropylene and polystyrene surfaces. The first type was single-scale sub-micron Laser-Induced Periodic Surface Structures (LIPSS), while the second one was Multi-scale Structures (MS) with both micron and sub-micron features. Droplet shedding characteristics of such LIPSS-LIS and MS-LIS substrates with water, milk and honey were examined under vibration and shear. The critical sliding angles at which liquid droplets attained motion on LIS were observed to be less than 32^{o} for all investigated liquids. However, the LIPSS-LIS substrates retained their functionality even after subjecting them to severe vibration, while the MS-LIS substrates partially lost their anti-adhesive characteristics. At the same time, the MS-LIS substrates exhibited premature pinning of droplets as compared to LIPSS-LIS substrates, under shear forces. Both vibration- and shear-induced loss of lubricant impacted the MS-LIS functionality.

Keywords: Food packaging, femtosecond laser, laser induced periodic surface structures, lubricant-impregnated surfaces, superhydrophobic surfaces, surface texturing.

3.1. Introduction

Annually, around 1.3 billion tonnes of food is wasted during the production, distribution and consumption stages, which has a tremendous impact on both economy and environment [1]. Although food waste occurs at all stages of the supply chain, private households represent a large fraction of this [2-3]. At the same time, a significant share of the food wastage in households is due to difficult-to-empty packaging, where the viscous food adheres to packaging surfaces. For example, it is estimated that 15% of the wastage in households is due to adherence of high-valued foods, such as yogurt, to the packaging surfaces [4-5]. Residual food on surfaces of the packaging also leads to an increase in cleaning cycles and recycling costs [6]. Furthermore, adhesion of viscous substances to process equipment such as pipework and mixing vessels in food industries also leads to cross-contamination, increased water load, and microbial growth [7]. Therefore, it is essential to design surfaces with anti-adhesive characteristics which are robust and durable. Such anti-adhesive surfaces that can minimise the adhesion and accelerate the mobility of various viscous liquids are of great importance to the food, cosmetic and agrochemical industries.

At large, anti-adhesive surfaces targeting food packaging can be achieved by two surface functionalisation approaches. In the first, coatings based on fluorine and silicone can be applied on packaging surfaces to lower their surface energy, thus imparting their hydrophobic and oleophobic properties. However, the negative effects of long chain perfluorinated compounds such as PFAS and PFOS on human health and environment have inspired efforts to develop alternative methods to lower the surface energies of materials [8]. Regarding the second approach, the surfaces are textured to produce micro/nanoscale topographies that induce Cassie-Baxter state. The entrapment of gas into micro/nanoscale cavities on such

textured surfaces results in high contact angles, thereby resulting in superhydrophobic and superoleophobic characteristics. However, the wetting transitions due to dissolution of gas into interacting liquids [9], moderate liquid pressure [10] and surface chemistry [11] affect their long-term durability in practice. At the same time, not all superliquiphobic surfaces with relatively high contact angles necessarily shed liquids from surfaces due to high Contact Angle Hysteresis (CAH). Thus, such surface functionalisation techniques have their own shortcomings that make them not ideal for non-stick food packaging applications.

A relatively new surface functionalisation technique based on lubricant impregnation of micro/nanotextured surfaces has gained much attention recently. Lubricant-Impregnated Surfaces (LIS) that are inspired by the Nepenthes pitcher plant can offer extremely low CAH and thus to shed liquids away easily without any adhesion. Based on the current practices, the requirements in producing LIS are: (i) the micro/nanotextured surfaces to retain the lubricant; (ii) the utilised lubricant and the repelling liquid should be immiscible; and (iii) the solid/base surface should be wetted by the lubricant instead of repelling it [12]. Due to their stability against wetting transition and very low CAH, LIS capabilities are extensively investigated for applications related to drag reduction [13-14], fog harvesting [15], anti-biofouling [16-17] and anti-frosting [18]. However, simple Newtonian liquids, especially water, were mostly investigated in the reported research.

Most of the liquid foods are composed of fats, stabilizers, surfactants and emulsifiers and therefore exhibit non-Newtonian behaviour. These components make the interaction of liquid foods with surfaces significantly different from that of water. Several investigations were reported recently that were focused on the interaction of complex liquids with LIS, aiming to achieve fouling-resistant and easy-to-empty packaging. Zhang et al. [19] employed sol-gel and hydrothermal methods to impregnate nanoporous Aluminium surfaces and demonstrate their

ant-wetting characteristics against various liquid foods. Lee et al. [20] prepared LIS employing nanotextured Aluminium substrates and investigated their anti-adhesive characteristics. They showed that non-connecting topographies can retain their non-sticking nature better than the connecting topographies even after subjecting them to continuous shear forces. Zouaghi et al. [21] demonstrated that LIS prepared using hierarchical textures produced through ultrashort laser processing of stainless steel could reduce dairy fouling compared to some reference superhydrophobic surfaces. Several other studies focused on preparing LIS on glass and silicon-based substrates examined their non-wetting properties when in contact with complex liquids [22-27]. Although most of these studies involved textured metallic and glass substrates, it should be noted that polymers are predominantly used as food packaging materials. In this regard, Mukherjee et al. [28] used oil absorbent polyethylene films to prepare LIS and demonstrated their anti-adhesive characteristics towards viscous liquid foods, such as ketchup and yoghurt. Recent investigations reported anti-adhesive properties of thermoplastic-based LIS prepared through solvent casting when in contact with liquid foods and detergents [29-30].

In summary, a significant progress was made in developing LIS for shedding complex liquids away from surfaces. However, few investigated LIS on thermoplastic materials that are of interest to food and cosmetic packaging industries. At the same time, durability aspects of LIS were not sufficiently studied while they are critical for their broader use. Since the LIS properties are shown to deteriorate quickly under liquid shear [31-32] and vibrational forces [33], it is important to understand the effects and impact of LIS topographies on their durability. Furthermore, the process chains employed in the reported research for producing LIS, especially their underpinning micro/nanoscale topographies, are not an industry practice

in food and cosmetic packaging applications, e.g. the use of LIS in producing containers, bottles, caps and various food and cosmetic handling equipment.

This research reports an investigation into the LIS properties achieved on sub-micron and multiscale topographies produced by employing metallic replication masters. The masters were textured by using ultrashort laser processing and then their topographies were replicated on commonly used food packaging thermoplastics, i.e. polystyrene and polypropylene, through hot embossing. Thermoplastic surfaces were impregnated with a silicone oil and their anti-adhesive response to three liquids, i.e. water, whole milk and honey, were investigated. In addition, durability tests were conducted on LIS samples with two types of topographies, in particular, sub-micron and multiscale ones, to study and compare their lubricant retention capacities under vibration and shear loading.

3.2. Materials and methods

3.2.1. Fabrication of sub-micron textured metallic moulds

Commercial X6Cr17 ferritic Stainless Steel (SS) plates with dimensions 30 x 20 x 0.7 mm and an average roughness (S_a) of 35 nm were used to produce on them two types of surface topographies. The SS substrates were textured at atmospheric conditions using an ultrafast Ytterbium-doped laser source (Satsuma, Amplitude Systems). The laser source has the following technical specification: a pulse duration of 310 fs at a nominal wavelength of 1030 nm and pulse repetition rate (f) up to 500 kHz with an average power (P) of 5 W. The laser texturing experiments were carried out on LASEA LS5 machine and its beam delivery system is shown in Fig. 3.1a. It was equipped with a 3D scan head mounted on a Z-axis stage and a telecentric focusing lens with 100 mm focal length to steer a linearly polarized Gaussian beam across the substrates with a maximum scanning speed (v) of 2000 mm/s. In addition, a high

precision stack of two rotary and two linear stages was used to position the substrates inside the machine working envelope. The SS substrates were processed with a constant scanning speed of 1000 mm/s and a spot diameter (2Ω) of 35 μm at the focal plane.

A horizontal raster scanning strategy was implemented to fabricate Laser-Induced Periodic Surface Structures (LIPSS) with sub-micron ripples. At the same time, a grid-like scanning strategy with multiple (40) scans was employed to produce Multi-scale Structures (MS) that included a combination of micron and sub-micron scale features. These two scanning strategies are illustrated in Fig. 3.1b. In order to obtain highly regular LIPSS, trials were conducted by varying the hatch distance (h) between two consecutive lines and also the average power at a repetition rate of 250 kHz. A similar strategy was adopted for obtaining the MS topographies, however, a repetition rate of 500 kHz was used in this case. The overlap (O) between pulses and the pulse fluence (φ_0) were calculated using the expressions reported in another research [34]. The optimised laser processing parameters used to produce the two topographies, i.e. LIPSS and MS ones, over an area of 30 x 20 mm^2 on the SS substrates are given in Table 3.1. The processing time for producing the LIPSS and MS topographies were 2 and 10 minutes, respectively.

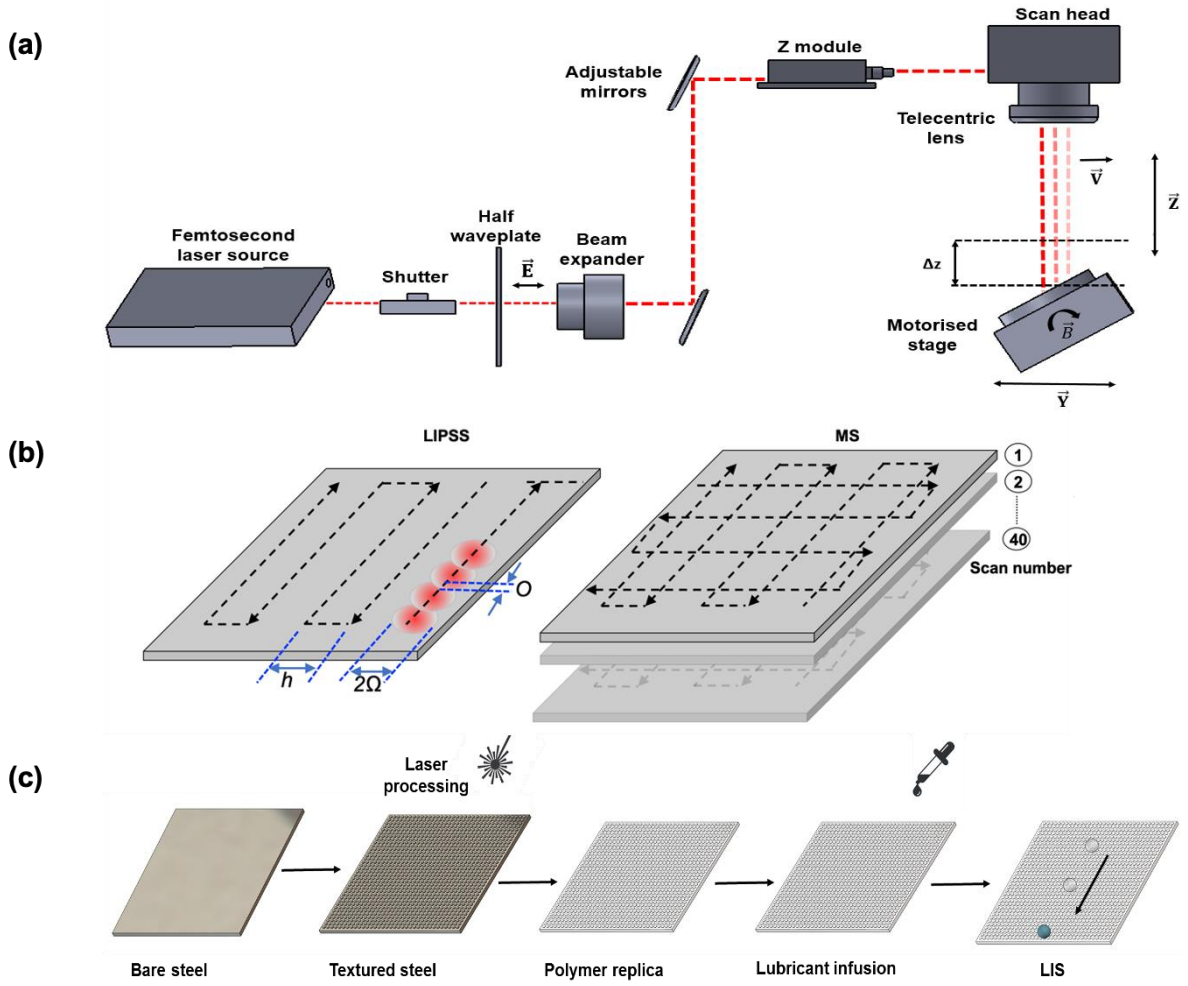

Fig. 3.1. The experimental set-ups: (a) a schematic of the used beam delivery system; (b) two scanning strategies for fabricating LIPSS (left) and MS (right) topographies; (c) an illustration of the process chain used to produce LIS.

Table 3.1. Optimum laser processing parameters for LIPSS and MS topographies.

Structure	f (kHz)	φ_0 (mJ/cm^2)	h (μm)	v (mm/s)	Number of scans	Scanning Strategy	Polarisation
LIPSS	250	210	5	1000	1	Horizontal	Linear (s)
MS	500	430	40	1000	40	Grid	Linear (s)

3.2.2. Polymer micro/nano replication and LIS preparation

The LIPSS and MS topographies on the SS plates were replicated onto Polystyrene (PS) and Polypropylene (PP) thermoplastic sheets (Alfa Aesar) of 1.6 mm thickness. In particular, a hot embossing set-up with a controllable hotplates' temperature and load was used to replicate the LIPSS and MS topographies on the sheet surfaces. During the replication process, the textured SS plates together with the blank thermoplastic sheets were placed between the hotplates and a pre-determined load was applied, and a temperature greater than the glass transition temperature of the thermoplastics was maintained for 5 minutes. To achieve as high as possible replication quality and samples' flatness, the operating temperature and load were optimised for the two thermoplastic materials used in the experiments. The optimised process settings together with the material properties are provided in Table 3.2.

Most of the reported studies employed perfluorinated oils [19-21, 23-24, 26, 29-30], essential and vegetable oils [27-28], and silicone oils [22, 25] as lubricants to demonstrate the LIS capabilities in food packaging applications. Although perflourinated oils are extensively used, such lubricants release fluorine similar to that of fluorinated coatings and therefore pose considerable health risks [35]. At the same time, essential and vegetable oils exhibit a strong aroma and also are not compatible with all liquid foods [36]. On the other hand, sufficient regulation standards are available for silicone-based lubricants as food additives [37] and therefore the silicone oil was selected as a lubricant in this study. Prior to the fabrication of LIS, all SS and thermoplastic replicas were cleaned with isopropyl alcohol to remove any surface debris or contamination. A silicone oil (Sigma-Aldrich) with 20 cSt viscosity at 25 °C was used as a lubricant. It was pipetted onto the textured SS and thermoplastic substrates for impregnation in the textures. The wetting and spreading of lubricant on micron and/or sub-micron scale cavities of textured substrates is mediated by the capillary length (l_c), which is

expressed as $l_c = (\gamma/\Delta\rho g)^{1/2}$ [38]. Here, γ (= 20.6 mN/m) is the surface tension between the silicone oil and air, $\Delta\rho$ (= 949 kg/m^3) is the density difference between silicone oil and air and g (= 9.81 m/s^2) is the gravitational constant. Consequently, the characteristic capillary length for silicone oil is approximately 1.5 mm. Since the length scale of MS and LIPSS topographies is much less than the characteristic capillary length, the capillary forces aid in wetting and spreading of silicone oil. After the textured substrates were completely wetted by the silicone oil, they were stored in a vacuum chamber for 15 minutes. The mild vacuum has further accelerated the impregnation process by releasing the entrapped air from sub-micron cavities. Thereafter, the LIS substrates were kept vertically for an hour, in order to drain any excess lubricant from the surfaces with the help of gravity. A schematic illustration of all the process chain steps used to attain LIS is provided in Fig. 3.1c.

Table 3.2. Material and processing conditions for hot embossing of PS and PP replicas.

Material	Load (kN)	Embossing Temperature (°C)	Melting temperature (°C)	Glass transition temperature (°C)	Hold time (min)
PS	0.16	100	240	100	5
PP	0.26	115	170	-10	5

3.2.3. Surface characterisation

The two surface topographies on SS and thermoplastic substrates were characterised using a Scanning Electron Microscope (SEM, JEOL JCM-600). A focus variation microscope (Alicona G5) was used to analyse the micro-scale topographies of the MS substrates. Whereas, an Atomic Force Microscope (AFM, MFP-3D, Asylum Research) was used to analyse sub-micron features of LIPSS and MS topographies. The 2D-FFT analysis was conducted using Gwyddion open-source image analysis software to obtain the LIPSS orientation and

periodicity. The wettability of as-received SS and thermoplastic sheets, textured SS and thermoplastic replicas and LIS was investigated by measuring the water contact angle of 5 µL droplets using a goniometer (Attension Theta, Biolin Scientific). Following this, the CAH was evaluated using the tilting stage of the goniometer. In particular, the advancing and receding contact angles were measured during the initiation of droplet movement when the substrate was tilted at an angle.

Furthermore, the Critical Sliding Angle (CSA) of droplets was measured on as-received SS plates and thermoplastic sheets, textured SS plates and replicas and LIS. Three test liquids, i.e. water, whole milk and honey, were used to investigate the LIS response. 15 µL droplets of each test liquid was pipetted onto the LIS samples to observe the droplet motion. The droplet movement on the surfaces was recorded using a motorised tilt stage with a positional accuracy of 10 arc seconds and a digital camera (Canon 2000D). To avoid any droplet impact on the sample surfaces, the pipette was held in a fixture very close to the surface of the samples. The distance between the tip of the pipette and sample surfaces was maintained at less than 2 mm. For each test run, five measurements were taken by placing droplets at different locations on the sample surfaces and the average CSA values were analysed.

3.2.4. LIS durability analysis

At the end of the food supply chain, the packaged food is transported to the retailers and ultimately to the households. During these stages, the packaging containers would be subjected to vibration. At the same time, the packaging surfaces would be also subjected to shear loads when liquid foods would be taken out/emptied from their containers by end-users. To account for these different types of loads, two tests were conducted to evaluate the durability of the thermoplastic LIS. First, the LIS samples were placed inside a container filled with water and

were subjected to vibration with 50 Hz frequency for 5 minutes. Thereafter, the shedding characteristics of the LIS samples were re-examined by measuring CSA of water, whole milk and honey droplets on vibrated surfaces. The amount of the lubricant retained by the samples after their exposure to vibration was evaluated by measuring the mass of samples before and after the tests using a precision weighing balance. Secondly, the thermoplastic LIS samples were tilted at an angle of 15^{o}, and the whole milk and honey droplets of 15 µL were deposited on a single track of the surface. The camera was used to record the droplet motion at 50 frames per second. The droplets of the test liquids were continuously dripped on the LIS samples until their motion was observed to stop. Each test run was conducted three times. Thereafter, the recorded videos were post-processed using "Tracker" video analysis software to evaluate the steady-state velocity of the whole milk and honey droplets on LIS samples. Finally, adhesion characteristics were also investigated by immersing the LIS samples into containers with milk and honey for up to 50 times.

3.3. Results and discussion

3.3.1. Analysis of surface topographies

Since regular and periodic textures allow a better understanding of liquid-surface topography interactions, the first efforts were focused on producing highly regular, periodic LIPSS and MS topographies on SS substrates. To minimise the effect of the Gaussian beam, a high overlap scanning strategy was adopted and thus to achieve highly regular LIPSS [39]. A pulse overlap fixed at 70%, the pulse fluence and the hatch distance were varied from 50 to 300 mJ/cm^2 and from 1 to 6 µm, respectively. As a result, the accumulated fluence per area from 1.5 – 53.3 J/cm^2 was attained. While different structures such as uniform ripples, a combination of ripples and roughness, and discontinuous ripples were observed in the investigated

parameter domain, the highly regular LIPSS were obtained at accumulated fluence of 7.4 J/cm^2.

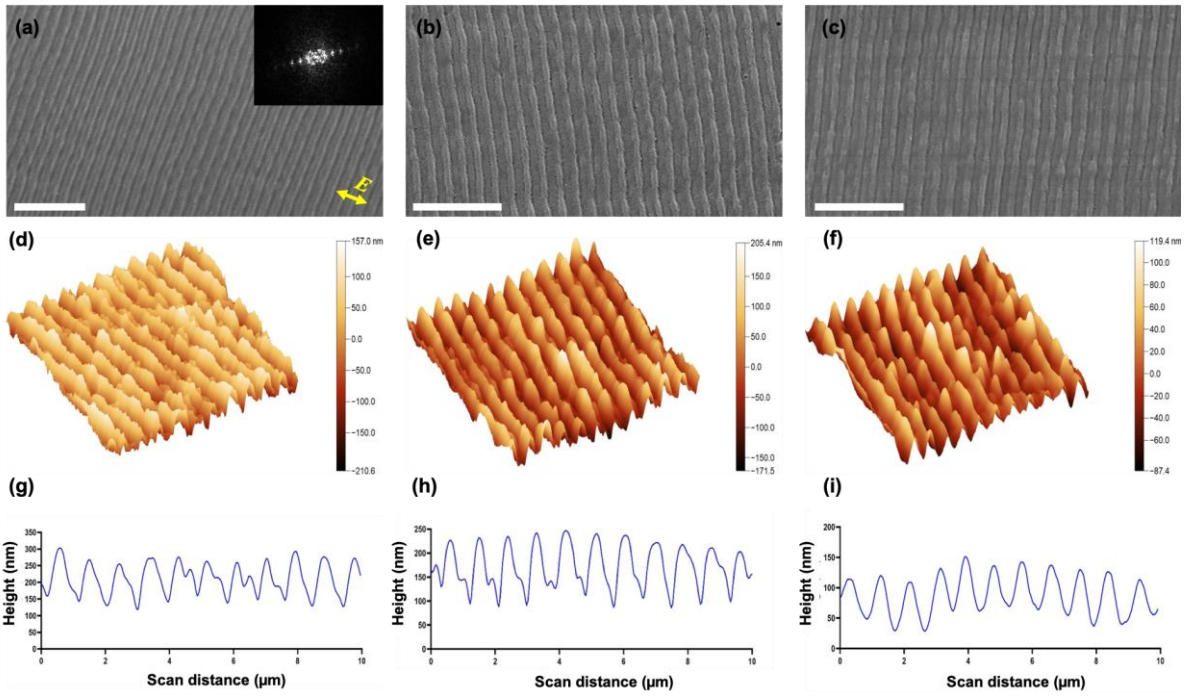

Fig. 3.2. The surface topography analysis of LIPSS substrates: (a-c) SEM micrographs SS, PS and PP substrate, respectively with a 2D-FFT image inset in (a); (d-f) AFM micrographs of SS, PS and PP substrates, respectively; (g-i) plots showing height profiles of SS, PS and PP substrates, respectively. Scale bar: 5 μm.

At the same time, to produce the MS topographies, in particular consisting of microscale pillars with superimposed sub-micrometre features, the hatch distance was varied from 25 - 50 μm while the number of scans from 5 to 40 at a fixed average power. The grid-like scanning strategy led to a higher accumulated fluence at the intersecting points and therefore valleys and bumps were formed on the surface. A topography with minimum surface defects, such as sporadic pits and roughness, was obtained with an inter-pillar spacing of 40 μm and a height of 10 μm. Although no surface defects were observed when a small number of scans were used, the height of the pillars was not sufficient to distinguish the resulting MS topography

from that of the single scale LIPSS substrates. Therefore, the MS replication master was produced with 40 scans as stated in Table 3.1. The LIPSS and MS masters were fabricated over the SS plates with the optimised settings in Table 3.1 and then replicated on thermoplastic sheets as explained previously.

The SEM micrographs of highly regular LIPSS on SS, PS and PP substrates are shown in Fig. 3.2a, b and c, respectively. The LIPSS were formed with an orientation normal to the beam polarisation vector (*E*) (see Fig. 3.2a). The clearly defined 2D-FFT (the inset in Fig. 3.2a) signify a high regularity of the fabricated LIPSS. Furthermore, the periodicity was evaluated to be in the range from 800 to 900 nm based on the SEM and 2D-FFT characterisation results that were less than the wavelength of the femtosecond laser and similar to that reported by other researchers [40-41]. The respective 3D AFM micrographs of highly regular LIPSS on SS, PS and PP substrates are provided in Fig. 3.2d, e and f and they depict a high replication quality. The AFM profiles (see Fig. 3.2g-i) show a mean height from 100 to 200 nm on all substrates. Furthermore, it is evident from the comparison of LIPSS average height on SS, PS and PP substrates at different locations over a scan length of 10 μm that a high replication performance was achieved, especially greater than 90%.

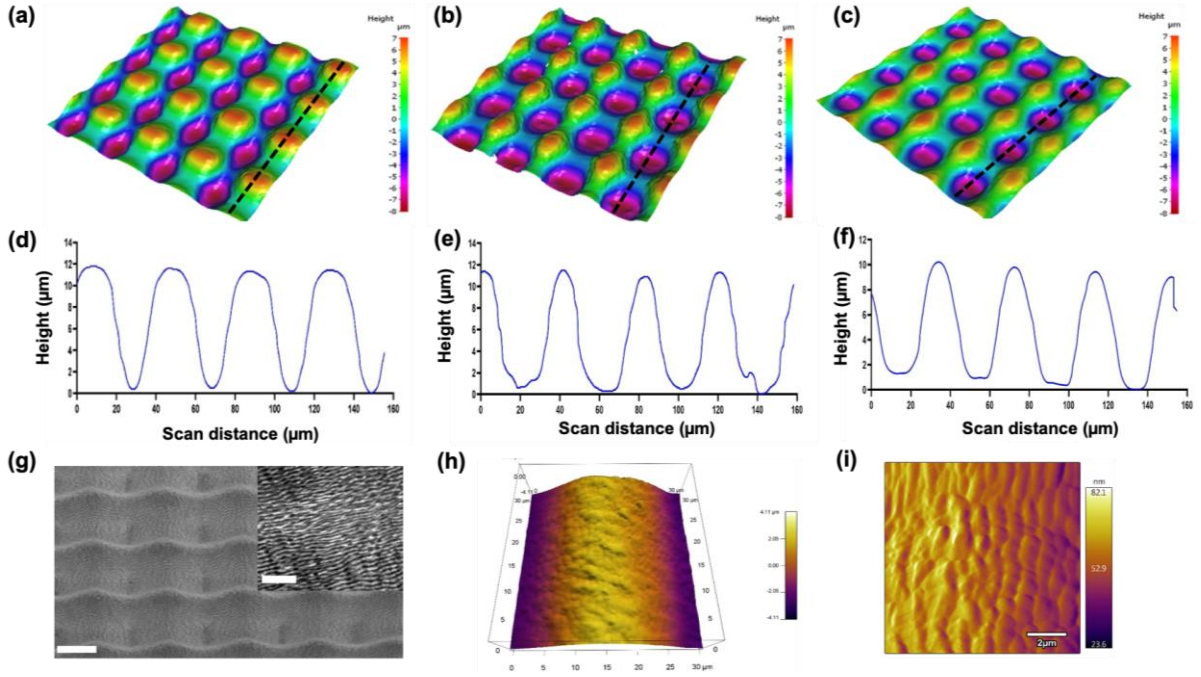

Fig. 3.3. The surface topography analysis of MS substrates: (a-c) the 3D micrographs of SS, PS and PP substrates, respectively; (d-f) plots showing height profiles on SS, PS and PP substrates; (g) the SEM micrograph of SS topographies (scale bar: 20 µm) with a magnified view of sub-micron features on pillars in the inset (scale bar: 5 µm); (h-i) the AFM micrographs showing sub-micron features on top of the pillar of PS and PP replicas, respectively.

The 3D micrographs of MS topographies on SS, PS and PP substrates are shown in Fig. 3.3a, b and c, respectively. The micrographs depict the negative patterns of the MS topography on SS surface that are then replicated on thermoplastic sheets. Furthermore, the height profiles of microscale pillars on both SS and thermoplastic substrates as shown in Fig. 3.3d-f where also the achieved replication performance of more than 95% is evident. The SEM micrographs in Fig. 3.3g depict sub-micron scale features superimposed on microscale pillars. Again, the replication quality of sub-micron features on thermoplastics replicas was assessed by analysing AFM micrographs taken on the top of the micro-scale pillars. It is evident that the sub-micron features were replicated on the PS MS samples as shown in Fig. 3.3h. A magnified view of

sub-micron features of a PP MS samples is provided, too, in Fig. 3.3i and again it depicts a high replication performance. The AFM measurements of SS and thermoplastic samples show that the height of sub-micron features was in the range from 50 to 100 nm, which was substantially less than that achieved on the LIPSS samples (see Fig. 3.3g-i).

3.3.2. Wettability characterisation

The average static water Contact Angle (CA) measured on as-received, textured and LIS of SS, PS and PP substrates are provided in Fig. 3.4a. Initially, textured SS substrates exhibited hydrophilicity, in particular, CA of 88.2^{o} and 67.5^{o} on LIPSS and MS samples, respectively. However, CAs significantly increased over a period of two weeks to reach the respective values of 113^{o} and 138^{o}. This can be explained with the exposure of laser textured SS substrates to the ambient environmental conditions and the accumulation of carbon from CO_2 decomposition on surfaces that lowered the surface energy as reported in previous research [42-43]. It is important to stress that the CA measurements on thermoplastic substrates were stable over the same time period of 2 weeks. The combined alteration of surface chemistry and topography was the reason for the CA increase on textured SS substrates. On the other hand, only the alteration of topography has caused the change in CA on inherently hydrophobic thermoplastic substrates. The MS topographies substantially increased the contact angles (CA > 130^{o}) on SS plates and their PS and PP replicas, whereas the influence of highly regular LIPSS on thermoplastic replicas was marginal.

At the same time, the LIPSS and MS topographies did not have any influence on CAs of lubricant-impregnated surfaces of SS and thermoplastics. However, a slight difference in the values of CA for LIPSS-LIS and MS-LIS of SS substrates is evident in Fig. 3.4b when compared to their LIS counterparts on thermoplastic substrates. In general, a droplet on LIS can assume a shape in any of the 12 possible thermodynamic states, which is determined by

the spreading coefficient of the lubricant on a substrate in the presence of water [12]. The noticeable difference in the CA values on LISs of SS substrates could be attributed to the appreciable difference in the spreading coefficients of LIPSS-LIS and MS-LIS. However, a further investigation is needed to explain the effects of the substrate material on the observed droplet shape on LIS. The images of water droplets on textured and LIS substrates are shown in Fig. 3.4b. The wetting ridge formed by the water at the periphery of the water droplet on LIS can be seen in the figure. Furthermore, the CAH of water droplets was measured to be less than 5^{o} on all the LIS.

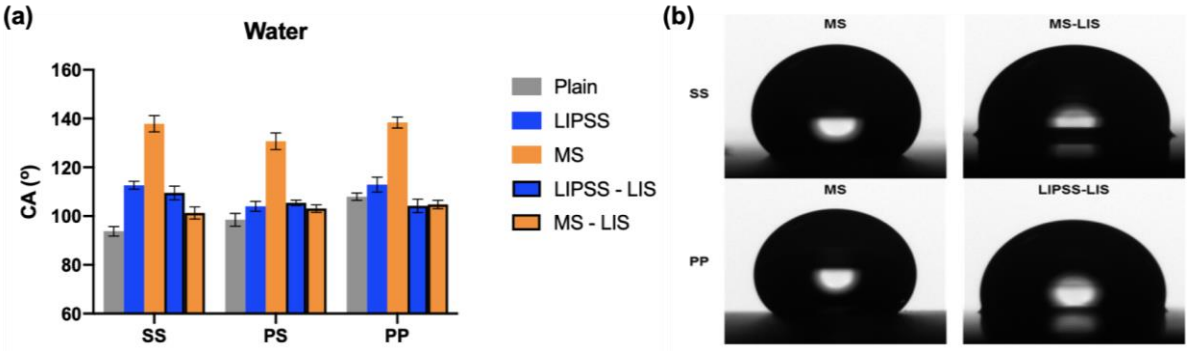

Fig. 3.4. The water CA measurements obtained after two weeks: (a) static water CA on as-received, textured and LIS topographies of SS, PS and PP substrates; (b) Images of the water droplet on textured and LIS of the SS and PP substrates.

Subsequently, the shedding behaviour of water, milk and honey droplets was characterised by measuring the critical sliding angle at a droplet motion was initiated. Droplets of the test liquids on SS and PS LIS surfaces are shown in Fig. 3.5d. It should be noted that the water and milk droplets were dyed for better visibility. The average CSA for all test liquids on as-received, textured and LIS topographies of SS and thermoplastic substrates are shown in Fig. 3.5a, b and c. The as-received and textured surfaces of the SS substrates pinned the test liquids even after the substrates were tilted at 90^{o}. At the same time, some droplet motion was observed at

CSA of less than 40^{o} on as-received thermoplastic surfaces for all test liquids. However, the droplets were observed to have sagged while sliding along the thermoplastic surfaces, leaving behind traces of test liquids as shown in Fig. 3.5d. Interestingly, the surface texturing on thermoplastic surfaces did not aid the droplet movement. In fact, the droplets were either pinned to the MS surfaces (see Fig. 3.5d) or CSA increased to more than 70^{o} and 60^{o} in the case of water on LIPSS PS and PP substrates, respectively. The lubricant infiltration into the textured surfaces dramatically reduced CSA on all substrates as shown in Fig. 3.5a-c. The mobility of the droplets on LIS regardless of the liquid type was aided by a slippage at the contact line and also the hemispherical shape of the droplet was preserved as shown in Fig. 3.5d. For most of the experimental domain, CSA was observed to be less than 10^{o}, except milk droplets on PS surfaces (CSA < 32^{o}).

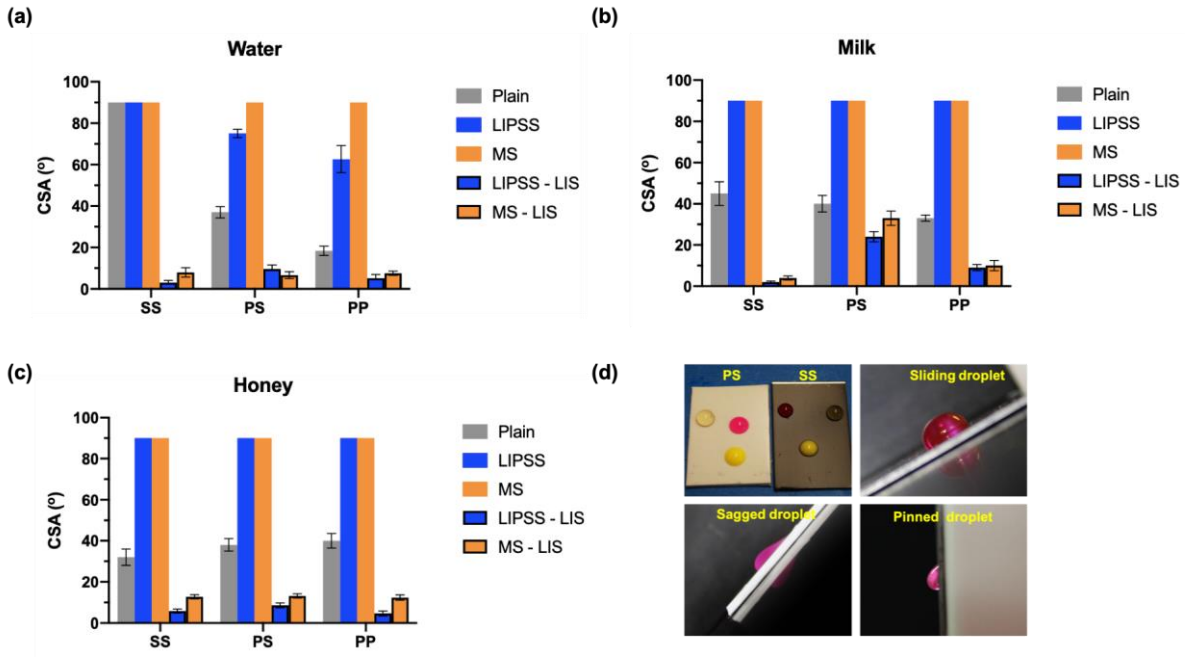

Fig. 3.5. CSA on as-received, textured and LIS topographies of the SS, PS and PP substrates for: (a) water, (b) milk and (c) honey droplets. (d) An image of water, milk and honey droplets on the MS-LIS surfaces of PS and SS samples together with different droplet shedding behaviours is shown.

3.3.3. Durability characterisation of LIS

3.3.3.1. Vibration assessments

A critical durability characteristic of LIS is their liquid shedding performance, especially the functional lubricant retention capacity of textured surfaces in the context of this research. Therefore, the durability of LIS substrates was examined by subjecting them to vibration. LIS of SS and thermoplastic substrates were agitated by using a standard laboratory vortex mixer for 5 minutes as shown in Fig. 3.6a. The amount of lubricant retained after the vibrations was assessed by measuring the substrate mass at fixed intervals of time. In particular, the lubricant locked into the sub-micron cavities of LIPSS substrates was too small to lead to any noticeable changes in the substrates' mass. However, this was not the case for the MS topographies and considerable changes in the substrates' mass were observed after the vibration tests. The Fig. 3.6b shows the amount of lubricant retained by PS and PP MS topographies with the increase of time they were subjected to vibrations. As can be seen, a large amount of lubricant was lost within a minute after subjecting the substrates to vibration. Overall, the MS topographies on the PP and PS substrates retained only approximately 20% and 40% of the lubricant, respectively, and reached their plateaus after subjecting them to only 2 min vibrations. The lubricant retention on these substrates can be attributed to the high capillary forces due to sub-micron cavities on both LIPSS and MS topographies. At the same time, the substantial vibration-induced loss of lubricant from microscale cavities onto the MS topographies can be explained with reduced capillary forces as depicted in Fig. 3.6c.

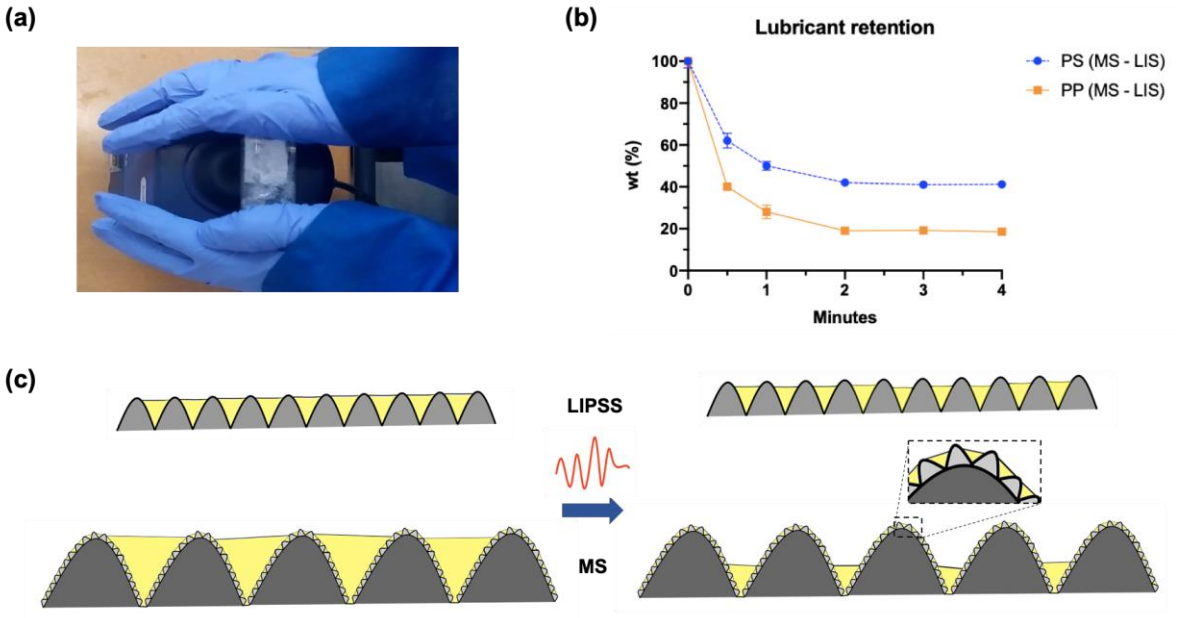

Fig. 3.6. An investigation into the lubricant retention capacity of LIS: (a) the experimental setup used for subjecting LIS substrates to vibration; (b) the lubricant retention capacity of MS topographies on the PS and PP substrates with time; (c) an illustration of vibration-induced loss of lubricant infused into LIPSS and MS topographies.

In addition, CSAs of droplets from the same test liquids as those investigated in Sub-section 3.3.2 were measured on LIS substrates. Fig. 3.7a shows the CSA change on LIS substrates before and after subjecting them to vibrations for 5 minutes. Large CSA changes were observed on MS topographies of both SS and thermoplastic substrates, while only marginal changes were noticed on LIPSS. The lubricant depletion of MS topographies on SS substrates even led to pinning of the water droplets to the surface and thus the anti-adhesive functionality was completely lost. The milk droplets had shown a similar behaviour as depicted in Fig. 3.7b. However, despite detecting a droplet sliding on MS-LIS topographies, the milk droplets left small ‘satellite’ droplets behind on the surfaces as shown in Fig. 3.7d. Thus, a partial loss of functionality was evident with the milk droplets on MS topographies after subjecting them to vibration. A similar phenomenon with viscoelastic droplets on superhydrophobic surfaces was

previously reported [44]. Fig. 3.7c shows the sliding behaviour of honey droplets on the LIS surfaces before and after vibration. Contrastingly, the loss of functionality on MS topographies in regards to the honey droplets was much less compared to that observed with water and milk droplets. However, this can be attributed to the higher density and viscosity of honey in comparison with water and milk that led to an altered surface response as a result of a different balance between the forces of gravity, viscosity and contact line pinning. For a profound understanding of the sliding behaviour, the rheological properties of the considered test liquids should be elucidated by correlating non-dimensional parameters of these forces [45], however, such a study is outside the scope of this research.

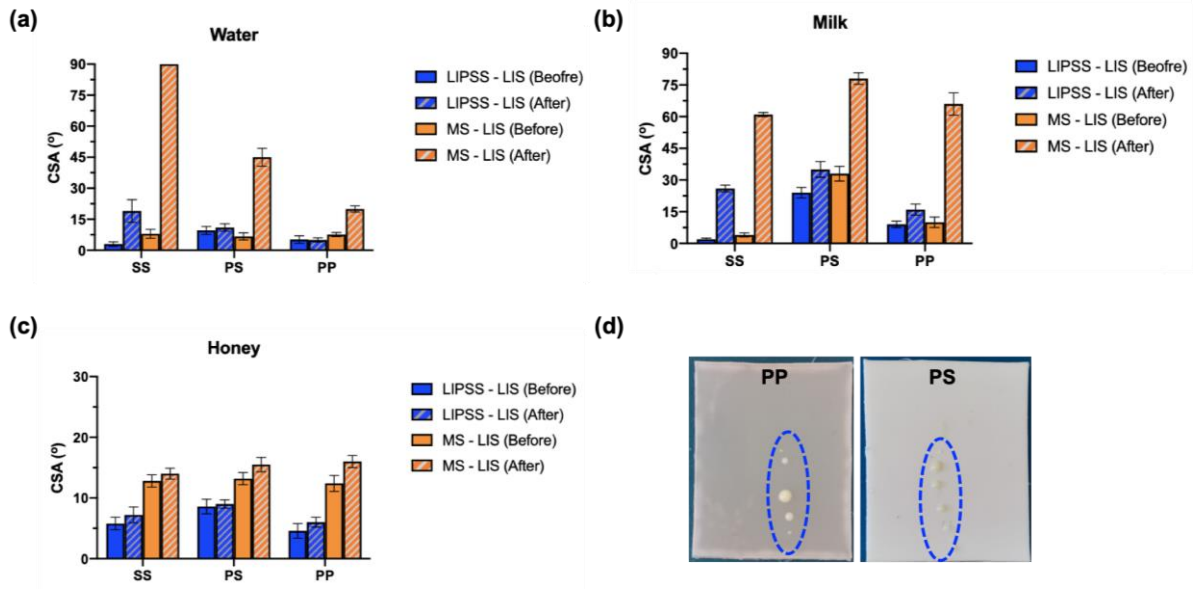

Fig. 3.7. CSA measurements of water (a), milk (b) and honey (c) droplets on LIS topographies before and after subjecting them to vibrations; (d) Images showing small 'satellite' droplets left behind by the milk droplet on MS-LIS topographies of PP and PS after the vibration test.

3.3.3.2. Shear assessments

The depletion of lubricant due to shear forces is another possible mode of LIS failures. The shear-induced loss of lubricant and its subsequent influence on LIS functionality was studied by subjecting the lubricant infused surfaces to shear, especially by continuous dripping of droplets on a single track as shown in Fig. 3.8a. Only LIS topographies on PP substrates were investigated due to their shedding properties against milk and honey at lower tilt angles compared to their PS counterparts. Figs. 3.8b and c show sliding velocities of milk and honey droplets as a function of the increasing number of droplets dripped consecutively one after another. It is apparent from this figure that the milk droplet velocity decreased gradually on both MS-LIS and LIPSS-LIS substrates before reaching zero. However, the LIPSS topographies had shown to endure a greater number of droplets than the MS topographies. The velocity decrease can be explained with the interaction between the wetting ridge and capillary suction that led to lubricant redistribution as a result of the liquid droplet train on LIS and thus to the loss of the lubricant [46]. In particular, the shear forces caused by the droplet train led to a lubricant redistribution along the interconnected valleys of the MS topographies, especially towards the end of the tracks [31]. This phenomenon is illustrated by the gradual shade of the track in Fig. 3.8a. In addition, there was a lubricant deprivation at the beginning of the track which led to pinning of the droplet on the surface. The continuous loss of lubricant with each droplet detrimentally affected the LIS slippery properties, which was evident from the decreasing droplets velocity. At the same time, the velocity of honey droplets decreased rapidly on both LIPSS-LIS and MS-LIS substrates. Thus, the viscosity contrast at the liquid-lubricant interface in the case of honey was higher than that of milk and therefore the lubricant depletion could have been quicker in the case of honey. Such shear-induced loss was in line with what was previously reported, especially that the greater contrast between the working

liquid and lubricant had a substantial impact on the LIS lubricant depletion [47]. Overall, the LIPSS-LIS topographies showed a better resistance than MS-LIS ones in regards to the effects of shear forces on the lubricant depletion.

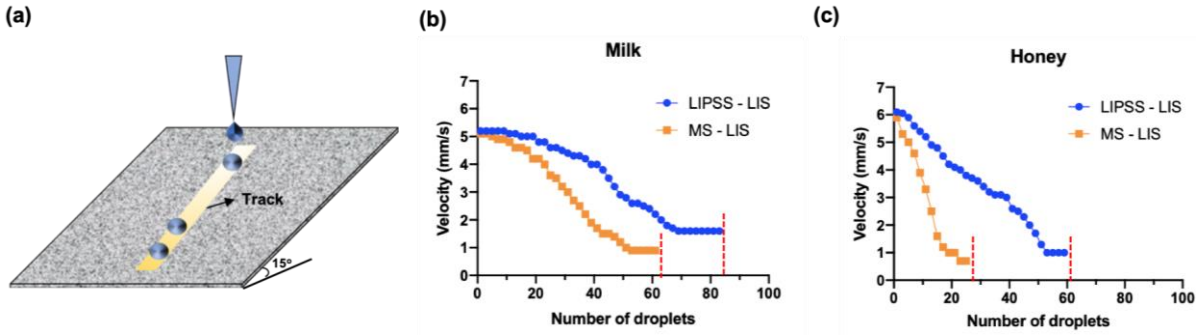

Fig. 3.8. Analysis of lubricant depletion due to shear forces: (a) an illustration of the shear test performed on LIS topographies; the variations of sliding velocity with the increasing number of milk (b) and honey (c) droplets on the PP surfaces with LIS topographies. *Note:* the red lines show the position where droplet velocity reached zero abruptly.

3.3.3.3. Immersion assessments

The LIS substrates were also investigated for their performance when exposed to bulk liquids. Fig. 3.9a shows the shedding behaviour of LIS on PP substrates exposed to honey and ketchup droplets of 250 µL. As it can be seen, the honey and ketchup droplets left behind traces on the as-received PP sheets, while LIS of the textured PP substrates exhibited an excellent anti-adhesive functionality. Thus, it is evident that LIS shed away not only viscous Newtonian liquids such as milk and honey but also yield stress liquids such as ketchup. In addition, the performance of thermoplastic-based LIS was investigated by conducting 50 dipping cycles into milk and honey. The honey was observed to stick to the as-received PS and PP sheets, however, their LIS counterparts resisted to any adhesion even after 25 cycles as shown in Fig. 3.9b. The LIPSS-LIS treatment of both thermoplastics led to excellent anti-adhesive properties

even after 50 cycles with all tested liquids, while there was a slight stickiness on the MS-LIS substrates after 43 and 20 dipping cycles in milk and honey, respectively. Especially, a similar behaviour such as small 'satellite' droplets was observed on both MS-LIS treated thermoplastics after the milk dipping cycles, whereas only small areas of MS-LIS had shown to lose their functionality after exposing them continuously to honey.

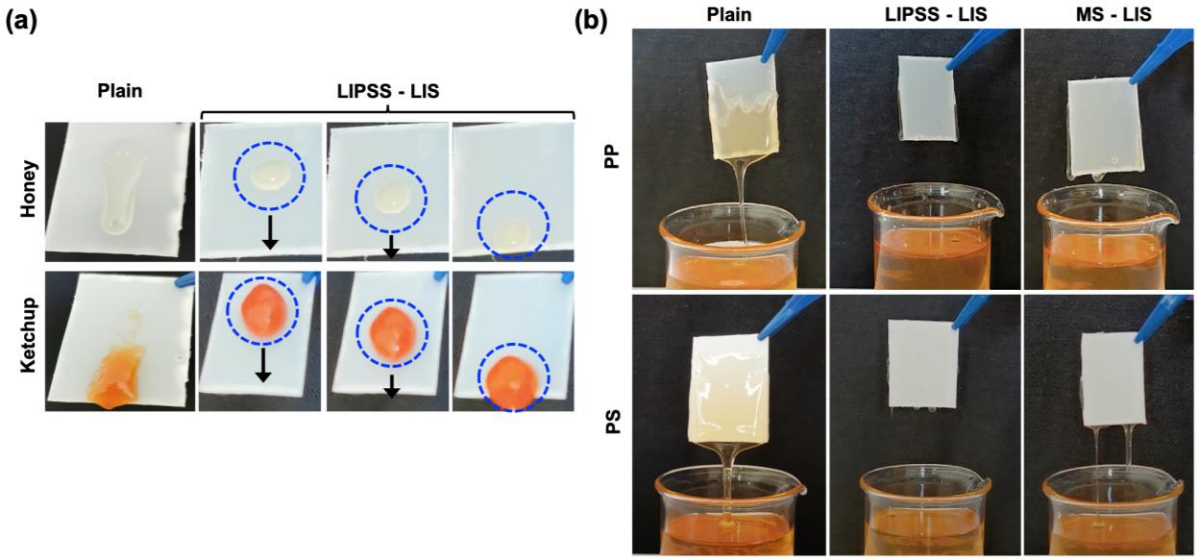

Fig. 3.9. Analysis of the shedding behaviour of lubricant infused textured substrates: (a) the sliding behaviour of 250 µL honey and ketchup droplets on as-received and LIPSS - LIS treated PP; (b) the dripping behaviour of as-received and LIPSS-LIS and MS-LIS treated PP and PS substrates after honey dipping cycles.

3.4. Conclusions

Lubricant impregnation of surfaces with micron/sub-micron topographies is a passive approach to achieve hydrophobic, lyophobic and lipophobic characteristics to surfaces. Such LIS exhibit greater stability and robustness than gas-cushioned textured surfaces because they usually fail under pressure- and/or dissolution-induced wetting instabilities. However, the LIS are also prone to other modes of failure such as vibration- and/or shear-induced instabilities.

Surface topographies play an important role in overcoming such LIS failure mechanisms. Therefore, the research investigated and experimentally validated the influence of two different length scale topographies (i.e. sub-micron and MS structures) on LIS functionality, especially in the context of their potential food packaging applications. To create such topographies onto thermoplastic materials, a cost-effective and scalable process chain combining femtosecond laser processing with polymer replication was employed. The single scale, highly regular LIPSS topographies exhibited a better resistance to the lubricant depletion against vibration- and shear-induced forces when compared with their MS counterparts. Consequently, it was demonstrated that an ultrafine layer of lubricant on LIPSS topographies could also minimise the lubricant leaching as the result of interactions with different liquids when compared to MS topographies. This was attributed to the higher capillary forces induced by the former surface topography. Furthermore, the LIS treatment of thermoplastics used for food packaging led to excellent anti-adhesive characteristics when exposed to complex and highly viscous liquid foods. Although the highly regular LIPSS showed a reasonable robustness against various failure modes, further in-depth investigations are needed to optimise their functional response, especially by tailoring their geometry, depth and periodicity to improve their performance. Since most of the thermoplastic-based packaging solutions are fabricated by blow and injection moulding, the femtosecond laser treatment of replication masters as demonstrated in this research could be a seamless and cost-effective solution to "imprint" sub-micron topographies for preparing functional LIS with required durability.

Acknowledgements

The research work is supported by European Commission H2020 project "High-impact injection moulding platform for mass-production of 3D and/or large micro- structured surfaces

with antimicrobial, self-cleaning, anti-scratch, anti-squeak and aesthetic functionalities" (HIMALAIA). It is also conducted within the framework of UKIERI-DST programme on "Surface functionalisation for food, packaging, and healthcare applications". The authors would like to acknowledge also the collaboration with LASEA SA, Belgium within the framework of the ESIF project "Smart Factory Hub" (SmartFub).

References

[1] United Nations, 2019. Sustainable Development Goals. About the Sustainable Development Goals. New York: UN. [Online]. Available at: https:// www.un.org/sustainabledevelopment/sustainable-development-goals/ [Accessed 10 January 2020].

[2] H. Williams, A. Lindström, J. Trischler, F. Wikström, and Z. Rowe, "Avoiding food becoming waste in households – The role of packaging in consumers' practices across different food categories," *Journal of Cleaner Production,* vol. 265, p. 121775, 2020.

[3] I. Djekic *et al.*, "Quantities, environmental footprints and beliefs associated with household food waste in Bosnia and Herzegovina," *Waste Management & Research,* vol. 37, no. 12, pp. 1250-1260, 2019.

[4] H. Williams, F. Wikström, T. Otterbring, M. Löfgren, and A. Gustafsson, "Reasons for household food waste with special attention to packaging," *Journal of Cleaner Production,* vol. 24, pp. 141-148, 2012.

[5] B. Wohner, E. Pauer, V. Heinrich, and M. Tacker, "Packaging-Related Food Losses and Waste: An Overview of Drivers and Issues," *Sustainability,* vol. 11, no. 1, p. 264, 2019.

[6] X. Liu *et al.*, "Adhesion of liquid food to packaging surfaces: Mechanisms, test methods, influencing factors and anti-adhesion methods," *Journal of Food Engineering,* vol. 228, pp. 102-117, 2018.

[7] J. P. Tuck, F. Alberini, D. Ward, B. Gore, and P. J. Fryer, "Cleaning of thick viscoplastic surface deposits using an impinging jet: Effect of process variables," *Journal of Food Engineering,* vol. 266, p. 109699, 2020.

[8] L. A. Schaider *et al.*, "Fluorinated Compounds in U.S. Fast Food Packaging," *Environmental Science & Technology Letters,* vol. 4, no. 3, pp. 105-111, 2017.

[9] M. Eriksson *et al.*, "Wetting Transition on Liquid-Repellent Surfaces Probed by Surface Force Measurements and Confocal Imaging," *Langmuir,* vol. 35, no. 41, pp. 13275-13285, 2019.

[10] A. Gaddam, A. Agrawal, S. S. Joshi, and M. C. Thompson, "Utilization of Cavity Vortex To Delay the Wetting Transition in One-Dimensional Structured Microchannels," *Langmuir,* vol. 31, no. 49, pp. 13373-13384, 2015.

[11] H. Sharma, K. John, A. Gaddam, A. Navalkar, S. K. Maji, and A. Agrawal, "A magnet-actuated biomimetic device for isolating biological entities in microwells," *Scientific Reports,* vol. 8, no. 1, p. 12717, 2018.

[12] J. D. Smith *et al.*, "Droplet mobility on lubricant-impregnated surfaces," *Soft Matter,* vol. 9, no. 6, pp. 1772-1780, 2013.

[13] T. Van Buren and A. J. Smits, "Substantial drag reduction in turbulent flow using liquid-infused surfaces," *Journal of Fluid Mechanics,* vol. 827, pp. 448-456, 2017.

[14] H. Sharma, A. Gaddam, A. Agrawal, and S. S. Joshi, "Slip flow through microchannels with lubricant-infused bi-dimensional textured surfaces," *Microfluidics and Nanofluidics,* vol. 23, no. 2, p. 28, 2019.

[15] X. Jing and Z. Guo, "Durable Lubricant-Impregnated Surfaces for Water Collection under Extremely Severe Working Conditions," *ACS Applied Materials & Interfaces,* vol. 11, no. 39, pp. 35949-35958, 2019.

[16] X. He, P. Cao, F. Tian, X. Bai, and C. Yuan, "Infused configurations induced by structures influence stability and antifouling performance of biomimetic lubricant-infused surfaces," *Surface and Coatings Technology,* vol. 358, pp. 159-166, 2019.

[17] R. Y. Siddiquie, A. Gaddam, A. Agrawal, S. S. Dimov, and S. S. Joshi, "Anti-Biofouling Properties of Femtosecond Laser-Induced Submicron Topographies on Elastomeric Surfaces," *Langmuir,* vol. 36, no. 19, pp. 5349-5358, 2020.

[18] T. Yamazaki *et al.,* "Antifreeze Liquid-Infused Surface with High Transparency, Low Ice Adhesion Strength, and Antifrosting Properties Fabricated through a Spray Layer-by-Layer Method," *Industrial & Engineering Chemistry Research,* vol. 58, no. 6, pp. 2225-2234, 2019.

[19] M. Zhang *et al.,* "Lubricant-infused coating by double-layer ZnO on aluminium and its anti-corrosion performance," *Journal of Alloys and Compounds,* vol. 764, pp. 730-737, 2018.

[20] J. Lee, Y. Jiang, F. Hizal, G.-H. Ban, S. Jun, and C.-H. Choi, "Durable omniphobicity of oil-impregnated anodic aluminum oxide nanostructured surfaces," *Journal of Colloid and Interface Science,* vol. 553, pp. 734-745, 2019.

[21] S. Zouaghi *et al.,* "Biomimetic surface modifications of stainless steel targeting dairy fouling mitigation and bacterial adhesion," *Food and Bioproducts Processing,* vol. 113, pp. 32-38, 2019.

[22] X. Zhu *et al.,* "Simple Way to a Slippery Lubricant Impregnated Coating with Ultrastability and Self-Replenishment Property," *Industrial & Engineering Chemistry Research,* vol. 58, no. 19, pp. 8148-8153, 2019.

[23] Y. Li *et al.,* "Bio-inspired Edible Superhydrophobic Interface for Reducing Residual Liquid Food," *Journal of Agricultural and Food Chemistry,* vol. 66, no. 9, pp. 2143-2150, 2018.

[24] Q. Li and Z. Guo, "Lubricant-infused slippery surfaces: Facile fabrication, unique liquid repellence and antireflective properties," *Journal of Colloid and Interface Science,* vol. 536, pp. 507-515, 2019.

[25] L. Rapoport, B. R. Solomon, and K. K. Varanasi, "Mobility of Yield Stress Fluids on Lubricant-Impregnated Surfaces," *ACS Applied Materials & Interfaces*, vol. 11, no. 17, pp. 16123-16129, 2019.

[26] M. Yu *et al.*, "Facile fabrication of biomimetic slippery lubricant-infused transparent and multifunctional omniphobic surfaces," *Journal of Materials Science*, vol. 55, no. 10, pp. 4225-4237, 2020.

[27] D. Wang, Z. Guo, and W. Liu, "Bioinspired Edible Lubricant-Infused Surface with Liquid Residue Reduction Properties," *Research*, vol. 2019, p. 1649427, 2019.

[28] R. Mukherjee, M. Habibi, Z. T. Rashed, O. Berbert, X. Shi, and J. B. Boreyko, "Oil-Impregnated Hydrocarbon-Based Polymer Films," *Scientific Reports*, vol. 8, no. 1, p. 11698, 2018.

[29] P. S. Brown and B. Bhushan, "Liquid-impregnated porous polypropylene surfaces for liquid repellency," *Journal of Colloid and Interface Science*, vol. 487, pp. 437-443, 2017.

[30] P. S. Brown and B. Bhushan, "Mechanically durable liquid-impregnated honeycomb surfaces," *Scientific Reports*, vol. 7, no. 1, p. 6083, 2017.

[31] J. S. Wexler, I. Jacobi, and H. A. Stone, "Shear-Driven Failure of Liquid-Infused Surfaces," *Physical Review Letters*, vol. 114, no. 16, p. 168301, 2015.

[32] P. Baumli *et al.*, "Flow-Induced Long-Term Stable Slippery Surfaces," *Advanced Science*, vol. 6, no. 11, p. 1900019, 2019.

[33] P. Sartori *et al.*, "Motion of Newtonian drops deposited on liquid-impregnated surfaces induced by vertical vibrations," *Journal of Fluid Mechanics*, vol. 876, p. R4, 2019.

[34] J.-M. Romano, A. Garcia-Giron, P. Penchev, and S. Dimov, "Triangular laser-induced submicron textures for functionalising stainless steel surfaces," *Applied Surface Science*, vol. 440, pp. 162-169, 2018.

[35] X. Trier, C. Taxvig, A. K. Rosenmai, and G. A. Pedersen, "PFAS in paper and board for food contact: Options for risk management of poly-and perfluorinated substances," *Nordic Council of Ministers*, 2018.

[36] R. Ribeiro-Santos, M. Andrade, N. R. d. Melo, and A. Sanches-Silva, "Use of essential oils in active food packaging: Recent advances and future trends," *Trends in Food Science & Technology*, vol. 61, pp. 132-140, 2017.

[37] E. Panel o. F. Additives *et al.*, "Re-evaluation of dimethyl polysiloxane (E 900) as a food additive," *EFSA Journal*, vol. 18, no. 5, p. e06107, 2020.

[38] G. McHale, B. V. Orme, G. G. Wells, and R. Ledesma-Aguilar, "Apparent Contact Angles on Lubricant-Impregnated Surfaces/SLIPS: From Superhydrophobicity to Electrowetting," *Langmuir*, vol. 35, no. 11, pp. 4197-4204, 2019.

[39] B. Tan and K. Venkatakrishnan, "A femtosecond laser-induced periodical surface structure on crystalline silicon," *Journal of Micromechanics and Microengineering*, vol. 16, no. 5, pp. 1080-1085, 2006.

[40] I. Gnilitskyi, T. J. Y. Derrien, Y. Levy, N. M. Bulgakova, T. Mocek, and L. Orazi, "High-speed manufacturing of highly regular femtosecond laser-induced periodic surface structures: physical origin of regularity," *Scientific Reports*, vol. 7, no. 1, p. 8485, 2017.

[41] A. H. A. Lutey *et al.*, "Towards Laser-Textured Antibacterial Surfaces," *Scientific Reports*, vol. 8, no. 1, p. 10112, 2018.

[42] C. Sciancalepore, L. Gemini, L. Romoli, and F. Bondioli, "Study of the wettability behavior of stainless steel surfaces after ultrafast laser texturing," *Surface and Coatings Technology*, vol. 352, pp. 370-377, 2018.

[43] A. Garcia-Giron *et al.*, "Durability and Wear Resistance of Laser-Textured Hardened Stainless Steel Surfaces with Hydrophobic Properties," *Langmuir*, vol. 35, no. 15, pp. 5353-5363, 2019.

[44] H. Xu, A. Clarke, J. P. Rothstein, and R. J. Poole, "Viscoelastic drops moving on hydrophilic and superhydrophobic surfaces," *Journal of Colloid and Interface Science*, vol. 513, pp. 53-61, 2018.

[45] S. Varagnolo, G. Mistura, M. Pierno, and M. Sbragaglia, "Sliding droplets of Xanthan solutions: A joint experimental and numerical study," *The European Physical Journal E*, vol. 38, no. 11, p. 126, 2015.

[46] M. J. Kreder *et al.*, "Film Dynamics and Lubricant Depletion by Droplets Moving on Lubricated Surfaces," *Physical Review X*, vol. 8, no. 3, p. 031053, 2018.

[47] Y. Liu, J. S. Wexler, C. Schönecker, and H. A. Stone, "Effect of viscosity ratio on the shear-driven failure of liquid-infused surfaces," *Physical Review Fluids*, vol. 1, no. 7, p. 074003, 2016.

CHAPTER 4: LASER-ENABLED SURFACE TREATMENT OF DISPOSABLE ENDOSCOPE LENS WITH SUPERIOR ANTIFOULING AND OPTICAL PROPERTIES

The research reported in this chapter was published online as a full-length article in the journal of "Langmuir" (2022):

T. Karkantonis[1], A. Gaddam[1], H. Sharma[2], G. Cummins[1], T. L. See[3], and S. Dimov[1], "Laser-Enabled Surface Treatment of Disposable Endoscope Lens with Superior Antifouling and Optical Properties," *Langmuir*, vol. 38, no. 37, pp. 11392-11405, 2022.

[1]*Department of Mechanical Engineering, School of Engineering, The University of Birmingham, Birmingham, B15 2TT, UK*

[2]*Department of Chemical and Biomolecular Engineering, University of Notre Dame, Notre Dame, Indiana 46556, USA*

[3]*The Manufacturing Technology Centre Ltd, Coventry, CV7 9JU, UK*

Authors' contribution:

T. Karkantonis: Main author, conceived the methodology, conducted the experiments and characterisations, performed the analysis and written the original draft. **A. Gaddam:** Assisted with the microalgae cultivation and adhesion test. **H. Sharma:** Supported with the protein adsorption tests. **G. Cummins:** Provided knowledge and expertise on medical devices. **T. L. See:** Supervision and proofreading. **S. Dimov:** Supervision and proofreading.

Abstract

Endoscopes are ubiquitous in minimally invasive or keyhole surgeries globally. However, frequent removal of endoscopes from the patient's body due to the lens contaminations results in undesirable consequences. Therefore, a cost-effective process chain to fabricate thermoplastic-based endoscope lenses with superior anti-fouling and optical properties is proposed in this research. Such multi-functional surface response was achieved by lubricant-impregnation of nanostructures. Two types of topographies were produced by femtosecond laser processing of metallic moulds, especially to produce single-tier Laser-Induced Periodic Surface Structures (LIPSS) and two-tier Multiscale Structures (MS). Then, these two LIPSS and MS masters were used to replicate them onto two thermoplastic substrates, namely polycarbonate and cyclic olefin copolymer, using hot embossing. Finally, the LIPSS and MS surfaces of the replicas were infiltrated by silicone oils to prepare lubricant-impregnated surfaces (LIS). Droplet sliding tests revealed that the durability of the as-prepared LIS improved with the increase of the lubricant viscosity. Moreover, the single-tier LIPSS replicas exhibited longer-lasting lubricant conservation properties than the MS ones. Also, LIPSS-LIS replicas demonstrated an excellent optical transparency, better than the MS-LIS ones, and almost match the performance of the reference polished ones. Furthermore, the LIPSS-LIS treatment led to superior anti-fouling characteristics, i.e., regarding fogging, blood adhesion, protein adsorption and microalgae attachment, and thus demonstrated its high suitability for treating endoscopic lenses. Finally, a proof-of-concept LIPSS-LIS treatment of endoscope lenses was conducted that confirmed their superior multi-functional response.

Keywords: Blood, Chlorella Vulgaris, endoscope, femtosecond laser, lens, LIPSS, lubricant-impregnated surfaces.

4.1. Introduction

In recent years, minimally invasive medical operations such as laparoscopy and endoscopy have attracted considerable attention among surgeons, as they are relatively quick and safe procedures to treat patients. Since such keyhole surgeries require small incisions, less blood loss is associated with them and also the infection risks are less, while the post-surgery recovery time of the patients is much shorter [1, 2]. For instance, endoscopes have been deployed widely to probe organs for cancer, collect biopsies from tissues and deliver treatments inside the human body. The principal procedures and overall performance of these contemporary techniques are strongly dependent on visualisation capabilities of optical devices, such as endoscopes, and thus their field of view must be maintained intact throughout these surgical interventions. However, the endoscope lenses can be contaminated/fouled by blood and other body fluids, i.e., fluids that contain fats and proteins, or even become foggy due to some condensations during endoscopic surgeries [3, 4]. In general, these substances can adhere to the lens surfaces, resulting in impaired vision, and hence low efficiency of such surgical interventions [5]. Therefore, there is a pressing need to design and manufacture endoscope lenses with enhanced anti-fouling functionalities without sacrificing their optical transparency under harsh surgical conditions.

To date, the most common methods for removing any impurities from the endoscope lenses in vivo surgeries involve manual wiping, i.e. the rubbing of the lens against adjacent tissues/organs or the extraction of the endoscope from the human body to wipe it off, and also the integration of extra working channels for irrigation and suction [6]. Although the clarity of endoscopic vision can be retained to a certain extent using these techniques, their practical implications might lead to internal organ injuries, surgical site infections, extended operation times due to unnecessary disruptions and patient discomfort [7].

To address such challenging requirements, various surface treatment methods have been deployed to tailor the functional responses of materials by modifying their surface topography and/or chemistry [8, 9]. Coating-based methods were proposed for creating hydrophilic surfaces with dual-functional antifogging/antibacterial response for optical devices [10-12]. Especially, a stable liquid film on the surface can be formed by applying such coatings that obstructs the creation of scattering droplets and thus inhibits fogginess and maintains transparency in humid environments. Nevertheless, without applying any after-treatment, e.g., rinsing with water, non-transparent liquids can spread and eventually adhere to such hydrophilic surfaces, and therefore they are prone to contaminations and vision losses during endoscopic surgeries.

Superhydrophobic surfaces have received great attention, too, from researchers owing to their excellent anti-wetting [13], anti-icing [14], anti-biofouling [15], anti-friction [16] and anti-bacterial [17] responses. Specifically, the use of a low surface energy coating, e.g. perfluorinated compounds, together with hierarchical micro/nanoscale topographies to entrap air were applied to achieve robust superhydrophobic and/or superoleophobic behaviours [18]. The heterogeneous wetting state, i.e., Cassie-Baxter State (CBS), on such surfaces can exhibit an extreme repellency even against complex fluids like blood [19, 20]. However, CBS is metastable, especially when exposed to low surface tension liquids [21] and moderate pressure [22], and a transition to the Wenzel state can completely destroy the attractive wetting properties of such surfaces. In addition, a relatively high surface roughness is beneficial for their superhydrophobic properties, while impacts negatively their transparency. Therefore, attaining both functionalities is technically challenging and hence time-consuming task [23, 24] that together with the limitations of such treatments can render them inadequate for fulfilling the requirements of medical optic devices.

At the same time, Lubricant-Impregnated Surfaces (LIS) have gained significant interest as a way to address the aforementioned shortcomings, especially by impregnating micro/nano structured surfaces with a low-energy lubricant. Specifically, LIS can offer excellent long-lasting liquid shedding characteristics, i.e. display very low Critical Sliding Angle (CSA) even against yield stress fluids [25], stability under high pressure and temperature conditions [26] and anti-biofouling/anti-bacterial/anti-thrombogenic/drag-reduction properties [27-29]. In addition, numerous studies have demonstrated that LIS with such functional characteristics can be prepared with coating techniques without compromising the optical properties of transparent materials [30-35].

Thanks to these advantages, LIS have emerged as a very promising option for improving the efficacy of endoscopic surgical procedures by keeping the camera lens clear from foulants. For example, two relatively similar treatments have been proposed to produce anti-biofouling materials for endoscope lenses by depositing silica nanoparticles onto glass substrates as a base porous structure and then lubricating it with either silicone or plant oil [36, 37]. Even though both materials were capable of maintaining a clear endoscopic vision by repelling blood and body fluids repeatedly, the employed surface treatment methods did not meet the requirements for their scale up production. In this regard, Tenjimbayashi et al. [38] reported a simple one-step procedure to produce a lubricated fiber-filled porous material, which can be synthesised in situ and then adhered to the endoscope lens for single use. Nevertheless, the nanofibrous LIS proposed in this research raised significant concerns about their mechanical durability and chemical stability. To overcome the intrinsic limitations associated with the coating-based techniques, Lee et al. [39] proposed an alternative surface treatment to functionalise endoscopic lenses by direct laser texturing. Prior to lubricant infusion, only a fluorinated self-assembled monolayer was applied to the textured surface and thus to enhance

the longevity of its anti-biofouling performance. While highly ordered structures could be produced selectively by laser surface texturing even onto freeform surfaces with high precision, the high operating costs associated with this stand-alone process hamper its broader application. At the same time, the use of coatings that contain long chain perfluorinated compounds for preparing LIS can have a negative impact on both human health and the environment [40, 41]. Therefore, further research is necessary to address the issue of vision loss in endoscopic surgeries by developing a cost-effective process chain for producing optical lenses with a multi-functional response. Also, the environmental impact of any method for their scale up manufacture should be considered, especially they should be recyclable without requiring any after-treatments.

This research reports an efficient and cost-effective process chain for producing recyclable disposable endoscopic lenses with superior durability while exhibiting excellent anti-fouling properties and transparency. The method that includes, first, the manufacture of metallic masters with both sub-micron and multiscale topographies, then replicating them on thermoplastic substrates and finally impregnating the replicas with silicone oil is described. Next, the optical and anti-adhesive properties of produced LIS together with their lubricant retention capabilities were investigated under shear flow conditions. To demonstrate the effectiveness of such lens treatment for preventing vision loss during endoscopy, LIS were further subjected to protein adsorption, microalgae adhesion, blood fouling and fogging tests. Finally, a set of LIS lenses was integrated into an inspection endoscope device to demonstrate the proof-of-concept.

4.2. Materials and methods

An overview of the proposed process chain for producing disposable and recyclable endoscopic polymer lenses that exhibit multi-functional responses is shown in Fig. 4.1. The employed processing steps in this chain together with the respective methods used to characterise the surface of produced lenses are described in this section.

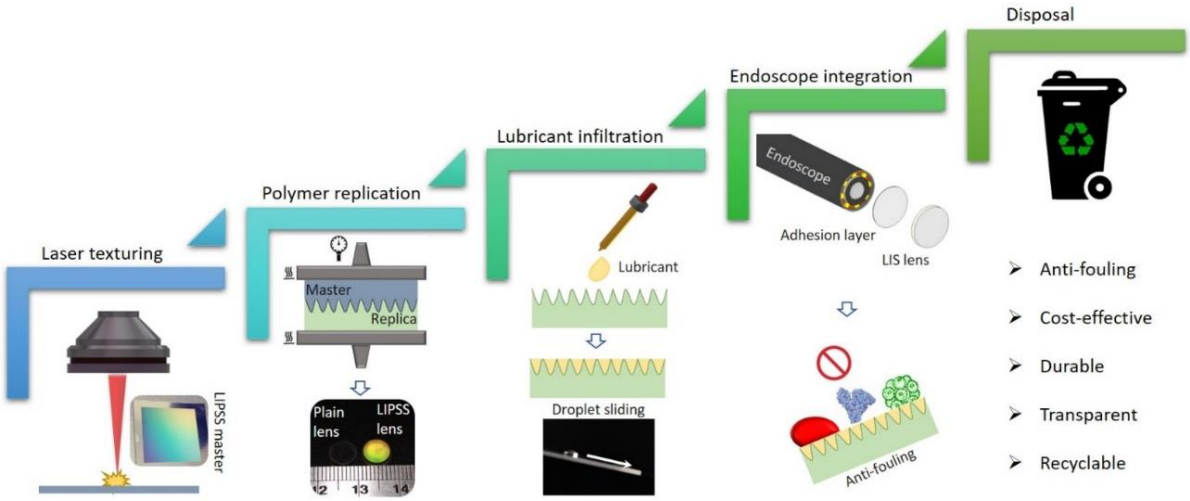

Fig. 4.1. An overview of the process chain employed to fabricate disposable endoscope lenses.

4.2.1. Fabrication of metallic masters

Commercially available AISI 316 Stainless Steel (SS) plates with a surface area of 40 × 40 mm^2 and thickness of 0.5 mm were used as metallic masters. The as-received substrates had an initial average surface roughness (S_a) of 35 nm and were then laser treated. The surface texturing was carried out on a laser processing workstation (LASEA LS5, Belgium) under atmospheric conditions. In particular, the system integrates a femtosecond Yb-doped laser source (Satsuma, Amplitude Systems) with the following technical specification: a pulse duration of 310 fs, nominal wavelength of 1030 nm, pulse repetition rate (f) up to 500 kHz and maximum average power of 5 W. In addition, a half waveplate was incorporated into the

beam delivery sub-system in order to texture the SS substrates with an s-polarised Gaussian beam. Thereafter, a galvo scan head was employed to deflect the focused laser beam across the samples at a maximum scanning speed (v) of 2000 mm/s and a 100 mm telecentric lens was used to focus the beam to a spot size of 40 μm at $1/e^2$ of the Gaussian intensity. Finally, a high precision stack of three linear motorised stages (X, Y, Z) in combination with a high-resolution camera were utilised for positioning samples with high accuracy and repeatably prior to the laser surface texturing operations.

Two different surface topographies, namely, single-tier Laser-Induced Periodic Surface Structures (LIPSS), i.e. nano-scale ripple-like structures, and two-tier Multi-scale Structures (MS), i.e. microscale protrusions with nanoscale ripples on top of them, were produced onto the SS substrates, following the approach reported in another research [42]. Briefly, MS had a grid like micro topography that was produced employing the following process settings: a fixed f of 500 kHz, v of 1000 mm/s and a constant hatch (h) distance of 40 μm between any two consecutive lines in X and Y. In total, 40 scans, i.e. 20 scans per line, with a single pulse fluence (φ_0) of 178 mJ/cm^2 was required to produce a relatively shallow grid of micro protrusions on the SS surface. At the same time, the single-tier LIPSS were generated employing a raster scanning strategy and a single pass over the surface with a fixed f of 250 kHz, v of 1000 mm/s, h of 3 μm and the same φ_0. The laser parameters used for creating the two surface topographies investigated in this research together with the overall processing time required to complete their texturing operations over an area of 30 × 30 mm^2 are summarised in Table 4.1.

Table 4.1. The key laser parameters used to produce the MS and LIPSS onto the SS moulds together with their corresponding processing time.

Topography	f (kHz)	v (mm/s)	φ_0 (mJ/cm^2)	h (μm)	Total number of scans	Processing time (min)
MS	500	1000	178	40	40	15
LIPSS	250	1000	178	3	1	4

4.2.2. Fabrication of lubricant impregnated polymer lenses

Single-tier LIPSS and two-tier MS textures on SS surfaces were replicated onto commercially available transparent Polycarbonate (PC) and Cyclic Olefin Copolymer (COC) sheets with a thickness of 1.5 mm (purchased from Microfluidic ChipShop, Germany) using a hot embossing system. These thermoplastics are commonly used for optical lenses and can withstand autoclave temperatures. The glass transition temperatures of these polymers as received are given in Table 4.2. During the embossing process, the textured SS moulds together with the as-received polymer sheets were pressed to each other at an elevated temperature, i.e. higher than their glass transition temperatures. Since the replication quality was strongly affected by the applied temperature and load, the influence of these two parameters was investigated to identify the optimum processing window for both polymer substrates. The process settings used to produce the PC and COC replicas are provided in Table 4.2.

Lastly, silicone oils (Sigma-Aldrich) with different viscosities, i.e., 5, 20 and 100 cSt, were used as lubricants to prepare LIS in this study. After the lubricant oil was pipetted and completely spread onto the entire surface of the textured replicas due to capillary forces, the samples were kept vertically for an hour in order to drain any excess oil. Compared to other

types of lubricants, e.g. perfluorinated oils, the rationale for selecting silicone-based ones for preparing LIS in this research is associated with the fact that they are nontoxic to the human body and also their use has been approved by both FDA [43] and EFSA [44] for medical applications as well as food additives. Therefore, the as-prepared thermoplastic LIS can be considered of being biocompatible and thus suitable for the usage as objective lenses in endoscopes.

Table 4.2. The optimised settings used to produce the PC and COC replicas together with their respective glass transition temperatures.

Polymer	Load (kN)	Operating temperature (°C)	Glass transition temperature (°C)	Compression time (min)
PS	9.2	150	145	10
COC	10.8	145	142	10

4.2.3. Morphology and optical characterisation

The LIPSS and MS topographies produced on the SS and then replicated on the thermoplastic substrates were initially inspected using a Scanning Electron Microscope (SEM, Hitachi TEM3030Plus). The dimensional characteristics of the MS structure were obtained using a focus variation optical microscope (Alicona G5). While, an Atomic Force Microscope (AFM, MFP-3D, Asylum Research) was employed to study the morphology of the nanoscale surface topographies. An open-source image analysis software (Gwyddion) was used to process the acquired 10 x 10 μm AFM scans and thus to obtain the LIPSS cross-sectional profiles. At the same time, this software was also utilised to gain information about their orientation and spatial periodicity by performing a 2D-FFT analysis. The transmittance of the as-received, textured and lubricated thermoplastic surfaces was analysed over the visible spectrum, i.e., from 400 to

700 nm, employing a UV-Vis spectrometer (Lambda 365, Perkin Elmer). To ensure the reliability and validity of these results, the transmittance measurements were conducted in triplicates.

4.2.4. Wettability characterisation

The wettability of the as-received, textured and lubricated thermoplastic substrates was investigated by using the sessile drop technique. Specifically, 5 μL water droplets were dispensed onto these surfaces and then their static Contact Angle (CA) values were measured using a goniometer (OCA 15EC, Data Physics GmbH, Germany). Also, the Contact Angle Hysteresis (CAH) of the aforesaid surface topographies was analysed by gradually increasing and decreasing the volume of the water droplet on the surface, and the difference between the advancing and receding contact angles was quantified. At the same time, the shedding characteristics of the thermoplastic plain, textured and LIS samples were examined, too. Firstly, the critical sliding angle (CSA) values of 10 μL water droplets were measured on these surfaces by employing a motorised tilting stage with positioning accuracy and resolution of 10 arcsec and 0.01°, respectively. Thereafter, CSA of other liquids, such as Xanthan Gum solution and pH liquids was investigated to simulate the response of LIS against viscous fluid substances, e.g., mucus and body fluids, gastric fluids with different pH levels. The concentration of Xanthan Gum in the aqueous solution was 2 g/L, whilst the preparation procedure and the shear viscosity properties of this liquid were analytically described in our previous study [45]. Finally, it should be stated that the average CA, CAH and CSA values reported in this study were calculated based on five repeated measurements taken at different locations on each sample.

4.2.5. Durability characterisation

Generally, the LIS performance is expected to degrade when body fluids start wetting continuously their surfaces. Sooner or later, this will allow contaminants to foul the camera lens and obstruct vision during endoscopic surgeries. The reason for the loss of the LIS functionality can be mainly attributed to the depletion of impregnated lubricant under persistent shear flow conditions [46]. In order to assess the LIS durability, LIS prepared with the silicone oils of varying viscosity were tilted at 15° using a motorised stage, while 10 μL water droplets were continuously dispensed on their surfaces up to the point where no motion could be detected, i.e., the droplet was completely pinned to the surface. To ensure that the droplets flowed at exactly the same spot and also to avoid them bouncing on the surface during the tests, a fixture was used to hold the pipette above the substrates and release the droplets from a maximum height of 2 mm. A camera (Canon 2000D) mounted on a tripod was employed to record the mobility of water droplets at 60 frames per second. Lastly, an open-source video analysis and modelling software (Tracker) was used to obtain the steady-state shedding velocity of the water droplets.

4.2.6. Anti-fouling characterisation

To characterise anti-fouling capabilities of LIS on the embossed thermoplastic substrates, three different tests were conducted with different foulants, as expected in potential endoscopic procedures, i.e., blood, protein and microorganisms. First, the experiments were conducted to examine the anti-adhesive ability of LIS against defibrinated sheep blood (Darwin Biological, UK). In particular, the mobility of single blood droplets was monitored on LIS when tilted at an angle of ~ 45°. Thereafter, their blood-shedding capabilities were tested by immersing them into containers filled with blood for up to 30 times.

Next, LIS were assessed for their protein adsorption. For this, the thermoplastic plain and LIS substrates were incubated overnight with a solution of CFSE (Carboxyfluorescein Succinimidyl Ester, $\lambda_{excitation}$: 492 nm, $\lambda_{emmision}$: 517 nm) dye (ThermoFischer Scientifics, USA) tagged Bovine Serum Albumin (Sigma Aldrich, USA) (1% (w/v)) in a petri dish under a dark environment. Subsequently, the plain and LIS substrates of both PC and COC were imaged using a CCD camera (Retiga EXi, QImaging) connected to an inverted fluorescence microscope (Olympus IX71) with a 4x magnification lens. Both, the bright field and the fluorescence images (Semrock LF488/561 green filter cube) of PC and COC were acquired using the microscope and were later merged into a composite image using ImageJ.

Finally, the Chlorella Vulgaris (CV) strain CCAP 211/11B (Darwin Biological, UK) was chosen for the assessment of microalgae adhesion to LIS. To this end, a pre-culture of CV along with the modified Bold's basal medium was added to the glass containers and the culture was incubated at 28 ^{o}C for a week under the cool white fluorescent illumination with a light-to-dark ratio of 12:12 hours. The plain and LIS substrates of both PC and COC were placed inside the glass containers during the incubation. After a week, the substrates were imaged using a custom-made setup by taking the advantage of the CV autofluorescence. To capture the fluorescence from the CV-settled substrates, a camera (Canon 2000D) fitted with a 18-55 mm lens and yellow and magenta filters was used. These fillers were employed to filter out the undesired wavelengths, apart from 680 nm red light, under the ultraviolet light excitation of the chlorophyll. In addition, a dioptre lens was also attached to the camera to obtain the magnified images. The obtained fluorescent images from the substrates were analysed using the ImageJ software to calculate the area covered by CV in percentages.

4.2.7. Proof-of-concept demonstration

Finally, to demonstrate the applicability of these surfaces for preventing blood fouling during endoscopy, the LIS lenses were integrated into a representative inspection endoscope device as follows: i) a round flat lens of 8 mm in diameter was cut out of the textured polymer replica, ii) the lens was thoroughly cleaned with isopropyl alcohol and lubricated as described in Sub-section 4.2.2 and (iii) an adhesion layer (Glue dots) was used to attach it onto the endoscope camera. In this research, the visibility through the LIS lenses was verified by directing the endoscope onto a printed QR code and then trying to read it with a smartphone camera. In addition, their resistance against blood fouling was assessed by immersing/dipping the endoscope into blood multiple times until its vision was totally lost, i.e. the treated lens was fouled by blood. It should be stated that this blood fouling test was repeated for three identical LIS lenses. During these experiments, the integrated endoscope camera was employed to capture images of a printed chessboard. Thereafter, they were post-processed with an open-source image analysis software (ImageJ) to quantify the percentage of the area visible after a certain number of dips.

4.3. Results and discussion

4.3.1. Surface morphology analysis

The first part of this study was focused on generating LIPSS and MS over an area of 30 x 30 mm^2 on the SS substrates. Figure 4.2a shows a SEM micrograph of LIPSS generated on the surface when the SS master was irradiated with the femtosecond pulsed laser. As can be seen, the surface topography obtained represents uniform periodic ripple-like structures with an orientation perpendicular to the laser beam polarisation vector (indicated by yellow double

arrows in Fig. 4.2a). From the 2D-FFT analysis performed at different areas on the textured SS surface, the main LIPSS spatial periodicity was slightly below the laser wavelength of 1030 nm and varied in the range from 800 to 900 nm. At the same time, the well-defined linear 2D-FFT image (see the inset of Fig. 4.2a) can be considered as proof of the LIPSS regularity on the SS surface. After the hot embossing process, the LIPSS topography was successfully replicated onto the thermoplastic substrates. SEM micrographs of the LIPSS embossed onto the PC and COC substrates are depicted in Fig. 4.2b and c, respectively. While, the 3D AFM images of LIPSS on the SS master and PC and COC substrates demonstrate the replication quality achieved and they are given in Fig. 4.2d-f, respectively. In addition, Fig. 4.2g shows their respective surface profiles over a scan distance of 8 μm. These cross-sectional profiles were obtained based on the average values of scans taken at five different locations on the textured SS master and its polymer replicas. Based on the AFM profiles, the LIPSS average height was calculated to be within the range of 152 to 172 nm on all substrates and this signifies an excellent replication quality. More specifically, the deviation in percentages from the average LIPSS height was less than 11% and 5%, when the average values obtained on PC and COC substrates were compared with that on the SS master, respectively.

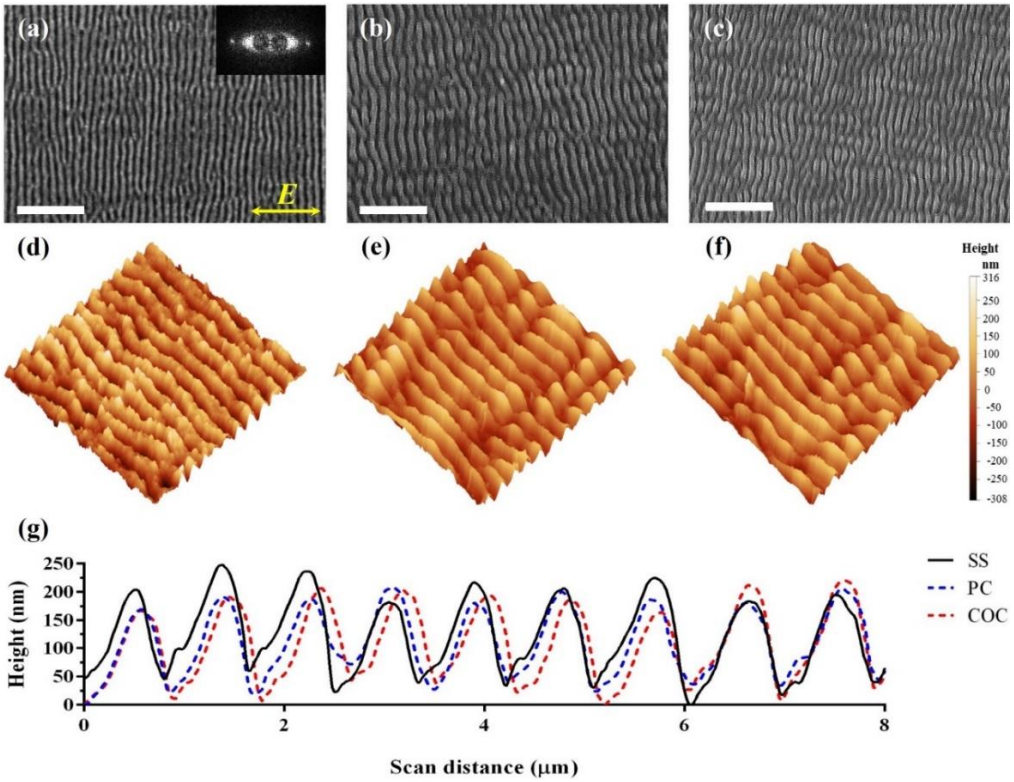

Fig. 4.2. Surface morphologies of LIPSS: (a-c) SEM and (d-f) 3D AFM micrographs of LIPSS on the SS, PC and COC surfaces, respectively; (g) a plot showing the surface profiles of LIPSS on the SS master and PC and COC replicas. Scale bar: 6 μm.

Next, the MS topographies were produced on a SS master. Due to the higher fluence accumulated at the intersecting points of the perpendicular beam vectors in the grid like scanning strategy, “peaks” and “valleys” were formed on the SS surface as shown in Fig. 4.3a. By taking a closer look at Fig. 4.3d, it is apparent that the micro topography is fully covered with nanoscale ripple-like structures. In reality, the dimensional and geometrical characteristics of these ripples should be almost identical to that of LIPSS. Following the embossing step, the negative patterns of the MS on the SS surface were replicated onto the PC and COC substrates as depicted in Fig. 4.3b and c. At the same time, it is evident from Fig. 4.3e and f that the nanoscale morphology on top of the peaks and valleys was replicated successfully onto the polymer substrates. To analyse further the replication quality achieved

during the embossing process, the height profiles of micro-peaks on the SS master and the PC and COC samples along X and Y were captured as shown in Fig. 4.3g and h, respectively. No significant discrepancies were detected in the peak spacings onto the SS and polymer surfaces, i.e. they were consistent close to 40 μm on all of them. However, some relatively small variations can be observed in their heights across the substrates. For instance, the average height of micro-peaks on the SS surface was 5.1 μm and 4.2 μm when measured at five different locations along X and Y, respectively. Whereas the same measurement procedure led to average heights of 4.8 μm and 3.9 μm on PC and 4.9 μm and 3.6 μm on COC along X and Y, respectively. Overall, it can be stated that the difference of thermoplastic replicas from their metallic masters was less than 14%.

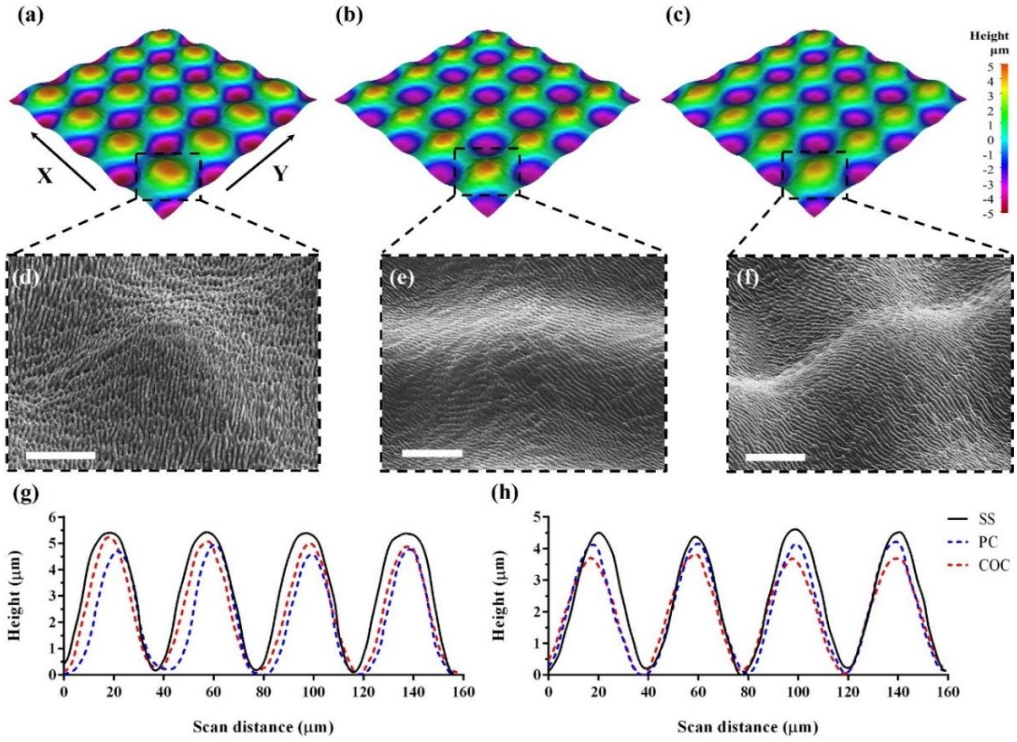

Fig. 4.3. Surface morphologies of MS: (a-c) the 3D height map and (d-f) the SEM images of MS on the SS master and PC and COC substrates, respectively; (g-h) the plots showing the height profiles of micro-peaks on the SS master and PC and COC substrates along X and Y, respectively. Scale bar: 20 μm.

4.3.2. Wettability analysis

An important part of this research was focused on characterising the wettability of all thermoplastic functionalised surfaces, while using as a reference untreated ones. The static CAs obtained on as-received (plain), textured (MS, LIPSS) and lubricated (MS-LIS, LIPSS-LIS) surfaces of PC and COC substrates are given in Fig. 4.4a. Initially, the plain surfaces of both thermoplastic materials exhibited a slightly hydrophobic behaviour with average CA values just above 90°. However, CAs increased substantially when the laser textured SS masters were embossed onto them. As expected, the surfaces covered with MS displayed higher CA values on both PC and COC replicas compared to those with single-tier LIPSS. For instance, the average CA value measured on the MS of COC replica was 131°, whilst the single-tier LIPSS embossed on the same material had CA of 114°. A 5 μL water droplet led to a larger CA on MS than that on LIPSS, as depicted in Fig. 4.4b. After the infusion of lubricant with 20 cSt viscosity onto the textured polymer substrates, the apparent CA decreased, especially on the MS-LIS samples, and a small wetting ridge appeared at the periphery of the hemispherical water droplets on all LIS (see the red arrows in Fig. 4.4b). The formation of such wetting ridge was attributed to the vertical component of the water's surface tension, which was high enough to lift the lubricant up [47]. At the same time, the differences in the average CA between MS-LIS and LIPSS-LIS on both polymer materials became marginal and did not exceed 2°. The insignificance of surface topography on the wettability of as-prepared LIS clearly suggests that both surface topographies were fully encapsulated by the lubricant and most likely sharing the same spreading coefficient.

Next, the shedding behaviour of water and Xanthan Gum solution droplets on the plain, MS, LIPSS, MS-LIS and LIPSS-LIS samples was investigated by measuring the minimum angle required to initiate their motion. Fig. 4.4c and d show CSAs of these liquids on all

aforementioned surfaces of PC and COC substrates. Low droplet mobility was observed at CSAs ranging between 26° and 47° on the plain surfaces for all the tested liquids. Surprisingly, the textured surfaces of both thermoplastic materials did not facilitate any droplet movement even when the substrates were positioned vertically, i.e., at an inclination angle of 90°. In this case, the high adhesion forces induced from the water/solid contact resulted in pinning the droplets onto these surfaces. Instead, all LIS exhibited great shedding characteristics against water as the droplets slid on their surfaces at an average CSA below 13°. At the same time, CAH of water droplets was measured to vary within the range of 8° to 13° and 5° to 8° on the MS-LIS and LIPSS-LIS samples, respectively. In reality, the infusion of lubricant into the textured surfaces dramatically lowered the contact line pinning and hence enabled the droplets to easily flow down their surfaces. However, it should be stated that only the LIPSS-LIS samples managed to repel both tested liquids at CSA smaller than 10°, indicating impressive shedding capabilities even against viscous liquids. Finally, since the endoscope lenses may be exposed to alkaline or acidic liquids, such as pancreatic and gastric juices, contained in the human body, CSAs for liquids with pH levels ranging from 1 to 9 were measured on all LIS onto the PC and COC substrates, as shown in Fig. 4.4e and f, respectively. All the pH-adjusted water droplets were observed to start sliding on LIPSS-LIS of both polymer samples at CSA below 7°, whilst larger tilt angles were required to aid their movement on the MS-LIS ones, i.e. CSAs ranging from 8° up to 18°. The aforementioned results demonstrate the potential of LIPSS-LIS treated surfaces to shed almost any kind of biological fluid.

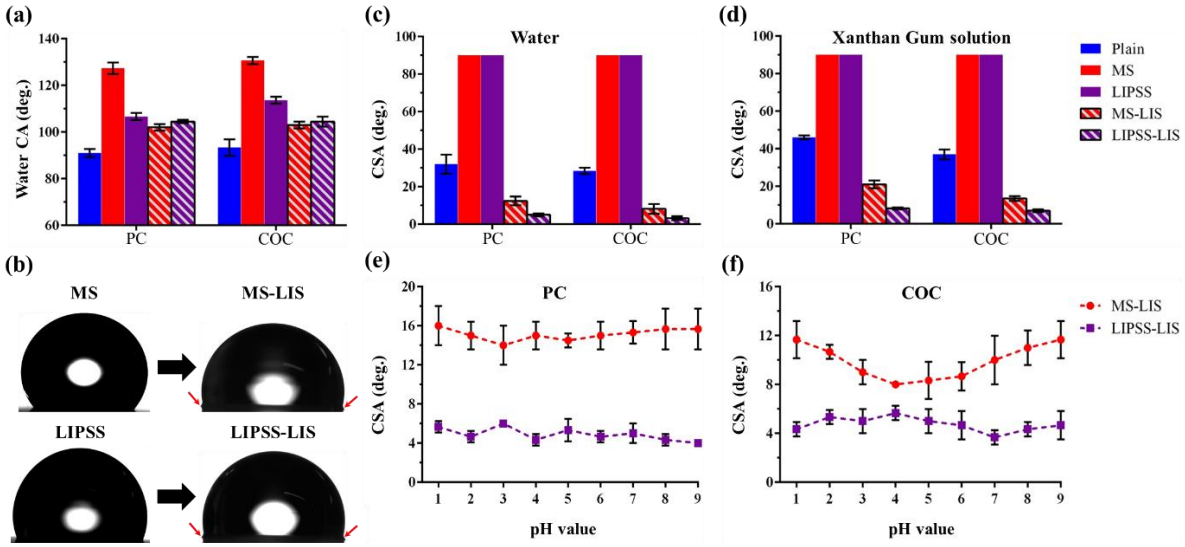

Fig. 4.4. Wettability analysis: (a) the static CAs measured on as-received, textured and lubricated surfaces of PC and COC substrates; (b) representative images of the water droplet on textured and lubricated surfaces of the COC substrate; the CSAs obtained on as-received, textured and lubricated surfaces of the PC and COC substrates for (c) water and (d) Xanthan Gum solution; the CSAs obtained on the lubricated surfaces of (e) PC and (f) COC.

4.3.3. Durability of LIS under shear flow conditions

As multiple single drops on LIS exert shear forces on them and thus, they can cause severe depletion of the impregnated lubricant and subsequently lead to their failure. Therefore, the effect of such shear-induced lubricant depletion on the LIS shedding characteristics was investigated. In particular, LIS were tilted at an angle of 15° as depicted in Fig. 4.5a and then subjected to water shear forces by repeatedly dispensing droplets at the same spot on their surfaces. Initially, all LIS exhibited low pinning forces regardless of the infused lubricant viscosity and hence the water droplets shed off their surfaces by the gravity. An example of a water droplet sliding down LIPSS-LIS impregnated with the 5 cSt lubricant is given in Fig 4.5a. At the same time, the average shedding velocities of water droplets are plotted in Fig.

4.5b and c as a function of the number of droplets deposited on the MS-LIS and LIPSS-LIS samples prepared with the lubricants of varying viscosity, respectively. In most cases, the droplet velocity decreased with the increase of lubricant viscosity because of the enhanced viscous dissipation at the liquid-lubricant interface. This trend agrees with previously reported studies [48, 49]. However, it should be noted that the lowest droplet sliding velocity was recorded on the MS-LIS sample when impregnated with the 5 cSt lubricant. This finding contradicts completely with the results obtained from the respective LIPSS-LIS one, on which the droplets exhibit the highest sliding velocity. It could be because there was not a stable entrapment of the low viscosity lubricant within the microscale topography of MS-LIS sample and most likely it overflowed from the valleys when the surface was tilted.

After dripping multiple water droplets on the MS-LIS and LIPSS-LIS substrates prepared with varying lubricant viscosities, their slippery performance started to degrade. Especially, the droplet velocity decreased, and eventually the droplets were pinned to their surfaces. The degradation of the LIS response can be attributed to the gradual lubricant depletion. More specifically, the sliding droplets took away and/or displaced the lubricant from the impregnated structures due to the shear forces, resulting in a severe lubricant depletion along their flow track. However, LIPSS sustained the shear forces from a greater number of droplets than the MS ones. This is because the relatively strong nanocapillary forces manifested by the nanoscale ripples have rendered a longer lubricant storage capacity, as illustrated in Fig. 4.5d. Whereas, the lubricant stored in the micron scale valleys of the MS topography was quickly depleted by the travelling train of droplets (see Fig. 4.5d) that impacted the performance of MS-LIS. The images in Fig. 4.5f also confirm that the infused lubricant was gradually removed by the sliding droplets and thus revealing the micro-pillar structures underneath the MS topographies. In addition to the strong capillary forces induced by the nanoscale structures

[50], the droplets on the LIPSS-LIS samples were highly mobile. This is because LIS with nanostructured topographies alter the molecular orientation of water near the liquid-lubricant interface and have weaken the hydrogen bonding interactions at the interface [51].

At the same time, it can be noticed in Fig. 4.5c that there are fluctuations in the shedding velocities of the droplets on LIPSS-LIS, irrespective of the lubricant viscosities. The lubricant redistribution might have caused a localised but temporarily finite replenishment of the lubricant layer [52], which can explain the fluctuations of droplet velocities. Especially, in the case of LIPSS, the depleted nanoscale ripple structures were swiftly replenished by the stored lubricant, due to their strong capillary action as depicted in Fig. 4.5e. Consequently, the velocity of the successive droplets increased until the next event of the lubricant depletion. This cyclic replenishment continues until all the stored lubricant had been completely depleted and then the final pinning of the droplet occurred. Furthermore, it can also be noted that the lubricant depletion from the topographies was at a much slower rate when its viscosity increased. For instance, the samples impregnated with 100 cSt lubricant were able to retain their slippery properties much longer than those impregnated with 5 and 20 cSt ones. Overall, the LIPSS-LIS sample with 100 cSt lubricant viscosity exhibited the most robust and stable performance and 160 droplets were required to lose completely its functionality.

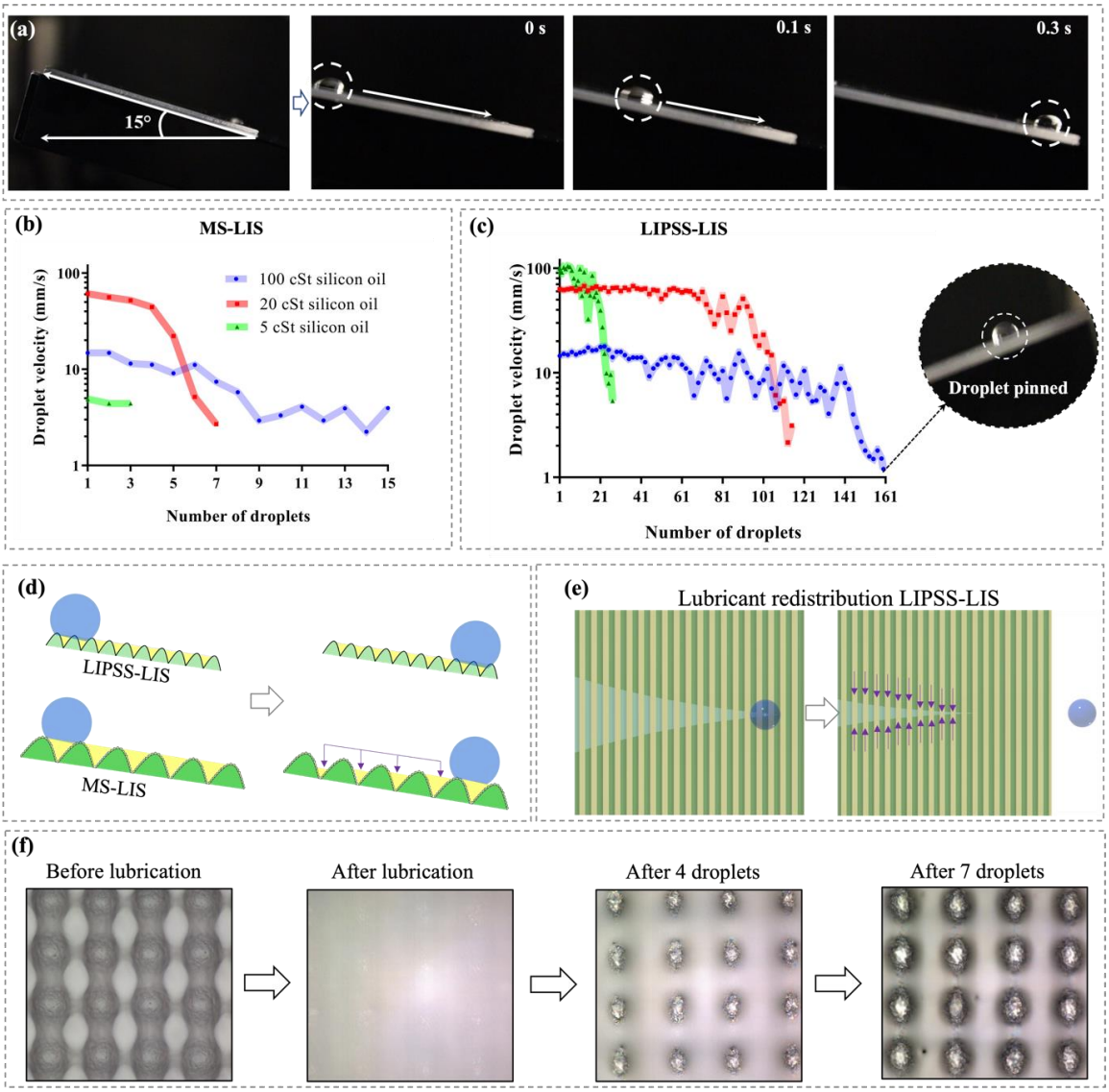

Fig. 4.5. The shear-induced lubricant depletion: (a) an image showing a tilted substrate before the shear test and a water droplet sliding on the LIPSS-LIS sample impregnated with 5 cSt lubricant; (b-c) the shedding velocities as a function of the increasing number of water droplets deposited on the MS-LIS and LIPSS-LIS substrates for the investigated lubricant viscosities, respectively. Inset shows an image of water droplet pinned to the surface of the LIPSS-LIS sample after the lubricant depletion; (d) an illustration showing the lubricant depletion on LIPSS and MS topographies; (e) an illustration showing lubricant redistribution after a droplet leaving the LIPSS-LIS treated surface; (f) images depicting the loss of the infused lubricant from the MS-LIS samples.

4.3.4. Optical analysis

One of the most critical requirements for endoscope lenses is their high transparency. Therefore, the optical properties of all treated thermoplastic surfaces together with the as-received ones were assessed. As the refractive index was the same for all lubricants (n ~ 1.4) used in this research irrespective of their viscosities, only the samples impregnated with 100 cSt lubricant were considered for these experiments. A comparison of the average transmittance obtained from the plain, MS, LIPSS, MS-LIS and LIPSS-LIS substrates of PC and COC over the visible spectrum (400 - 700 nm) is provided in Fig. 4.6a. As expected, the plain surfaces of both polymer materials showed an outstanding transparency of the visible light with peak transmittance values slightly below 90%. On the contrary, all the textured thermoplastic surfaces exhibited significantly low transmittance, indicating a translucent behaviour. Such a dramatic loss of light was mainly attributed to its scattering by the relatively rough surfaces of the treated samples [53, 54]. Since such effect is typically more pronounced on surfaces with microscale roughness, the substrates with LIPSS appeared to be less opaque compared to the MS ones.

After the lubricant infusion into the textured thermoplastic surfaces, a substantial increase in transmittance was detected. Actually, the infused lubricant was able to minimise the negative effects of both light scattering and reflectance by smoothening the textured topographies and also reducing the large step change in the refractive index [55] between air (n = 1) and the two thermoplastic materials (n_{PC} = 1.59 and n_{COC} = 1.4), as shown in Fig. 4.6b. However, it should be stated that only the LIPSS-LIS samples exhibited an excellent transmittance of the visible light due to the relatively small surface area for a diffusive reflectance. In particular, the transmittance spectrum of the LIPSS-LIS sample almost matched that obtained on the plain COC one, whereas it dropped up to 10% on the treated PC surfaces within the visible spectrum.

To compare further the transparency of the plain PC surface to that of LIPSS-LIS and MS-LIS, images of a colourful logo were captured with a camera when the samples were placed in contact with it and also with an offset distance of 30 mm as shown in Fig. 4.6c. In the former case, the logo was clearer through the LIPSS-LIS sample than the MS-LIS one and it was also comparable with that taken through the plain surface. After positioning the substrates at a particular distance, the logo image appeared blurry through the MS-LIS sample due to light scattering by its microscale surface topography whilst its visibility was almost preserved through the LIPSS-LIS one. Therefore, only the LIPSS-LIS substrates were selected for further investigation in this research.

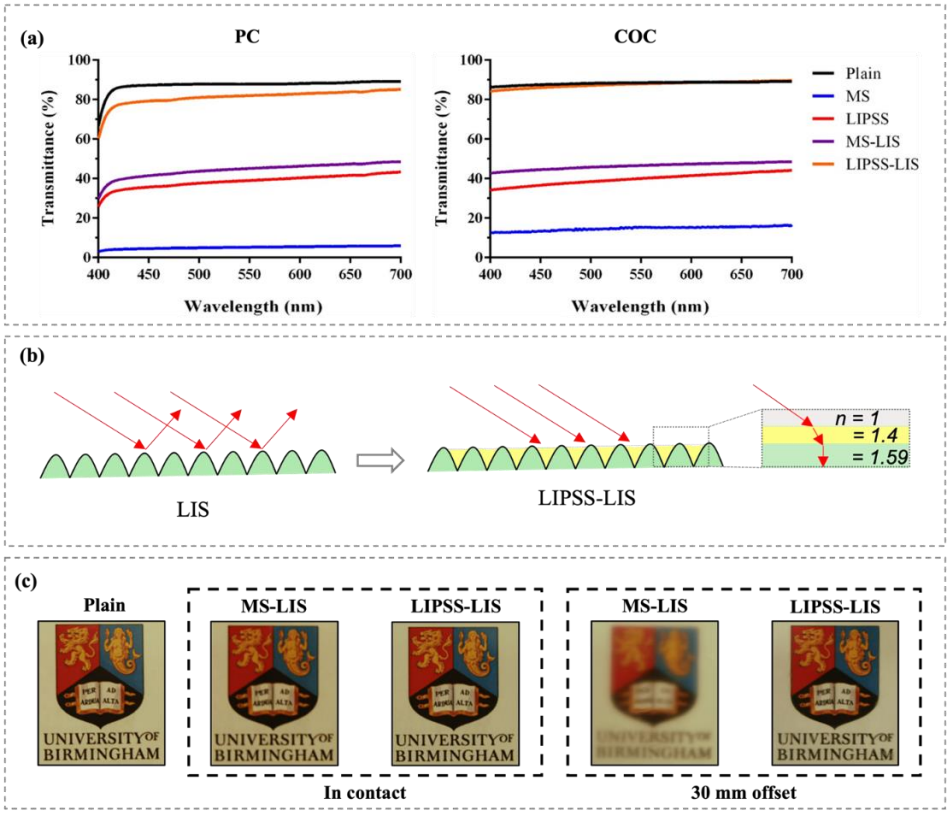

Fig. 4.6. Analysis of optical properties: (a) the transmittance of the as-received, textured and lubricated surfaces of PC and COC, respectively; (b) schematic illustrations of the improved light transmittance after the lubricant infusion; (c) the captured images of a logo through the as-received, textured and lubricated PC surfaces.

4.3.5. Anti-fouling properties

4.3.5.1. Anti-fogging and blood fouling resistance

The clarity of endoscope lenses can significantly be reduced due to fogging or blood fouling, resulting in impaired vision and consequently unnecessary disruptions during surgical procedures. Therefore, water condensation and blood adhesion experiments were performed to assess the functional response of LIPSS-LIS substrates. It should be stated that only the LIPSS-LIS samples prepared with the 100 cSt lubricant were subjected to testing because of their long-lasting slippery properties. Fig. 4.7a shows the motion of a 10 μL blood droplet both on the plain and LIPSS-LIS samples of PC when tilted at an angle of ~ 45°. The shedding behaviour of such droplet on these surfaces can also be seen in the supplementary video S1. It is apparent that the droplet slowly slid along the plain surface and seemed to have sagged, leaving behind traces of blood. In contrast, a high blood droplet mobility was observed on the LIPSS-LIS sample without leaving any stain behind, which indicates an exceptional anti-fouling response. Similar results were obtained by the respective COC surfaces, too. Thereafter, the anti-fouling performance of LIPSS-LIS samples was evaluated by performing 30 dipping cycles into blood. Fig. 4.7b shows that only a single dip was sufficient for the blood to adhere to the as-received PC and COC sheets. In contrast, the LIPSS-LIS samples of both polymer materials exhibited an excellent fouling resistance against blood since only a few microdroplets of blood were left behind on their surfaces after 30 blood dipping cycles (see Fig. 4.7b).

Some fogging usually appears on lenses when the endoscopes enter the patient's body due to the sudden change in humidity and temperature levels. Therefore, the anti-fogging properties of the LIPSS-LIS PC substrate were evaluated using the so-called hot-vapour method and they

were compared with those obtained on the plain surface. More specifically, a printed QR code was attached to the back of these samples and then they were placed vertically at a distance of roughly 50 mm above hot water (~80 °C). Snapshots of the QR code through the plain and LIPSS-LIS samples were captured with a camera every 10 s and thus to test if they can retain their initial transparency. The sequential images in Fig. 4.7c reveal that the hot vapour condensed on both surfaces and initially formed as small water droplets, exhibiting a "dropwise" condensation behaviour. However, it should be stated that the nucleation rate of water droplets was more intense on the plain surface, whilst the low surface energy lubricant infused into the LIPSS-LIS sample delayed their formation. Such findings are consistent with a recent study, which investigated the droplet condensation on low and high surface energy materials [56]. Within a period of 1 minute, the small droplets appeared to gradually grow on the plain surface via a direct condensation and merged with the neighbouring droplets to form larger ones. However, they were still not capable of shedding off the surface due to strong pinning forces. As a result, the large droplets formed on the surface scattered the transmitted light and distorted the vision through the plain sample (see the distorted image of the QR code in Fig. 4.7c). In contrast, it can be seen in Fig. 4.7c that some of the droplets condensed onto the LIPSS-LIS sample were removed due to some coalescence between them within less than 60 s, and thus the QR code could be clearly visible through the droplet-vacant regions. This shows that the low CAH of the LIPSS-LIS substrate led to high mobility of the condensed water droplets, which then promoted their fast coalescence with nearby droplets and led to droplets sweeping by gravitational force.

4.3.5.2. Protein and microalgae fouling resistance

In clinical environments, the usage of endoscopes in surgical procedure where they are in contact with blood increases the risk of thrombosis [57]. The plasma protein adsorption on

blood-contacting surfaces is the first event in the thrombus formation. Thus, the inhibition of protein adhesion to such surfaces is imperative in designing endoscopes, especially this applies to their lens surfaces. Therefore, the anti-adhesive response of LIPSS-LIS when in contact with serum albumin has been investigated in this research as it is one of the most common blood proteins. Figs. 4.7d and 4.7e show the composite fluorescent and brightfield images of albumin-fouling onto plain and LIPSS-LIS surfaces of PC and COC and their fluorescent intensity obtained, respectively. The serum albumin adhered to the plain PC and COC surfaces in a distinct dendritic pattern due to the NaCl present in the buffer after the thin film of a protein solution was evaporated, which is in accordance with the previous studies [58]. At the same time, it is apparent that the protein adhesion is greatly inhibited on LIPSS-LIS when compared to the plain ones, especially there was more than 90% reduction. So, the LIPSS-LIS treatment of endoscope lenses can decrease the risk of thrombus occurrence and thus reduces the probability of post-surgical complications in patients.

Microbial attachments to the endoscope surfaces, including lenses, during the surgical procedures can lead to endogenous infections. Therefore, there is a need to design the lens surfaces in such a way that they can inhibit the microbe's adhesion. In our previous research, it was demonstrated that LIPSS and LIPSS-LIS exhibited anti-bacterial (*E.coli*) properties on polymer materials [59]. The anti-fouling functionalities of thermoplastic LIPSS-LIS were investigated in this research under the influence of a microalgae CV. Fig. 4.7f shows the experimental setup used to investigate the CV's attachment onto LIPSS-LIS treated PC and COC substrates. As it is evident from both optical and fluorescent images in Fig. 4.7g, CV favoured the plain surfaces for settlement, while the LIPSS-LIS ones inhibited the CV's adhesion to a larger extent. The image analysis results showed that LIPSS-LIS reduced the CV's adhesion by almost 80% when compared to the plain surfaces (see Fig. 4.7h). To assess

further the durability of the LIPSS-LIS functional response, a set of substrates was initially attached to the wall of a glass container filled with water and then the shear force was applied with a magnetic stirrer for 8 hours. Such shear-induced LIPSS-LIS substrates were kept in culture baths as stated in Sub-section 4.2.7 and the fluorescent images were obtained to compare their performance with that of fresh LIPSS-LIS substrates. Impressively, even the shear-induced LIPSS-LIS have shown to reduce the CV's adhesion by half when compared to the plain surfaces (see Fig. 4.7g and h). This indicates that the strong nanoscale capillary forces of LIPSS resisted the lubricant depletion even under harsh condition and their functionality was retained for longer.

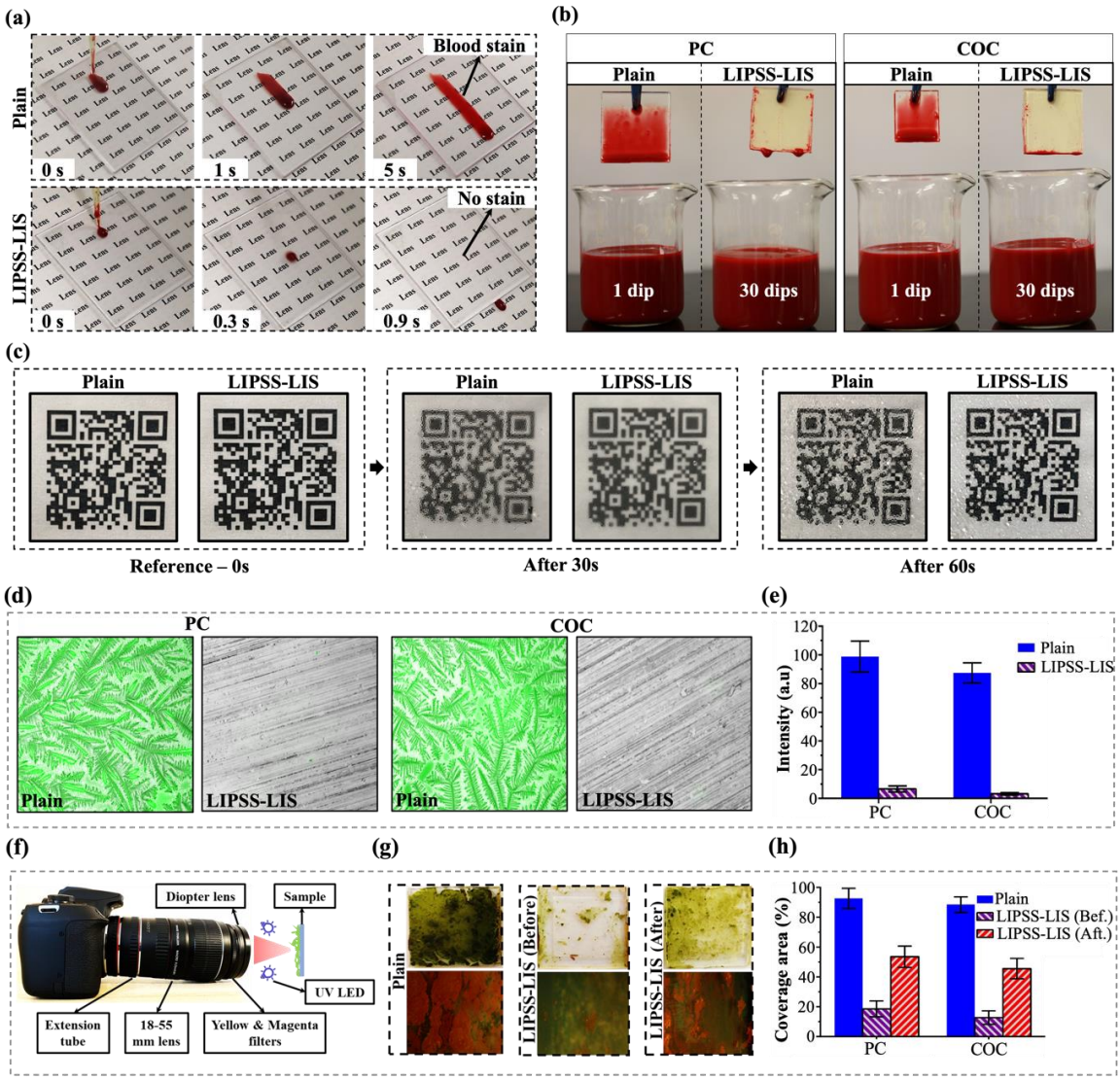

Fig. 4.7. Evaluation of anti-fouling/anti-fogging performance: (a) the shedding behaviour of 10 µL blood droplet on the PC plain and LIPSS-LIS samples; (b) the fouling resistance of PC and COC plain and LIPSS-LIS samples after the blood dipping test. It should be noted that the plain back sides of LIPSS-LIS samples were covered with a yellow coloured tape to prevent their fouling by blood; (c) the sequential images taken from the PC plain and LIPSS-LIS samples after their exposure to hot vapour; (d) fluorescence micrographs depicting the protein adsorption onto the PC and COC plain and LIPSS-LIS samples; (e) a plot showing the fluorescence intensity of adsorbed protein as measured on the PC and COC plain and LIPSS-LIS samples; (f) the experimental setup used for assessing and quantifying the adhesion of

algae onto the surfaces; (g) autofluorescence and optical images of algae adhesion onto the PC and COC plain surfaces together with their respective LIPSS-LIS samples before and after subjecting them to shear forces; (h) the area coverage with algae calculated on the samples.

4.3.6. Pilot application

As proof-of-concept, a set of LIS lenses was integrated into an inspection endoscope device as stated in Sub-section 4.2.6 and then in vitro experiments were conducted to demonstrate its performance. In particular, LIPSS-LIS treated COC lenses with 100 cSt lubricant were used in these tests as they fulfilled the criteria for slippery, durable, anti-fouling and transparent surfaces. Firstly, their vision performance was analysed by reading a QR code. As shown in Fig. 4.8a and supplementary video S2, the QR code was imaged clearly through the LIPSS-LIS lens and the time required to read it was less than 1 s, which was comparable with that achieved with the plain COC lens. In addition, the effectiveness of the LIPSS-LIS lens in maintaining a clear surgical field was investigated, too, by immersing the endoscope into blood once and then observing a printed boarding chess. From Fig. 4.8b and supplementary video S3, it is apparent that the visibility through the plain lens was immediately lost due to blood adhesion, whilst the LIPSS-LIS lens resisted blood fouling and retained its original clarity.

Finally, it was essential to test the LIPSS-LIS lens under harsh surgical conditions that might be encountered, e.g., when there are surgical complications with severe bleeding. Therefore, to validate its anti-fouling response under such conditions, the endoscope was repeatedly immersed into blood until the boarding chess could not be recognised anymore. In this regard, the visible area in percentages was measured every 5 blood dipping cycles and the average results obtained from three LIPSS-LIS lenses are plotted in Fig. 4.8c. From this plot, it is evident that the as-treated endoscope lenses did not exhibit any adhesion of blood after 30

dipping cycles (see inset in Fig. 4.8c), retaining 100% visibility. At the same time, only a small droplet of blood was formed on all the LIPSS-LIS lenses after 35 dips as shown in Fig. 4.8d, leading to an average visibility decline of 20%. These findings confirm the superior blood fouling resistance of the LIPSS-LIS lenses in severe bleeding conditions and reinforce its performance advantages in minimising vision losses in surgical endoscopic procedures. However, it should be noted that the anti-fouling performance of LIPSS-LIS lenses deteriorated dramatically afterwards, i.e., after further immersion cycles into blood as evident by the sequential images in Fig. 4.8d. For instance, a partial loss of visibility, i.e. an average vision loss of 46%, was observed after 40 dips. This was mostly due to the adherence of a bigger blood droplet onto lens surfaces (see inset in Fig. 4.8c) and the visual field was less than 15% after 45 dips. At the end, the vision through the integrated camera was totally lost after 50 consecutive dipping cycles in blood (see Fig. 4.8d) and they did not have any blood anti-fouling properties anymore (see the inset in Fig. 4.8c).

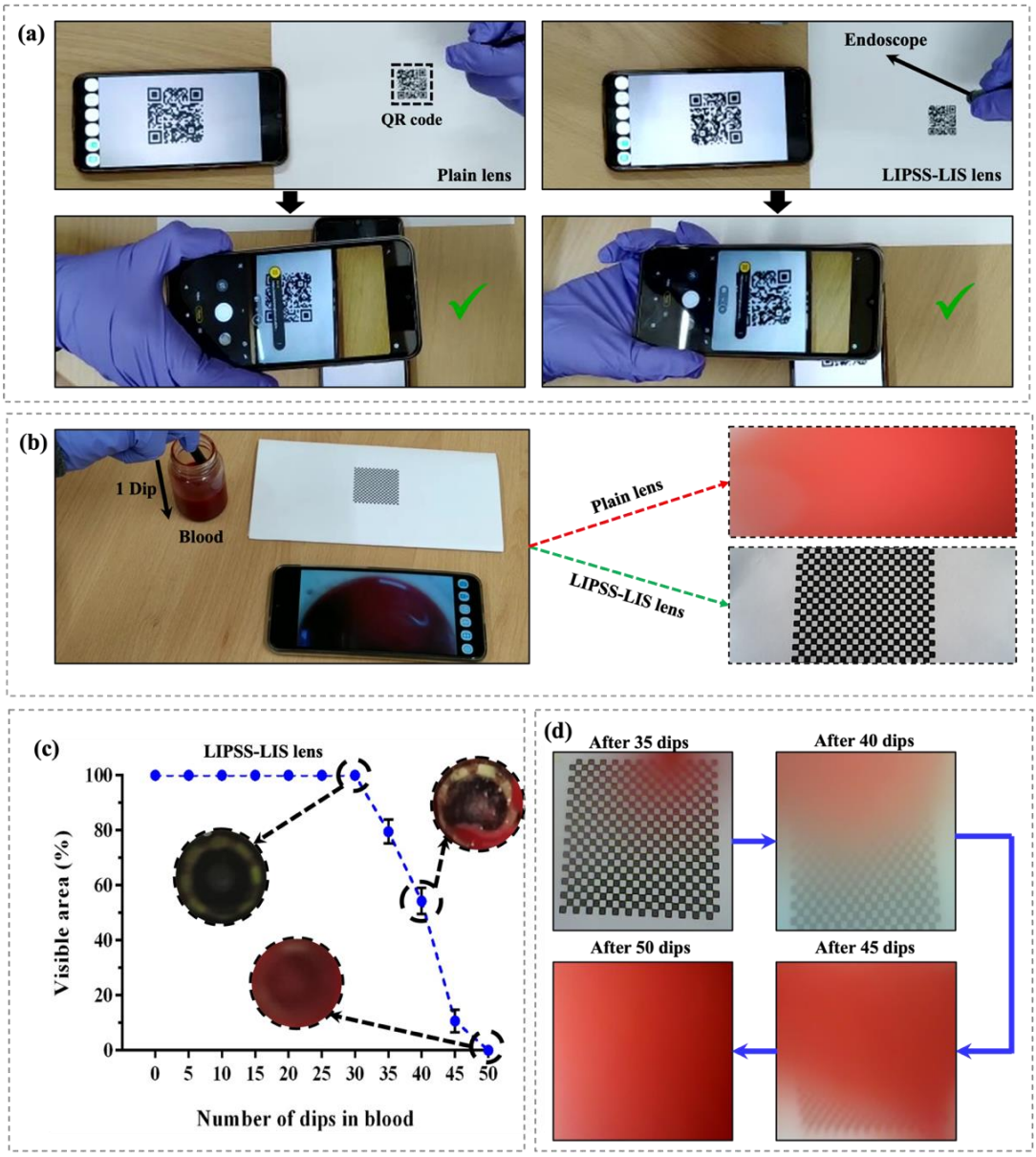

Fig. 4.8. A pilot application of the LIPSS-LIS treated endoscope lenses: (a) the test procedure used to verify the vision performance after integrating the plain (left) and LIPSS-LIS (right) treated COC lenses into an endoscope device; (b) the blood dipping experimental setup and the visual fields retained by the plain and LIPSS-LIS treated COC lenses after a single dip; (c) the visible area in percentages of an endoscope with LIPSS-LIS lenses as a function of the dipping cycles number. *Note:* Insets in (c) depict the surface of LIPSS-LIS lens after a certain number of dips; (d) sequential images showing the field of view after 35, 40, 45 and 50 dips, again for the LIPSS-LIS lens.

4.4. Conclusions

Surface contamination and fouling of endoscope lenses by body fluids is a critical issue in surgical procedures and therefore a cost-effective method for “imprinting” an anti-fouling functionality on them is proposed in this research. This is achieved by combining the strong capillary forces of LIPSS with the advantage of LIS in achieving long lasting anti-fouling properties without transparency losses. To fabricate lenses with such LIPSS-LIS treatments serially on thermoplastics, a process chain is proposed that combines synergistically the capabilities of a laser-based surface texturing of metallic masters with polymer micro/nano replication followed by lubricant infiltration onto the nanoscale surface ripples. Although, a femtosecond laser was used to “imprint” LIPSS onto the masters, such topographies could be realised by less expensive pico and nanosecond laser sources, which can further reduce the manufacturing cost. At the same time, micro injection moulding technologies could be utilized instead of the lab-scale hot embossing to scale-up the production of such LIPSS-LIS treated thermoplastic lenses, as demonstrated in our previous research [60].

Since the glass transition temperatures of PC and COC are less than the autoclave temperatures, such LIPSS-LIS thermoplastic lenses could be re-used by employing standard sterilisation procedures. Furthermore, it is worth noting that the LIPSS-LIS thermoplastic lenses produced with the proposed process chain are fully recyclable as no coatings are required to impart the anti-fouling functionalities. A simple washing step can remove the lubricant from the lenses for downstream recycling after their disposal. Furthermore, the functionality and durability of the proposed LIPSS-LIS treatments can be further improved by taking advantage of the LIPSS tunability. For example, instead of one-dimensional LIPSS employed in this research, two-dimensional triangular LIPSS [61] can offer isotropic surface

properties that can impart both the lubricant depletion of LIS and also their functional response.

Supporting Information

- Experimental video showing: a 10 μL blood droplet sliding on the PC plain and LIPSS-LIS samples (Video S1); the visibility through an endoscope with COC plain and LIPSS-LIS lenses (Video S2); the blood fouling resistance of an endoscope integrated with LIPSS-LIS lenses (Video S3).

The above Supporting Information can be accessed via the following link: https://pubs.acs.org/doi/10.1021/acs.langmuir.2c01671

Acknowledgements

The authors would like to acknowledge the financial support offered under the ERDF "Smart Factory Hub" (SmartFub) project. Also, the authors would like to thank the Manufacturing Technology Centre (MTC) for the financial support of Themistoklis Karkantonis's Ph.D. research.

References

[1] V. Palvia, A. Gonzalez, R. Vigh, and J. Anasti, "A randomized controlled trial comparing laparoscopic lens defogging techniques through simulation model," *Gynecology and Minimally Invasive Therapy,* vol. 7, no. 4, pp. 156-160, 2018.

[2] G. S. Quah, G. D. Eslick, and M. R. Cox, "Laparoscopic appendicectomy is superior to open surgery for complicated appendicitis," *Surgical Endoscopy,* vol. 33, no. 7, pp. 2072-2082, 2019.

[3] H. Tatsuki *et al.*, "A novel one-step lens cleaning device using air and water flow for endoscopic surgery," *PLOS ONE,* vol. 13, no. 7, p. e0200749, 2018.

[4] T. G. Manning *et al.*, "Laparoscopic lens fogging: solving a common surgical problem in standard and robotic laparoscopes via a scientific model," *Surgical Endoscopy,* vol. 32, no. 3, pp. 1600-1606, 2018.

[5] H. Okuda, J. Okamoto, Y. Takumi, S. Kakehata, and Y. Muragaki, "The iArmS Robotic Armrest Prolongs Endoscope Lens–Wiping Intervals in Endoscopic Sinus Surgery," *Surgical Innovation,* vol. 27, no. 5, pp. 515-522, 2020.

[6] D. Kreeft, E. A. Arkenbout, P. W. J. Henselmans, W. R. van Furth, and P. Breedveld, "Review of Techniques to Achieve Optical Surface Cleanliness and Their Potential Application to Surgical Endoscopes," *Surgical Innovation,* vol. 24, no. 5, pp. 509-527, 2017.

[7] M. A. Cassera, T. A. Goers, G. O. Spaun, and L. L. Swanström, "Efficacy of Using a Novel Endoscopic Lens Cleaning Device: A Prospective Randomized Controlled Trial," *Surgical Innovation,* vol. 18, no. 2, pp. 150-155, 2011.

[8] K. Harawaza, B. Cousins, P. Roach, and A. Fernandez, "Modification of the surface nanotopography of implant devices: A translational perspective," *Materials Today Bio,* vol. 12, p. 100152, 2021.

[9] S. Zhang, Y. Zhou, H. Zhang, Z. Xiong, and S. To, "Advances in ultra-precision machining of micro-structured functional surfaces and their typical applications," *International Journal of Machine Tools and Manufacture,* vol. 142, pp. 16-41, 2019.

[10] H. Guo *et al.,* "A multifunctional anti-fog, antibacterial, and self-cleaning surface coating based on poly(NVP-co-MA)," *Chemical Engineering Journal,* vol. 351, pp. 409-417, 2018.

[11] A. S. Topçu Kaya and U. Cengiz, "Fabrication and application of superhydrophilic antifog surface by sol-gel method," *Progress in Organic Coatings,* vol. 126, pp. 75-82, 2019.

[12] S. Bai, X. Li, Y. Zhao, L. Ren, and X. Yuan, "Antifogging/Antibacterial Coatings Constructed by N-Hydroxyethylacrylamide and Quaternary Ammonium-Containing Copolymers," *ACS Applied Materials & Interfaces,* vol. 12, no. 10, pp. 12305-12316, 2020.

[13] F. Geyer *et al.,* "When and how self-cleaning of superhydrophobic surfaces works," *Science Advances,* vol. 6, no. 3, p. eaaw9727, 2020.

[14] A. Gaddam, H. Sharma, T. Karkantonis, and S. Dimov, "Anti-icing properties of femtosecond laser-induced nano and multiscale topographies," *Applied Surface Science,* vol. 552, p. 149443, 2021.

[15] T. Kim, S. Kwon, J. Lee, J. S. Lee, and S. Kang, "A metallic anti-biofouling surface with a hierarchical topography containing nanostructures on curved micro-riblets," *Microsystems & Nanoengineering,* vol. 8, no. 1, p. 6, 2022.

[16] H. Sharma, K. John, A. Gaddam, A. Navalkar, S. K. Maji, and A. Agrawal, "A magnet-actuated biomimetic device for isolating biological entities in microwells," *Scientific Reports,* vol. 8, no. 1, p. 12717, 2018.

[17] S. A. Jalil *et al.*, "Creating superhydrophobic and antibacterial surfaces on gold by femtosecond laser pulses," *Applied Surface Science,* vol. 506, p. 144952, 2020.

[18] K. Ellinas, P. Dimitrakellis, P. Sarkiris, and E. Gogolides, "A Review of Fabrication Methods, Properties and Applications of Superhydrophobic Metals," *Processes,* vol. 9, no. 4, p. 666, 2021.

[19] N. Celik, F. Sahin, M. Ruzi, M. Yay, E. Unal, and M. S. Onses, "Blood repellent superhydrophobic surfaces constructed from nanoparticle-free and biocompatible materials," *Colloids and Surfaces B: Biointerfaces,* vol. 205, p. 111864, 2021.

[20] Z. Li, B. L. Nguyen, Y. C. Cheng, J. Xue, G. MacLaren, and C. H. Yap, "Durable, flexible, superhydrophobic and blood-repelling surfaces for use in medical blood pumps," *Journal of Materials Chemistry B,* vol. 6, no. 39, pp. 6225-6233, 2018.

[21] M. Eriksson *et al.*, "Wetting Transition on Liquid-Repellent Surfaces Probed by Surface Force Measurements and Confocal Imaging," *Langmuir,* vol. 35, no. 41, pp. 13275-13285, 2019.

[22] A. Gaddam, A. Agrawal, S. S. Joshi, and M. C. Thompson, "Utilization of Cavity Vortex To Delay the Wetting Transition in One-Dimensional Structured Microchannels," *Langmuir,* vol. 31, no. 49, pp. 13373-13384, 2015.

[23] Y. Lin *et al.*, "Durable and robust transparent superhydrophobic glass surfaces fabricated by a femtosecond laser with exceptional water repellency and thermostability," *Journal of Materials Chemistry A,* vol. 6, no. 19, pp. 9049-9056, 2018.

[24] C. Kunz, F. A. Müller, and S. Gräf, "Multifunctional Hierarchical Surface Structures by Femtosecond Laser Processing," *Materials,* vol. 11, no. 5, p. 789, 2018.

[25] L. Rapoport, B. R. Solomon, and K. K. Varanasi, "Mobility of Yield Stress Fluids on Lubricant-Impregnated Surfaces," *ACS Applied Materials & Interfaces,* vol. 11, no. 17, pp. 16123-16129, 2019.

[26] T.-S. Wong *et al.*, "Bioinspired self-repairing slippery surfaces with pressure-stable omniphobicity," *Nature,* vol. 477, no. 7365, pp. 443-447, 2011.

[27] M. Badv, S. M. Imani, J. I. Weitz, and T. F. Didar, "Lubricant-Infused Surfaces with Built-In Functional Biomolecules Exhibit Simultaneous Repellency and Tunable Cell Adhesion," *ACS Nano,* vol. 12, no. 11, pp. 10890-10902, 2018.

[28] S. Yuan, S. Luan, S. Yan, H. Shi, and J. Yin, "Facile Fabrication of Lubricant-Infused Wrinkling Surface for Preventing Thrombus Formation and Infection," *ACS Applied Materials & Interfaces,* vol. 7, no. 34, pp. 19466-19473, 2015.

[29] H. Sharma, A. Gaddam, A. Agrawal, and S. S. Joshi, "Slip flow through microchannels with lubricant-infused bi-dimensional textured surfaces," *Microfluidics and Nanofluidics,* vol. 23, no. 2, p. 28, 2019.

[30] A. B. Gurav, H. Shi, M. Duan, X. Pang, and X. Li, "Highly transparent, hot water and scratch resistant, lubricant-infused slippery surfaces developed from a mechanically-weak superhydrophobic coating," *Chemical Engineering Journal,* vol. 416, p. 127809, 2021.

[31] M. Zhang *et al.*, "Ultra-transparent slippery surface," *Smart Materials in Medicine,* vol. 2, pp. 38-45, 2021.

[32] M. Zhang, Q. Liu, J. Liu, J. Yu, and J. Wang, "Self-healing liquid-infused surfaces with high transparency for optical devices," *MRS Communications,* vol. 9, no. 1, pp. 92-98, 2019.

[33] P. Zhang, H. Chen, L. Zhang, T. Ran, and D. Zhang, "Transparent self-cleaning lubricant-infused surfaces made with large-area breath figure patterns," *Applied Surface Science,* vol. 355, pp. 1083-1090, 2015.

[34] K. Manabe, K.-H. Kyung, and S. Shiratori, "Biocompatible Slippery Fluid-Infused Films Composed of Chitosan and Alginate via Layer-by-Layer Self-Assembly and Their Antithrombogenicity," *ACS Applied Materials & Interfaces,* vol. 7, no. 8, pp. 4763-4771, 2015.

[35] M. Liu, Y. Hou, J. Li, L. Tie, and Z. Guo, "Transparent slippery liquid-infused nanoparticulate coatings," *Chemical Engineering Journal,* vol. 337, pp. 462-470, 2018.

[36] S. Nishioka *et al.*, "Facile design of plant-oil-infused fine surface asperity for transparent blood-repelling endoscope lens," *RSC Advances,* vol. 6, no. 53, pp. 47579-47587, 2016.

[37] S. Sunny *et al.*, "Transparent antifouling material for improved operative field visibility in endoscopy," *Proceedings of the National Academy of Sciences,* vol. 113, no. 42, p. 11676, 2016.

[38] M. Tenjimbayashi *et al.,* "In Situ Formation of Slippery-Liquid-Infused Nanofibrous Surface for a Transparent Antifouling Endoscope Lens," *ACS Biomaterials Science & Engineering,* vol. 4, no. 5, pp. 1871-1879, 2018.

[39] Y. Lee *et al.*, "Lubricant-infused directly engraved nano-microstructures for mechanically durable endoscope lens with anti-biofouling and anti-fogging properties," *Scientific Reports,* vol. 10, no. 1, p. 17454, 2020.

[40] E. M. Sunderland, X. C. Hu, C. Dassuncao, A. K. Tokranov, C. C. Wagner, and J. G. Allen, "A review of the pathways of human exposure to poly- and perfluoroalkyl substances (PFASs) and present understanding of health effects," *Journal of Exposure Science & Environmental Epidemiology,* vol. 29, no. 2, pp. 131-147, 2019.

[41] J. Han *et al.*, "Chemical Aspects of Human and Environmental Overload with Fluorine," *Chemical Reviews,* vol. 121, no. 8, pp. 4678-4742, 2021.

[42] T. Karkantonis, A. Gaddam, T. L. See, S. S. Joshi, and S. Dimov, "Femtosecond laser-induced sub-micron and multi-scale topographies for durable lubricant impregnated surfaces for food packaging applications," *Surface and Coatings Technology,* vol. 399, p. 126166, 2020.

[43] E. Ozkan *et al.*, "Bioinspired ultra-low fouling coatings on medical devices to prevent device-associated infections and thrombosis," *Journal of Colloid and Interface Science,* vol. 608, pp. 1015-1024, 2022.

[44] EFSA Panel on Food Additives and Flavourings (FAF) *et al.*, "Re-evaluation of dimethyl polysiloxane (E 900) as a food additive," *EFSA Journal,* vol. 18, no. 5, p. e06107, 2020.

[45] A. Gaddam, H. Sharma, R. Ahuja, S. Dimov, S. Joshi, and A. Agrawal, "Hydrodynamic drag reduction of shear-thinning liquids in superhydrophobic textured microchannels," *Microfluidics and Nanofluidics,* vol. 25, no. 9, p. 73, 2021.

[46] P. Baumli *et al.*, "The challenge of lubricant-replenishment on lubricant-impregnated surfaces," *Advances in Colloid and Interface Science,* vol. 287, p. 102329, 2021.

[47] P. Sartori *et al.*, "Motion of Newtonian drops deposited on liquid-impregnated surfaces induced by vertical vibrations," *Journal of Fluid Mechanics,* vol. 876, p. R4, 2019.

[48] A. Keiser, L. Keiser, C. Clanet, and D. Quéré, "Drop friction on liquid-infused materials," *Soft Matter*, vol. 13, no. 39, pp. 6981-6987, 2017.

[49] S. Adera, J. Alvarenga, A. V. Shneidman, C. T. Zhang, A. Davitt, and J. Aizenberg, "Depletion of Lubricant from Nanostructured Oil-Infused Surfaces by Pendant Condensate Droplets," *ACS Nano*, vol. 14, no. 7, pp. 8024-8035, 2020.

[50] W. S. Y. Wong, K. I. Hegner, V. Donadei, L. Hauer, A. Naga, and D. Vollmer, "Capillary Balancing: Designing Frost-Resistant Lubricant-Infused Surfaces," *Nano Letters*, vol. 20, no. 12, pp. 8508-8515, 2020.

[51] C. Zhang, S. Adera, J. Aizenberg, and Z. Chen, "Why Are Water Droplets Highly Mobile on Nanostructured Oil-Impregnated Surfaces?," *ACS Applied Materials & Interfaces*, vol. 13, no. 13, pp. 15901-15909, 2021.

[52] I. Jacobi, J. S. Wexler, and H. A. Stone, "Overflow cascades in liquid-infused substrates," *Physics of Fluids*, vol. 27, no. 8, p. 082101, 2015.

[53] M. Zhang *et al.*, "Highly transparent and robust slippery lubricant-infused porous surfaces with anti-icing and anti-fouling performances," *Journal of Alloys and Compounds*, vol. 803, pp. 51-60, 2019.

[54] S. Ahmad, H. Sharma, A. Agrawal, and S. S. Joshi, "Light Harvesting Using Biomimetic Micro-textured Transparent Films for Photovoltaic Applications," *Transactions of the Indian National Academy of Engineering*, vol. 6, no. 3, pp. 775-785, 2021.

[55] Z. Wang and Z. Guo, "Biomimetic self-slippery and transferable transparent lubricant-infused functional surfaces," *Nanoscale*, vol. 10, no. 42, pp. 19879-19889, 2018.

[56] H. Cha *et al.*, "Dropwise condensation on solid hydrophilic surfaces," *Science Advances*, vol. 6, no. 2, p. eaax0746, 2020.

[57] S. V. Venkatachalapathy, G. Evans, and A. F. Muller, "Endoscopy and the Risk of Venous Thromboembolism: A Case-Control Study," *Endosc Int Open,* vol. 2, no. 01, pp. E2-E5, 2014.

[58] K. Shiba, T. Honma, T. Minamisawa, K. Nishiguchi, and T. Noda, "Distinct macroscopic structures developed from solutions of chemical compounds and periodic proteins," *EMBO reports,* vol. 4, no. 2, pp. 148-153, 2003.

[59] R. Y. Siddiquie, A. Gaddam, A. Agrawal, S. S. Dimov, and S. S. Joshi, "Anti-Biofouling Properties of Femtosecond Laser-Induced Submicron Topographies on Elastomeric Surfaces," *Langmuir,* vol. 36, no. 19, pp. 5349-5358, 2020.

[60] F. Baruffi *et al.*, "Correlating nano-scale surface replication accuracy and cavity temperature in micro-injection moulding using in-line process control and high-speed thermal imaging," *Journal of Manufacturing Processes,* vol. 47, pp. 367-381, 2019.

[61] J.-M. Romano, A. Garcia-Giron, P. Penchev, and S. Dimov, "Triangular laser-induced submicron textures for functionalising stainless steel surfaces," *Applied Surface Science,* vol. 440, pp. 162-169, 2018.

CHAPTER 5: THE INFLUENCE OF PROCESSING ENVIRONMENT ON LASER-INDUCED PERIODIC SURFACE STRUCTURES GENERATED WITH GREEN NANOSECOND LASER

The research reported in this chapter was published online as a full-length article in the journal of "Surfaces and Interfaces" (2022):

T. Karkantonis[1a], A. Gaddam[1a], X. Tao[1b], T. L. See[2], and S. Dimov[1], "The influence of processing environment on laser-induced periodic surface structures generated with green nanosecond laser," *Surfaces and Interfaces*, vol. 31, p. 102096, 2022.

[1a]*Department of Mechanical Engineering, School of Engineering, The University of Birmingham, Birmingham, B15 2TT, UK*

[1b]*School of Metallurgy and Materials research, The University of Birmingham, Birmingham, B15 2TT, UK*

[2]*The Manufacturing Technology Centre Ltd, Coventry, CV7 9JU, UK*

Authors' contribution:

T. Karkantonis: Main author, conceived the methodology, conducted the laser processing experiments and characterisations, performed the analysis and written the original draft. **A. Gaddam:** Assisted with laser setup and sample preparation. **X. Tao:** Assisted with the acquisition of SEM micrographs. **T. L. See:** Supervision and proofreading. **S. Dimov:** Supervision and proofreading.

Abstract

Laser-Induced Periodic Surface Structures (LIPSS) are nanometric surface undulations produced by short and ultrashort pulsed lasers. The production of high-quality LIPSS is essential to obtain the required surface responses in various applications. In this work, the LIPSS were fabricated on stainless steel surfaces by a 515 nm nanosecond laser operating under ambient and argon enriched atmospheres to investigate their quality. The LIPSS quality is correlated to the diffracted light intensity and their key geometric parameters such as periodicity and amplitude. The LIPSS formation was observed at an accumulated fluence of above 13.9 J/cm^2 and the optimal processing window was sustained up to 46.2 J/cm^2 before the oxidation occurred. The LIPSS generated in the argon environment exhibited a relatively higher intensity of the diffracted light than those processed in the ambient conditions. Furthermore, LIPSS generated in argon showed minimum surface defects and higher amplitude ripples compared to those in air. The X-ray photoelectron spectroscopy analysis revealed that the ratio of oxygen to metal species decreased in the argon atmosphere and thus minimal surface oxidation occurred on the samples. Since the generation of high-quality LIPSS is a prerequisite for an accurate predictive modeling of surface responses, the results reported here show that good nanostructured surfaces can be produced with cost-effective nanosecond green lasers.

Keywords: Argon, fluence, LIPSS, nanosecond, oxidation, XPS.

5.1. Introduction

Surface functionalization technologies have received significant attention from industry and research as an important enabler for imparting attractive surface functionalities to products without changing their bulk material properties. In particular, various surface treatment methods, such as coatings, photolithography, chemical etching, sol-gel, ultra-precision machining and laser micro-machining, have been deployed to tailor the functional properties of surfaces by modifying their topography and/or surface microstructure and composition [1-2]. Compared to the other technologies, laser surface texturing (LST) can be considered as a more environmentally friendly process that offers selectivity, relatively high processing accuracy, productivity and even the flexibility of processing freeform surfaces [3]. At the same time, it can be employed as a simple one-step surface treatment to selectively fabricate micron and submicron structures on almost any engineering material without requiring any hazardous chemicals. In addition, LST alters simultaneously the surface chemistry together with the topography, thus, eliminating the need for fluorinated coatings [4].

Laser-Induced Periodic Surface Structures (LIPSS) are periodical ripple-like nanostructures that can be imprinted on a variety of materials by employing linearly or azimuthally polarized laser sources [5]. These surface structures can be clustered into Low Spatial Frequency LIPSS (LSFL) and High Spatial Frequency LIPSS (HSFL) with periodicities close to and much smaller than the laser wavelength, respectively. Among them, only LSFL, referred to as LIPSS in this research, can be obtained both with ultra-short (femtosecond and picosecond) [6] and short (nanosecond) [7] pulse durations and have attracted attention from researchers. Owing to their wide applicability and varying geometrical characteristics, these ripple-like structures have been extensively investigated as a means for functional surface treatments. More specifically, surfaces textured with such nanoscale ripples have displayed anti-bacterial [8-9],

anti-icing [10], anti-reflective [11], hydrodynamic drag reduction [12], lubricant-retention [13], secondary electron yield reduction [14] and improved cell-adhesion [15-16] properties in applications related to food packaging, biomedical and energy storage sectors.

Predictive analytical and computational modeling offers the possibility to tailor the surface responses by varying the periodic nanometric geometries in the aforesaid functional applications. For instance, recent efforts employing the computational modeling have shed light on the interaction mechanisms of periodic nanometric surface structures with matter to obtain optimal surface responses in applications related to anti-biofouling [17], hydrodynamic drag reduction [18], anti-reflection [19] and condensation [20]. However, it is imperative to imprint LIPSS homogeneously with sufficient repeatability and reproducibility, and only then the predictive results can be sufficiently accurate within some pre-define limits. To date, most studies have been focused on the use of ultra-short pulse lasers to attain homogeneous LIPSS onto plain and freeform surfaces while maintaining their geometric characteristics within pre-defined ranges [21-22]. Although high precision, controllability and minimum Heat-Affected Zone (HAZ) can be achieved by employing ultrashort lasers, their average power is relatively low and consequently this entails longer processing times. While the usage of multi-beam processing [23] and high repetition rate (MHz or GHz) [24] can reduce the processing time, they increase substantially the required capital investment. As a result of these inherent shortcomings, the broader use of LIPSS treatments in industrial applications is hampered. On the contrary, nanosecond lasers are a cost-effective alternative to treat large surface areas without requiring substantial investments.

One of the main concerns when employing lasers with longer pulse durations for texturing/structuring metallic surfaces is that this is thermal processing with the associated heat-induced negative side effects, i.e., oxidation and re-cast formations on the surface.

Nevertheless, it has been shown that the level of laser-induced oxidation can be minimized upon irradiation in a controlled environment when nanosecond lasers are used for polishing operations [25-26]. In general, the use of nanosecond lasers on metals has been mostly limited to the creation of superhydrophobic surfaces by taking advantage of their negative side effects, i.e., by roughening the surface [27] or the fabrication of LIPSS when operating at near-infrared wavelengths [28]. Although the importance of this technology for functionalizing surfaces at an industrial level is recognized through these studies, only a few publications were focused on investigating the generation of LIPSS on metallic substrates using visible wavelengths (400-700 nm) [29-30]. However, some investigations are reported on processing semiconductors [31], polymers [32] and glasses [33-34] using green (500-550 nm) nanosecond pulsed lasers. By operating in the green wavelength regime, nanostructures with a periodicity close to 500 nm can be formed on surfaces.

Nürnberger et al. [29] elucidated the effect of material crystal orientation on the formation of LIPSS when a 532 nm wavelength nanosecond laser was used to process stainless steel and silicon. Simões et al. [30] applied a green nanosecond pulsed laser to investigate the evolution of LIPSS on stainless steel surfaces by employing different process parameters and proposed an approach based on the diffracted light to assess the quality of the LIPSS. However, investigations onto the improvements of the quality and homogeneity of LIPSS have not been reported. In addition, the surface chemical changes of metallic surfaces processed with green nanosecond lasers have not been studied earlier. Therefore, this research reports an investigation into the formation, evolution, and properties of LIPSS generated with a green nanosecond pulsed laser on stainless steel substrates under ambient and argon enriched conditions to assess their impact on LIPSS quality. In particular, this research elucidates the influence of processing environment on LIPSS geometrical characteristics, i.e., amplitude and

periodicity, and surface chemistry, and subsequently their combined influence on wetting properties. Moreover, the effects of the nanoscale surface topography are analyzed with light diffraction to qualitatively assess their homogeneity.

5.2. Materials and methods

5.2.1. Experimental setup and process parameters

The AISI 316 Stainless Steel (SS) rectangular plates with a 0.5 mm thickness and an average roughness (S_a) of 35 nm were used in the LST experiments. In this work, the as-received substrates were laser textured immediately after removing the plastic tape from surfaces without any pretreatment. The experiments were conducted on the state-of-the-art LASEA LS4 laser micro-machining workstation and its main beam delivery component technologies are shown in Fig. 5.1a. The platform integrates a s-polarized nanosecond fiber laser source (GLPN -500-1.5-50-M, IPG) with the following main technical characteristics: a pulse duration of 1.5 ns at a nominal wavelength, λ, of 515 nm and pulse repetition rate up to 1 MHz with a maximum average power of 50 W. A scan head (LS-Scan XY 20) is used to steer the laser beam across the samples at a maximum scanning speed of 2 m/s. A telecentric lens with 100 mm focal distance was utilized to focus the laser beam down to a spot size ($2w_0$) of 40 μm at the focal plane. Thereafter, the accurate positioning of the samples inside the machine's working envelope and specifically at the focal plane was performed using a stack of two rotary and three linear motorized stages in combination with a high-resolution positioning camera (Dino-Lite Premier, AM7013MT).

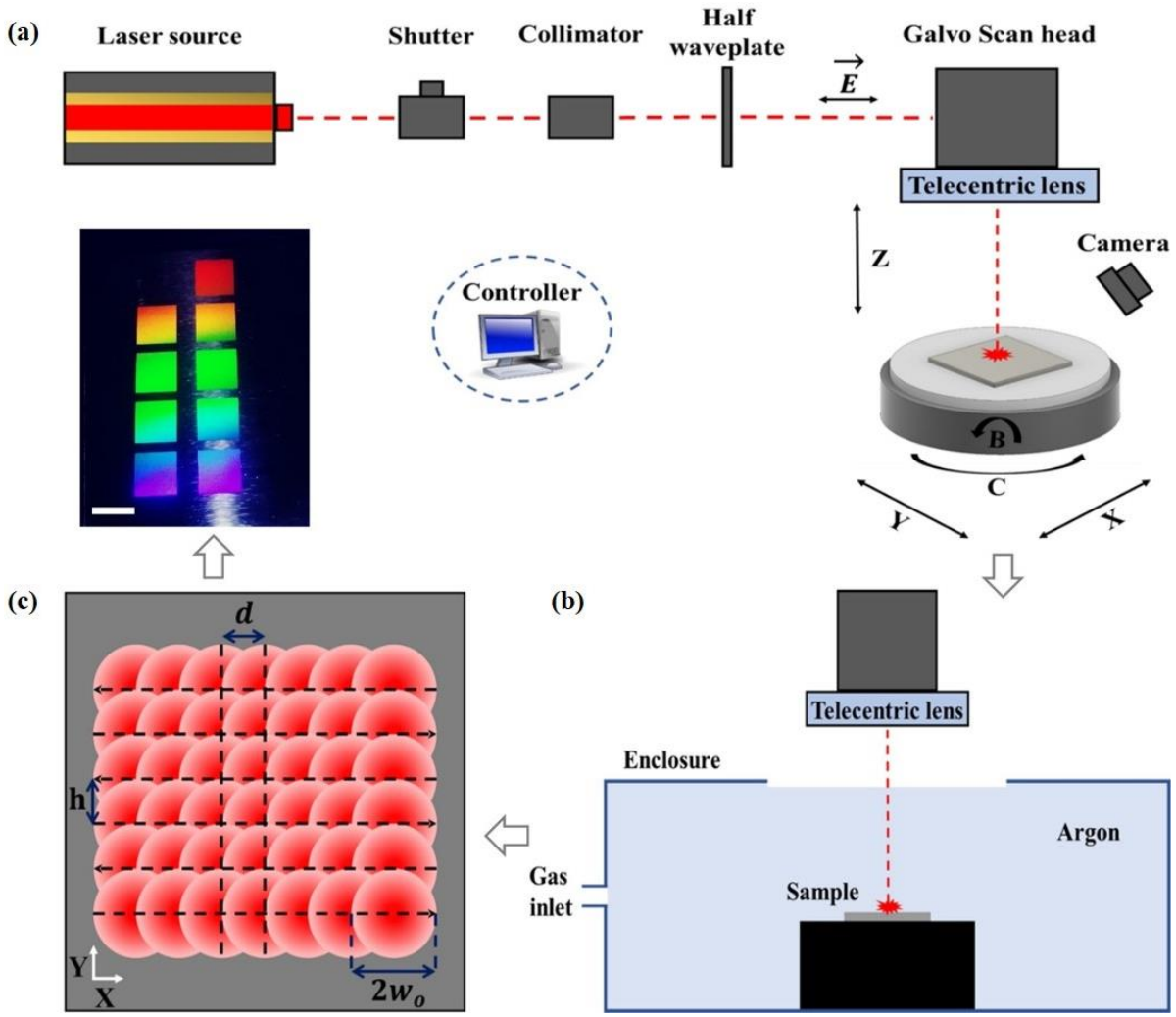

Fig. 5.1. Schematic illustration of: (a) laser processing set-up; (b) the process used to texture the samples in argon environment; (c) the scanning strategy used to generate LIPSS. The optical image shows diffraction colors resulted from generated LIPSS (scale bar: 10 mm).

To study the generation and evolution of LIPSS on surfaces, the influence of three critical laser processing parameters was investigated, i.e. (i) average power (ii) scanning speed and (iii) hatch distance. The SS substrates were textured by using a horizontal raster scanning strategy as illustrated in Fig. 5.1c. The distance between successive scanning lines is defined as a hatch one (h), which was varied in the range from 1 to 3 μm. The laser texturing was carried out at various scanning speeds (v) from 0.3 to 2 m/s and average power (P) between 0.189 and 0.671

W. All the experimental trials were conducted at a fixed pulse repetition rate (f) of 100 kHz. As the laser beam was scanned across the surface area, the pulse-to-pulse distance ($d = v/f$) varies and consequently the effective number of pulses (N_{eff}) or number of pulses per unit area on the surface can be determined from Eq. 5.1.

$$N_{eff} = \frac{\pi w_0^2}{dh} \tag{5.1}$$

Similarly, the substrates were subjected to different pulse fluence (F_0) by varying the average power, and this is calculated with Equation 5.2.

$$F_0 = \frac{P}{\pi w_0^2 f} \tag{5.2}$$

The combined influence of these two parameters increases the accumulated fluence per unit area (F_{acc}) on the surface, which can be calculated using Equation 5.3.

$$F_{acc} = N_{eff} F_0 = \frac{P}{fdh} \tag{5.3}$$

Initially, the laser processing was restricted over an area of 5 × 5 mm^2 on the SS substrates in order to assess the formation of LIPSS on the surface. Thereafter, larger areas of 25 × 25 mm^2 were textured for investigating their functional response. The experiments were conducted under atmospheric and argon gas environments to investigate their impact on both surface morphology and chemical state after undergoing LIPSS treatments. The laser texturing of samples in a controlled argon gas environment was conducted inside a hollow cylindrical aluminium chamber as illustrated in Fig. 5.1b. As argon is heavier compared to air, the SS samples were placed at the bottom of the chamber while the gas filled the enclosed area at a constant flow rate of 12 L/min.

5.2.2. Surface characterisation techniques

The surface topographies of the textured SS substrates were initially characterized using a Scanning Electron Microscope (SEM, Hitachi TEM3030Plus). To capture the first-order diffracted light ($m = 1$) out of the treated surfaces, an optical microscope (Alicona G5) was employed by holding a collimated white light beam (70 Lumens) at an incident angle (θ) of 60° relative to the sample surface. Both, the light source and its incident angle were kept constant in regard to the treated surface during the measurements and an open-source image analysis software (ImageJ) was used to obtain the mean intensity (I) of diffracted light. The morphology of the nanoscale topographies was captured by using Atomic Force Microscopy (AFM, MFP-3D, Asylum Research, USA) together with 2D Fast Fourier Transformation (FFT) analysis to evaluate their spatial periods. The acquired AFM and SEM scan images were analyzed using an open-source image analysis software (Gwyddion).

To inspect the surface chemistry of the substrates produced under air and argon gas environments, the X-ray Photon Spectroscopy (XPS) was conducted by using a Kratos Axis SUPRA spectrometer. These experiments were performed using a monochromatic Al kα (1486.69 eV) X-ray source over an analysis area of 700 × 300 μm^2, operating at 15 mA emission and 15 kV HT (225W). The instrument was calibrated to gold metal Au 4f (83.95 eV) and dispersion adjusted give a binding energy of 932.6 eV for the Cu2p (3/2) line of metallic copper. The instrumental resolution was determined to be 0.29 eV at 10 eV pass energy using the Fermi edge of the valence band for metallic silver. The survey scans in the range of 0 to 1200 eV binding energy were recorded at pass energies of 160 eV, whilst the high-resolution ones were obtained at pass energies of 40 eV. The step sizes were 1 and 0.1 eV, respectively. Charge neutralization was not required due to high sample conductivity. All data was recorded at a base pressure of below 9×10^{-9} Torr and a room temperature of 294 K.

The curve fitting was implemented in CasaXPS v2.3.19PR1.0 using a Shirley background prior to component analysis. O1s components were fit using a lineshape of GL(30).

The wetting properties of the treated surfaces were assessed with a goniometer (OCA 15EC, Data Physics GmbH, Germany). Specifically, water droplets of 4 μL were deposited on the surface and the corresponding static contact angle values were recorded. It is worth noting that the same measurement procedure was repeated five times at different locations on the samples' surfaces to assess the repeatability of the measurements.

5.3. Results and discussion

5.3.1. LIPSS evolution and quality in ambient environment

The first part of this research was focused on investigating the LIPSS evolution with a single-pass laser processing in ambient environment. The primary goal was to identify the minimum accumulated fluence required for LIPSS generation on the irradiated surface when operating at high processing speeds, which is a key aspect for their broader implementation in industrial applications. Therefore, the SS substrates were textured with a scanning speed of 2 m/s and different accumulated fluences by adjusting only the average power. As can be seen in Fig. 5.2, the surface remained intact up to an accumulated fluence of 12.9 J/cm^2, whilst further increase led to the appearance of LIPSS on the surface. So, the accumulated fluence threshold for the LIPSS generation with an effective number of pulses of 63 was determined to be as low as 13.9 J/cm^2. Thereafter, the irradiation of SS samples was conducted above the predetermined LIPSS threshold with varied pulse fluence but at a fixed effective number of pulses to assess their evolution onto the surface.

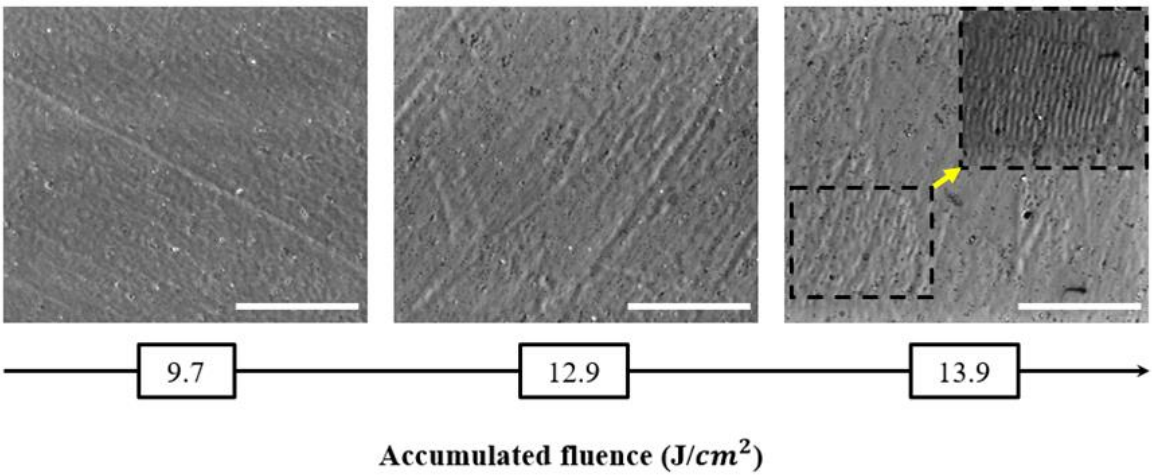

Fig. 5.2. Evolution of LIPSS with the increase of accumulated fluence at a scanning speed of 2 m/s (scale bar: 10 μm). *Note:* The black dashed rectangle on the upper right corner is a magnified view showing the first LIPSS formation.

The first-order diffracted light was captured from these surfaces to determine the LIPSS quality as illustrated in Fig. 5.3a. First, the LIPSS spatial periodicity was measured at various pulse fluence levels while keeping the effective number of pulses at 209. To obtain information about their spatial periods, the acquired SEM images of the samples were processed and analyzed by using 2D FFT. The plot in Fig. 5.3b shows the main spatial periodicities of LIPSS against pulse fluence. As can be seen, the spatial periodicities of LIPSS were below the laser wavelength (λ = 515 nm) for a normal beam incident angle and varied from 473 to 498 nm. Moreover, the 2D FFT image as shown in Fig. 5.3c also shows excellent LIPSS regularity at a pulse fluence of 171.2 mJ/cm^2.

Three representative SEM images of LIPSS formation on the surface by increasing pulse fluence are shown in Fig. 5.3d. Here, the effective number of pulses is 126. For normal beam incidence angle, the orientation of LIPSS was found to be perpendicular to the laser beam polarization vector (indicated by yellow double-sided arrows) regardless of the applied pulse fluence. In the early stage of LIPSS generation, i.e., at F_o = 153.6 mJ/cm^2, some pits/holes

were observed on the surface which gradually disappeared as the pulse fluence was further increased to 206.2 mJ/cm^2. Typically, the LIPSS begin to develop on the surface between the melting and the ablation threshold of the material [35]. Thus, the formation of these surface defects may be attributed to some low-level heating and consequently not well pronounced melting of the material. These experimental observations confirm the hypothesis that the LIPSS generation upon irradiation with nanosecond pulsed lasers is strongly related to the melting of an adequate layer thickness on the surface [30]. By increasing the pulse fluence further to 220.5 mJ/cm^2, more consistent and pronounced LIPSS formed on the surface. A further increase of pulse fluence beyond 220.5 mJ/cm^2 led again to a gradual LIPSS deterioration, whilst the oxidation effects started to become pronounced at a pulse fluence higher than 261.9 mJ/cm^2.

Since the LIPSS periodicity is 470-500 nm, the first-order diffracted light has wavelength in the same range, which is predominantly blue light. As can be seen in Fig. 5.3d, the intensity of the blue light emitted from the textured surfaces increased with the increase of LIPSS quality. In addition, the surfaces covered with pits/holes at low pulse fluence did not emit intense blue light when compared to ones without any such defects. Next, the influence of the effective number of pulses on the evolution of LIPSS at a fixed pulse fluence was analyzed. Representative SEM micrographs in Fig 5.3e depict the LIPSS generated with pulse fluences of 171.2 mJ/cm^2 but with the different effective number of pulses. It is evident that both laser processing parameters had a significant impact on the LIPSS evolution onto the surface. As the distance between two successive pulses decreased and consequently the effective number of pulses increased, the necessary pulse fluence to produce good-quality LIPSS was significantly decreased, too. This is also apparent from the blue light intensity of the corresponding LIPSS topographies. In general, there was a narrow window of pulse fluence

up to 220.5 mJ/cm^2 at 209 effective number of pulses that led to LIPSS without surface oxidation. This phenomenon is associated with the material-dependent incubation effect, which leads to a reduction in the material's ablation threshold when the number of pulses per spot increases [36]. The most homogeneous LIPSS obtained at a pulse fluence of 171.2 mJ/cm^2 and an effective number of 209 pulses in ambient environment exhibited a diffracted light intensity of 199.9.

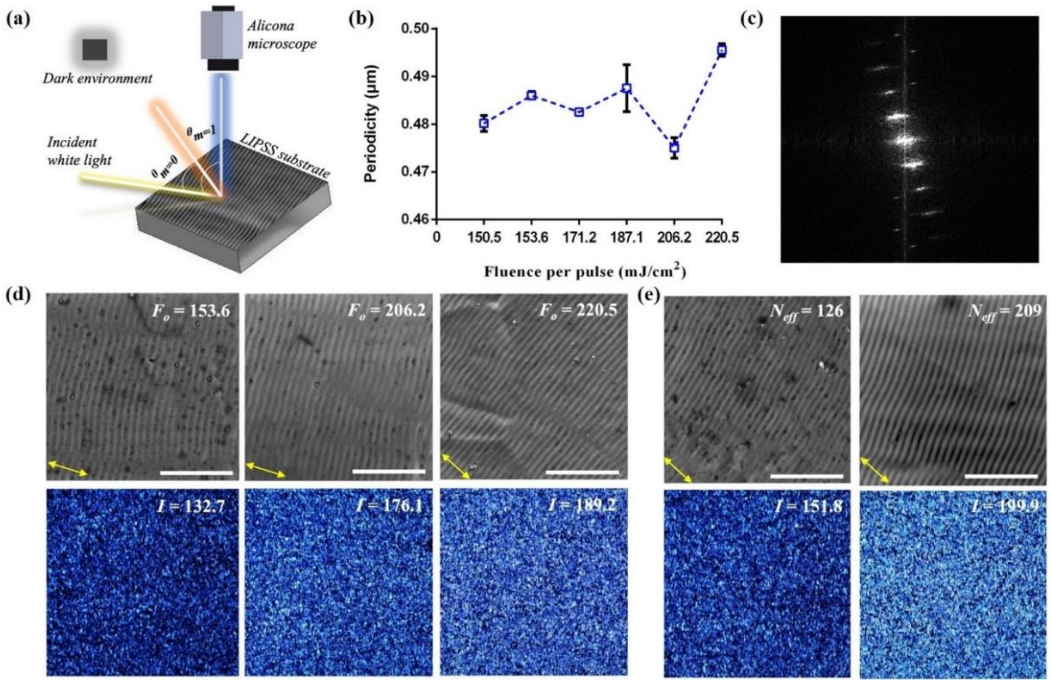

Fig. 5.3. (a) An illustration of the experimental set-up to obtain first-order diffraction blue light images from LIPSS. (b) The periodicity of LIPSS produced with 209 pulses and pulse fluences varying from 150.5 up to 220.5 mJ/cm^2. (c) 2D FFT image showing the regularity of the LIPSS generated with 209 pulses and pulse fluence of 171.2 mJ/cm^2. The LIPSS formation with (d) the increase of pulse fluence in the range of 153.6 to 220.5 mJ/cm^2 and a constant effective number of pulses set at 126 (scale bar: 5 μm) and (e) the increase of effective number of pulses from 126 to 209 at a constant pulse fluence of 171.2 mJ/cm^2 (scale bar: 5 μm). The corresponding blue light diffraction images are also shown. *Note*: The yellow double-sided arrows represent laser beam polarisation vector.

At the same time, irradiation of surfaces with an effective number of 209 pulses and pulse fluences higher than a specific level also led to surface coloration due to the oxidation effects. Fig. 5.4a shows oxidation colors appearing at different pulse fluences and effective number of pulses. This color generation is caused by the thin film interference phenomena and depends on the thickness of the oxide layer in the laser processed area [37]. For instance, beyond the pulse fluence of 220.5 mJ/cm^2 at an effective number of pulses of 209, the LIPSS started to disappear, and the surface showed a yellow (F_0 = 320.9 mJ/cm^2), which is followed by orange (F_0 = 386.9 mJ/cm^2) colors. Moreover, a further increase in effective number of pulses to 419 resulted in purple (F_0 = 386.9 mJ/cm^2) and blue (F_0 = 457.0 mJ/cm^2) colors. Furthermore, the higher accumulated fluence at the edges of the processed area, where the laser beam had to accelerate/decelerate along its scanning path, led to the appearance of the blue color as shown in Fig. 5.4b.

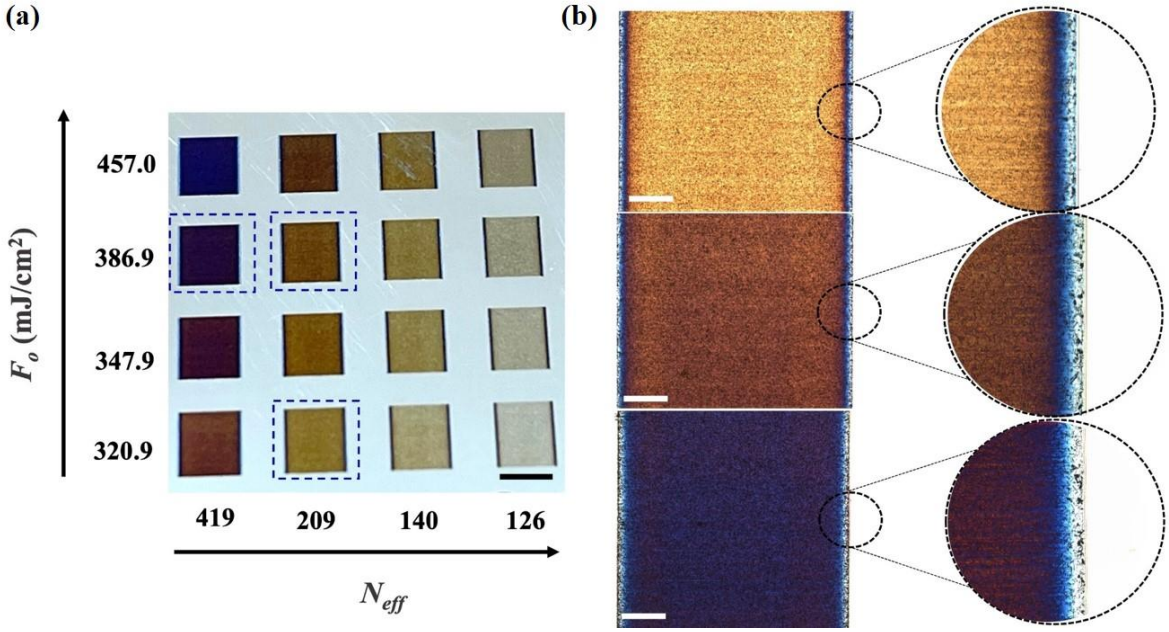

Fig. 5.4. Oxidation colors on SS substrates: (a) the matrix shows the colors appearing at high pulse fluences and a higher number of pulses (scale bar: 5 mm); (b) the corresponding magnified optical images showing yellow, orange, and purple colors as a result of the increasing accumulated fluence (scale bar: 1 mm). The corresponding inset image shows the blue color at the edge of the squares due to beam deceleration/acceleration and the resulting high accumulated fluence there.

Finally, it was observed by analysing the captured SEM images that the LIPSS formed on the SS surfaces had a relatively superior overall quality, i.e. better homogeneity/regularity and less defects, when the diffracted blue light intensity was above 160. As a result, the threshold value of blue light intensity was set at 160 to determine the quality of LIPSS in this research. Therefore, LIPSS that exhibited $I < 160$ were considered as low-quality ones, whereas those with $I > 160$ were deemed as LIPSS with a satisfactory quality. Fig. 5.5 shows the map of morphologies obtained within the investigated processing window. The surface morphologies were clustered into four categories, i.e., no LIPSS formation, low- and high-quality LIPSS and excessive oxidation on the surface. Overall, it is worth stating that the accumulated fluence

during the LIPSS generation with the green nanosecond laser was identified to be in the range from 13.9 to 46.2 J/cm^2. While the use of laser settings outside this processing window led to either no LIPSS formation or alterations in surface chemistry, i.e., oxidation over the processed area. As can be seen, an effective number of pulses between 105 and 209 led to the generation of high-quality LIPSS on the surface.

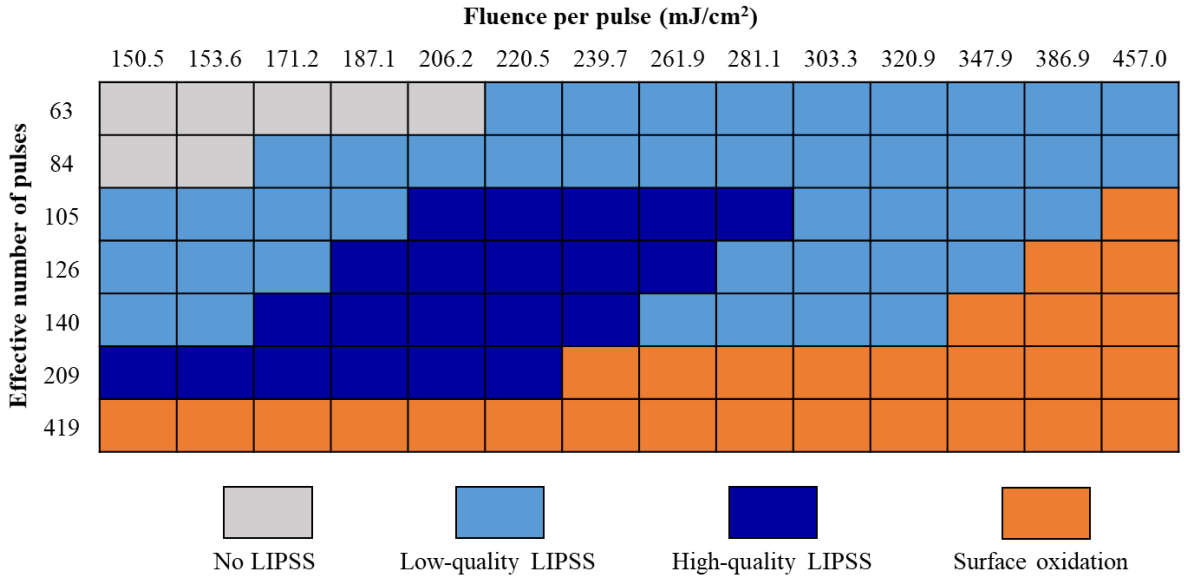

Fig. 5.5. LIPSS morphologies as a function of the pulse fluence and the effective number of pulses.

5.3.2. LIPSS quality in argon gas environment

Experiments were also carried out in argon environment with the process parameters used to obtain good quality LIPSS in the ambient one. In particular, the pulse fluences used were in the range from 150.5 mJ/cm^2 to 220.5 mJ/cm^2 with an effective number of pulses kept the same at 209 during these experiments. Fig. 5.6a shows SEM images of LIPSS generated in the ambient and argon environments along with their corresponding blue light images. At a pulse fluence of 150.5 mJ/cm^2, the LIPSS topographies were also covered by pits/holes when laser processing was conducted in the ambient environment. In contrast, such defects were not

anymore present on LIPSS processed in argon. Consequently, the corresponding blue light images appear to be brighter for the samples produced in argon environment compared to those in the ambient one. When the fluence was increased to 171.2 mJ/cm^2, the LIPSS showed no more defects even in the ambient environment. At the same time, it is worth noting that the LIPSS generated in argon environment were defect-less under the same pulse fluence, too. In both environments, the LIPSS had almost the same periodicities. Although the SEM micrographs show no remarkable differences, the blue light images reveal that LIPSS generated in argon environment are brighter than those in air. When the blue light intensities are plotted at three different pulse fluences as shown in Fig. 5.6b, it immediately divulges that the quality of LIPSS produced in argon environment is better.

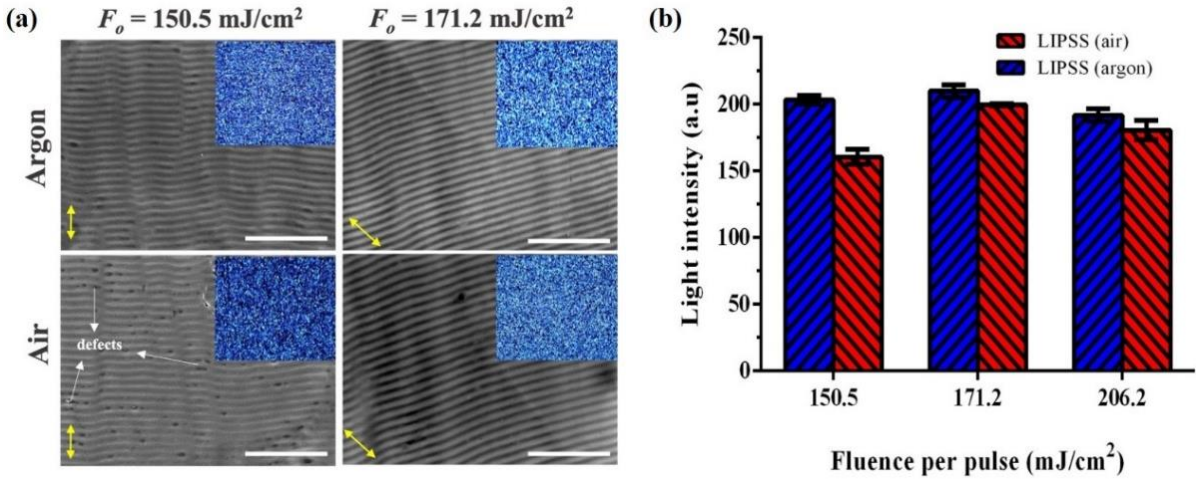

Fig. 5.6. (a) The SEM images of LIPSS generated under ambient and argon atmospheres with 209 pulses and pulse fluences of 150.5 and 171.2 mJ/cm^2 (scale bar: 5 μm). Their corresponding blue light diffraction images are shown as insets. (b) Comparison of blue light intensities of LIPSS generated with pulse fluences of 150.5, 171.2 and 206.2 mJ/cm^2 and 209 pulses in ambient and argon atmospheres. *Note*: The yellow double-sided arrows show the laser beam polarization vector.

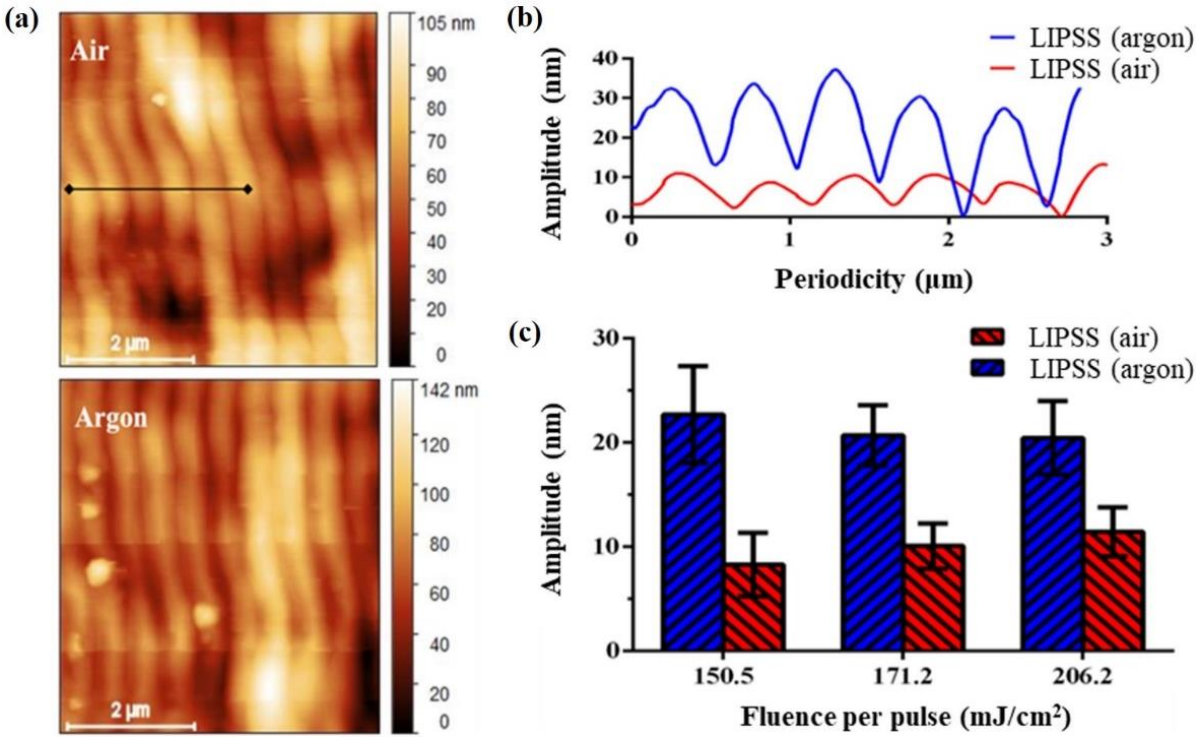

Fig. 5.7. (a) AFM images of LIPSS and (b) the height profiles of the samples processed in ambient and argon environments at a pulse fluence of 171.2 mJ/cm^2 and an effective number of 209 pulses. (c) The comparison of the LIPSS amplitude at different pulse fluences and a fixed effective number of 209 pulses.

To investigate further the differences in blue light intensities of LIPSS produced in the two environments, AFM measurements were taken to analyze the LIPSS amplitude. Fig. 5.7a and b present the AFM images of LIPSS together with their extracted height profiles, respectively. It is evident that the LIPSS topographies have higher amplitudes when they were processed in argon than those in air. In particular, the amplitudes vary from 5 to 14 nm and 17 to 27 nm in ambient and argon environments, respectively. This clearly shows that LIPSS generated in argon exhibit heights that are twice higher than those in air. If the mean height of the LIPSS topographies generated in both environments at different pulse fluences are compared, as shown in Fig. 5.7c, it is obvious that the argon ones exhibit higher aspect ratios. This further

underline why the blue light intensity of the samples produced in argon is more pronounced even though the SEM images have shown no discernible differences.

5.3.3. Surface chemistry analysis

To further understand why the quality of LIPSS differs in argon and ambient environments, XPS analysis was conducted to investigate the alterations in surface chemistry. Fig. 5.8a-e presents the XPS survey spectrums obtained on the untreated SS substrate and the LIPSS ones processed in both argon and ambient conditions. Here, the LIPSS-I and LIPSS-II are the ones processed with an effective number of pulses of 209 and pulse fluences of 150.5 mJ/cm^2 and 171.2 mJ/cm^2, respectively. A quick look at the spectra shows that oxygen, carbon, chromium, and iron elements dominate on the surface, whereas the influence of other elements, such as nickel and manganese, was not considered as their atomic concentrations were barely quantified. The surface chemical compositions of these LIPSS treated samples are given in Table 5.1.

Table 5.1. Elemental composition extracted from the XPS survey spectra of untreated and laser processed SS surfaces.

Surface	C (at%)	O (at%)	Fe (at%)	Cr (at%)	O/Fe	O/Cr
Untreated	59.95	35.00	3.50	1.55	10.00	22.58
LIPSS-I (argon)	37.02	46.75	8.64	7.59	5.41	6.16
LIPSS-I (air)	44.33	44.62	6.00	5.05	7.44	8.84
LIPSS-II (argon)	35.05	48.18	10.26	6.51	4.70	7.40
LIPSS-II (air)	45.00	42.79	7.52	4.69	5.69	9.12

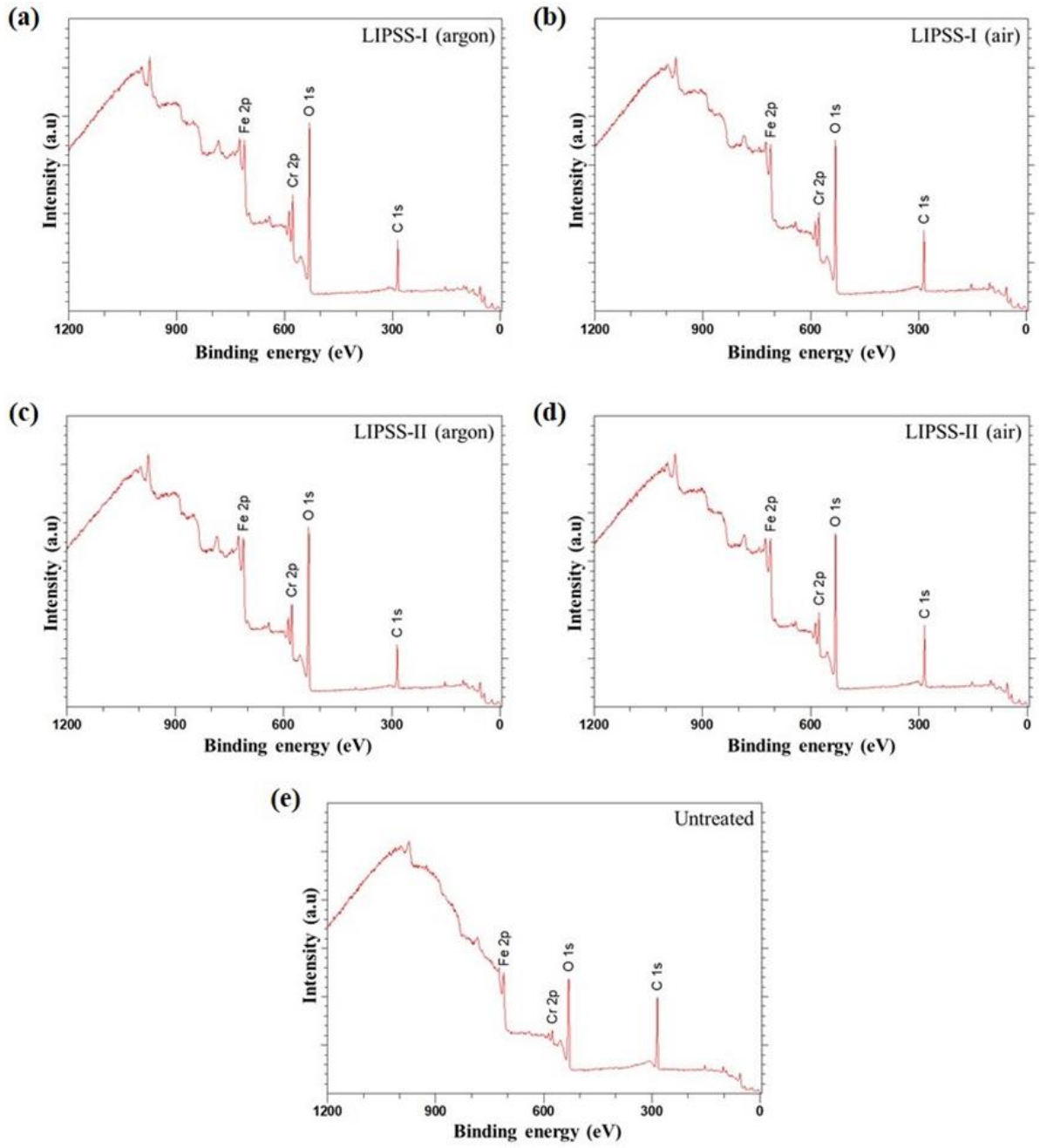

Fig. 5.8. The XPS survey spectra for: (a-d) LIPSS fabricated on SS substrates with 209 pulses and pulse fluences of 150.5 and 171.2 mJ/cm^2 after irradiation in argon and air environments, respectively; (e) untreated SS surface.

The elemental composition of the untreated SS sample is characterized by a higher concentration of carbon compared to oxygen and a significantly low concentration of iron and chromium. The detection of non-zero carbon quantity clearly indicates that this surface was

contaminated, and the primary source of such contamination is the adsorption of organic matter from the atmosphere [38]. On the other hand, a remarkable reduction of the carbon content was observed on all laser textured surfaces, which should be attributed to the removal of the pre-existing adventitious carbon during laser irradiation. This cleaning phenomenon was more pronounced on the surfaces processed in argon and the one treated with a higher pulse fluence resulted in the sharpest decrease of the carbon content. Furthermore, significant variations in the oxygen content were observed among the various analyzed surfaces, too. In particular, the oxygen amount increased together with that of Fe and Cr on the surfaces subjected to laser treatment, especially in those samples processed in argon. However, the ratio of oxygen to iron (O/Fe) and chromium (O/Cr) shows that the LIPSS processed in ambient conditions are oxygen-rich as compared to the ones in argon.

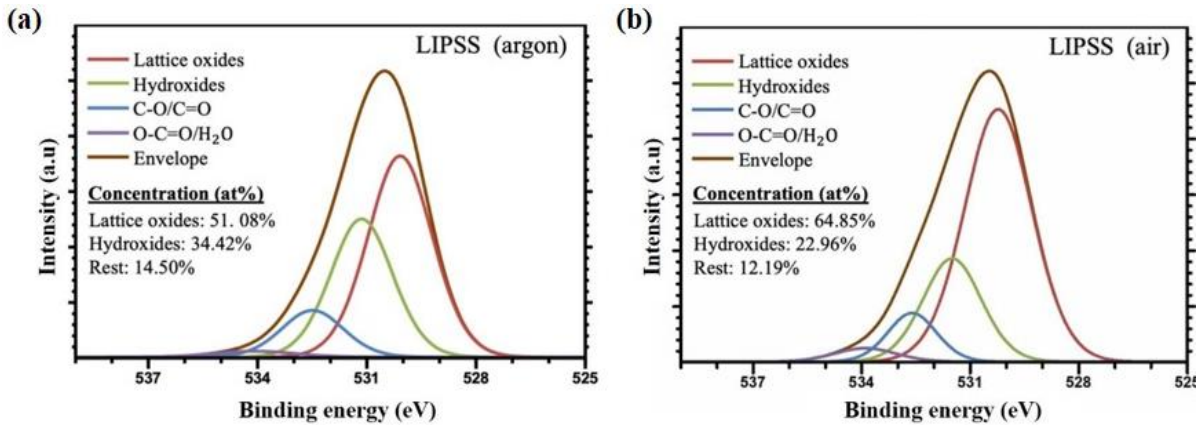

Fig. 5.9. High-resolution O1s spectra of LIPSS treated under (a) argon and (b) ambient environments.

To evaluate the oxygen contribution, the deconvolution of O1s spectra was analyzed as shown in Fig. 5.9. It revealed that two contributions related to oxygen in the form of lattice oxides at 530 ± 0.2 eV and hydroxides at 531.5 ± 0.1 eV dominate on the surface while the rest (C-O/C=O at 532.6 ± 0.2 and O-C=O/H_2O at 534 ± 0.2 eV) are minor. As can be seen, most of

the oxygen on LIPSS substrates was the result of oxidation reactions, followed by the formation of hydroxides and organic compounds. More specifically, the concentration of lattice oxides was found to be greater on the laser-treated surfaces, while they dominated in those processed in air. It can be inferred that the LIPSS generation led to the exposure of more Fe and Cr from the bulk to the ambient air, which instantly reacted and formed a mixed oxide layer at the surface. On the other hand, the hydroxides had more contribution to the LIPSS processed in argon.

To determine the reason for more hydroxide formation on the LIPSS generated in argon, the high-resolution spectra of metallic elements were also analyzed. The Cr2p (3/2, 1/2) XPS spectra as extracted from the laser-treated surfaces are presented in Fig. 5.10a, where the resultant positions of the major components are specified. In all the cases, the existence of Cr (III) oxide, Cr_2O_3, was observed on the surfaces at a binding energy of 576.6 eV. However, a second maxima was presented on all the laser-treated surfaces at around 577.1 eV and it is more pronounced on the LIPSS textured in argon, which most likely is ascribed to the hydroxides $Cr(OH)_3$. On the other hand, by analyzing the Fe2p spectrum as shown in Fig. 5.10b, it can be inferred that the Fe (III) oxide state, Fe_2O_3, dominates on all the surfaces at a peak position of 711 eV. This observation can also be verified by the weak satellite peak situated at around 719 eV, which is characteristic of Fe (III) oxide. At the same time, the contribution of Fe (II) oxide components, FeO, at a binding energy of approximately 709 eV was more pronounced on the surfaces subjected to laser treatment. Among these surfaces, no distinguishable signal of Cr or Fe in the metallic state was observed over the background noise on the substrates processed in air, which can confirm the formation of a uniform oxide layer on their surfaces. On the other hand, it should be highlighted that the samples processed in argon gas had some contribution of pure metallic components at 707 eV and thus the thickness

of the oxide layer on these surfaces was less than 10 nm (the photoelectron's penetration depth in XPS measurements) [39]. This observation underlines that the thickness of the oxide layer has contributed to less depth of ripples in LIPSS processed in the air as evident from the AFM measurements.

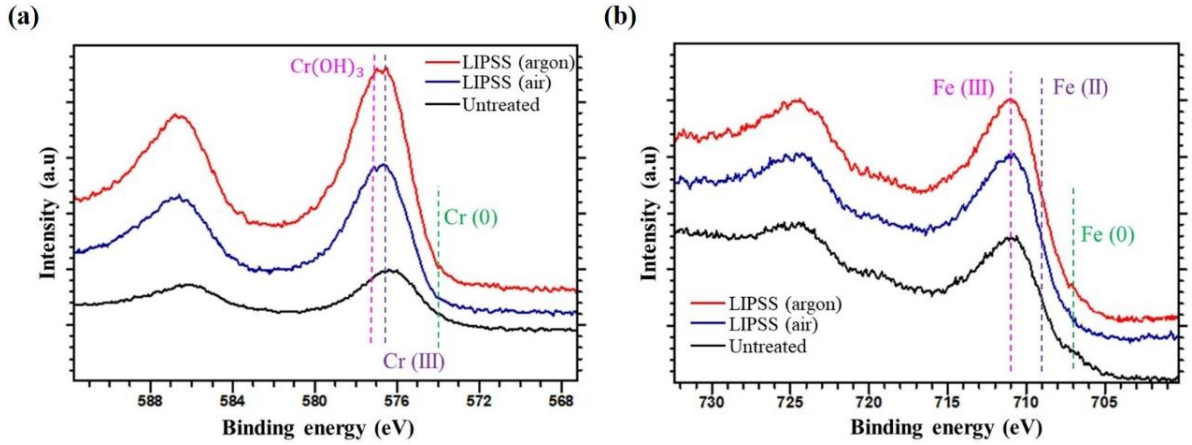

Fig. 5.10. High-resolution XPS spectra of (a) Cr2p and (b) Fe2p of untreated surface and LIPSS generated in argon and ambient environments.

Based on the observations from first-order diffraction response (blue light intensity), surface topography (SEM and AFM) and chemistry (XPS) responses, Fig. 5.11 illustrates evidently the processing environment influence on surface topography and chemistry at low and high accumulated fluences. Apparently, at low accumulated fluences (< 50.1 J/cm^2), the interaction of the green nanosecond laser beam with the SS surface results in the formation of LIPSS in ambient environment. However, the formation of a thin layer of oxide during the processing suppresses the amplitude of the LIPSS. A change of processing environment to argon decreases the thickness of the oxide layer, which is evident from the decrease in oxygen content (O/Fe ratio) as shown in Table 5.1. The thickness of the oxide layer (t) can be estimated to be less than 20 nm, as evident from AFM profiles of LIPSS produced in ambient and argon environments (see Fig. 5.7b). On the other hand, high accumulated fluences (≥ 50.1 J/cm^2)

generate roughness on the substrate along with a thick oxide layer. For instance, a recent investigation onto green nanosecond laser coloring of stainless steel surfaces in an ambient environment showed that the oxide film thickness varies from 200 to 600 nm, which led to different colors [40]. At the same time, the surface roughness of these thick oxide covered areas ranged from 0.5 to 1.2 μm.

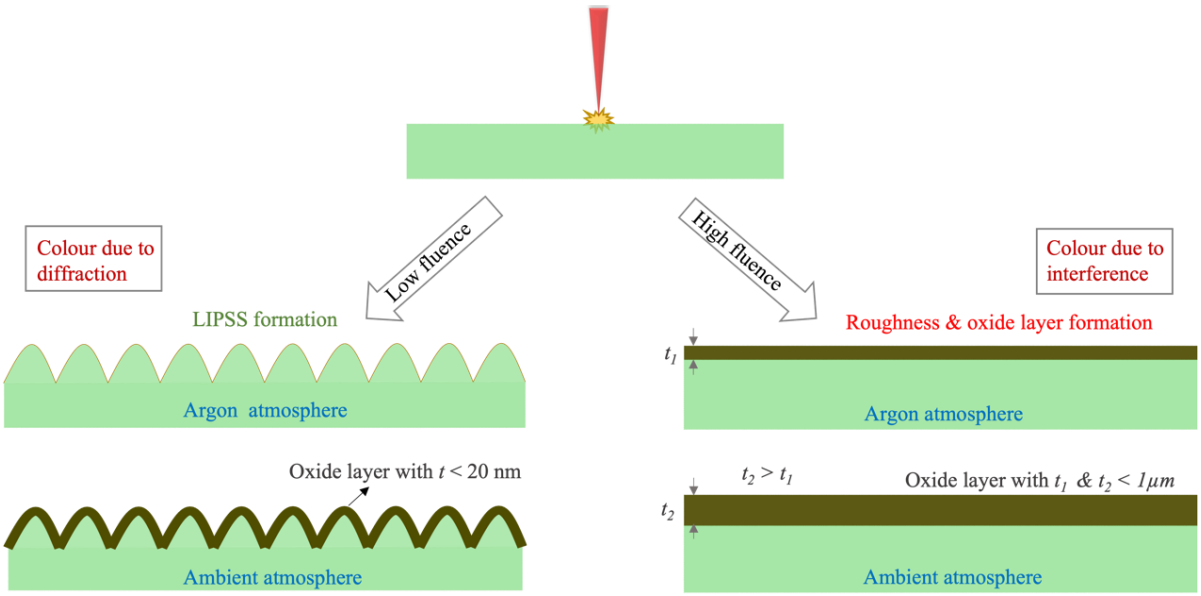

Fig. 5.11. An illustration showing the influence of processing environment on oxide layer formation at low and high accumulated fluences with a green nanosecond laser.

5.3.4. Contact angle analysis

To investigate the combined influence of surface topography and chemistry on macroscopic properties, the contact angle measurements were conducted on the LIPSS surfaces produced in air and argon environments. Contact angle variations over a period of two weeks on the surfaces are shown in Fig. 5.12. On the untreated SS surface, the contact angle was measured to be $71.2^{o} \pm 1.2^{o}$. It is apparent that the contact angle decreased immediately after the LIPSS treatment in both air and argon environments. The magnitude of this decrease is more on the surfaces that were processed in argon when compared to those treated in air. However, the

contact angle gradually increased on both LIPSS topographies after day 3 and reached a maximum of $90.8^{o} \pm 2.8^{o}$ in argon exhibiting hydrophobicity.

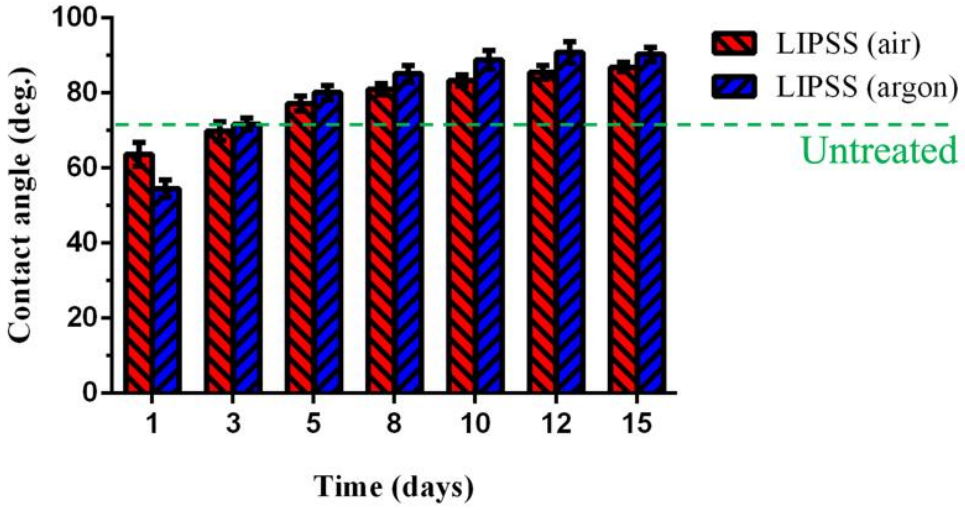

Fig. 5.12. Contact angle evolution as a function of time in number of days on untreated and LIPSS treated substrates in the air and argon environments.

One of the key indicators of surface chemistry to determine the wetting state is the oxygen-to-carbon ratio (O/C) on the surfaces, which influences the contact angle of the laser-treated surfaces [41]. The lack of oxygen species on the surfaces processed in argon exhibited a lower contact angle immediately after laser processing. However, over a period of time, the CO_2 decomposes from the atmosphere and hence the O/C ratio increases on the surfaces. The decomposition of CO_2 leads to a transfer of O^{2-} ions to oxygen-deficient magnetite $Fe_3O_{4-\delta}$ ($0 < \delta < 1$) and results in the formation of Fe_3O_4 [42]. On the surfaces processed in argon, the decomposition of CO_2 favors the formation of Fe_3O_4 and the surface becomes rich in oxygen-to-carbon ratio. For instance, the O/C on samples processed in argon is 1.2 - 1.3 whereas on the ones treated in the air is 0.9 - 1.0. At the same time, the LIPSS are deeper in the samples processed in argon than those in air. Therefore, the combined effects of topography and surface chemistry have led to an increase in the contact angle on LIPSS generated in an argon

environment. However, it should also be noted that the magnitude of the difference is not significant between the ones processed in argon and air as the LIPSS exhibit a low roughness factor (a ratio of actual surface area to the projected one).

5.4. Conclusions

Laser texturing/structuring of surfaces with LIPSS topographies has been extensively deployed as a means for tailoring their functional characteristics. However, the generation of high-quality homogeneous LIPSS cost-effectively on relatively large surfaces is an important step toward the broader use of this technology for functionalizing surfaces at an industrial scale. Thus, a laser treatment to generate high-quality uniform LIPSS in a cost-effective manner was demonstrated in this research. Specifically, a green nanosecond laser was investigated for producing LIPSS on AISI 316 stainless steel under argon environment, and then their formation was compared with those obtained in air. The quality of LIPSS generated in both environmental conditions was evaluated through the SEM, AFM and XPS analysis and correlated with their blue light diffraction response. In an argon environment, the intensity of the diffracted light increased, and this was indicative of the improved quality and homogeneity of LIPSS generated on the surfaces. The relatively low-quality LIPSS produced in the air can be attributed to the formation of oxides as a side effect compared to the laser processing in argon. Since the intensity of the first-order diffracted light depends only on the LIPSS periodicity and depth and not on the surface chemistry, the topographical changes (e.g., periodicity/depth) of the LIPSS could be qualitatively captured by first-order diffracted light (blue light intensity). Therefore, the blue light intensity can act as a global/macroscopic parameter to judge about the quality of the LIPSS, instead of time-consuming local

measurements, such as SEM/AFM. A higher blue light intensity is indicative of better quality LIPSS, which means that LIPSS are deeper and devoid of pits.

Moreover, the high amplitude LIPSS produced in argon environment could be used for texturing replication masters that can find applications in soft/compression and injection molding. For instance, such masters with high aspect ratio LIPSS treatments could be utilized for producing high quality textured replicas through micro injection molding [43]. At the same time, considering these capabilities for producing sub-wavelength nanostructures, i.e., LIPSS with the green nanosecond laser, such LIPSS treatments can be used to enhance the antireflection properties of surfaces on various materials. Thus, the proposed nanosecond laser treatment in this research could be a potentially cost-effective solution for fabricating functional nanostructured surfaces that can find applications in energy storage, optoelectronics and sensors. For instance, one such application could be to design broad-band ultralow optical reflective surfaces. Future in-depth research will be conducted to explore the optical properties of the nanostructured surfaces. At the same time, the fabrication of multi-scale structures (LIPSS on top of microscale structures) could be an interesting step towards designing cost-effective superhydrophobic metallic surfaces for anti-bacterial and anti-icing applications.

Acknowledgments

The X-ray photoelectron (XPS) data collection was performed at the EPSRC National Facility for XPS (“HarwellXPS”), operated by Cardiff University and UCL, under Contract No. PR16195.

References

[1] S. Zhang, Y. Zhou, H. Zhang, Z. Xiong, and S. To, "Advances in ultra-precision machining of micro-structured functional surfaces and their typical applications," *International Journal of Machine Tools and Manufacture,* vol. 142, pp. 16-41, 2019.

[2] Y.-Y. Quan, Z. Chen, Y. Lai, Z.-S. Huang, and H. Li, "Recent advances in fabricating durable superhydrophobic surfaces: a review in the aspects of structures and materials," *Materials Chemistry Frontiers,* vol. 5, no. 4, pp. 1655-1682, 2021.

[3] M. Liu, M.-T. Li, S. Xu, H. Yang, and H.-B. Sun, "Bioinspired Superhydrophobic Surfaces via Laser-Structuring," *Frontiers in Chemistry,* vol. 8, no. 835, 2020.

[4] A. Samanta, Q. Wang, S. K. Shaw, and H. Ding, "Roles of chemistry modification for laser textured metal alloys to achieve extreme surface wetting behaviors," *Materials & Design,* vol. 192, p. 108744, 2020.

[5] C. Florian, S. V. Kirner, J. Krüger, and J. Bonse, "Surface functionalization by laser-induced periodic surface structures," *Journal of Laser Applications,* vol. 32, no. 2, p. 022063, 2020.

[6] Y.-F. Gao *et al.,* "Picosecond laser-induced periodic surface structures (LIPSS) on crystalline silicon," *Surfaces and Interfaces,* vol. 19, p. 100538, 2020.

[7] M. J. Kang *et al.,* "Periodic surface texturing of amorphous-Si thin film irradiated by UV nanosecond laser," *Opt. Mater. Express,* vol. 9, no. 11, pp. 4247-4255, 2019.

[8] R. Y. Siddiquie, A. Gaddam, A. Agrawal, S. S. Dimov, and S. S. Joshi, "Anti-Biofouling Properties of Femtosecond Laser-Induced Submicron Topographies on Elastomeric Surfaces," *Langmuir,* vol. 36, no. 19, pp. 5349-5358, 2020.

[9] X. Luo *et al.*, "Biocompatible nano-ripples structured surfaces induced by femtosecond laser to rebel bacterial colonization and biofilm formation," *Optics & Laser Technology*, vol. 124, p. 105973, 2020.

[10] A. Gaddam, H. Sharma, T. Karkantonis, and S. Dimov, "Anti-icing properties of femtosecond laser-induced nano and multiscale topographies," *Applied Surface Science*, vol. 552, p. 149443, 2021.

[11] S. Sarbada, Z. Huang, Y. C. Shin, and X. Ruan, "Low-reflectance laser-induced surface nanostructures created with a picosecond laser," *Applied Physics A*, vol. 122, no. 4, p. 453, 2016.

[12] A. Gaddam, H. Sharma, R. Ahuja, S. Dimov, S. Joshi, and A. Agrawal, "Hydrodynamic drag reduction of shear-thinning liquids in superhydrophobic textured microchannels," *Microfluidics and Nanofluidics*, vol. 25, no. 9, p. 73, 2021.

[13] T. Karkantonis, A. Gaddam, T. L. See, S. S. Joshi, and S. Dimov, "Femtosecond laser-induced sub-micron and multi-scale topographies for durable lubricant impregnated surfaces for food packaging applications," *Surface and Coatings Technology*, vol. 399, p. 126166, 2020.

[14] J. J. J. Nivas *et al.*, "Secondary electron yield reduction by femtosecond pulse laser-induced periodic surface structuring," *Surfaces and Interfaces*, vol. 25, p. 101179, 2021.

[15] M. Martínez-Calderon *et al.*, "Surface micro- and nano-texturing of stainless steel by femtosecond laser for the control of cell migration," *Scientific Reports*, vol. 6, no. 1, p. 36296, 2016.

[16] A. Batal, R. Sammons, and S. Dimov, "Response of Saos-2 osteoblast-like cells to laser surface texturing, sandblasting and hydroxyapatite coating on CoCrMo alloy surfaces," *Materials Science and Engineering: C,* vol. 98, pp. 1005-1013, 2019.

[17] A. Velic, J. Hasan, Z. Li, and P. K. D. V. Yarlagadda, "Mechanics of Bacterial Interaction and Death on Nanopatterned Surfaces," *Biophysical Journal,* vol. 120, no. 2, pp. 217-231, 2021.

[18] L. Bao, N. V. Priezjev, and H. Hu, "The local slip length and flow fields over nanostructured superhydrophobic surfaces," *International Journal of Multiphase Flow,* vol. 126, p. 103258, 2020.

[19] S. Ahmad, H. Sharma, A. Agrawal, and S. S. Joshi, "Light Harvesting Using Biomimetic Micro-textured Transparent Films for Photovoltaic Applications," *Transactions of the Indian National Academy of Engineering,* vol. 6, no. 3, pp. 775-785, 2021.

[20] M. Hiratsuka, M. Emoto, A. Konno, and S. Ito, "Molecular Dynamics Simulation of the Influence of Nanoscale Structure on Water Wetting and Condensation," *Micromachines,* vol. 10, no. 9, p. 587, 2019.

[21] A. Batal, A. Michalek, P. Penchev, A. Kupisiewicz, and S. Dimov, "Laser processing of freeform surfaces: A new approach based on an efficient workpiece partitioning strategy," *International Journal of Machine Tools and Manufacture,* vol. 156, p. 103593, 2020.

[22] A. Michalek *et al.*, "Modelling ultrafast laser structuring/texturing of freeform surfaces," *Applied Surface Science Advances,* vol. 2, p. 100036, 2020.

[23] O. Hofmann, J. Stollenwerk, and P. Loosen, "Design of multi-beam optics for high throughput parallel processing," *Journal of Laser Applications,* vol. 32, no. 1, p. 012005, 2020.

[24] G. Bonamis *et al.*, "High efficiency femtosecond laser ablation with gigahertz level bursts," *Journal of Laser Applications,* vol. 31, no. 2, p. 022205, 2019.

[25] D. Bhaduri *et al.*, "Laser polishing of 3D printed mesoscale components," *Applied Surface Science,* vol. 405, pp. 29-46, 2017.

[26] C. P. Ma, Y. C. Guan, and W. Zhou, "Laser polishing of additive manufactured Ti alloys," *Optics and Lasers in Engineering,* vol. 93, pp. 171-177, 2017.

[27] Z. Yang, Y. Tian, Y. Zhao, and C. Yang, "Study on the Fabrication of Super-Hydrophobic Surface on Inconel Alloy via Nanosecond Laser Ablation," *Materials,* vol. 12, no. 2, p. 278, 2019.

[28] J. S. Hwang, J.-E. Park, G. W. Kim, H. Lee, and M. Yang, "Fabrication of printable nanograting using solution-based laser-induced periodic surface structure process," *Applied Surface Science,* vol. 547, p. 149178, 2021.

[29] P. Nürnberger *et al.*, "Influence of substrate microcrystallinity on the orientation of laser-induced periodic surface structures," *Journal of Applied Physics,* vol. 118, no. 13, p. 134306, 2015.

[30] J. G. A. B. Simões, R. Riva, and W. Miyakawa, "High-speed Laser-Induced Periodic Surface Structures (LIPSS) generation on stainless steel surface using a nanosecond pulsed laser," *Surface and Coatings Technology,* vol. 344, pp. 423-432, 2018.

[31] P. Nürnberger *et al.*, "Orthogonally superimposed laser-induced periodic surface structures (LIPSS) upon nanosecond laser pulse irradiation of SiO2/Si layered systems," *Applied Surface Science,* vol. 425, pp. 682-688, 2017.

[32] S. Y. Son *et al.*, "In-depth optical characterization of poly(3-hexylthiophene) after formation of nanosecond laser-induced periodic surface structures," *Nanoscale,* 10.1039/C8NR10075F vol. 11, no. 16, pp. 7567-7571, 2019.

[33] S. Durbach and N. Hampp, "Generation of 2D-arrays of anisotropically shaped nanoparticles by nanosecond laser-induced periodic surface patterning," *Applied Surface Science,* vol. 556, p. 149803, 2021.

[34] H. M. Reinhardt, P. Maier, H.-C. Kim, D. Rhinow, and N. Hampp, "Nanostructured Transparent Conductive Electrodes for Applications in Harsh Environments Fabricated via Nanosecond Laser-Induced Periodic Surface Structures (LIPSS) in Indium–Tin Oxide Films on Glass," *Advanced Materials Interfaces,* vol. 6, no. 16, p. 1900401, 2019.

[35] J. Eichstädt, G. R. B. E. Römer, and A. J. Huis in 't Veld, "Determination of irradiation parameters for laser-induced periodic surface structures," *Applied Surface Science,* vol. 264, pp. 79-87, 2013.

[36] Z. Sun, M. Lenzner, and W. Rudolph, "Generic incubation law for laser damage and ablation thresholds," *Journal of Applied Physics,* vol. 117, no. 7, p. 073102, 2015.

[37] H. Liu, W. Lin, and M. Hong, "Surface coloring by laser irradiation of solid substrates," APL Photonics, vol. 4, no. 5, p. 051101, 2019.

[38] S. Tardio, M.-L. Abel, R. H. Carr, J. E. Castle, and J. F. Watts, "Comparative study of the native oxide on 316L stainless steel by XPS and ToF-SIMS," *Journal of Vacuum Science & Technology A,* vol. 33, no. 5, p. 05E122, 2015.

[39] G. Li *et al.*, "Evolution of aluminum surface irradiated by femtosecond laser pulses with different pulse overlaps," *Applied Surface Science,* vol. 276, pp. 203-209, 2013.

[40] X. Ma et al., "Effect of nanosecond pulsed laser parameters on the color making of 304 stainless steel," Optics & Laser Technology, vol. 126, p. 106104, 2020.

[41] A. Žemaitis *et al.,* "Controlling the wettability of stainless steel from highly-hydrophilic to super-hydrophobic by femtosecond laser-induced ripples and nanospikes," *RSC Advances,* vol. 10, no. 62, pp. 37956-37961, 2020.

[42] A.-M. Kietzig, S. G. Hatzikiriakos, and P. Englezos, "Patterned Superhydrophobic Metallic Surfaces," *Langmuir,* vol. 25, no. 8, pp. 4821-4827, 2009.

[43] F. Baruffi *et al.,* "Correlating nano-scale surface replication accuracy and cavity temperature in micro-injection moulding using in-line process control and high-speed thermal imaging," *Journal of Manufacturing Processes,* vol. 47, pp. 367-381, 2019.

CHAPTER 6: LASER MICRO-MACHINING OF FREEFORM SURFACES: ACCURACY, REPEATABILITY AND REPRODUCIBILITY ACHIEVABLE WITH MULTI-AXIS PROCESSING STRATEGIES

The research reported in this chapter was published online as a full-length article in the journal of "Precision Engineering" (2022):

T. Karkantonis[1], P. Penchev[1], V. Nasrollahi[1], H. Le[1], T. L. See[2], D. Bruneel[3], J. A. Ramos-de-Campos[3], and S. Dimov[1]**,** "Laser micro-machining of freeform surfaces: Accuracy, repeatability and reproducibility achievable with multi-axis processing strategies," *Precision Engineering*, vol. 78, pp. 233-247, 2022.

[1]*Department of Mechanical Engineering, School of Engineering, The University of Birmingham, Birmingham, B15 2TT, UK*

[2]*The Manufacturing Technology Centre Ltd, Coventry, CV7 9JU, UK*

[3]*LASEA S.A., Liège Science Park, Rue Louis Plescia 31, 4102 Seraing, Belgium*

Authors' contribution:

T. Karkantonis: Main author, conceived the methodology, conducted the experimental work, performed the analysis and written the original draft. **P. Penchev:** Assisted with laser setup and data interpretation. **V. Nasrollahi:** Supported with data collection. **H. Le:** Contributed with data analysis. **T. L. See:** Supervision and proofreading. **D. Bruneel:** Provided technical support. **J. A. Ramos-de-Campos:** Proofreading. **S. Dimov:** Supervision and proofreading.

Abstract

The requirements that complex 3D miniaturised components have to satisfy are constantly increasing for various application areas, e.g. in aerospace, biomedical and electronics, and hence there is a sustained drive to broaden the capabilities of precision manufacturing processes. In this regard, state-of-the-art Laser-based Micro-Machining (LMM) systems have been attracting significant industrial interest with their emerging capabilities for multi-axis machining. However, intrinsic limitations of component technologies of such systems can impact the machining Accuracy, Repeatability, and Reproducibility (ARR), especially in complex processing strategies requiring the simultaneous use of multiple axes, and consequently to affect the overall processing uncertainty. Herein, the aim of this research is to propose a systematic method for assessing the overall performance of such LMM systems when they are deployed for laser structuring/patterning/texturing of freeform surfaces. In particular, the method employs a series of laser processing tests on spherical samples to quantify the contributions of different error sources on the machining ARR when implementing simultaneous multi-axis processing strategies under quasi-static and dynamic conditions. An experimental validation of the proposed method is conducted on a representative state-of-the-art LMM system and then conclusions are drawn about its capabilities to determine the processing ARR of multi-axis LMM systems. This research provides an insight into the limitations and manufacturing challenges in deploying such systems for the fabrication of complex 3D components.

Keywords: Machining test, laser micro-machining system, performance evaluation, precision metrology, freeform surface, multi-axis simultaneous laser processing, accuracy, repeatability, reproducibility, uncertainty.

6.1. Introduction

Over the last decade, technological advances in different industrial sectors, i.e. biomedical, aerospace, electronics and telecommunications, have driven the demand for producing highly accurate miniaturised components with intricate geometries [1, 2]. To address these challenging requirements, various conventional and non-conventional manufacturing technologies have been deployed to fabricate high-precision micro-structures/features in products [3-5]. Traditionally, such features were manufactured through CNC micro-milling, however inherent limitations of this technology with respect to tool wear, spindle speed and available cutting tool sizes constrain its broader use.

On the other hand, non-contact chip-less machining processes have attracted the interest of industry and research due to their intrinsic characteristics. Among them, Laser-based Micro-Machining (LMM) can offer an attractive alternative in performing different high resolution operations, e.g. structuring/texturing/scribing, drilling, polishing and cutting, on freeform surfaces in a fully integrated manufacturing platform. Compared to lithographic processes, this technology offers relative higher processing efficiency, flexibility and reliability while it does not require a clean-room environment for its use [6]. At the same time, it is a process that can be used to machine almost any engineering material, such as glass [7], metals [8], ceramics [9] and polymers [10], by selecting a suitable laser source.

Recently, the LMM technology has been extensively deployed as a surface modification technique to fabricate micro/nano structures on planar surfaces of new or existing products and thus to "imprint" attractive surface functionalities, e.g. anti-biofouling [11], anti-corrosion [12], anti-bacterial [13], anti-icing [14], anti-reflective [15], anti-adhesive [16] and cell-adhesion [17]. Despite that, it is recognised that laser machining of micro/nanoscale structures

onto complex 3D surfaces with significant variations in their curvature, e.g. on medical implants and contact lenses, is of great importance and could broaden the LMM industrial applications [18-21]. Therefore, multi-axis LMM systems, which combine the capabilities of 5 axes CNC systems together with that of scanning heads, can be used to execute complex 3D laser processing strategies that were considered not achievable until recently.

To date, the most well-recognised approach to texture/structure large freeform/curved surfaces is to apply a tessellation/partitioning method to divide them into planar scanning fields and layers by taking into account the constraints introduced by the beam delivery sub-systems [22, 23]. In these cases, mechanical stages are used only to position the centre of each field to be normal to the laser beam, and then the scanning head executes the necessary processing strategy. Nonetheless, there are specific challenges/limitations that should be taken into consideration when laser processing 3D surfaces. More specifically, the variations of Beam Incidence Angle (BIA) and Focal Offset Distance (FOD) due to the surface curvature might impact the dimensional accuracy and/or functional characteristics of structures/textures. Therefore, some processing constraints should initially be determined for both factors according to the application-specific requirements and then used to drive the surface partitioning process [24-26]. At the same time, the overall machining accuracy also depends on the component technologies of LMM systems, i.e. mainly determined by the employed optical and mechanical axes, when executing multi-axis processing strategies. Therefore, their machining performance has been evaluated separately or in combination under a "positioning mode" for precision LMM using optical metrology systems [27-29].

Lately, state-of-the-art multi-axis LMM platforms have been introduced to the market that can operate in a "simultaneous mode" and hence enable the synchronous motion control of multiple optical and mechanical axes during the laser processing operations. As a result, this

technology enables LMM improvements related to the overall processing uniformity and efficiency, especially when curved or even freeform surfaces are processed. In particular, such operations can benefit and employ the highly accurate mechanical axes and the fast scanning capabilities of optical ones, simultaneously. However, multi-axis simultaneous processing strategies are associated with inferior overall machining accuracy due to the spatial accumulated errors of multiple axes and their interactive effects on tool/beam positioning in regard to the workpiece [30]. An analytical description of the error sources affecting the LMM operations is further elaborated by other researchers [31]. Even though information about Accuracy, Repeatability and Reproducibility (ARR) of optical and mechanical axes are provided in the technical specifications by the manufacturers, it is not possible to estimate the machining ARR when executing multi-axis motions and the uncertainty associated with such processing strategies. Therefore, the use of systematic evaluation procedures for assessing the machines' overall ARR are essential as they are required to determine the geometrical and dimensional tolerances achievable when processing complex 3D components.

In this respect, various test pieces, such as a semi-sphere, a cone frustum in NAS 979 or a S-shaped piece in ISO 10791-7, requiring multi-axis simultaneous machining have been proposed as indirect assessment methods for evaluating the overall performance of conventional 5-axis machine tools under quasi-static and/or dynamic states [32-35]. In such machining tests, the motion errors of all employed axes are combined/superimposed onto the finished part and hence they can be used as a final acceptance test for machine tools after their installation on-site. Nevertheless, a similar verification test has not been reported for LMM systems, yet, most likely because simultaneous multi-axis LMM capabilities have only been introduced to the market, recently. Thus, further efforts are necessary to develop a systematic

method for assessing ARR of LMM systems when executing simultaneous multi-axis processing strategies that combine both optical and mechanical axes.

This research reports an investigation into the capabilities of state-of-the-art multi-axis LMM systems that are specially designed and implemented for processing complex 3D components. Firstly, the generic concept for laser texturing/structuring/scribing of freeform/curved surfaces is introduced that offers a higher processing efficiency due to the simultaneous control of both optical and mechanical axes. Thereafter, a generic method is proposed for assessing the impact of different error sources on the ARR of such laser processing setups. An experimental study was conducted to quantify and compare ARR when both optical and mechanical axes were simultaneously utilised in different combinations/processing strategies for precision laser texturing/structuring/scribing operations under quasi-static and dynamic conditions. Lastly, the validity of the proposed method is discussed, and conclusions are made about its capability to assess the performance of multi-axis LMM systems.

6.2. Multi-axis simultaneous laser processing

In general, there are various types of multi-axis LMM system configurations available on the market, however the most common one includes three linear-axis drivers (X, Y, Z), two rotary-axis drivers (C, B or A) and a galvo scan head. An example of such multi-axis LMM system is provided in Sub-section 6.4. The basic principles of simultaneous multi-axis LMM are very similar to those in conventional machining. The axes' motions are coordinated, e.g. the movements from an initial to a final position can be defined as machining/beam vectors according to the number of axes involved. For LMM of freeform/curved surfaces, the axes are programmed to start/end their movements at the same time. Compared to conventional machining, the LMM technology involves two additional optical axes (Gx, Gy) realised with

beam deflectors integrated into the galvo scanners. As such, laser texturing/structuring/scribing operations allow variations of FOD and BIA along the beam paths to benefit from their high beam deflection speed. Thus, this inherent characteristic can contribute not only to minimise the overall machining time, but also to circumvent the use of an optical Z module for dynamically refocusing the laser beam on the surface. Nevertheless, the FOD and BIA, i.e. the angle (θ) between the laser beam and the surface tangent at the incident point, variations should be constrained within an effective processing area where their negative side effects do not jeopardise the desired machining performance. As can be seen in Fig. 6.1a, this area should be equal to or smaller than the lenses' Field of View (FOV) on curved surfaces and is typically defined by the Rayleigh length.

Furthermore, the generation of beam paths with a certain directionality, e.g. vertical, horizontal or diagonal, and the synchronous control of optical and mechanical axes motions has specific requirements and cannot be implemented using stand-alone universal Computer-Aided Design (CAD)/Computer-Aided Manufacturing (CAM) tools. Therefore, specially developed postprocessors are necessary and they should be integrated into existing CAD/CAM packages. They output the programmed movements into beam vectors while considering the points where the laser source should be turned on/off. For clarity, a graphical representation of a geometry projected on a sphere's periphery that should be processed/scribed using simultaneous multi-axis LMM strategy is shown in Fig. 6.1b. In such processing strategies, the orientation of beam paths and the motion of mechanical axes should be perpendicular to each other. In particular, both optical axes should be deployed to execute the desired processing strategy, whilst the mechanical axes are simultaneously used to maintain the centre of each beam path at the focal plane and the BIA normal to the surface. For processing large surface areas, i.e. when their size along the beam scanning direction exceeds either the laser's

effective processing area or lens's FOV, they must be partitioned into multiple scanning fields. In contrast, it should be noted that there is no need for partitioning the surfaces along the mechanical axes trajectory and thus the stitching errors can be reduced when executing multi-axis simultaneous LMM strategies. After partitioning the surfaces, each scanning field is processed individually and then the mechanical stages are deployed to reposition the laser beam between them. Generally, the surface partitioning process can be implemented using algorithms/tools available in most commercial CAD packages by specifying some geometrical constraints [24].

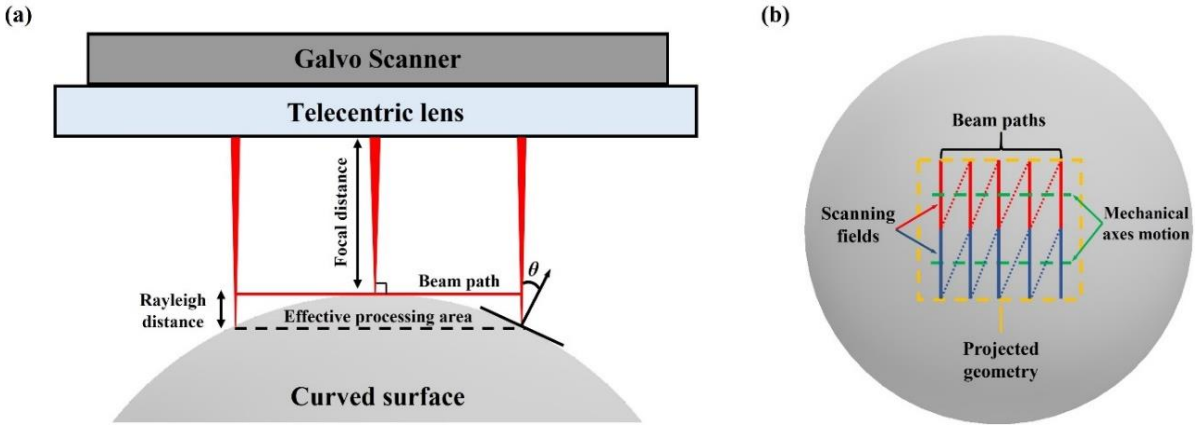

Fig. 6.1. A schematic representation of: (a) a single beam path on a curved surface; (b) a geometry projected on a spherical surface that should be scribed using a simultaneous multi-axis LMM strategy. *Note:* The red and blue dashed lines in (b) represent the motions of optical axes when the laser source is inactive.

6.3. Methodology

A generic empirical method is proposed for assessing the overall performance of multi-axis simultaneous laser structuring/texturing/engraving operations under both quasi-static and dynamic conditions. An overview of all the steps involved is given in Fig. 6.2. The prerequisites for implementing this method are to: i) predefine an effective processing window

for machining freeform/curved surfaces; and ii) compensate the negative dynamic effects of the optical beam deflectors before investigating the dynamic capabilities of such laser processing setups. These two aspects in the proposed methodology are introduced/discussed briefly in the next two sub-sections for completeness before the generic method for assessing the capabilities of multi-axis LMM systems is described.

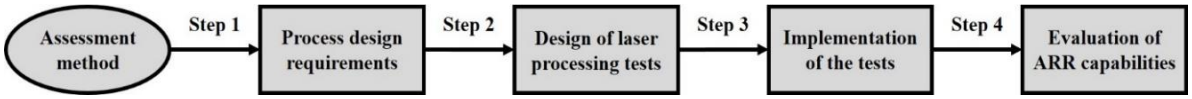

Fig. 6.2. The sequence of steps to execute the proposed assessment method.

6.3.1. Effective processing window

In laser processing of freeform/curved surfaces, the beam paths cannot anymore lay fully onto the focal plane (see Fig. 6.1a) and thus an acceptable range of FOD variations should be defined for obtaining satisfactory machining results. Theoretically, this FOD limit should be equivalent to the Rayleigh length as the laser beam is considered in focus within this range. However, in the case of LMM operations requiring high precision, any displacements from the focal plane may influence the width and depth of machined structures depending on the used laser source and workpiece material. Therefore, alternative strategies should be followed as proposed in [36] to define the effective processing area by conducting some preliminary laser trials. In brief, these strategies require to scribe a set of structures onto a planar workpiece with varying FODs while BIA is kept normal to the surface. In this way, the impact of FOD on the ablation depth can be quantified and the processing performance satisfactory cut-off value can be determined. An example of such preliminary trials is provided in Sub-section 6.4.2.

6.3.2. Dynamic effects of optical beam deflectors

In LMM operations, the optical beam deflectors, i.e. optical axes, are used for steering the laser beam across the workpiece surface and thus they accelerate/decelerate whenever its velocity or motion trajectory has to change. Without applying any compensations, this can have a significant impact on the achievable quality and dimensional accuracy of machined structures. For instance, the existence of acceleration/deceleration regions at the beginning and end of each beam path can result in discrepancies between the desired and actual machined patterns on surfaces as shown in Fig. 6.3a. At the same time, it can lead to variations in the ablation depth of the machined structures. As can be seen in Fig. 6.3b, a higher removal rate can be detected in the processed areas where the effects of accelerations/decelerations are present. In reality, such errors are more pronounced at high scanning speeds and are mainly attributed to the inertia of deflectors' driving motors [37]. Therefore, it is essential to counteract the aforesaid negative dynamic effects of beam deflectors prior to investigating the LMM system's ARR capabilities under dynamic conditions. Especially, an empirical method should be used to compensate these dynamic effects and thus to attain a constant velocity along the beam vectors when the laser source is triggered. Firstly, the process requires the acceleration/deceleration regions of the beam deflectors to be determined experimentally using a strategy similar to that proposed in [38]. As such regions are dependent on the set scanning speeds and the specific LMM setups, an example of how they could be determined is provided in Sub-section 6.4.2. Thereafter, the beam vectors should be adjusted to include these compensations. As a result, accelerations/decelerations occur only in these regions while the laser source is switched off.

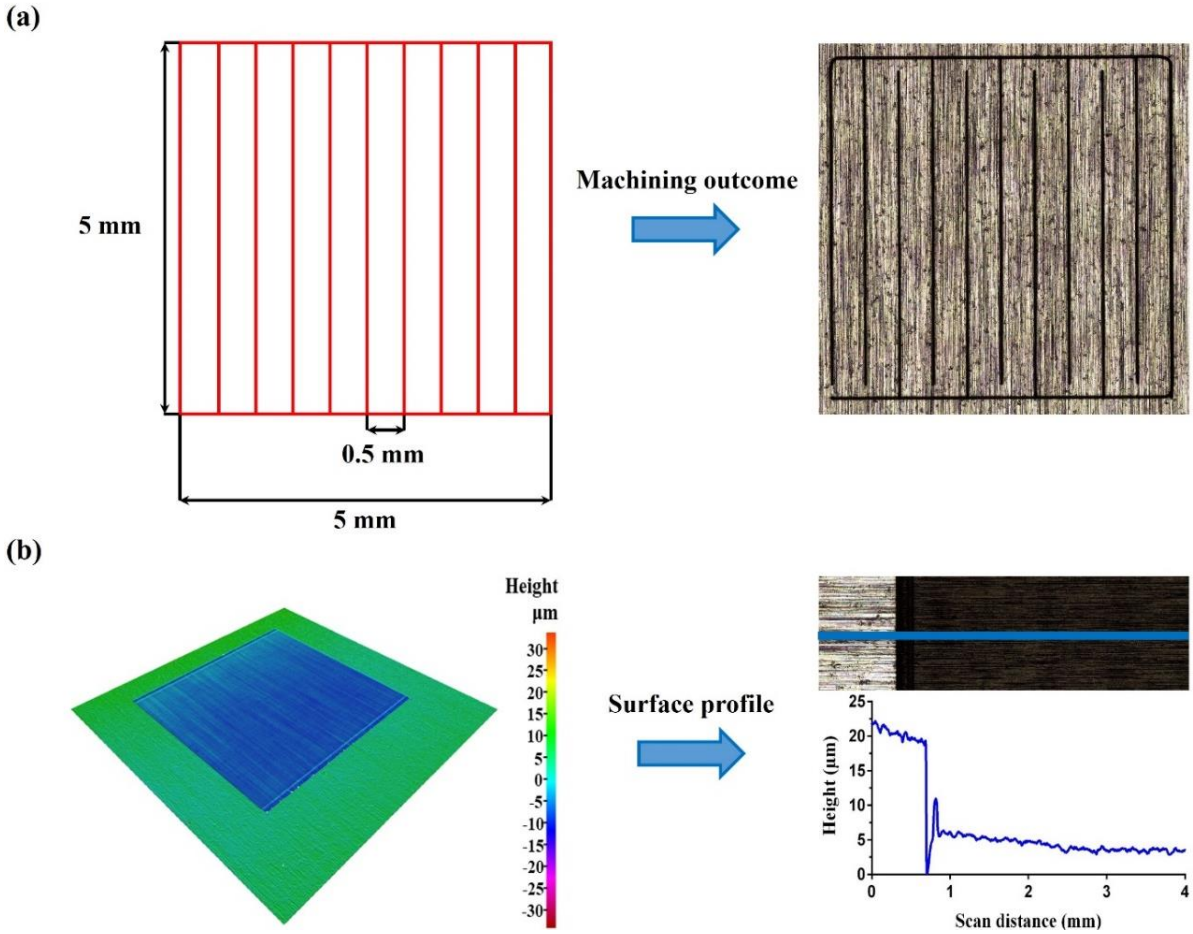

Fig. 6.3. Negative dynamic effects of beam deflectors at a scanning speed of 500 mm/s without applying any compensation method: (a) dimensional discrepancies between the programmed (red lines on the left side) and the actual beam scribing (line-like structures on the right side); (b) a height map of the processed area (left) and surface profile (right) of a pocket with non-uniform ablation at the walls (beam trajectories change points). *Note:* The blue profile in (b) shows the effect of the beam acceleration and deceleration in executing the processing strategies.

6.3.3. Method for assessing simultaneous multi-axis laser processing strategies

The assessment method is proposed in this research that requires four Laser Processing Tests (LPTs), namely LPT 1, LPT 2, LPT 3 and LPT 4, to be performed onto spherical test pieces

to judge the ARR capabilities of LMM systems when conducting simultaneous multi-axis texturing/scribing/structuring operations on curved/freeform surfaces. In particular, this method requires, first, an accurate 3D model of the spherical samples to be created using a CAD/CAM software. Thereafter, a set of four patterns, which should be scribed on the surface in the four LPTs, has to be designed and projected onto it as shown in Fig. 6.4a. For clarity, each projected pattern in the set is used for a different test. It is worth noting that the patterns' dimensions should be selected in such a way that they should be within the effective processing area of the laser. In addition, the intrinsic constraints introduced by the rotational ranges of A or B axes should be taken into consideration when selecting their dimensions, too.

The LPTs were specially designed to investigate all available options in executing multi-axis laser texturing/scribing/structuring operations that require simultaneous control of both mechanical and optical axes. Therefore, a different processing strategy should be utilised to process the pattern for each test. For instance, the most common scanning strategies, i.e. vertical, horizontal and diagonal at 45° and - 45° to the horizontal one, which at the same time include all the possible simultaneous combinations of optical and mechanical axes, are depicted in Fig. 6.4b. For LMM system configurations that include either B or A rotary-axis, the combinations of simultaneous multi-axis motions required to execute the processing strategies in each LPT are summarised in Table 6.1. Even though this research refers mainly to the most common LMM configuration and scanning strategies, the fundamental idea behind the design of this assessment tests and method can easily be extended to evaluate any type of multi-axis LMM configuration and scanning strategy.

Table 6.1. The processing strategies with their respective simultaneous axes motions employed in executing the four tests on a LMM system with either B or A rotary-axis.

LPT no.	Scanning strategy	Multi-axis LMM system configurations with	
		B rotary-axis	A rotary-axis
LPT 1	Vertical	C, Gx, Gy	C, Gx, Gy
LPT 2	Horizontal	X, Z, B, Gx, Gy	Y, Z, A, Gx, Gy
LPT 3	Diagonal (45°)	X, Z, B, C, Gx, Gy	Y, Z, A, C, Gx, Gy
LPT 4	Diagonal (- 45°)	X, Z, B, C, Gx, Gy	Y, Z, A, C, Gx, Gy

In all test strategies, a constant offset distance (h_1) between any two consecutive beam scribing vectors should be set to produce line-like structures on the surface with only a single pass. Ideally, this distance should be selected according to the application-specific requirements. However, it should be sufficiently big so that the scribing lines do not overlap even in the case when the maximum predetermined FOD and BIA limits are present. Meanwhile, another set of equally distant (h_2) beam scribing vectors, i.e. three perpendicular to the other ones (see the blue lines in Fig. 6.4b), should also be added to the tests and then used as reference to evaluate the geometrical accuracy of the scribing lines produced with the former set of beam vectors. Thus, it should be noted that the execution of these beam vectors and the relative positioning movements between them must be performed only with X and Y mechanical axes due to their higher ARR compared to the optical axes.

Furthermore, the proposed test method aims to assess the ARR capabilities of LMM systems. Therefore, pseudo-repeatability and reproducibility tests should be carried out by repeating the four LPTs on the same and on another spherical sample using the same laser processing parameters, respectively. As such, three sets of identical scribing patterns should be produced

on the two samples, namely Pattern Set 1 (PS 1) on sample 1, Pattern Set 2 (PS 2) on sample 1 and Pattern Set 3 (PS 3) on sample 2. Thereby, the ARR capabilities of a LMM system to execute the LPTs should be assessed based on the results obtained from these three Pattern Sets. To judge the overall performance of LMM systems under quasi-static, i.e. with no dynamic influences and servo control limitations, and dynamic states, the whole experimental procedure needs to be conducted at both low (e.g. less or equal to 10 mm/s) and high (e.g. equal or above 100 mm/s) scanning speeds. However, when investigating their dynamic capabilities, the beam vectors should be adjusted as described in the previous sub-section to avoid/minimise the negative dynamic effects associated with optical axes. At the same time, it is necessary to ensure that the compensation for the first beam vector is sufficient to allow a constant velocity to be reached along the mechanical axes at the beginning of each laser processing operation.

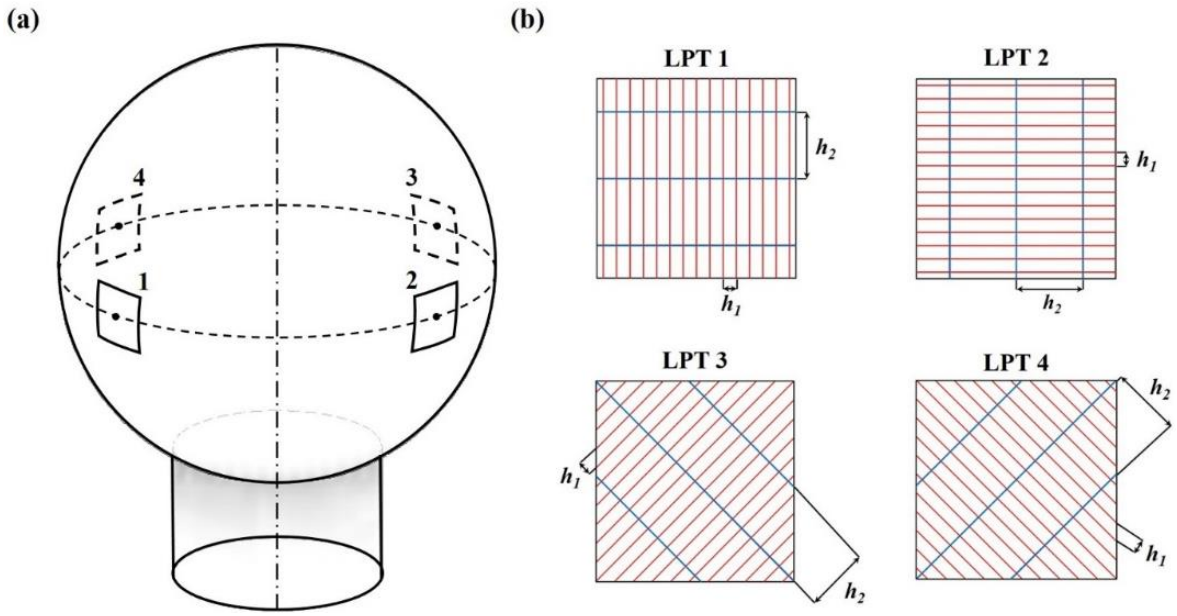

Fig. 6.4. The LPTs in the proposed method for assessing the performance of different simultaneous multi-axis LMM strategies: (a) a schematic illustration of the patterns that should be scribed on the spherical surface in the four LPTs; (b) the scribing strategies employed to produce the four patterns in the tests.

Due to the contactless nature of the LMM technology, laser texturing/scribing/structuring operations can tolerate some deviations in BIA from normal together with some FOD variations until evident alterations of the machined structures can be observed [39]. As a result, the actual processing errors, i.e. in the width and depth of the scribing lines, may not be truly reflected onto the surface and hence they cannot be quantified accurately. Therefore, only the deviations in the length (d_1), pitch (d_2) and geometrical accuracy of the scribing lines produced with a single pass should be considered in assessing the ARR achievable with the investigated simultaneous multi-axis LMM strategies. However, the d_2 and geometrical accuracy can vary along the scribing lines due to the simultaneous movements of mechanical and optical axes required to execute the programmed beam vectors in the four LPTs. Therefore, their average values should be determined based on multiple measurements taken at different places along the scribing lines. An example on how to measure the three aforementioned parameters is given in Sub-section 6.4.5. At this point, it should be stated that their geometrical accuracy can be quantified by measuring their perpendicularity (g) against the reference ones produced using only the mechanical stages. Regarding the scribing lines' d_1 and d_2, the processing accuracy should be assessed based on their maximum deviations from their nominal/programmed values. On the other hand, the repeatability and reproducibility should be evaluated by comparing the measured values with their respective average values obtained from samples 1 and 2, respectively. Lastly, to ensure that the ARR capabilities of LMM systems can be quantified in a reliable and repeatable manner using the proposed test method, the uncertainty associated with the employed measuring equipment and procedures must be kept to a minimum. A flowchart is provided in Fig. 6.5 that summarises the main steps and methodology proposed in this research to evaluate the overall performance of LMM systems.

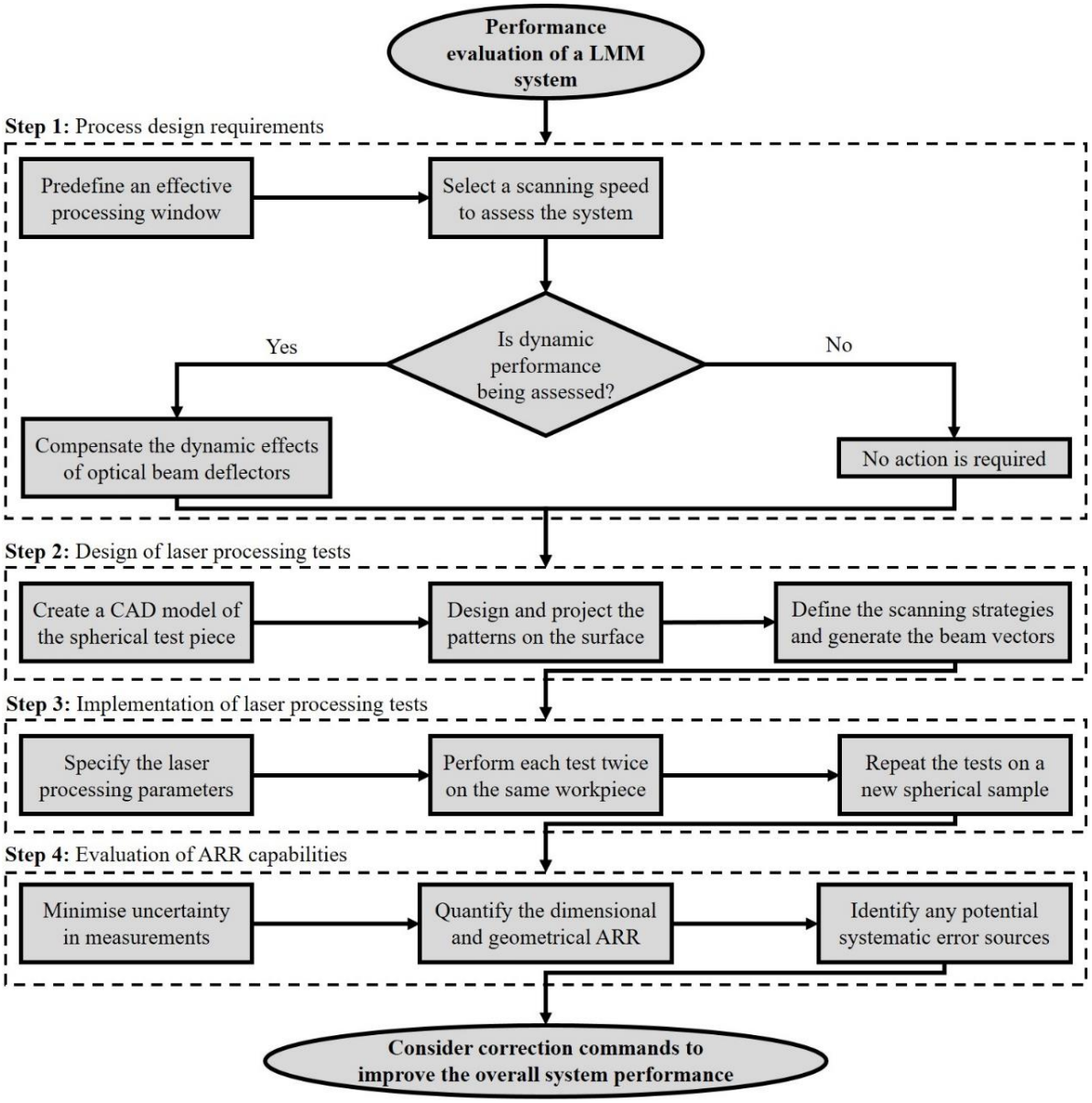

Fig. 6.5. Flowchart summarising the procedure to evaluate the performance of a LMM system.

6.4. Pilot implementation

A pilot implementation of the proposed methodology is provided in this section. To demonstrate the applicability of the proposed method, a multi-axis LMM system was selected that was capable of executing the considered LPTs and thus to show what quantitative data about the ARR capabilities of such systems can be obtained.

6.4.1. Experimental set-up and analysis tools

The experimental trials were conducted on the state-of-the-art LASEA LS4 LMM workstation and its main component technologies, i.e. beam delivery sub-system and the multi-axis setup, are depicted in Fig. 6.6. In particular, the system is equipped with a high precision stack of two rotary-axis drivers (B, C) and three linear (X, Y, Z) mechanical stages to tilt, rotate and position the workpiece inside the machine's working envelop. The C rotary stage is on top of the B one and it can rotate continuously, whereas the latter is limited to the range of - 100° to + 30°. In addition, a reconfigurable work-holding device is mounted on the C rotary stage to precisely load and unload the samples. A galvo scan head, mounted on the Z stage, with two optical beam deflectors (Gx, Gy) is incorporated in the beam delivery sub-system that allows the laser beam to be steered with a maximum scanning speed of 50 rad/s. For multi-axis processing strategies, the motions of optical and mechanical axes are fully synchronised and are controlled by a PC-based multi-axis motion controller (Aerotech A3200). To ensure that the beam deflectors operated within their technical specifications, as stated in Table 6.2, an automated calibration process was carried out prior to the LMM operations. At the same time, the positioning ARR of the linear stages (see Table 6.2) were measured using a laser interferometer and were then error mapped by the manufacturer during the installation.

Table 6.2. Technical specifications of component technologies (as provided by the manufacturer) integrated into the LS4 workstation.

Specifications	X/Y axis	Z axis	B axis	C axis	Optical axes
Travel range	500/300 mm	200 mm	-100° to +30°	continuous	37°
Resolution	0.1 μm	1 μm	0.01°	0.01°	0.0006°
Max travel speed	200 mm/s	150 mm/s	200 deg/s	200 deg/s	2865 deg/s
Acceleration rate	3000 mm/s^2	1250 mm/s^2	500 deg/s^2	500 deg/s^2	-
Accuracy	± 1 μm	± 1.75 μm	5 arc sec	6 arc sec	± 5 μm
Repeatability	± 0.4 μm	± 1 μm	3 arc sec	3 arc sec	± 0.0006°
Thermal drift	-	-	-	-	± 0.001°
Tracking error	-	-	-	-	160 μs

Furthermore, the LS4 workstation integrates a 10 W ultrafast femtosecond laser source (Yuja, Amplitude Systems) with a central wavelength of 1030 nm delivering pulse energies up to 100 μJ at 100 kHz, pulse durations in the range from 300 fs to 10 ps, and maximum repetition rates up to 2 MHz. Also, the workstation integrates a 50 W pulsed nanosecond fibre laser (GLPN series, IPG) that operates at a central wavelength of 515 nm. In this research, the experimental work was conducted using the ultrashort pulse laser in order to attain a higher structuring quality, i.e. edge definition, and thus to minimise the measurement uncertainty in quantifying the system's ARR capabilities. Nevertheless, it should be noted that the proposed assessment method can be implemented onto any multi-axis LMM system irrespectively of the laser source integrated into it.

Commercially available aluminium spheres, with a nominal diameter of 40 mm and deviations from sphericity within ± 0.5 μm, were used in this pilot implementation of the proposed

method. The spheres were attached to a shaft extension of 15 mm, and they were utilised to evaluate the machining ARR capabilities of the LMM system. The substrates were processed with a nearly Gaussian beam ($M^2 < 1.3$), which was focused down to a beam spot diameter of 35 μm at the focal plane using a telecentric lens with a focal length of 100 mm and FOV of 40 × 40 mm^2. As it was already stated in Sub-section 6.2, variations of BIA from normal are always present when processing curved surfaces, which can result in a non-uniform ablation along the beam paths. Therefore, to maintain as consistent as possible ablation along the beam paths regardless of BIA, a quarter waveplate was integrated into the beam delivery system to convert the linear polarisation into a circular polarisation [40]. Moreover, it is worth noting that the four LPTs were initially carried out at a relatively low scanning speed of 10 mm/s in order to characterise the performance of the system under quasi-static conditions. Thereafter, the same tests were repeated at a speed of 100 mm/s to assess the capabilities of the LMM system under dynamic conditions. However, it should be stressed that a constant pulse energy of 50 μJ and a pulse-to-pulse distance of 2 μm was maintained throughout all the experimental procedures, unless otherwise stated.

A fully automated setting up routine, like those in conventional machining, was implemented for correlating the workpiece coordinate system to the machine's one using a CAD/CAM software (GibbsCam). This setting up routine aligns precisely the samples at the focal plane and at the centre of the lens' FOV prior to the LMM operations. In addition, a dedicated module, namely "Laser Process", is integrated into this software which is capable of programming multi-axis LMM movements to execute complex processing strategies. Therefore, it was employed in this research to generate the necessary beam paths and output the respective beam motion commands.

The inspection of the machined structures was performed with the Focus Variation (FV) technology optical microscope (Alicona Infinite Focus G5), which incorporates software tools to perform both surface texture and form measurements on parts with complex 3D geometries. To do so, the system is equipped with a clamping device, which was used for mounting and securing the spherical samples in an exact 90° position and also to move between different machining patterns on them. At the same time, the three integrated linear motorised stages allow X-Y scanning of the processed areas and images of the surface topography to be captured. Thereafter, each single topography captured was automatically combined into a full 3D model of the machined patterns by using for this the overlapping areas of different scan fields. In the stitching process, any motion errors from the linear stages can be neglected as the system compensates them, automatically. Once the real 3D surface was obtained, a range of software tools were employed to extract the surface forms out of the 3D dataset and then the machined structures were inspected offline.

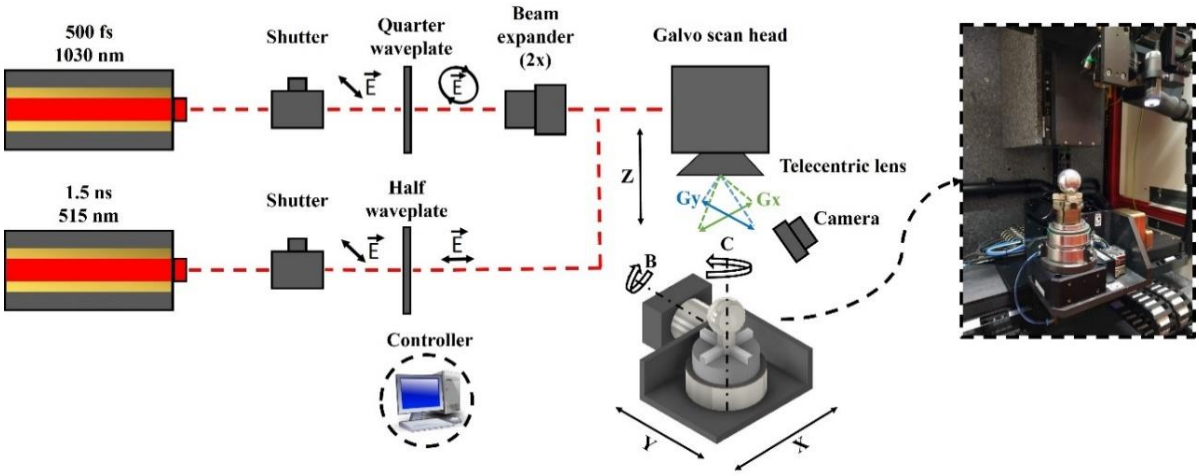

Fig. 6.6. Schematic illustration of the employed multi-axis LMM set up.

6.4.2. Process design requirements

Prior to assessing the ARR capabilities of the LMM system, a series of preliminary trials were conducted on planar aluminium substrates. They were used to determine the effective processing window for machining freeform/curved surfaces and also to compensate any negative dynamic effects of the optical beam deflectors. Each experimental procedure was repeated five times to judge the reliability of the obtained results. The machined structures were analysed using the FV microscope with 50x objective lens and lateral and vertical resolutions of 1 μm and 20 nm, respectively.

6.4.2.1. Effective processing window

To define the effective processing window of the laser source integrated in the LMM system, a vertical scanning strategy was employed to produce scribing lines with a single pass on the surface as depicted in Fig. 6.7a. Each scribing line was produced with increasing FOD, both above (positive) and below (negative) the focal plane, by moving the Z stage in increments of 100 μm. The laser scribing operations were performed with FODs varying in the range of ± 700 μm, and therefore a relatively large spacing of 200 μm was set between the lines. In this way, any overlaps between the lines, especially due to the increasing beam spot size, can be avoided. As can be seen in Fig. 6.7b, significant variations were observed in the ablation depth along the lines processed with FODs in the range from – 700 to + 700 μm. For instance, FOD of ± 300 μm led to an average depth decrease of more than 32%. In this research, the acceptable range of FOD variations, and hence the effective processing window, was defined as a maximum Z offset from the focal plane that entailed an average ablation depth reduction of less than 25% for each scribing line. Therefore, the scribing process was considered effective when the FOD deviations were restricted within ± 200 μm and thus a relatively uniform

scribing depth could be maintained along the beam paths. Nevertheless, this is just an assumption in this research and it should be tailored according to the specific laser-material interaction effects that can affect the conducted LPTs.

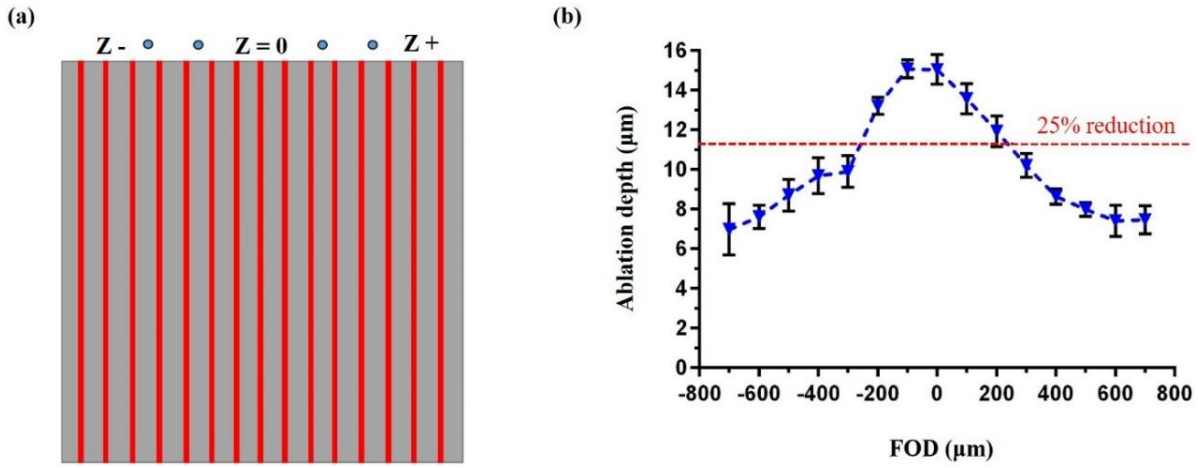

Fig. 6.7. The effective ablation range analysis: (a) the scribing lines produced with a single pass that were used to identify the acceptable FOD limit; (b) the measured depth of the scribing lines at different FODs.

6.4.2.2. Dynamic effects of optical beam deflectors

An empirical procedure was implemented to determine the acceleration/deceleration regions of the scan head beam deflectors when used simultaneously with a scanning speed of 100 mm/s. A set of five beam vectors were employed to produce trains of craters on the surface as illustrated in Fig. 6.8a while the pulse-to-pulse distance was set to 50 µm. Thereafter, the distance between the craters was measured using the automatic fitting tools provided by the 2DImageMeasurement module of Alicona G5 to determine the acceleration/deceleration regions of the beam deflectors. As can be seen in Fig. 6.8b, a non-uniform distance was observed between the craters at the beginning of the beam vectors owing to their acceleration. Once the laser beam reached its steady-state velocity, the pulse-to-pulse distance stabilises and

as a result the distance between the craters becomes uniform. For example, the average acceleration/deceleration length of the beam deflectors employed in this research was 90.2 ± 0.7 μm at a scanning speed of 100 mm/s. Thus, to ensure a constant velocity along the optical axes during the LPTs, this value was added at the start and end of each beam vector to compensate for the beam deflector's dynamic effects. At the same time, the laser source was switched off during the acceleration /deceleration regions along the beam vectors.

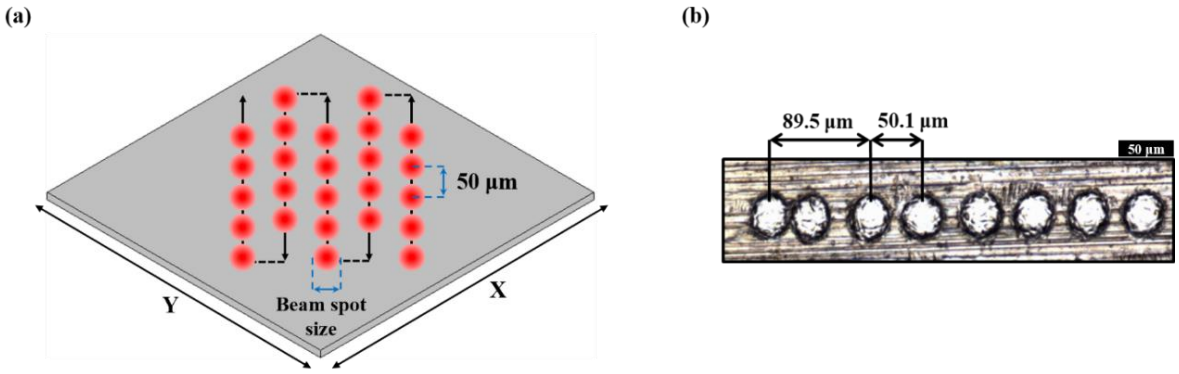

Fig. 6.8. Analysis of negative dynamic effects along the optical axes: (a) the test procedure used to identify the acceleration/deceleration regions along the beam vectors; (b) the varying craters' distance along one of the beam vectors used to determine the respective acceleration/deceleration regions at a scanning speed of 100 mm/s.

6.4.3. Design of laser processing tests

The proposed LPTs for assessing the ARR capabilities of the used multi-axis LMM system were implemented as shown in Fig. 6.9 and the procedure that was followed is explained below in detail. First, an accurate 3D model of the aluminium spheres used in the method pilot implementation was created by using GibbsCAM. Then, the same software was used to design and project the patterns onto the surface of the test sphere. They were four equidistantly 3 × 3 mm^2 square patterns and each of them was used for a different LPT. The size of these four

processing fields was chosen so that the FOD variations along the beam paths did not exceed ± 200 μm. A different laser processing strategy was employed to scribe the respective patterns in each test. The desired orientation of the beam vectors in each LPT was defined with guide curves in the used CAD/CAM software that were overlaid onto the 3D sample. Especially, these guide curves determined the direction of mechanical axes' movements during the scribing operations, and thus the beam vectors were oriented perpendicularly to them. It is worth noting that the processing strategies and the combinations of simultaneous multi-axis motions used to execute each LPT were as defined in Table 6.1 for a multi-axis LMM configuration with B rotary-axis.

Furthermore, a constant offset distance of 0.2 mm was set between any two consecutive beam scribing vectors and the patterns were produced with a single pass. In addition, three beam vectors, which were 1 mm apart, were also included in the tests to produce reference scribing lines. They would be used to assess the geometrical accuracy, i.e. their *g* to the other scribing lines produced in the LPTs, and also to position the patterns at the centre of the FV microscope's FOV when scribing them. As stated in Sub-section 6.3.3, the relative positioning movements between these three beam vectors were performed with only the X and Y mechanical axes to achieve the maximum possible accuracy in the used laser processing configuration. At this point, it should be noted that the width of the scribing lines produced on the test pieces was depended on the beam spot diameter at a given FOD and BIA. Based on our initial scribing trials in Sub-section 6.4.2, variations of scribing lines' width were marginal, within FOD of ± 200 μm. At the same time, taking into consideration both the test piece geometry and the predetermined maximum FOD limit, the BIA variations had a relatively small impact on the resulting scribing lines in the LPTs. Similar observations were also reported in [39], which found that small BIA variations had an almost negligible impact on the

morphology of the scribing lines. Thus, the beam spot size and the width of the scribing lines can be deemed constant inside the predetermined effective processing window. Meanwhile, it should be reiterated that the beam vectors were modified as described in the previous section to avoid/minimise the negative dynamic effects of optical axes. Specifically, corrections, i.e. in/out movements for each scribing vector, were introduced in the generated beam paths with GibbsCAM. At the same time, the mechanical axes had a constant velocity that was attained by adjusting the first lead into the beam movement at the beginning of each operation. Finally, a pseudo-repeatability test was performed by repeating the four LPTs on the same sample with a predefined angular displacement of 22.5° from the first patterns along the C axis. Thereafter, a reproducibility test was also carried out on another identical spherical sample using the same laser processing parameters.

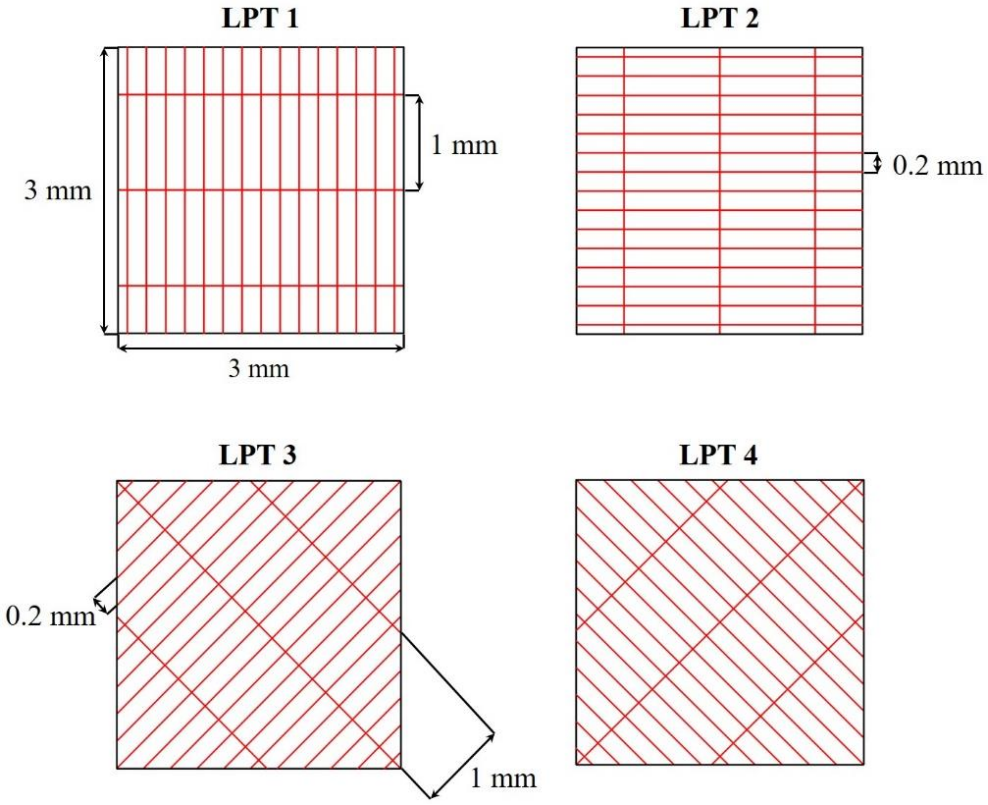

Fig. 6.9. The implemented LPTs to assess the performance of the employed multi-axis LMM system.

6.4.4. Uncertainty assessment

The focus variation technology was used for inspecting the scribing lines and quantifying the system's ARR capabilities in this research. Therefore, the uncertainty (u_a) related to the instrument's measurement repeatability was analysed regarding the three measurands. Then, the overall uncertainty (U) in assessing the ARR of simultaneous multi-axis LMM strategies was calculated in accordance to GUM as follows [41]:

$$U_i = max\left(u_{a,i}, u_{b,i}, u_{c,i}\right) \tag{6.1}$$

where: $i = d_1$, d_2 and g, the measurands used to quantify the processing ARR capabilities; $u_{a,i}$ - the experimental standard deviation of 10 repeated measurements of the same scribing line; $u_{b,i}$ - the experimental standard deviation of repeated measurements on different scribing lines from the two similar patterns produced on the same sample to evaluate the machining repeatability; and $u_{c,i}$ - the experimental standard deviation of repeated measurements on different scribing lines produced on the two samples in order to assess the system's reproducibility. To avoid overestimating the influence of the instrument's repeatability on the overall uncertainty, the largest uncertainty contributor among the calculated type A uncertainties, i.e. (u_a, u_b, u_c), was chosen [42].

Furthermore, the employed measuring procedure itself can significantly affect the instrument's repeatability and consequently the uncertainty in quantifying the system's ARR. Thus, its uncertainty contribution must be minimised in order to perform a reliable analysis. In this regard, a pattern as those produced on the spherical samples in the proposed assessment method was fabricated on a planar substrate and the distance between two lines was measured 10 times as shown in Fig. 6.10a. It is worth noting that the surface was scanned using only the

objectives that provide a lateral resolution better than 1 μm, whilst the measurements were performed by using two methods that minimise the subjective errors associated with the operator. First, the distance between the edges of the 1st and the 2nd lines was measured using the 2DImageMeasurement module available in Alicona software, i.e. by employing an automatic edge detection. Secondly, the distance was measured by using two respective cross-sectional profiles of the lines. Especially, the distance between two points with the maximum depth in these profiles was measured using the ProfileFormMeasurement module. The calculated average values of these measurements and their corresponding standard uncertainties for the considered three Alicona objectives are plotted in Fig. 6.10b. As expected, the measurement uncertainty decreased with the increase of the objectives' magnification with both measurement methods. A higher scattering of the measurement results was obtained with the second method and therefore the 2DImageMeasurement module was used to perform all the measurements in this research. The measurement uncertainty of this method, employing the three objectives, is stated in Table 6.3. Considering both the precision of the measurement results and the time required to obtain them, the 50x objective was selected to conduct all measurements in this research.

Table 6.3. The measurement uncertainty associated with the three objectives when using the 2DImageMeasurement module.

Objectives	Vertical resolution (μm)	Lateral resolution (μm)	u_a (μm)
20x	0.10	0.90	0.9
50x	0.04	0.64	0.5
100x	0.02	0.44	0.3

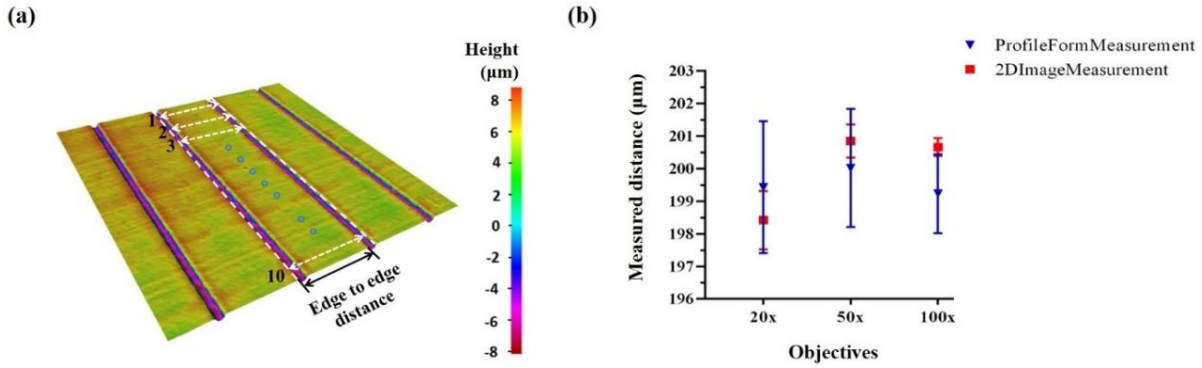

Fig. 6.10. The measurements conducted by using the two methods: (a) a representative 3D image of the scribing lines with 10 measurements between two consecutive ones; (b) a plot of the standard uncertainties and average values obtained when measuring the distances between two scribing lines with the three objectives and the two methods.

6.4.5. Results and discussion

The results of the pilot implementation of the proposed methodology are presented and discussed in this section. Fig. 6.11a-d shows PS 1, i.e. one of the three Pattern Sets produced with the four LPTs on the two samples. 10 different scribing lines on each of the pattern (see Fig. 6.11a-d) in the three sets, i.e. PS 1, PS 2 and PS 3, were measured to assess the capabilities of the multi-axis LMM system. Especially, the measurements of scribing lines' d_1, d_2 and g were taken on the patterns produced with each test as shown in Fig. 6.11e. The average value of 10 repeated measurements were used to calculate the deviations from the programmed and executed beam vectors. Since d_2 and g may vary along the scribing lines as stated in Sub-section 6.3.3, their average values were determined based on repeated measurements taken at 10 and 3 equally distant places along the scribing lines, respectively. By applying the measuring procedure described in Sub-section 6.4.4, the overall uncertainty, U, associated with the measurands d_1, d_2 and g was better than 0.9 µm, 0.5 µm and 0.1° in this research, respectively.

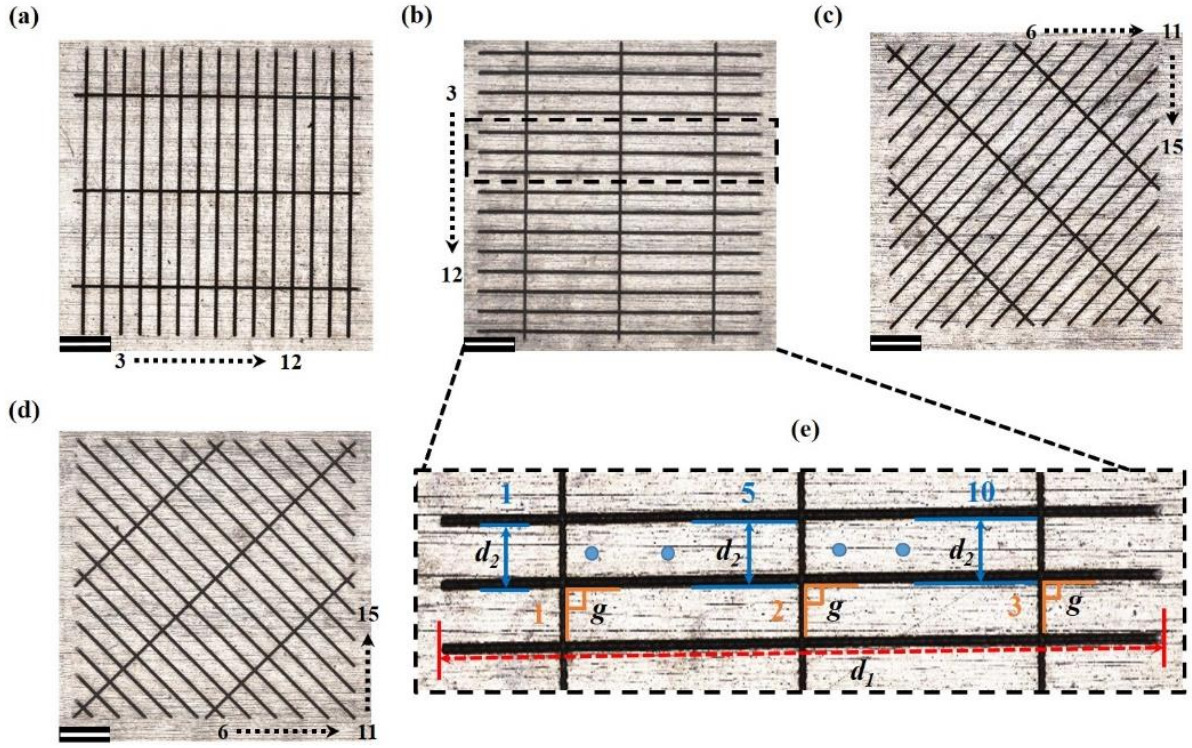

Fig. 6.11. The patterns in PS 1 that were produced with the four LPTs: (a-d) top view of the four patterns in PS 1 produced with a scanning speed of 10 mm/s; (e) a close view of three scribing lines in (b), which depicts the procedure followed to measure the d_1 (the arrow red dashed line), d_2 (the arrow blue line) and g (the orange 90^0 angle sign). *Note:* The black arrow dashed lines and numbers in (a-d) signify the scribing lines measured on the patterns produced in the four LPTs. Scale bar: 500 μm.

6.4.5.1. Laser processing test 1

The processing ARR achievable when the C rotary-axis is used simultaneously with both optical ones, i.e. the beam deflectors, to execute a given LMM strategy is analysed experimentally in this test. The measurements conducted to assess the system's performance under quasi-static conditions, i.e. when laser processing was carried out at a lower scanning speed of 10 mm/s, are depicted graphically in Fig. 6.12a-c. The graphs show the deviation of actual measured values from the programmed beam vectors for the scribing lines produced

with the vertical scanning strategy in the three Pattern Sets (PSs 1, 2 and 3). As can be seen in Fig. 6.12a, the maximum deviations observed regarding d_1 of the scribing lines were 32.4 μm, 34.4 μm and 40.5 μm for PSs 1, 2 and 3 on the two samples, respectively. Therefore, it can be stated that the accuracy in executing the beam movements along the programmed beam vectors was better than 40.5 μm. However, the repeatability and reproducibility were less than 3.5 μm and 7 μm based on the average measurements from samples 1 and 2, respectively. It is evident from these results that the deviations were mainly due to systematic errors and therefore they can be compensated. Conversely, the deviations of d_2 between the scribing lines were much smaller as shown in Fig. 6.12b. Thus, it can be judged that the accuracy achievable between two consecutive beam vectors was better than 2.9 μm, whilst the repeatability and reproducibility were 1.4 μm and 2.6 μm, respectively. At the same time, Fig. 6.12c presents the geometrical accuracy of the scribing lines, i.e. their g in regard to the reference ones, in PSs 1, 2 and 3 on the two samples. These results show that the deviation of the scribing lines from their g was less than 0.49°, whereas the respective geometrical repeatability and reproducibility were better than 0.28° and 0.39°, respectively. Finally, the processing uncertainties associated with the conducted LPT were calculated in the same way as the measurement uncertainties using Equation 6.1. Based on these calculations, it can be stated that the overall processing uncertainty, U, in producing the patterns in LPT 1 was ± 3.7 μm and ± 1.5 μm with regard to the scribing lines' d_1 and d_2, respectively, while regarding their g, it was ± 0.35°.

Thereafter, the same test was performed at a higher scanning speed of 100 mm/s to assess the dynamic performance of the system and the measurement results are presented in Fig. 6.12d-f. As expected, the dimensional accuracy of the scribing lines worsened as the processing speed increased. More specifically, the accuracy of d_1 and d_2 dropped down to 69.7 μm and 5.4 μm,

respectively, while their deviation from g was less than 0.66° based on the results from the three Pattern Sets. Again, the relatively large deviations of the scribing lines' d_1 were mostly due to systematic errors as the repeatability and reproducibility achieved in executing them was found to be 13.3 μm and 17.7 μm, respectively. This was true for their d_2, too, because the repeatability achieved between two consecutive lines was better than 2.5 μm, while the reproducibility was 3.6 μm. On the contrary, it was evident in Fig. 6.12f that the repeatability and reproducibility in regard to the scribing lines' geometrical accuracy worsened, as the maximum absolute errors obtained when comparing the measured values with the average ones from either one or two samples was 0.62°. Such relatively high geometrical deviations during the machining were mainly ascribed to random errors that would be difficult to compensate/reduce without increasing the overall processing performance of the LMM system. Thus, it can be stated that the processing uncertainty, U, regarding the scribing lines' d_1 and d_2 were ± 10 μm and ± 3.1 μm, respectively, while regarding their g, it was ± 0.63°. Considering the results presented in Fig. 6.12, it can be concluded that there is an obvious difference between the dimensional accuracy achieved on the sample 1 and sample 2 for both, quasi-static and dynamic, conditions during this LPT. In contrast, this was not the case regarding the geometrical accuracy (see Figs. 6.12c and f), as the results obtained from the three Pattern Sets on the two samples were quite similar. This difference can mainly be explained with the use of a reconfigurable work-holding device and/or the precision of mechanical stages employed to position the sample at the centre of the lens's FOV prior to the LMM operations.

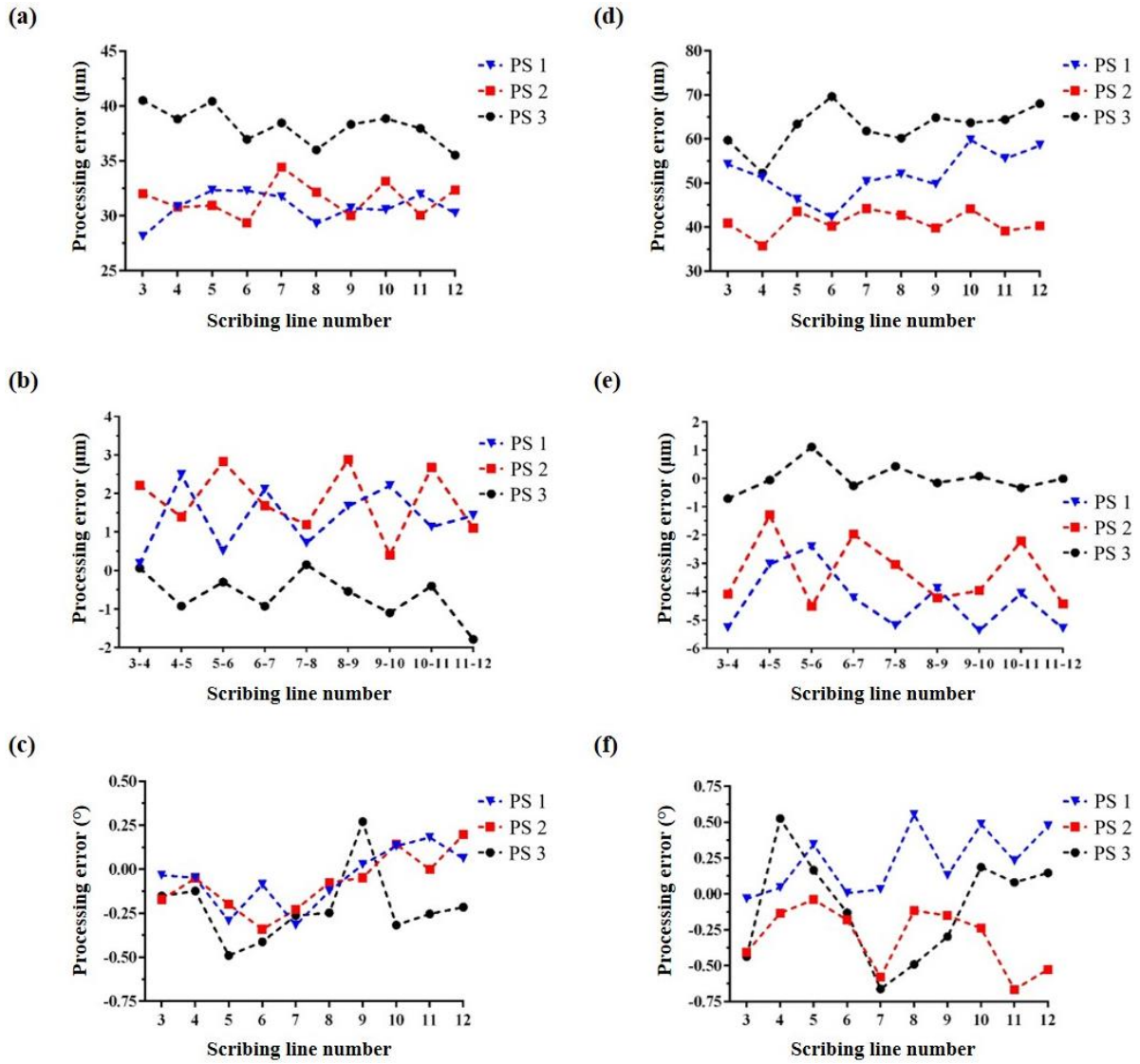

Fig. 6.12. The effects of multi-axis laser processing errors on d_1, d_2 and g of the scribing lines produced in LPT 1 under quasi-static (a-c) and dynamic (e-f) conditions, respectively.

6.4.5.2. Laser processing test 2

The aim of this LPT was to assess the processing ARR achievable when 5-axis, i.e. 3 mechanical and 2 optical axes, are utilised simultaneously to execute a given LMM strategy. Initially, the systems' performance was tested at a relatively low scanning speed of 10 mm/s, especially at quasi-static LMM conditions, and the measurement results are provided in Fig. 6.13a-c. As can be seen in Fig. 6.13a, the largest deviation of the scribing lines' d_1 from the

programmed beam vectors was less than 40.3 μm based on the measurements of the three Pattern Sets on the two samples. Despite that, the corresponding repeatability and reproducibility achieved was better than 3.4 μm and 6.3 μm based on their average d_1 calculated from the patterns processed on one and two samples, respectively. Once again, the observed deviations from the d_1 of the programmed beam vectors were mostly attributed to systematic errors and hence the processing accuracy can be improved substantially by compensating them. At the same time, it can be noted that there were no significant discrepancies between the LPTs 1 and 2 regarding the scribing lines' d_1. Even though different combinations of mechanical and optical axes were used to execute the beam vectors in these tests, both LMM strategies led to almost equal cumulative errors regarding scribing lines' d_1. Therefore, the dimensional accuracy achieved regarding d_1 might be explained with the cumulative tracking error of the galvo scanner. Nevertheless, this was not the case regarding the d_2 between any two consecutive scribing lines where the errors were higher in comparison to those in LPT 1. Especially, the deviations identified in their d_2 were in the range of 0.4 to 4.9 μm for the three Pattern Sets on the two samples. Thus, the ARR capabilities of the system to execute consecutive beam vectors in producing the three patterns were better than 4.9 μm, 1.6 μm and 2.3 μm, respectively. Moreover, a thorough analysis of the scribing lines' geometrical accuracy revealed that their deviations from g were ranging from 0.1° to 0.5° on the three Pattern Sets. Therefore, the machining ARR achieved regarding the geometry of the three patterns were better than 0.52°, 0.48° and 0.48°, respectively. Finally, it is worth noting that the overall processing uncertainty, U, regarding the scribing lines' d_1, d_2 and g in the LPT 2 was ± 3.7 μm, ± 1.9 μm and ± 0.44°, respectively.

Next, the whole experimental procedure was repeated to assess the influence of dynamic effects on LMM patterns. Figs. 6.13d-f show the processing errors about the scribing lines' d_1,

d_2 and g when the scanning speed was set at 100 mm/s. Generally, the ARR capabilities of the system have worsened significantly under these dynamic conditions. For instance, the dimensional accuracy regarding the scribing lines' d_1, d_2 and g declined to 79.9 μm, 8.7 μm and 0.9°, respectively. At the same time, the negative dynamic effects due to the higher processing speed led to a lower machining repeatability and reproducibility, too. Especially, the repeatability and reproducibility regarding the scribing lines' d_1, d_2 and g under these dynamic conditions were found to be better than 15.3 μm, 4.3 μm and 0.89°, and 28.3 μm, 5.6 μm and 0.85°, respectively. Thus, it can be stated that the processing uncertainty, U, in regard to their d_1, d_2 and g under these dynamic conditions were ± 15.9 μm, ± 3.1 μm and ± 0.69°, respectively.

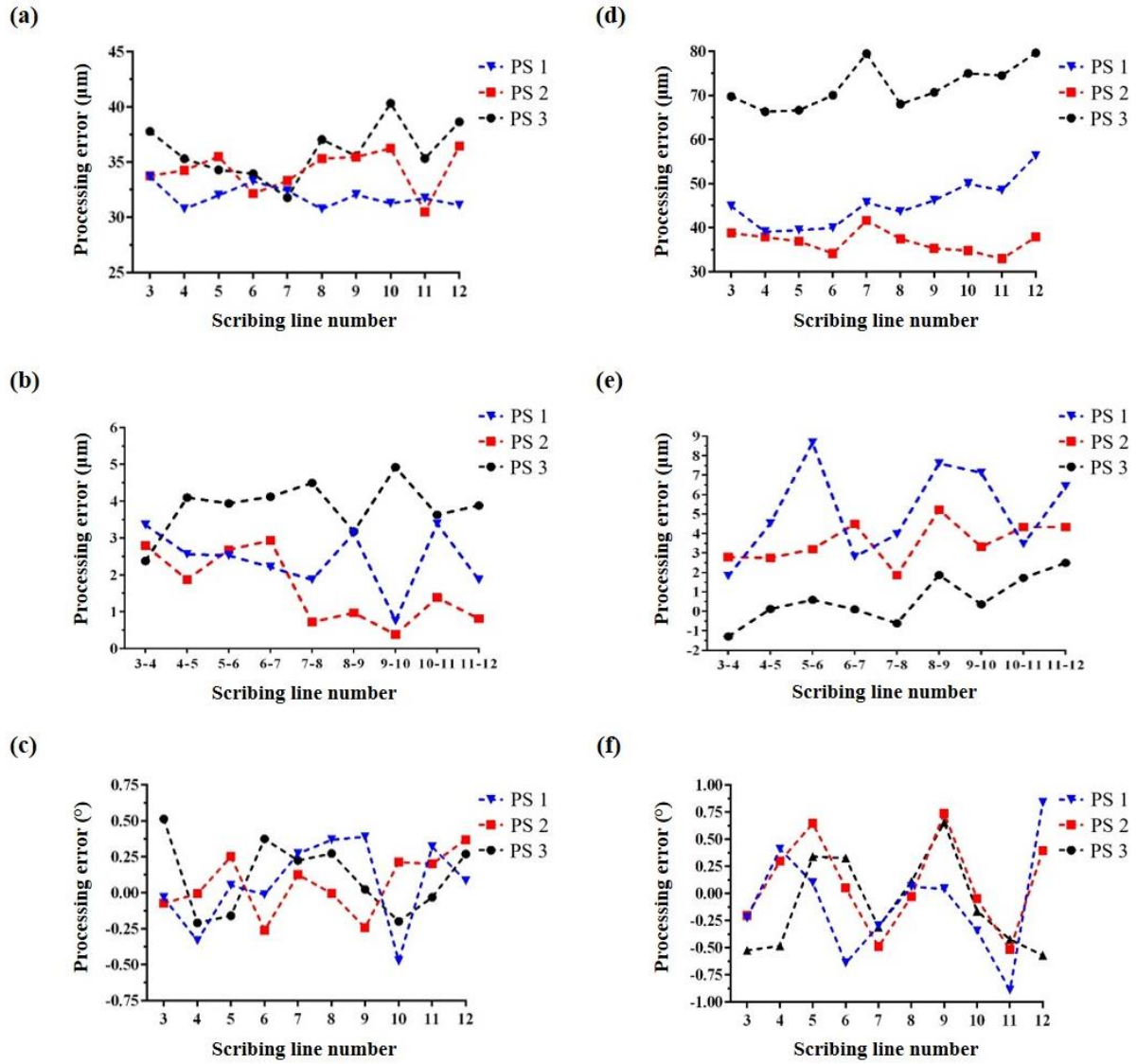

Fig. 6.13. The effects of multi-axis processing errors on d_1, d_2 and g of the scribing lines produced in LPT 2 under quasi-static (a-c) and dynamic (e-f) conditions, respectively.

6.4.5.3. Laser processing test 3 and 4

These LPTs aimed to assess the processing ARR achievable when simultaneous 6-axis movements are required to execute a given LMM strategy. Fig. 6.14 presents the measurement results obtained from the scribing lines processed at a quasi-static conditions, especially at a lower scanning speed of 10 mm/s. Fig. 6.14a-c displays the deviation of actual measurements from the programmed values for the lines scribed using the diagonal 45° scanning strategy.

The analysis of the three Pattern Sets showed that the maximum deviation of d_1 was 62.3 μm. At the same time, the maximum absolute error with regard to d_2, i.e. the relative distances achieved with two consecutive beam vectors, was 5.0 μm, whilst their deviation from g was 0.52°. On the other hand, the dimensional accuracy of the three patterns produced with the diagonal -45° scanning strategy in LPT 4 was better as it is shown in Fig. 6.14d-f. It can be seen in Fig. 6.14d-f that the dimensional accuracy with regard to the scribing lines' d_1 had improved and was better than 45.8 μm. The same applied to the scribing lines' d_2 and g, as the deviations from the programmed values were smaller than those in LPT 3. More specifically, the error regarding d_2 was less than 2.9 μm, whilst their deviation from g was less than 0.38° on the two samples. Therefore, it can be stated that the processing accuracy achieved with regard to the scribing lines' d_1, d_2 and g was better than 62.3 μm, 5.0 μm and 0.52°, respectively, with both 6-axis LMM strategies in LPTs 3 and 4. Additionally, the repeatability achieved in these two LPTs was 19.5 μm, 1.2 μm and 0.48°, and 14.0 μm, 1.4 μm and 0.40° with regard to the dimensional and geometrical accuracy of PS 1 and PS 2, respectively. Thus, it can be stated that the repeatability achieved in the LPTs 3 and 4 was better than 19.5 μm, 1.4 μm and 0.48° about the scribing lines' d_1, d_2 and g, respectively. At the same time, the respective reproducibility achieved in these two tests was better than 19.6 μm, 3.3 μm and 0.48° with regard to the same dimensional and geometrical characteristics of the three Pattern Sets, respectively. Thus, it can be stated that the overall processing uncertainty, U, in producing the three patterns with the simultaneous 6-axis LMM strategies in LPTs 3 and 4 was ± 10.1 μm, ± 1.7 μm and ± 0.42° about the scribing lines' d_1, d_2 and g, respectively.

By comparing the results of LPTs 1 and 2 in Figs. 6.12 and 6.13 with those in LPTs 3 and 4, it can be seen that a lower machining ARR was attained regarding the scribing lines' d_1. The relatively lower ARR can be attributed to the varying d_1 of the beam vectors in LPTs 3 and 4.

It can be clearly seen in Fig. 6.14a and d that accuracy gradually decreases with the increase of vectors' d_1 and therefore if the processing errors are normalised, it will be very similar across all vectors' d_1. For instance, after normalising the data obtained from the scribing lines in these two tests, it can be stated that the largest deviation in their d_1 was less than 0.8%.

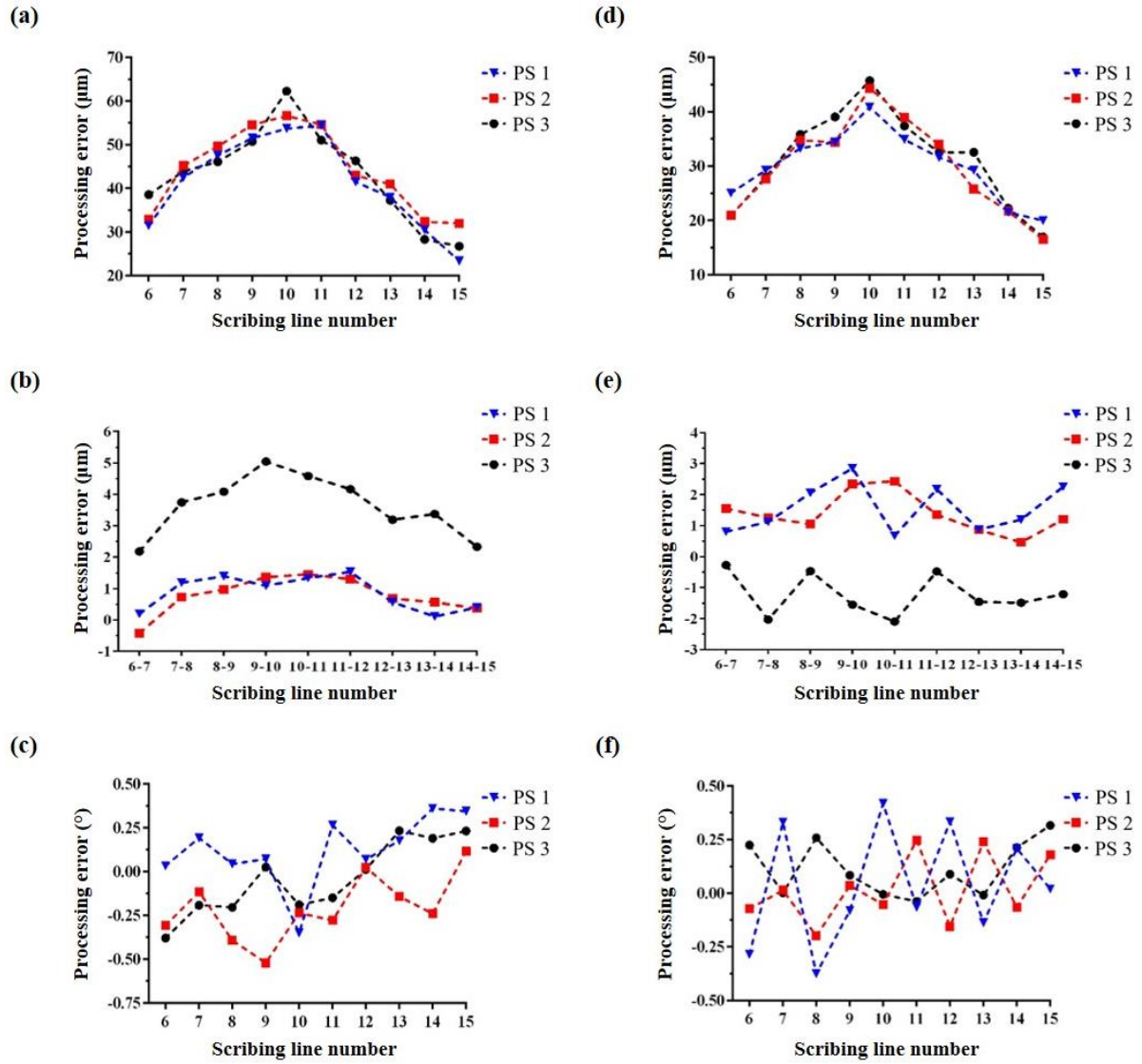

Fig. 6.14. The effects of multi-axis processing errors on d_1, d_2 and g of the scribing lines produced in LPTs 3 (a-c) and 4 (e-f) under quasi-static conditions, respectively.

The LPTs 3 and 4 were repeated at a higher scanning speed of 100 mm/s to assess, again, the dynamic performance when a simultaneous 6-axis LMM strategy is used, and the results are

provided in Fig. 6.15. Especially, Fig. 6.15a-c presents the deviations of the actual measured values from the programmed ones when the diagonal 45° LMM strategy was used in LPT 3. As expected, again, the processing errors increased and the dimensional and geometrical accuracies were better than 64.1 μm, 4.9 μm and 0.91° in regard to the scribing lines' d_1, d_2 and g on both samples, respectively. On the contrary, as it was the case with LPT 4 under the quasi-static conditions, the dynamic machining performance was better, again (see Fig. 6.15d-f). The analysis of the scribing lines of the three Pattern Sets revealed that the processing error regarding the lines' d_1 was less than 58.4 μm, whilst their deviation from g was less than 0.66°. At the same time, the machining error in regard to d_2, i.e. the relative distances between two consecutive lines, was less than 2.3 μm.

Considering the results obtained in both tests, it can be stated that the processing accuracy was better than 64.1 μm, 4.9 μm and 0.91° in regard to the scribing lines' d_1, d_2 and g, respectively, when the two 6-axis LMM strategies were used. Apart from g, it can be concluded that both LMM strategies achieved a higher accuracy under dynamic conditions compared to the results obtained in LPTs 1 and 2. The superior performance of these 6-axis LMM strategies might partly be attributed to the acceleration/deceleration effects of mechanical axes when executing the programmed beam vectors. For example, the mechanical axes had to adjust their velocity, i.e. accelerate or decelerate, to maintain the scanning speed and compensate for the different distances covered by the optical axes. Additionally, it should be stressed that the effects of multiple geometric errors together with the motion errors of each individual axis were combined and led to the processing errors in both 6-axis LMM tests. As such, some of the factors affecting the machining performance in these two tests might have cancelled each other. Therefore, it can be stated that the proposed method can be used to assess the overall

ARR of multi-axis LMM systems but cannot determine the individual contributions of the different axes employed in the tests.

As with the other two tests, the machining repeatability achieved with these two multi-axis LMM strategies was assessed, too. Especially, the repeatability achievable with LPTs 3 and 4 was less than 20.8 µm, 2.2 µm and 0.48° and 17.7 µm, 2.04 µm and 0.81° in regard to the scribing lines' d_1, d_2 and g based on the PSs 1 and 2 results, respectively. Overall, it can be stated that the two simultaneous 6-axis LMM strategies could execute complex beam paths with a repeatability better than 20.8 µm and 2.2 µm regarding the d_1 and d_2 of the scribing lines, respectively, and with a geometrical accuracy better than 0.81°. Additionally, the reproducibility achieved in these two LPTs was 23.2 µm, 2.8 µm and 0.90°, and 18.5 µm, 2.5 µm and 0.86° in regard to the scribing lines' d_1, d_2 and g based on the average results from PSs 1, 2 and 3 on the two samples, respectively. Thus, it can be stated that the two simultaneous 6-axis LMM strategies could execute complex beam paths with a reproducibility better than 23.2 µm and 2.8 µm regarding the d_1 and d_2 of the scribing lines, respectively, while regarding their geometrical accuracy it was better than 0.86°. Overall, the processing uncertainty, U, regarding the d_1 and d_2 of the scribing lines produced with these complex multi-axis LMM strategies was ± 11.1 µm and ± 2.02 µm, respectively, and ± 0.72° regarding their geometrical accuracy.

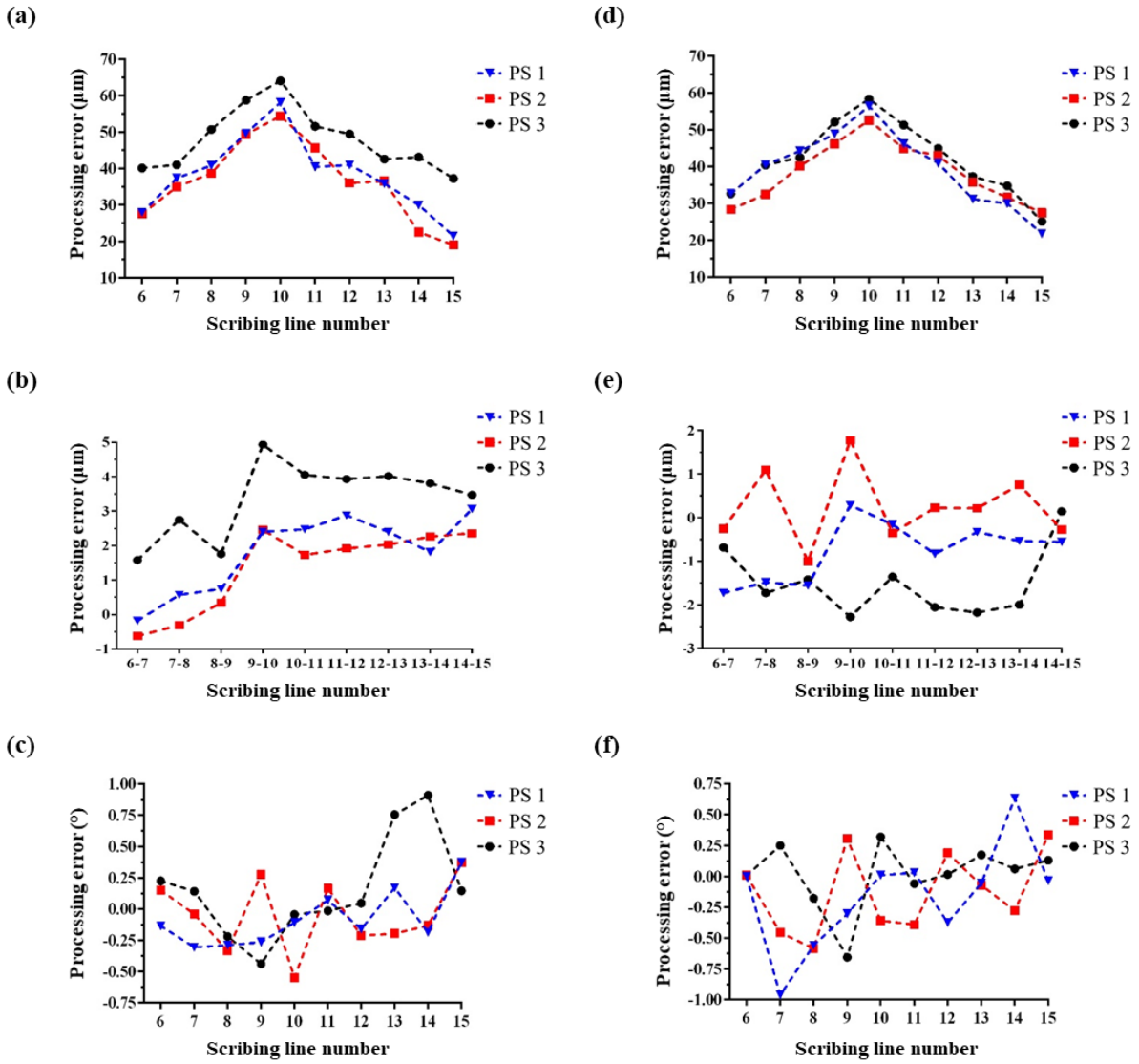

Fig. 6.15. The effects of multi-axis processing errors on d_1, d_2 and g of the scribing lines produced in LPTs 3 (a-c) and 4 (e-f) under dynamic conditions, respectively.

6.5. Conclusions

A novel method for assessing the capabilities of multi-axis LMM systems is presented in this paper, especially when executing complex laser processing strategies. The method requires a series of LPTs to be performed on spherical samples when both optical and mechanical axes are used simultaneously. These tests are then employed to investigate and compare the

achievable ARR capabilities of such processing strategies under both quasi-static and dynamic conditions. Especially, the tests include strategies requiring the simultaneous use of all possible combinations of optical and mechanical axes available in a given LMM system. By employing this method, the influence of multiple error sources on achievable dimensional and geometrical ARR can be determined when executing any simultaneous multi-axis LMM strategy feasible on a given LMM system. However, some preliminary trials have to be conducted to implement efficiently the proposed test procedure for a given multi-axis LMM system. Especially, they are important for determining the effective processing window of the integrated laser source, compensating the negative dynamic effects of optical axes and also minimising the measurement uncertainty in quantifying their processing capabilities.

The pilot implementation of the proposed method demonstrates what ARR data could be obtained about any multi-axis LMM strategies when executing processing strategies employing the simultaneous use of up to 6 optical and mechanical axes. In addition, the systematic analysis of the obtained results made possible some generic conclusions to be made about the capabilities of multi-axis LMM systems. Especially, the experimental results revealed that systematic errors were mostly responsible for the relatively low dimensional accuracy in executing multi-axis processing strategies. Therefore, it could be stated in general that the overall system performance of such LMM systems can be improved, substantially, by compensating them. In contrast, it could be stated that the geometrical accuracy achievable with different simultaneous multi-axis LMM strategies could be very similar. However, the respective repeatability and reproducibility achieved could be lower when compared with the dimensional one. In general, the increase of processing speed could lead to an increase of negative dynamic effects on the machining performance of the multi-axis LMM system. When assessing their ARR capabilities, it should be noted that combined processing errors due to the

use of different optical and mechanical axes simultaneously are coming into play and they are due to a range of systematic and stochastic factors. Thus, it can be stated that the proposed method can be a valuable tool for assessing the combined effects of multiple geometric errors together with the motion errors of individual axis. Therefore, as such, some of the factors affecting the multi-axis processing performance might cancel each other and these effects could be more pronounced in 6-axis LMM tests. So, it should be stressed that the proposed method can assess, mostly, the overall ARR of multi-axis LMM systems and not the individual contributions of employed optical and mechanical axis. Accordingly, it is reasonable to conclude that this method is more suitable for assessing the overall ARR achievable with such systems. Especially, the proposed methodology can be used after the installation of a given multi-axis LMM system on-site and then after any changes of its multi-axis configuration or after specific time periods to make sure that its overall performance is still within acceptable limits.

Further research should be conducted to evaluate other factors affecting ARR of LMM systems. For instance, the machining accuracy achievable over larger surface areas exceeding the focusing lenses' FOV will be affected by the stitching errors between the processing fields, especially when processing freeform surfaces. Therefore, such stitching errors should be investigated, and ways to minimise them when executing multi-axis LMM strategies have to be proposed. Also, the machining capabilities of LMM systems should be assessed in simultaneous multi-axis strategies that require sharp changes in the motion trajectory of rotary axes and thus to better account for their dynamic performance.

Acknowledgments

The research reported in this paper was supported by a H2020 Factory of the Future projects, “High-Impact Injection Moulding Platform for mass-production of 3D and/or large micro-structured surfaces with Antimicrobial, Self-cleaning, Anti-scratch, Anti-squeak and Aesthetic functionalities” (HIMALAIA) (grant no. 766871). The authors would like to thank the Manufacturing Technology Centre (MTC) for the financial support of Themistoklis Karkantonis’s Ph.D. research and acknowledge also the collaboration with LASEA SA, Belgium within the framework of the ESIF project “Smart Factory Hub” (SmartFub) (grant no. 50R18P02795).

References

[1] J. Zettl, M. Klar, S. Rung, C. Esen, and R. Hellmann, "Laser turning with ultrashort laser pulses," *Journal of Manufacturing Processes,* vol. 68, pp. 1562-1568, 2021.

[2] B. Z. Balázs, N. Geier, M. Takács, and J. P. Davim, "A review on micro-milling: recent advances and future trends," *The International Journal of Advanced Manufacturing Technology*, vol. 112, no. 3, pp. 655-684, 2021.

[3] Y. Qin *et al.*, "Micro-manufacturing: research, technology outcomes and development issues," *The International Journal of Advanced Manufacturing Technology,* vol. 47, no. 9, pp. 821-837, 2010.

[4] S. Zhang, Y. Zhou, H. Zhang, Z. Xiong, and S. To, "Advances in ultra-precision machining of micro-structured functional surfaces and their typical applications," *International Journal of Machine Tools and Manufacture,* vol. 142, pp. 16-41, 2019.

[5] P. Penchev *et al.*, "System-level integration tools for laser-based powder bed fusion enabled process chains," *Journal of Manufacturing Systems,* vol. 50, pp. 87-102, 2019.

[6] A. Piqué, R. C. Y. Auyeung, H. Kim, N. A. Charipar, and S. A. Mathews, "Laser 3D micro-manufacturing," *Journal of Physics D: Applied Physics,* vol. 49, no. 22, p. 223001, 2016.

[7] Y. Lin *et al.*, "Durable and robust transparent superhydrophobic glass surfaces fabricated by a femtosecond laser with exceptional water repellency and thermostability," *Journal of Materials Chemistry A,* vol. 6, no. 19, pp. 9049-9056, 2018.

[8] J. G. A. B. Simões, R. Riva, and W. Miyakawa, "High-speed Laser-Induced Periodic Surface Structures (LIPSS) generation on stainless steel surface using a nanosecond pulsed laser," *Surface and Coatings Technology,* vol. 344, pp. 423-432, 2018.

[9] M. Friedrich, M. Seiler, S. Waechter, J. Bliedtner, and J. P. Bergmann, "Precision structuring and functionalization of ceramics with ultra-short laser pulses," *Journal of Laser Applications,* vol. 30, no. 3, p. 032501, 2018.

[10] A. Riveiro, A. L. B. Maçon, J. del Val, R. Comesaña, and J. Pou, "Laser Surface Texturing of Polymers for Biomedical Applications," *Frontiers in Physics,* vol. 6, no. 16, 2018.

[11] Y. Lee *et al.*, "Lubricant-infused directly engraved nano-microstructures for mechanically durable endoscope lens with anti-biofouling and anti-fogging properties," *Scientific Reports,* vol. 10, no. 1, p. 17454, 2020.

[12] G. Xin, C. Wu, W. Liu, Y. Rong, and Y. Huang, "Anti-corrosion superhydrophobic surfaces of Al alloy based on micro-protrusion array structure fabricated by laser direct writing," *Journal of Alloys and Compounds,* vol. 881, p. 160649, 2021.

[13] S. A. Jalil *et al.*, "Creating superhydrophobic and antibacterial surfaces on gold by femtosecond laser pulses," *Applied Surface Science,* vol. 506, p. 144952, 2020.

[14] W. Xing, Z. Li, H. Yang, X. Li, X. Wang, and N. Li, "Anti-icing aluminum alloy surface with multi-level micro-nano textures constructed by picosecond laser," *Materials & Design,* vol. 183, p. 108156, 2019.

[15] T. Chen, W. Wang, T. Tao, A. Pan, and X. Mei, "Broad-Band Ultra-Low-Reflectivity Multiscale Micro–Nano Structures by the Combination of Femtosecond Laser Ablation and In Situ Deposition," *ACS Applied Materials & Interfaces,* vol. 12, no. 43, pp. 49265-49274, 2020.

[16] T. Karkantonis, A. Gaddam, T. L. See, S. S. Joshi, and S. Dimov, "Femtosecond laser-induced sub-micron and multi-scale topographies for durable lubricant impregnated

surfaces for food packaging applications," *Surface and Coatings Technology,* vol. 399, p. 126166, 2020.

[17] A. Klos *et al.*, "Ultrafast Laser Processing of Nanostructured Patterns for the Control of Cell Adhesion and Migration on Titanium Alloy," *Nanomaterials,* vol. 10, no. 5, p. 864, 2020.

[18] L. Orazi, R. Pelaccia, O. Mishchenko, B. Reggiani, and M. Pogorielov, "Fast LIPSS based texturing process of dental implants with complex geometries," *CIRP Annals,* vol. 69, no. 1, pp. 233-236, 2020.

[19] K. E. C. Vidyasagar, V. Aggarwal, S. S. Sinha, and S. K. Saha, "Laser based micro texturing of freeform surfaces of implants using a Stewart platform," *Precision Engineering,* vol. 72, pp. 294–303, 2021.

[20] J. Dong, M. Pacella, Y. Liu, and L. Zhao, "Surface engineering and the application of laser-based processes to stents - A review of the latest development," *Bioactive Materials,* vol. 10, pp. 159-184, 2022.

[21] R. Moreddu, V. Nasrollahi, P. Kassanos, S. Dimov, D. Vigolo, and A. K. Yetisen, "Lab-on-a-Contact Lens Platforms Fabricated by Multi-Axis Femtosecond Laser Ablation," *Small,* vol. 17, no. 38, p. 2102008, 2021.

[22] M. Jiang, X. Wang, S. Ke, F. Zhang, and X. Zeng, "Large scale layering laser surface texturing system based on high speed optical scanners and gantry machine tool," *Robotics and Computer-Integrated Manufacturing,* vol. 48, pp. 113-120, 2017.

[23] G. Cuccolini, L. Orazi, and A. Fortunato, "5 Axes computer aided laser milling," *Optics and Lasers in Engineering,* vol. 51, no. 6, pp. 749-760, 2013.

[24] A. Batal, A. Michalek, P. Penchev, A. Kupisiewicz, and S. Dimov, "Laser processing of freeform surfaces: A new approach based on an efficient workpiece partitioning

strategy," *International Journal of Machine Tools and Manufacture,* vol. 156, p. 103593, 2020.

[25] X. Wang, J. Duan, M. Jiang, S. Ke, B. Wu, and X. Zeng, "Study of laser precision ablating texture patterns on large-scale freeform surface," *The International Journal of Advanced Manufacturing Technology,* vol. 92, no. 9, pp. 4571-4581, 2017.

[26] A. Michalek *et al.*, "Modelling ultrafast laser structuring/texturing of freeform surfaces," *Applied Surface Science Advances,* vol. 2, p. 100036, 2020.

[27] D. Bhaduri, P. Penchev, S. Dimov, and S. L. Soo, "An investigation of accuracy, repeatability and reproducibility of laser micromachining systems," *Measurement,* vol. 88, pp. 248-261, 2016.

[28] B. Daemi, P. Ekberg, and L. Mattsson, "Lateral performance evaluation of laser micromachining by high precision optical metrology and image analysis," *Precision Engineering,* vol. 50, pp. 8-19, 2017.

[29] P. Penchev, S. Dimov, D. Bhaduri, and S. L. Soo, "Generic integration tools for reconfigurable laser micromachining systems," *Journal of Manufacturing Systems,* vol. 38, pp. 27-45, 2016.

[30] C. Hong, S. Ibaraki, and A. Matsubara, "Influence of position-dependent geometric errors of rotary axes on a machining test of cone frustum by five-axis machine tools," *Precision Engineering,* vol. 35, no. 1, pp. 1-11, 2011.

[31] V. Nasrollahi, P. Penchev, S. Dimov, L. Korner, R. Leach, and K. Kim, "Two-Side Laser Processing Method for Producing High Aspect Ratio Microholes," *Journal of Micro and Nano-Manufacturing,* vol. 5, no. 4, 2017.

[32] S. Ibaraki, S. Tsujimoto, Y. Nagai, Y. Sakai, S. Morimoto, and Y. Miyazaki, "A pyramid-shaped machining test to identify rotary axis error motions on five-axis

machine tools: software development and a case study," *The International Journal of Advanced Manufacturing Technology,* vol. 94, no. 1, pp. 227-237, 2018.

[33] Z. Su and L. Wang, "Latest development of a new standard for the testing of five-axis machine tools using an S-shaped test piece," *Proceedings of the Institution of Mechanical Engineers, Part B: Journal of Engineering Manufacture,* vol. 229, no. 7, pp. 1221-1228, 2015.

[34] N. Huang, Y. Jin, X. Li, L. Liang, and S. Wu, "Identification of integrated geometric errors of rotary axis and setup position errors for 5-axis machine tools based on machining test," *The International Journal of Advanced Manufacturing Technology,* vol. 102, no. 5, pp. 1487-1496, 2019.

[35] Z. Zhang, Q. Cheng, B. Qi, and Z. Tao, "A general approach for the machining quality evaluation of S-shaped specimen based on POS-SQP algorithm and Monte Carlo method," *Journal of Manufacturing Systems,* vol. 60, pp. 553-568, 2021.

[36] J. Noh, J. Suh, and S. Na, "Fabrication of Microgrooves on Roll Surfaces Using a Scanner and a Telecentric Lens," *Japanese Journal of Applied Physics,* vol. 49, no. 5, p. 05EC01, 2010.

[37] M. Pothen, K. Winands, and F. Klocke, "Compensation of scanner based inertia for laser structuring processes," *Journal of Laser Applications,* vol. 29, no. 1, p. 012017, 2017.

[38] P. Penchev, S. Dimov, D. Bhaduri, S. L. Soo, and B. Crickboom, "Generic software tool for counteracting the dynamics effects of optical beam delivery systems," *Proceedings of the Institution of Mechanical Engineers, Part B: Journal of Engineering Manufacture,* vol. 231, no. 1, pp. 48-64, 2017.

[39] A. Garcia-Giron, J. M. Romano, A. Batal, A. Michałek, P. Penchev, and S. S. Dimov, "Experimental investigation of processing disturbances in laser surface patterning," *Optics and Lasers in Engineering*, vol. 126, p. 105900, 2020.

[40] L. Overmeyer, J. F. Duesing, O. Suttmann, and U. Stute, "Laser patterning of thin film sensors on 3-D surfaces," *CIRP Annals*, vol. 61, no. 1, pp. 215-218, 2012.

[41] "Uncertainty of Measurement–Part 3: Guide to the Expression of Uncertainty in Measurement (GUM: 1995)," ISO/IEC 98-3:2008, 2008.

[42] G. Tosello, F. Marinello, and H. N. Hansen, "Characterisation and analysis of microchannels and submicrometre surface roughness of injection moulded microfluidic systems using optical metrology," *Plastics, Rubber and Composites*, vol. 41, no. 1, pp. 29-39, 2012.

CHAPTER 7: CONTRIBUTIONS TO KNOWLEDGE AND FUTURE RESEARCH

This chapter summarises the major contributions to knowledge that are claimed in this PhD research. Moreover, potential future work and research directions are disclosed, too.

7.1. Contributions to knowledge

The overall aim of this PhD research was to broaden the use of the LMM technology for functionalising surfaces at an industrial scale. The cost-effective fabrication of such surfaces in a sustainable manner was achieved by combining LMM with polymer micro/nano replication followed by lubricant infiltration into a process chain. Several functional characteristics of the as-prepared thermoplastic LIS were considered, such as anti-adhesive/antifouling, anti-fogging and optical properties, to demonstrate their potential. In particular, the suitability of such treated surfaces for food packaging applications was presented in **Chapter 3** while their effectiveness to prevent vision loss during endoscopy was demonstrated in **Chapter 4.** The effects of surface topography and lubricant viscosity on LIS functionality and durability were investigated in these two chapters, too. A laser surface treatment was proposed in **Chapter 5** that enables the cost-effective generation of highly regular and uniform sub-wavelength structures by employing a green nanosecond pulsed laser and thus to reduce even further the manufacturing costs in producing polymer replicas with functional topographies. Finally, a generic methodology for assessing the capabilities and limitations of multi-axis laser processing strategies for texturing/structuring of complex 3D surfaces is proposed and its pilot implementation for a given multi-axis LMM system was presented in **Chapter 6**.

The objectives stated in the Introduction Chapter were fully met and the contributions to knowledge claimed are as follows:

1. *Develop an efficient and cost-effective manufacturing process chain for producing recyclable polymer LIS.*
    - Instead of using complex and potentially environmentally harmful manufacturing processes, a one-step laser surface treatment was developed and validated for fabricating two different length scale structures onto SS replication masters (**Chapters 3 and 4**). To obtain these surface topographies, various laser parameters, i.e. fluence, hatch distance, pulse overlap and number of repeated scans, were investigated and then optimum processing conditions were determined. Highly regular and homogeneous LIPSS with a periodicity in the range of 800 to 900 nm and an amplitude varying from 100 to 200 nm were generated using a linearly polarised ultrashort pulsed laser source. The same laser processing setup was also utilised to attain two-tier MS topographies. In this case, microscale protrusions fully covered with nanoscale ripple-like structures were formed on the SS surface. The spacing of these ripples was very similar to that of LIPSS, whilst their amplitude was two times smaller. On the other hand, the periodicity and height of the grid-like microtopography was defined by the hatch distance and number of repeated scans.
    - A cost-effective and scalable process for producing polymer substrates with textured surfaces by replicating LMM generated functional topographies was designed and validated (**Chapters 3 and 4**). Following an optimisation procedure, the two surface topographies “imprinted” onto the SS masters were successfully replicated onto thermoplastics through hot embossing. Overall, it was demonstrated that the replication

fidelity achieved with this process was better than 14% when the deviations of topographies on replicas were compared with those on the masters.

- A simple and fast procedure was proposed to prepare stable LIS and thus to impart anti-fouling functionalities (**Chapters 3 and 4**). To accelerate the lubricant impregnation process, the textured replicas were fully wetted with silicone-based oils, which are biocompatible and safe to use as food additives, and then stored in a vacuum chamber for 15 min. Unlike other manufacturing methods reported in literature, no chemicals or coatings were required throughout the proposed process chain and hence the as-prepared functional polymers can be considered less harmful to the ecosystem.

2. *Investigate the functional properties and durability of the as-prepared polymer LIS.*

- The wettability of the as-received, textured and LIS thermoplastic substrates was characterised (**Chapters 3 and 4**). The plain surfaces of all the thermoplastic substrates studied in this research were slightly hydrophobic. However, a considerable increase in CA was observed when the laser textured SS masters were embossed onto them. The alteration of surface topography was responsible for the change in CA on the thermoplastic substrates. In general, the surfaces covered with MS structures led to higher CA values compared to those with LIPSS. After infusing the lubricant oil into the textured replicas, the apparent CA was reduced and also marginal differences were observed between the two different length scale topographies.
- The shedding behaviour of water droplets was firstly investigated by measuring both CSA and CAH. A low droplet mobility was detected on all the as-received thermoplastics and droplet motion was initiated at average CSAs in the range from 18° to 40°. On the contrary, the water droplets completely adhered to the polymer replicas, with CSA values more than 90°. Thus, only the alteration of surface topography was not

sufficient to impart an anti-adhesive functionality. However, all the LIS samples exhibited great water-repellency since the droplets slid on their surfaces at an average CSA and CAH below 15° and 10°, respectively. To simulate the functional response of the as-prepared polymer LIS under the proposed use scenarios, their shedding characteristics were also characterised against various food, biological and viscous liquids. At the same time, their anti-adhesive performance against fluids with different pH levels was evaluated, too. The findings of these investigations were reported in **Chapters 3 and 4**, where the impressive shedding capabilities of the thermoplastic LIS produced with LIPSS are demonstrated.

- The optical properties of all treated transparent thermoplastic surfaces together with as-received/untreated substrates were analysed using standardised methods (**Chapter 4**). The textured replicas had significantly low transmittance due to their rough surface topographies, especially because of their light scattering response. Since such effect is typically more intense on surfaces with micro-roughness, the samples with LIPSS were less opaque compared to the MS ones. Overall, these results suggested that the as textured polymer replicas could not meet the requirements of optical lenses. On the other hand, the LIS samples exhibited higher transmittance, which was partly attributed to the light scattering reduction by the infused lubricant. However, only the LIPSS-LIS substrates attained an excellent transparency, resulting in less than 10% reduction when compared with that achieved on as-received/untreated thermoplastic substrates. In addition, as shown in **Chapter 4,** relatively common methods were employed to explore other surface functionalities of these samples. Specifically, it was demonstrated that the LIPSS-LIS substrates also exhibited a great ability to inhibit protein adsorption, fog formation and microalgae formation.

- The degradation of LIS properties was assessed by following accepted methods that used to quantify their durability, i.e. when exposed to shear loadings and bulk liquids **(Chapter 3 and 4)**. In addition, the LIS durability was investigated against vibration-induced forces, which has not been studied previously. All the aforesaid test conditions led to a serious lubricant depletion on MS topographies, which had a major impact on LIS functionality. Instead, the LIS substrates produced with LIPSS preserved their anti-adhesive characteristics even after subjecting them to vibration for 5 minutes, and also sustained the shear forces from a high number of droplets. Moreover, these samples exhibited a better fouling resistance against both Newtonian and non-Newtonian liquids, too. The superior functional response of LIPSS-LIS substrates was attributed to the stronger capillary forces induced by their narrower cavities when compared to that of MS ones. Finally, the influence of lubricant viscosity on the functional performance of LIS was analysed, too **(Chapter 4)**. This investigation revealed that high viscosity lubricants were depleted at a much slower rate from the impregnated structures and thus can be used to enhance the performance of LIS.

3. *Investigate the influence of processing environment on LIPSS generated with green nanosecond laser.*

- For the first time, a cost-effective laser surface treatment was proposed to improve the quality and homogeneity of LIPSS with short pulsed lasers **(Chapter 5)**. The method involved laser processing in a controlled gas environment to mitigate the thermal side effects associated with such lasers. The concept was validated on SS surfaces by using a linearly polarised green nanosecond laser. The formation of LIPSS over relatively large surface was initially investigated upon irradiation in ambient conditions and then compared to those generated in argon gas.

- The effects of two critical laser parameters, i.e. pulse fluence and the number of pulses per unit area, were studied to assess the evolution of LIPSS on the surface and an effective processing window for their formation was determined. 2D-FFT analysis of LIPSS images showed that there was no significant influence of the processing environment on LIPSS spatial periodicity and orientation, which were found to be close to the operating wavelength and perpendicular to the laser beam polarisation, respectively.

- The quality and homogeneity of LIPSS generated in both environmental conditions were evaluated through microscopy analysis. Moreover, a correlation between LIPSS quality and their diffracted light intensity was established. It was revealed for first time that LIPSS formed in a controlled argon gas environment exhibited not only less surface defects but also higher amplitude ripples compared to those in air. The improved overall quality of LIPSS produced in argon was also verified by the higher diffracted light intensity obtained from their surfaces.
- The surface chemistry of LIPSS substrates produced with a green pulsed nanosecond laser in both gas environments was studied in detail, since it has not been reported previously. XPS analysis revealed that the ratio of oxygen to metal species decreased when the samples were processed in the argon atmosphere, and thus the surface oxidation was minimal. As a result, the relatively low-quality of LIPSS produced in air was mainly attributed to the formation of oxides as a side effect of nanosecond laser processing.
- The wetting properties of LIPSS generated in both processing environments were characterised. The findings of this research suggested that the combined effects of surface topography and chemistry were responsible for the higher CA obtained 3 days

after the fabrication of LIPSS in argon gas compared to those in air. However, the differences between them were marginal.

4. *Develop a method for assessing the capabilities of multi-axis LMM systems for processing complex 3D components.*

   A novel generic method was developed for assessing the performance of multi-axis LMM systems when processing freeform/curved surfaces. Specifically, a series of tests were designed to investigate the achievable ARR of LMM systems under quasi-static and dynamic conditions when executing simultaneous multi-axis strategies that involve both mechanical and optical axes motions. A pilot implementation of this method was demonstrated on a representative multi-axis LMM system that could execute such processing tests, and the main findings are as follows **(Chapter 6)**:

- Line-like structures were produced on the surface of spherical samples in all the test strategies but with different axes combinations. The width of these lines was depended on the beam spot size, whilst their length was defined by the predetermined maximum FOD limit. A measurement procedure was proposed to quantify the dimensional and geometrical accuracy of the scribing lines in a reliable manner, and then these results were used to judge about the processing capabilities of multi-axis LMM systems.
- Systematic errors were mostly responsible for the relatively low dimensional accuracy in executing simultaneous multi-axis processing strategies, and thus the overall system performance can be improved significantly by applying specifically designed corrective actions/commands. On the contrary, the geometrical accuracy achievable with the different simultaneous multi-axis LMM strategies was very similar. However, the results revealed that the geometrical deviations were mainly ascribed to random error sources,

which would be difficult to compensate/reduce without increasing the overall processing performance of the LMM system.

- The increase of processing speed led to an increase of negative dynamic effects on the machining performance of the multi-axis LMM system. Thus, dynamic errors can become a major obstacle for the broader use of such systems, especially in applications where high-throughput is required.
- The proposed method proved to be a valuable tool for assessing and then improving the overall performance of multi-axis LMM systems after their installation on-site. However, it cannot be used to quantify the individual contributions of each employed optical and mechanical axis.

7.2. Future research

Based on the investigations conducted in this PhD research, some new directions for future research have been identified:

1. The thermoplastic LIS produced with LIPSS exhibited great anti-adhesive properties against non-Newtonian liquids, and their suitability for food packaging and optical lenses was demonstrated. However, more in-depth research is needed to further optimise their overall performance. For instance, the functionality and durability of such LIS could be enhanced by properly tailoring the geometrical and dimensional characteristics of LIPSS. At the same time, the functional response of thermoplastic LIS with triangular LIPSS could be evaluated, too, and thus to minimise or eliminate any anisotropic surface properties that can affect the lubricant depletion and consequently improve the LIS durability.
2. In this research, the intensity of first-order diffracted light was proved to be a key indicator of LIPSS regularity and homogeneity. Since the captured intensity mainly depends on the

LIPSS morphology, further efforts are required to better understand their interdependences and identify correlations between them. Then, light diffraction can be used as a qualitative tool to judge about LIPSS topographical characteristics, and thus eliminating the need for conducting time-consuming local measurements, such as SEM and AFM.

3. Considering the geometrical and dimensional characteristics of LIPSS generated with the green nanosecond laser, such structures can be used for imprinting attractive functionalities to surfaces. In particular, the proposed LIPSS treatment could be a potentially cost-effective solution for fabricating surfaces with anti-reflective functionalities. For example, one such application could be the manufacture of broad-band ultralow optical reflective surfaces. Thus, further in-depth research should be focused on investigating the functional responses, e.g. optical and anti-bacterial properties, of as-prepared laser-induced structures.
4. Future research should be carried out to assess other factors affecting the machining performance of multi-axis LMM systems. Firstly, the ARR achievable when processing relatively large surface areas, i.e. those exceeding either the focusing lenses' FOV or the laser's effective area, onto freeform components will be affected by the stitching errors between the scanning fields. Therefore, such stitching errors should be investigated, and then strategies to eliminate them should be designed. One such possible solution could be to randomise the starting and end positions of the beam vectors in the boundary/overlapping regions between two scanning fields. Secondly, to get a better indication of the LMM systems' dynamic response, their processing capabilities should also be tested when executing simultaneous multi-axis strategies with sharp changes in the motion trajectories of rotary axes.

APPENDIX

Table A.1. The water CA and CSA values measured on all the tested plain surfaces.

Material	CA	CSA
X6Cr17 ferritic SS	93.8° ± 1.6°	Pinning (90°)
AISI 316 SS	71.2° ± 1.2°	Pinning (90°)
PS	98.5° ± 2.1°	37.0° ± 2.3°
PP	108.0° ± 1.2°	18.4° ± 2.0°
PC	91.0° ± 1.4°	32.0° ± 4.5°
COC	93.3° ± 2.9°	28.4° ± 1.5°

Table A.2. The water CA and CSA values measured on all the textured topographies.

Material	Surface topography			
	MS		LIPSS	
	CA	CSA	CA	CSA
X6Cr17 ferritic SS	137.9° ± 2.7°	Pinning (90°)	112.7° ± 1.3°	Pinning (90°)
PS	130.7° ± 2.8°	Pinning (90°)	104.0° ± 1.6°	78° ± 2.0°
PP	138.4° ± 1.8°	Pinning (90°)	112.9° ± 2.5°	62.6° ± 6.0°
PC	127.3° ± 2.1°	Pinning (90°)	106.7° ± 1.2°	Pinning (90°)
COC	130.7° ± 1.2°	Pinning (90°)	113.7° ± 1.2°	Pinning (90°)

Table A.3. The water CA measurements obtained from all the different LIS substrates.

Material	Surface topography	
	MS-LIS	LIPSS-LIS
X6Cr17 ferritic SS	100.9° ± 2.1°	109.5° ± 2.3°
PS	103.1° ± 1.3°	105.5° ± 0.9°
PP	104.8° ± 1.4°	104.2° ± 2.2°
PC	102.0° ± 1.0°	104.5° ± 0.5°
COC	103.0° ± 1.0°	104.5° ± 1.5°

Table A.4. The water CSA and CAH values measured on the various LIS substrates.

Material	Surface topography			
	MS-LIS		LIPSS-LIS	
	CSA	CAH	CSA	CAH
X6Cr17 ferritic SS	8.4° ± 2.0°	4.9° ± 1.0°	2.8° ± 1.0°	3.0° ± 1.1°
PS	6.8° ± 1.7°	3.5° ± 1.2°	9.4° ± 2.1°	4.0° ± 1.0°
PP	7.6° ± 0.8°	4.5° ± 0.5°	5.2° ± 1.6°	3.0° ± 1.0°
PC	12.4° ± 2.1°	11.0° ± 1.6°	5.0° ± 0.7°	6.3° ± 1.2°
COC	8.2° ± 2.3°	9.7° ± 1.2°	3.3° ± 0.8°	5.3° ± 0.5°

Table A.5. The CSA values of milk and honey droplets measured on the plain, textured and LIS topographies of SS, PS and PP substrates.

Surface topography	Material		
	X6Cr17 ferritic SS	PS	PP
	Milk		
Plain	45.0° ± 4.5°	38.4° ± 3.0°	33.0° ± 0.9°
MS	Pinning (90°)	Pinning (90°)	Pinning (90°)
LIPSS	Pinning (90°)	Pinning (90°)	Pinning (90°)
MS-LIS	4.0° ± 1.0°	31.9° ± 2.0°	9.8° ± 1.3°
LIPSS-LIS	2.0° ± 0.5°	24.2° ± 2.7°	9.4° ± 2.2°
	Honey		
Plain	32.0° ± 3.0°	38.0° ± 2.1°	42.0° ± 3.0°
MS	Pinning (90°)	Pinning (90°)	Pinning (90°)
LIPSS	Pinning (90°)	Pinning (90°)	Pinning (90°)
MS-LIS	12.8° ± 0.7°	13.0° ± 0.9°	12.4° ± 1.0°
LIPSS-LIS	5.8° ± 0.7°	7.6° ± 1.4°	4.6° ± 1.0°

Table A.6. The CSA values of water, milk and honey droplets measured on the various LIS substrates after subjecting them to vibrations.

Surface topography	Material		
	X6Cr17 ferritic SS	PS	PP
	Water		
MS-LIS	Pinning (90°)	44.8° ± 4.3°	20° ± 1.2°
LIPSS-LIS	18.5° ± 5.2°	11.0° ± 1.6°	4.5° ± 0.5°
	Milk		
MS-LIS	61.0° ± 0.7°	77.5° ± 2.4°	66.0° ± 4.6°
LIPSS-LIS	25.8° ± 1.5°	34.7° ± 3.7°	15.5° ± 2.0°
	Honey		
MS-LIS	13.0° ± 0.6°	13.4° ± 0.5°	14.8° ± 1.0°
LIPSS-LIS	6.2° ± 0.7°	8.6° ± 1.0°	5.4° ± 0.5°

Table A.7. The CSA values obtained from the plain, textured and LIS topographies of PC and COC substrates for droplets of Xanthan Gum solution.

Surface topography	Material	
	PC	COC
Plain	46.0° ± 0.8°	37.0° ± 2.2°
MS	Pinning (90°)	Pinning (90°)
LIPSS	Pinning (90°)	Pinning (90°)
MS-LIS	21.0° ± 1.9°	13.5° ± 1.1°
LIPSS-LIS	8.3° ± 0.4°	7.0° ± 0.7°

Table A.8. The CSA values of pH-adjusted droplets measured on the LIS of PC and COC.

pH level	Material/Surface topography			
	PC		COC	
	MS-LIS	LIPSS-LIS	MS-LIS	LIPSS-LIS
1	16.0° ± 1.6°	5.7° ± 0.5°	11.7° ± 1.2°	4.3° ± 0.5°
2	15.0° ± 1.0°	4.7° ± 0.5°	10.7° ± 0.5°	5.3° ± 0.5°
3	14.0° ± 1.6°	6.0° ± 0.0°	9.0° ± 0.8°	5.0° ± 0.8°
4	15.0° ± 1.0°	4.3° ± 0.5°	8.0° ± 0.0°	5.7° ± 0.5°
5	14.5° ± 0.5°	5.3° ± 0.9°	8.3° ± 1.2°	5.0° ± 0.8°
6	15.0° ± 1.0°	4.7° ± 0.5°	8.7° ± 0.9°	4.7° ± 0.9°
7	15.3° ± 0.9°	5.0° ± 0.8°	10.0° ± 1.6°	3.7° ± 0.5°
8	15.7° ± 1.7°	4.3° ± 0.5°	11.0° ± 1.0°	4.3° ± 0.5°
9	15.7° ± 1.7°	4.0° ± 0.0°	11.7° ± 1.2°	4.7° ± 0.9°

Table A.9. The evolution of water CA on the LIPSS produced in air and argon environments.

Time (days)	LIPSS	
	Air	Argon
1	63.7° ± 3.2°	54.5° ± 2.3°
3	69.8° ± 2.5°	71.7° ± 1.6°
5	77.1° ± 2.0°	80.1° ± 1.9°
8	81.0° ± 1.5°	85.1° ± 2.3°
10	83.4° ± 1.5°	88.9° ± 2.5°
12	85.5° ± 1.8°	90.8° ± 2.8°
15	86.9° ± 1.2°	90.3° ± 1.9°